Theranostic MRI-Active Responsive Polymer-Mesoporous Silica Nanocomposites for Hepatocellular Carcinoma

Marwa Mohamed Ibrahim Elsayed Rizk

A thesis submitted to University College London
to fulfil the requirements for the degree of
Doctor of Philosophy

Department of Chemistry
University College London
October 12th, 2023

Declaration

I, Marwa Mohamed Ibrahim Elsayed Rizk, confirm that the work presented in this thesis is my own. Where information has been derived from other sources, I confirm that this has been indicated in the thesis.

Marwa M.I Rizk, 2023

Acknowledgements

First of all, I would like to express my sincere gratitude to my supervisor, Dr Gemma-Louise Davies. This PhD journey has been extremely challenging, especially as an international student, during the pandemic, but the support I received from Gemma has made this all possible. I would also like to profoundly thank my second supervisor, Prof Gareth Williams, for his guidance, support, and reassurance over the last few years.

Dearest Davies group, I want to express how lucky I feel having met you all. It’s not always the case that you are friends first, colleagues second, but this was certainly the case here. You welcomed me from my first day arriving at UCL, and there were never any barriers concerning culture or language, you accepted me fully with open arms and hearts. To Connor, Aaron, Viliyana, Sam, Mary, Clarissa, Adila, Isabel, Mark, Fuqiang, Vytenis, Ziwei, Joe, and Aoife, thank you for everything. Especially, to Connor and Isabel for running the ICP samples, and to Aaron and Mary for all your help and training. I would also like to thank friends I’ve met at UCL, Nathalie, Natalie, Kuda and Shams, for all the late night support whilst working in the lab and providing chocolate to keep me going!

Thank you to all the collaborators, staff members, and technicians who helped me achieve this thesis, including Dr Pratik Gurnani, Prof Mauro Botta, Prof Fabio Carniato, Prof Geoff JM Parker, Dr. Mina Kim, Dr Eve Carter, Dr Rebecka Isaksson, Dr Derek MacMillan, Steve Firth, Martyn Towner, Tony Field, Ninik Smith, and Abil Aliev.

At long last, heartfelt appreciation goes out to my dearest friend and partner in the crime Dr Connor Wells. He has been a constant presence, believing in me and providing unwavering support through every step and challenge. Working tirelessly together into the late hours, he always encouraged me, assuring me that the end of this journey was within reach.

To my family in Egypt, a heartfelt thank you for always having faith in your daughter over the years and encouraging me to pursue my dreams, even when the path was challenging. Your prayers, love, and unwavering belief in me continue to drive me towards dreaming without boundaries.

أهدي هذه الرسالة إلى والدتي ووالدي وعائلتي لكل الحب و الدعم طوال هذه السنوات و الايمان بأحلامي و دفعي لتحقيقها.

شكراً جزيلاً .

(الحمد لله الذي بِنِعْمَتِهِ تتم الصالحات وبشكره تدوم النعم)

Abstract

This thesis presents a comprehensive approach to address the complicated challenges in advanced-stage treatment and early diagnosis of hepatocellular carcinoma (HCC). A multifunctional thermo-responsive system was designed using mesoporous silica nanoparticles (MSNs) as the foundational platform, loaded with doxorubicin HCl or sorafenib tosylate, and Gd^{3+}-DOTA chelates for sensitive and more accurate MRI. MSNs grafted with thermo-responsive polymers enable precise drug release and water gating, reflecting cargo release through MRI signal changes. This innovative approach aims to provide an all-in-one solution for HCC management, balancing advanced treatment options, improved bioavailability, and precise early-stage diagnostics.

In this thesis we focused on optimising drug-loading capacity within MSNs for both hydrophilic doxorubicin and hydrophobic sorafenib tosylate. By carefully considering factors such as pore channel chemistry, loading methods, solvent selection, and pore size, effective drug loading has been achieved. This optimisation served as a foundation for more efficient drug delivery systems, ultimately improving therapeutic effectiveness.

Moreover, this project delved into enhancing Gd-DOTA MRI-active theranostic MSNs. We investigated factors influencing MRI signals, including the placement of Gd-chelates within the pore channels and the influence of drug loading. Furthermore, this thesis explored the fine-tuning of the transition temperature of UCST polymers, crucial for biomedical applications, by manipulating monomer ratios and polymerisation times. This optimisation approach holds promise for future biomedical applications, contributing to progress in the field.

Furthermore, we have successfully grafted thermo-responsive polymers and linkers onto MSNs, enabling controlled drug release. These advancements, combined with promising results in cell viability assessments, suggest the potential of these theranostic systems for targeted cancer treatment. This represents significant progress in controlled drug release, ultimately leading to improved therapeutic outcomes.

In summary, this research significantly advances the field of stimuli-responsive theranostics for HCC. Key contributions include optimised drug loading techniques, refined MRI contrast agents, fine-tuning of transition temperatures for biomedical applications, and successful grafting strategies enabling controlled drug release.

Impact statement

Liver cancer is a pressing global health issue, ranking as the sixth most prevalent cancer by incidence and the third deadliest. Alarmingly, the World Health Organization (WHO) indicate a continuous rise in liver cancer cases, predicting approximately 1.3 million lives at risk by 2040. Hepatocellular carcinoma (HCC) stands out as the most predominant form, accounting for over 80% of primary liver cancer cases and driving intensive research and intervention efforts.

Sorafenib tosylate, known as NEXAVAR® oral tablets, has stood as the primary first-line treatment for advanced-stage HCC since its FDA approval in 2007. Clinical trials have demonstrated its ability to significantly extend median overall survival, although modestly by 2-3 months, compared to a placebo. Adverse effects such as hand-foot skin reaction (HFSR), fatigue, and diarrohea are common, necessitating effective management to optimise the treatment efficacy.

In the realm of diagnosis, HCC does not always require histological evidence for confirmation. Advanced medical imaging technologies, particularly magnetic resonance imaging (MRI), have substantially enhanced diagnostic capabilities, offering superior sensitivity, spatial resolution, and soft tissue contrast. However, accurate detection of small lesions in early stages remains a challenge, leading to late-stage diagnoses and less favourable treatment outcomes. Addressing these diagnostic and treatment challenges is crucial for improving patient outcomes and reducing the global burden of liver cancer.

This thesis endeavors to offer a robust solution to the multifaceted challenges encountered in both advanced-stage treatment and the early diagnosis of hepatocellular carcinoma. This will be accomplished by developing a multifunctional thermo-responsive system using mesoporous silica nanoparticles (MSNs) as the foundational platform. These MSNs will be meticulously loaded with active pharmaceutical ingredients (doxorubicin HCl or sorafenib tosylate), strategically augmented with the inclusion of Gd-DOTA chelate - an essential element for MRI. Surface grafting with thermo-responsive polymers will permit fine control over the drug release and concomitant water entry to internalised MRI-active Gd species, resulting in signal changes reflective of drug release. This innovative approach aims to deliver a comprehensive and effective solution for the management of HCC, encompassing advanced treatment options with minimal side effects, improved bioavailability, and precise early-stage diagnostics.

Table of contents

List of Abbreviations

TMB	1,3,5-trimethylbenzene
DOTA	1,4,7,10-tetraazacyclododecane-1,4,7,10-tetraacetic acid
DO3A	1,4,7,10-tetraazacyclododecane-1,4,7-triacetic acid trisodium salt
EDC	1-Ethyl-3-(3-dimethylaminopropyl)carbodiimide
DOTA-NHS-ester	2,2',2''-(10-(2-((2,5-dioxopyrrolidin-1-yl)oxy)-2-oxoethyl)-1,4,7,10-tetraazacyclododecane-1,4,7-triyl)triacetic acid
ACVA	2,2'-azobis(2-methylpropionitrile)
Aam	Acrylamide
AN	Acrylonitrile
A	Alpha
APTES	Aminopropyltriethoxysilane
Aq	Aqueous
A.U.	Arbitrary units
RGD	Arginine-glycine-aspartate
AP	Asia-Pacific
AR	Aspect ratio
AIBN	azobisisobutyronitrile
BCLC	Barcelona Clinic Liver Cancer
β	Beta
BSA	Bovine serum albumin
BET	Brunauer-Emmett-Teller
Ca^{2+}	Calcium(II)
CLIP	Cancer of the Liver Italian Program
CTAB	cetyltrimethylammonium bromide
CT	computed tomography
CA	Contrast agent
°	Degree
°C	Degree Celsius
DNA	Deoxyribonucleic acid

DCM	Dichloromethane
DTPA	Diethylenetriaminepentaacetic acid
DMF	Dimethylformamide
Dox	Doxorubicin HCl
EE	Drug entrapment efficacy
DLC	Drug loading capacity
DLS	Dynamic light scattering
TE	Echo time
T_{1e}	Electron spin relaxation time
EPR	Enhanced permeation and retention
EtOH	Ethanol
E	Exponential
ECM	Extracellular matrix
FFC-NMR	Fast field cycling nuclear magnetic resonance
FOV	Field of view
e.g.	For example
FTIR	Fourier transform infrared spectroscopy
FID	Free induction decay
Gd^{3+}	Gadolinium(III)
G	Gamma
GRAS	Generally Recognised as Safe
τ_{RG}	Global rotational correlation time
AuNPs	Gold nanoparticles
G	Grams
Γ	Gyromagnetic ratio
HFSR	Hand-foot skin reaction
HCC	Hepatocellular carcinoma
HPLC	High-performance liquid chromatography
HKLC	Hong Kong Liver Cancer
H	Hour
HSA	Human serum albumin
q	Hydration number
HCl	Hydrochloric acid

DH	Hydrodynamic diameter
HMSNs	Hydrophilic mesoporous silica nanoparticles
HPMSNs	Hydrophobic mesoporous silica nanoparticles
IgG	Immunoglobulin G
ICP-OES	Inductively coupled plasma optical emission spectroscopy
IS	Inner sphere
KIT	Korea Advanced Institute of Science and Technology
ω_0	Larmor frequency
L	Litre
τRL	Local rotational correlation time
R_1	Longitudinal relaxation rate
T_1	Longitudinal relaxation time
r_1	Longitudinal relaxivity
LDL	Low-density lipoprotein
LCST	lower critical solution temperature
B_0	Magnetic field
MRI	Magnetic resonance imaging
Mxy	Magnetisation in the xy-plane
Mz	Magnetisation in the z-axis
MHz	Megahertz
MSN	Mesoporous silica nanoparticle
MeOH	Methanol
μ	Micro
m	Milli
mV	Millivolt
Min	Minutes
MCM	Mobil Composition of Matter
M	Molar (moles per litre)
Mol	Moles
MPS	Mononuclear phagocyte system
nm	Nanometre
NP	Nanoparticle
NIR	Near-infrared

M_0	Net magnetisation
NHS	N-hydroxysuccinimide
PABTC-NHS	N-hydroxysuccinimide ester of 2-propanoic acid butyl trithiocarbonate
NIPAM	N-Isopropylacrylamide
HNO_3	Nitric acid
N_2	Nitrogen gas
NMR	Nuclear magnetic resonance
NMRD	Nuclear magnetic resonance dispersion
OS	Outer sphere
P	Partition coefficient
ppm	Parts per million
%	Percentage
PhTMS	Phenyltrimethoxy silane
PBS	Phosphate-buffered saline
Π	Pi
PGRFR-B	Platelet-derived growth factor receptor-β
PNIPAm	Poly(N-Isopropylacrylamide)
(PNIPAAm -b-PCL2)	poly(N-isopropylacrylamide-block-[poly(ε-caprolactone)]2
PdI	Polydispersity index
PEG	Polyethylene glycol
PEO	Polyethylene oxide
PVA	Polyvinyl alcohol
PET	Positron emission tomography
Ph	Potential of hydrogen
^1H	Proton nucleus
RF	Radiofrequency
RFA	Radiofrequency ablation
Raf	Rapidly accelerated fibrosarcoma
T_R	Repetition time
τ_M	Residence lifetime of bound water
τ_R	Rotational correlation time

Rpm	Rounds per minute
SBA	Santa Barbara
s	Second
SS	Second sphere
NaOH	Sodium hydroxide
SBM	Solomon-Bloembergen-Morgan
SHARP	Sorafenib Hepatocellular Carcinoma Assessment
Sor	Sorafenib tosylate
SPION	Superparamagnetic iron oxide nanoparticle
TUD	Technical Delft University
T	Tesla
TEOS	Tetraethoxysilane
THF	Tetrahydrofuran
TMOS	tetramethyl orthosilicate
i.e.	That is
TGA	Thermogravimetric analysis
via	Through
t	Time
TACE	Transcatheter arterial chemoembolization
τ_D	Translational diffusion time
TEM	Transmission electron microscopy
R_2	Transverse relaxation rate
T_2	Transverse relaxation time
r_2	Transverse relaxivity
TFA	Trifluoroacetic acid
UV	Ultraviolet
FDA	United States Food and Drug Administration
UCST	upper critical solution temperature
VEGFR	vascular endothelial growth factor receptors
vs	Versus
Vis	Visible
λ	Wavelength
cm^{-1}	Wavenumber

WHO	World Health Organisation
ZP	Zeta potential

List of equations

List of figures

List of tables

Chapter 1.

Introduction

1.1 Hepatocellular carcinoma (HCC)

Liver cancer is a significant global health concern, ranking as the sixth most common cancer in terms of incidence and the third deadliest cancer. In 2020, the World Health Organization (WHO) recorded a staggering 905,677 new cases of liver cancer, accompanied by a tragic 830,180 deaths (as depicted in Figure 1. 1 A-C). Alarmingly, WHO's projections suggest that the toll of liver cancer will continue to rise, with an estimated 1.3 million lives at risk by 2040 (Figure 1. 1 D).[1, 2]

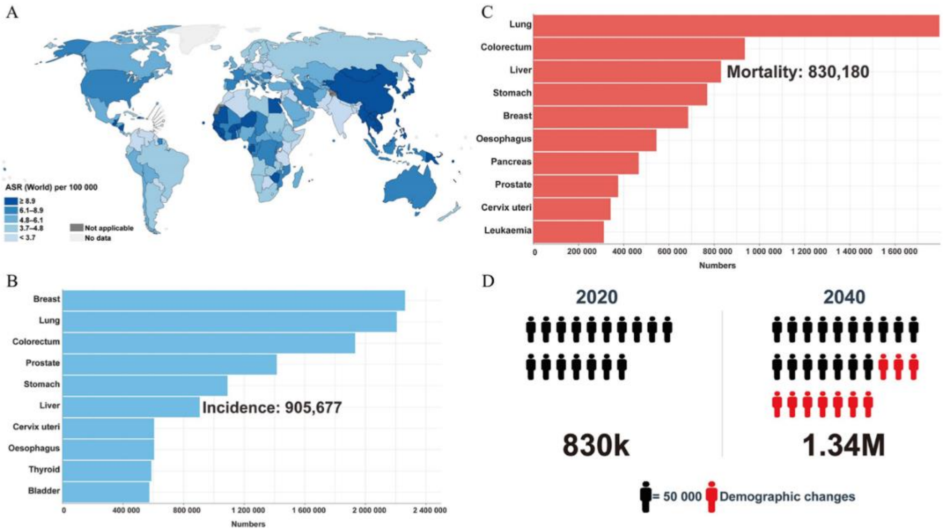

*Figure 1. 1: Worldwide Epidemiology of Liver Cancer in 2020. Data source: GLOBOCAN 2020 (http://gco.iarc.fr/).[1] (**A**) The estimated age-standardised incidences of liver cancer worldwide in 2020. (**B**) Bar charts of the estimated number of incident cases worldwide. (**C**) Bar charts of the estimated number of deaths worldwide. (**D**) WHO estimated the number of deaths from liver cancer from 2020 to 2040.*

HCC emerges as the dominant player, accounting for over 80% of all primary liver cancer cases, making it the primary focus of research and intervention efforts.[3] The development of HCC is intricately linked to chronic inflammation-induced hepatic injury, which initiates a cycle of hepatocyte necrosis and regeneration, resulting in chronic liver disease and often cirrhosis.[4] Cirrhosis, marked by significant liver scarring, is the primary precursor to HCC. Importantly, HCC can also develop in livers without cirrhosis, albeit less commonly.[5]

1.1.1 Causes and origins of HCC

The aetiology of hepatocellular carcinoma is multifaceted, with various factors influencing its development and progression.[6] These risk factors include chronic infections with hepatitis B and C viruses, alcoholic liver disease, non-alcoholic steatohepatitis, tobacco smoking, obesity, diabetes, consumption of aflatoxin-contaminated food, and haemochromatosis.[7-9] These diverse contributors play pivotal roles in the pathogenesis of HCC.

1.1.2 Classification of HCC

Various staging systems have been utilised to categorise hepatocellular carcinoma (HCC), such as Okuda, CLIP (Cancer of the Liver Italian Program) score, and HKLC (Hong Kong Liver Cancer) staging.[10] Nevertheless, the most widely adopted staging system is the Barcelona Clinic Liver Cancer (BCLC) staging.[11] The BCLC staging system, illustrated in Figure 1. 2,[12] classifies HCC into five stages - 0 (very early stage), A (early stage), B (intermediate stage), C (advanced stage), and D (terminal stage) - based on several variables including tumour status, liver function, physical condition, and cancer-related symptoms. These stages are closely associated with a treatment algorithm.[13]

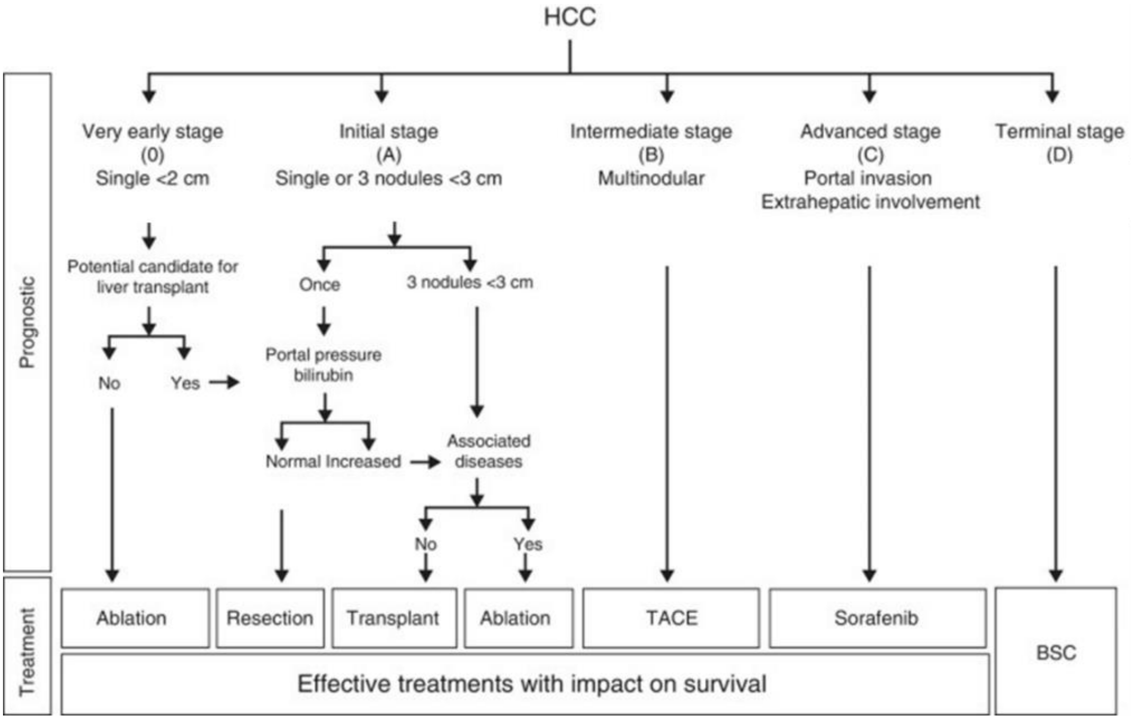

Figure 1. 2: Clinical guidelines of HCC, (BSC) best supportive care, obtained with permission from Elsevier.[12]

1.1.3 Treatment strategies

The prognosis for HCC is challenging due to its insidious onset and the absence of clear symptoms during the early stages, leading to frequently missed and misdiagnosed cases.[14] By the time HCC is usually diagnosed based on typical symptoms, the disease is often at an advanced stage. Despite some patients benefiting from early detection and timely surgical interventions like resection or liver transplantation, the overall outlook for HCC remains grim.[15] Median survival time is generally less than a year, with a 5-year survival rate falling below 10%, and a substantial risk of recurrence.[16, 17]

Early-stage treatment: For early-stage HCC patients without cirrhosis or portal hypertension, surgical resection is recommended, though it is associated with a high recurrence rate of about 60-70% at 5 years.[18] Liver transplantation can also benefit early-stage patients with liver dysfunction, with a survival rate exceeding 80% under the Milan criteria (single tumour ≤5 cm or three tumours all ≤3 cm at the time of transplantation).[19] However, early HCC often lacks symptoms, making timely detection challenging and contributing to high mortality rates.

Intermediate-stage treatment: Patients with intermediate-stage HCC and intact liver function may be eligible for treatments like transcatheter arterial chemoembolization (TACE) or radiofrequency ablation (RFA), aimed at preventing the progression of unresectable tumours.[20] The effectiveness of these treatments in terms of survival remains a subject of debate and requires further investigation.

Advanced-stage treatment: The main treatment options are systemic therapies. These include traditional chemotherapy like the FOLFOX4 regimen (fluorouracil, leucovorin, oxaliplatin), although it is not commonly used in HCC.[21] More targeted approaches involve drugs like sorafenib, a multikinase small molecule inhibitor that targets vascular endothelial growth factor receptors (VEGFR) 1–3, platelet-derived growth factor receptor-β (PGRFR-β), and rapidly accelerated fibrosarcoma (Raf) family kinases. For almost a decade, sorafenib was the primary first-line systemic targeted drug available for advanced HCC, providing a survival benefit of approximately 3 months.[21] However, newer drugs like regorafenib (approved in 2017),[22] lenvatinib (approved in 2018),[23] cabozantinib (approved in 2019),[24] and ramucirumab (approved in 2019) have become available,[25] targeting similar pathways.

Immunotherapy is an evolving area in HCC treatment, particularly relevant due to HCC often arising from chronic liver disease. In such cases, T cells become exhausted and less effective in fighting the cancer. Immunotherapy aims to reverse this T-cell exhaustion and enhance the immune response against the tumour.[26] Two major approaches are immune checkpoint inhibitors (e.g., nivolumab, approved in 2017) and CAR T-cell therapy. Nivolumab, an inhibitor of PD-1, has been approved as a second-line treatment for HCC.[27] Combining nivolumab with ipilimumab (a monoclonal antibody targeting CTLA-4, approved in 2020) has also shown efficacy for certain patients.[28] Ongoing research explores combining PD-1/PD-L1 inhibitors with receptor tyrosine kinase inhibitors to increase treatment efficacy, with some showing promising results. Notably, a combination of atezolizumab (targeting PD-L1) and bevacizumab (a monoclonal antibody targeting VEGF) has demonstrated better overall (67.2% at 12 months vs. 54.6%) and progression-free (6.8 months vs. 4.3 months) survival than those treated with sorafenib alone, as observed in a study between 2017 and 2019.[29]

1.1.4 Challenges in managing HCC

1.1.4.1 Treatment approach

Sorafenib tosylate, NEXAVAR® oral tablets, has been the primary first-line treatment for advanced-stage HCC since its Food and Drug Administration (FDA) approval in 2007.[30] Clinical trials, such as the Sorafenib Hepatocellular Carcinoma Assessment Randomized Protocol (SHARP) and the sorafenib Asia-Pacific (AP) trial,[30, 31] have shown that 400 mg twice a day of sorafenib prolongs median overall survival by approximately 2-3 months for patients with advanced HCC compared to a placebo. However, the partial response rate remains relatively low, with few achieving complete responses. Additionally, sorafenib's clinical application is hindered by factors like tumour heterogeneity, tumour resistance, and the absence of predictive biomarkers.

In terms of adverse effects, hand-foot skin reaction (HFSR), fatigue, and diarrhoea are the most common grade 3/4 sorafenib-related events. Managing these side effects, particularly HFSR, is crucial for optimising treatment. Some adverse events, notably skin-related ones, may offer insights as potential biomarkers for predicting sorafenib's effectiveness due to their correlation with patient survival.[32]

1.1.4.2 Diagnostic approach

Unlike many solid cancers, diagnosing hepatocellular carcinoma (HCC) does not always require histological evidence. Advances in medical imaging technologies, such as computed tomography (CT) and magnetic resonance imaging (MRI), have greatly enhanced the diagnostic and evaluative capabilities for HCC. In early HCC screening, patients with an alpha-fetoprotein (AFP) level exceeding 100 ng/ml or ultrasound results indicating nodules larger than 1.0 cm typically undergo CT or MRI examinations.[33]

MRI, in particular, offers superior sensitivity, spatial resolution, and soft tissue contrast without exposing patients to radiation. It also provides valuable insights into a patient's metabolism, physiology, and pathology, aiding in treatment decisions.[34] Consequently, MRI has become a widely used tool in clinical liver examinations. Although conventional enhanced MRI is generally effective in diagnosing HCC, it still faces challenges in accurately detecting small lesions with a diameter of 2.0 cm or less in early stages where curative treatments are available.[35] In this context, a significant number of HCC patients receive their diagnosis at advanced and late stages, resulting in unfavourable treatment outcomes.

1.1.5 Coping with hurdles: strategies to address HCC challenges

Scientific research on HCC has seen remarkable exponential growth, highlighting a heightened interest in comprehending HCC's development and devising effective combat strategies. Despite having multiple approved drugs, treating unresectable, advanced HCC often does not yield desired outcomes due to various factors. These include limited drug bioavailability and non-specific drug delivery, resulting in high risks of side effects and low drug concentrations in the intended target tissue.[36] Enhancing treatment effectiveness involves pivotal approaches such as utilising nanoparticles and developing new systemic therapies.[37] However, progress in developing new systemic drugs has been slow, taking nearly a decade to expand the medication range beyond sorafenib.[38]

Nanotechnology, a well-established research field for over a century, has propelled revolutionary developments since Nobel laureate Richard P. Feynman introduced the term "nanotechnology" during his iconic 1959 lecture "There's Plenty of Room at the Bottom".[39] This area of study has facilitated the development of a wide range of nanoscale particles using a variety of materials, all with dimensions less than 1000 nm (Figure 1. 3).[40] These particles exhibit diverse shapes and sizes, classified as 0D, 1D, 2D, or 3D depending on their structural characteristics.[41]

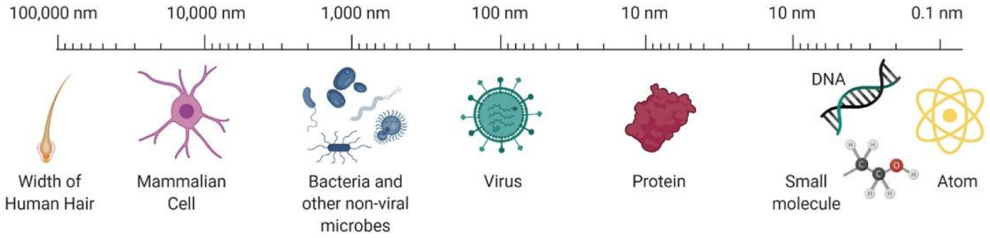

Figure 1. 3: Scale of biological world, with permission from AIChE under the terms of the Creative Commons CC BY license.[42]

Nanoparticles play a critical role in delivering anticancer drugs, offering key advantages like a stable drug payload, precise delivery to tumour sites, efficient uptake by cells, a high surface-to-volume ratio, and the ability to co-encapsulate multiple therapeutic agents.[43]

In addition, nanotechnology represents a promising frontier, extending beyond cancer treatment to potential breakthroughs in cancer diagnostics and imaging. Advancements of efficient medical diagnostics and therapeutic agents with reduced side effects offer an elegant solution to existing challenges. The recent emphasis has shifted towards theranostic nanomedicine - a strategy merging therapeutic and diagnostic agents within delivery systems. Theranostics show promise in enhancing cancer chemotherapy, early cancer detection, and real-time monitoring of therapeutic responses. This heralds a new era in nanomedicine, employing nanoscale devices to significantly enhance disease diagnosis and therapy in the 21st century.

There is a wide array of nanoparticle types, including polymeric micelles, quantum dots, liposomes, polymer–drug conjugates, dendrimers, biodegradable nanoparticles, silica nanoparticles, and more (Figure 1. 4).[42] This diversity has spurred increased research into hepatocellular carcinoma (HCC). Notably, the utilisation of nanomaterials in HCC treatment has seen an upswing in research publications over the past two decades.[44] These advancements offer significant promise, not only in the realm of cancer treatment but also for the effective management of HCC.

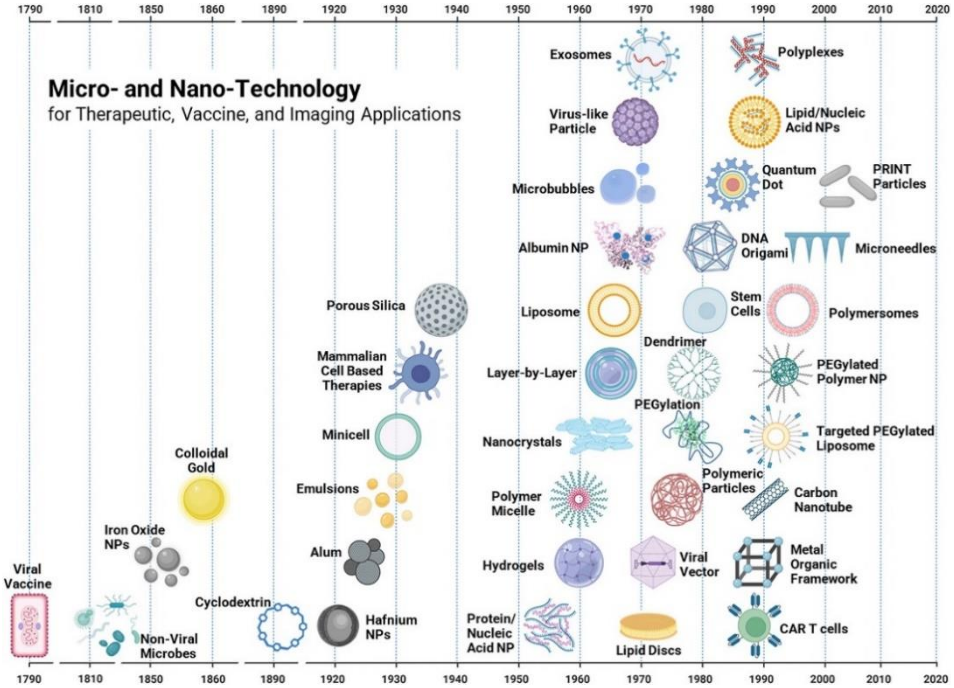

Figure 1. 4: Timeline of micro and nano technology used for biomedical applications, with permission from AIChE under the terms of the Creative Commons CC BY license.[42]

In this thesis, our research has delved into the application of mesoporous silica nanoparticles (MSNs) as a versatile theranostic nanocarrier for sorafenib tosylate, coupled with the MRI contrast agent Gd-chelate. This approach aims to address the challenges discussed earlier in the management of HCC.

1.2 Mesoporous silica nanoparticles (MSNs)

Silica nanoparticles, especially those exhibiting mesopores, have garnered substantial interest within the scientific community for their potential applications in the field of nanomedicine. In the realm of pharmaceuticals, silica nanoparticles are categorised into two types based on pore size: microporous and mesoporous nanoparticles.[45] Microporous silica, featuring pores up to 2 nm, primarily finds utility in chromatographic columns and molecular sieve synthesis, while mesoporous silica, characterised by pores ranging between 2 and 50 nm, serves as a versatile platform for delivering drug molecules.[45]

MSNs stand out as crucial multifunctional nanocarriers for drugs and/or diagnostic agents because of multiple characteristics such as (i) high surface area and pore volume that facilitates high drug loading capacity, (ii) easily manipulated particle size in a range of 50-300 nm, allowing cellular uptake by endocytosis, (iii) reproducible and controlled drug release due to the narrow pore size distribution, (iv) high dispersibility and stability of these particles with varying pH or temperature, (v) easily functionalised internal and external surfaces that permits both controlled drug release kinetics and specific targeting, respectively, (vi) biocompatibility where silica is classified as "Generally Recognised as Safe" (GRAS) by the FDA and is used in cosmetics and as a food-additive, (vii) finally, pore capping by a stimuli-responsive material allowing a triggered mechanism of controlling drug release either through tumour microenvironment stimuli or externally applied triggers.[46-49]

1.2.1 Types of MSNs

Mesoporous silica nanoparticles (MSNs) form a versatile family of nanomaterials extensively used across diverse applications. The inception of MSNs can be traced back to the 1970s,[50-52] and substantial progress was achieved in the 1990s by Mobil Research and Development Corporation.[53] This era saw the introduction of MSNs through a template derived from liquid crystals, giving rise to the group known as Mobil Composition of Matter or Mobil Crystalline Materials (MCM-41, MCM-48, MCM-50). MSNs exhibit a structured pore arrangement with adjustable diameters ranging from 2 to 50 nm, made possible through specific surfactants and precise reaction conditions. [54-56]

Surfactants used in the synthesis of MSNs can be classified based on their electrical charges: cationic (e.g., cetyltrimethylammonium bromide, CTAB), anionic (containing sulfonic acid, phosphoric acid), non-ionic (like polyethylene oxide, PEO), and ampholytic. Variations in templating agents and reaction conditions yield distinct members within the MCM family.[56, 57] For instance, MCM-41 showcases a two-dimensional hexagonal arrangement with pore sizes from 2.5 nm to 6 nm.[57] MCM-50, however, follows a lamellar arrangement with its own set of distinct characteristics.[58]

Within the realm of Mobile Crystalline Materials, the Santa Barbara (SBA) materials, including SBA-1, 2, 3, 6, 12, 15, 16, stand out with larger pores (ranging from 4.6 to 30 nm) and thicker silica walls. The initial templating agents greatly influence the symmetry and structure of these materials, resulting in various mesoporous configurations like cubic and hexagonal mesostructures (SBA-11, SBA-12, SBA-15, SBA-16).[59]

Another noteworthy type, FSM-16, finds applications beyond catalyst and adsorbent uses, extending into diverse pharmaceutical applications.[60] Other mesoporous materials developed by institutions like the Korea Advanced Institute of Science and Technology (KIT) and Technical Delft University (TUD-1)[61, 62] offer distinct symmetries and pore shapes. MCM-41, MCM-48, SBA-15, and SBA-16 find extensive use in drug and gene delivery (Figure 1. 5).

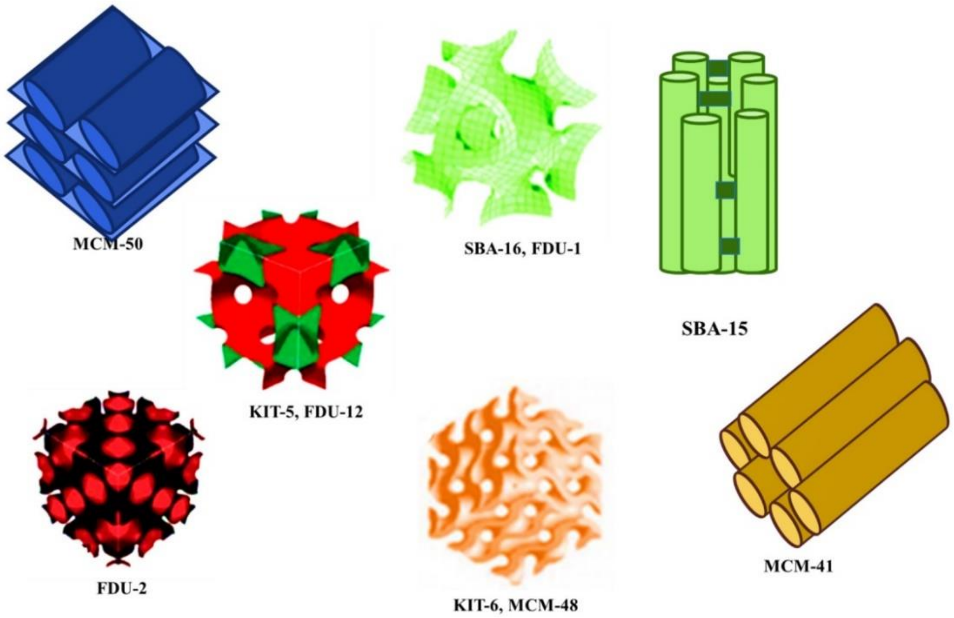

Figure 1. 5: Different types of MSNs, obtained with permission from Elsevier under the Creative Commons CC-BY-NC-ND license.[56]

1.2.2 Synthesis of mesoporous silica nanoparticles

MSNs can be synthesised using a variety of methods, each with its unique approach. These methods include the soft or hard templating method, fast self-assembly, Stöber method, modified aerogel methods, hydrothermal technique, and dissolving reconstruction method.[63-66]

One of the pioneering methods for the synthesis of spherical micron-sized silica nanocarriers is attributed to Stöber. He developed this method through specific chemical reactions, which subsequently became known as

'Stöber synthesis'.[63] The Stöber synthesis, often referred to as the sol-gel method, is widely adopted for the fabrication of MSNs. In this approach, the sol phase is generated through hydrolysis reactions, leading to the production of colloidal particles under alkaline or acidic pH conditions. Simultaneously, the condensation of these colloidal particles results in the formation of a gel phase with a three-dimensional structure, achieved through the cross-linking of siloxane bonds.[67] This general reactions can be shown in Figure 1. 6.

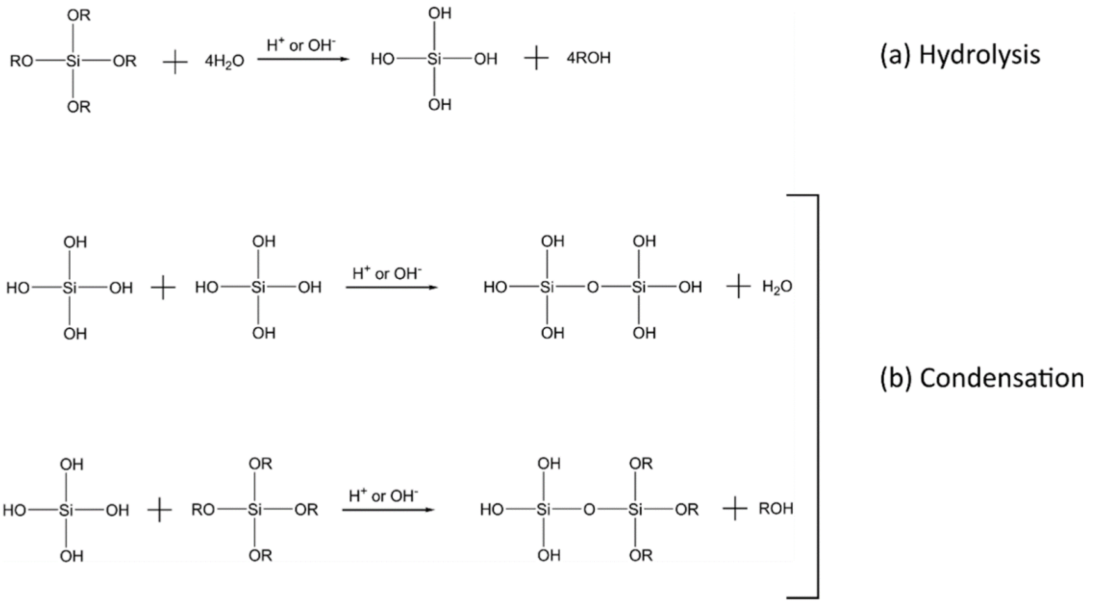

Figure 1. 6: Synthesis of silica through sol-gel process involves both (a) the hydrolysis and (b) the condensation reactions of a silicon alkoxide precursor ($Si(OR)_4$), obtained with permission from MDPI under the Creative Commons CC-BY-NC-ND license.[68]

These reactions are central to the formation of MSNs using the sol-gel or Stöber method, allowing for precise control over the nanoparticle synthesis process. The hydrolysis of alkoxide groups is dependent on several factors, including the molar concentration of Si/H_2O and specific reaction conditions. The condensation process occurs following hydrolysis, with repeated condensation events leading to the formation of a chain-like structure in the colloidal solution. In the gel form, this condensation results in the creation of an extensive network of Si-O-Si groups.[69] Substantial research efforts have been directed towards obtaining stable, monodisperse and non-porous nanoparticles using Stöber method.[70] This method is particularly advantageous due to its simplicity, cost-effectiveness, uniform structure, controllable properties, and reduced usage of excipients, ultimately saving time.[71, 72]

Two other prominent techniques for porous MSN synthesis are the soft and hard templating methods. In the soft templating approach, organic templating agents are employed to create porosity within the MSNs. Subsequent heat treatment removes the templating material, yielding pure mesoporous carriers.[66] On the other hand, the hard templating method, also known as the nano-casting technique, involves silica precursors filling templating mesopores through capillary action. Following this, chemical or thermal treatment removes the templating agent, ultimately producing the desired mesoporous structure.[73] Both the soft and hard templating methods contribute to the creation of a complementary structure of mesoporous silica dictated by the template.[73] For instance, to achieve nanometric particles with a high degree of order and diverse shapes, Wang et al. proposed several modifications.[64] One significant adaptation involved employing a cationic surfactant as a template, resulting in the silica network condensing around these micelles, and the surfactant can then be removed to yield the 'empty' porous networks of spherical MSNs as shown in Figure 1. 7.[64, 74]

In addition, the hydrothermal technique for MSN synthesis traces its origins to British geologist Roderick Murchison. Initially used for mineral formation from hot water solutions in cooling magmas, this process involves a reaction within a sealed container at high pressure and temperature.[65] While akin to the sol-gel process, the mixture is transferred to a Teflon-lined autoclave at a specific temperature, followed by template removal. MSNs produced through this method exhibit improved regularity and enhanced hydrothermal stability.[75]

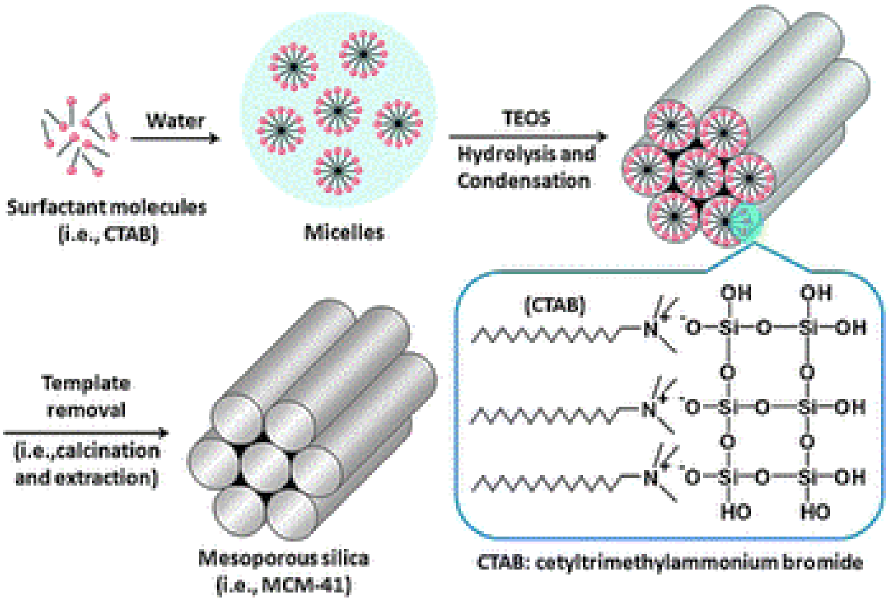

Figure 1. 7: Schematic representation of MCM-41 mechanism of synthesis, obtained with permission from Chemical Society Reviews.[74]

1.2.3 Tuning of MSNs

The cellular uptake of MSNs by target cells is influenced by several crucial factors: particle size, pore size, shape, and surface modification. Achieving an ideal carrier for drug delivery entails uniform particle shapes with larger pore volumes is key to creating MSNs with aspect ratios tailored to specific biomedical applications. The following parameters affect the key properties of MSNs.

1.2.3.1 Particle size of MSNs

Particle size is a pivotal factor impacting carrier properties and the effective delivery of entrapped agents to target sites. Smaller particle diameters are generally preferred for efficient agent delivery with improved cellular uptake properties.[76] The particle size of MSNs is influenced by factors such as pH, temperature, reaction time, and the addition of functional organo-silanes during the synthesis.

The initial pH of the reaction medium significantly affects particle size by influencing the hydrolysis and condensation rates. At higher pH levels, the rate of hydrolysis increases, impacting particle size, while the rate of condensation is higher at pH 8.4, with subsequent reduction as pH alters.

Optimal particle size can be achieved at pH 9-10, emphasising the influence of condensation rates as shown in Figure 1. 8.[77] Triethanolamine (TEA) has been employed to create a basic environment, acting as a complexing agent and base catalyst, resulting in smaller, discrete particles.[78]

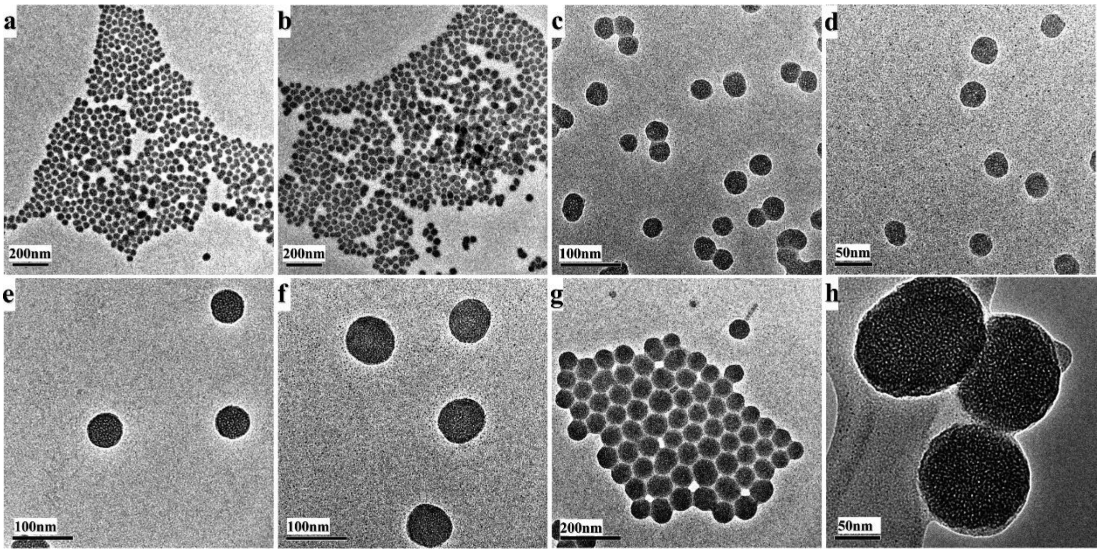

Figure 1. 8: TEM images of the samples synthesized with different initial pH values: (a) 10, (b) 9, (c) 8.5, (d) 8, (e) 7.5, (f) 7, and (g and h) 6, obtained with permission from American Chemical Society (ACS) Publications.[77]

The duration of the reaction is another factor that exerts a discernible impact on particle size. Research by Chiang *et al.* underscores this influence, where the size of particles initially increases before trending downwards as the reaction period elongates from 2 to 10 hours.[79] Furthermore, the inclusion of solvents or additives can effectively modify particle size. For instance, ethylene glycol demonstrates a significant potential for reducing particle size, potentially by mitigating surfactant-silica precursor interactions and impeding particle growth.[80]

Additionally, alterations in the alkoxide group composition of tetraalkoxysilanes and variations in surfactant concentrations (e.g. CTAB) play their respective roles in affecting particle size, either homogenising distributions or promoting agglomeration.[81] The concentration of polymers like F127 and the level of tetraethyl orthosilicate (TEOS) also exercise notable influence over particle size dynamics. Higher TEOS concentrations tend to correlate with larger particles, albeit not in strict proportionality, signifying a nuanced impact on particle size.[79] Moreover, elevating TEOS concentration can usher in a transition from a monodisperse to a heterogeneous particle size distribution, attributable to an excess of silica precursor yielding new nuclei among already-formed particles.[82]

Introducing capping agents, such as PEG-silanes, plays a transformative role in governing particle sizes through steric stabilisation. The timing of PEG-silane addition is critical, with immediate incorporation after tetramethyl orthosilicate (TMOS) introduction effectively constraining particle size, whereas delayed addition leads to larger particles.[83] The rate of stirring and the temperature during synthesis are crucial determinants of particle size. Slower stirring tends to yield larger particles, while faster agitation promotes the formation of finer particles.[84] Also, elevating the temperature from 30°C to 70°C triggers an increase in MSN particle size, potentially due to augmented polycondensation rates culminating in a denser silica structure.[82]

In essence, a nuanced interplay of these multifaceted factors dictates the particle size of MSNs, allowing for meticulous tailoring to meet specific drug delivery requirements, optimise performance, and ultimately enhance cellular uptake.

1.2.3.2 Pore Size

Pore size and structure constitute pivotal attributes in the realm of MSNs, directly influencing the drug-carrying capacity within the nanoparticle system. The optimal pore size holds immense importance, serving as a critical determinant to thwart premature release of the encapsulated cargo molecules.[85] Surfactants act as potent structure-directing agents, wielding control over pore size. Furthermore, fabrication conditions, including the silica source, reaction duration, temperature, and concentration of the base catalyst, exert a profound influence on both pore dimensions and the overall structure.[86]

In this context, the modulation of pore size has been demonstrated through the alteration of the molar ratio between the amphiphilic octadecyl trimethoxysilane (C18 TMS) and TEOS. An increase in the molar concentration of C18 TMS: TEOS leads to a corresponding expansion of pore dimensions due to the formation of larger micelles. However, a molar ratio beyond 0.74 of C18 TMS: TEOS triggers a contrary effect, resulting in a reduction of pore size instead of an anticipated increase due to micelle deformation as illustrated in Figure 1. 9.[87]

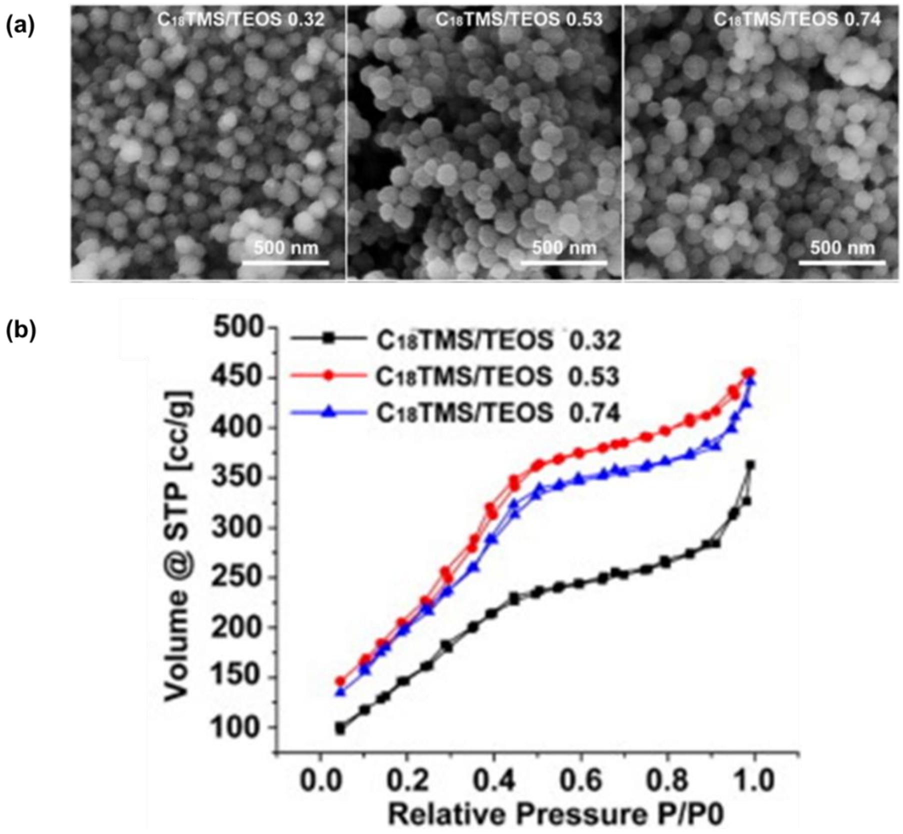

Figure 1. 9: SEM images (a) and N_2 adsorption-desorption isotherms (b) of MSNs synthesized with different C18TMS/TEOS molar ratios, modified with permission from Elsevier.[87]

Other approaches are available to regulate the pore size of mesoporous materials through adding swelling agents to form larger micelles. In previous studies, compounds such as 1,3,5-trimethylbenzene (TMB)[88] and triisopropylbenzene[89] have served as pore expanders, resulting in mesoporous materials with pore sizes exceeding 8.0 nm.[90]

1.2.3.3 Shape of MSNs

The shape of MSNs is a crucial factor influencing their uptake and trafficking into cells.[91] Various studies emphasise the impact of different shapes on cellular uptake behaviour. Trewyn *et al.* demonstrated that tubular MSNs exhibit more efficient uptake by normal and cancerous cells compared to spherical ones, highlighting the significance of shape in cellular uptake.[92]

Huang *et al.* conducted research on the influence of particle shape on the *in vivo* bio-distribution of nanocarriers, revealing that shorter rods of MSNs distribute more in the liver, while longer rods of MSNs are more concentrated in the spleen. Polyethylene glycol (PEG) modification further affects their distribution in the lungs.[93]

The morphology of MSNs can vary from spherical to non-spherical shapes like cubes, rods, ellipsoids, sheets, or films, depending on factors such as the molar concentration of TEOS, surfactant, base catalyst, and water. However, spherical MSNs are generally favoured for drug delivery applications.[94] Research by Cai *et al.* demonstrated the synthesis of MSNs in various shapes by altering concentrations of surfactants and alkyl alcohols as co-surfactants (Figure 1. 10).[95] Different shapes of MSNs were also obtained using dodecanol as a soft templating agent, resulting in sphere-like, yolk-shell, hollow, and peanut-like structures.[96] Various methods, such as changing micellar concentrations or utilising co-solvents, can produce MSNs with different aspect ratios and shapes, including rods.[97, 98]

Ellipsoidal MSNs are another shape relevant to drug delivery, however, retaining this shape can be challenging due to surface energy considerations. Nonetheless, they can be generated using specific agents like ethanol, co-surfactants, and potassium chloride.[99] Additionally, highly porous platelet-shaped MSNs can be designed by modifying concentrations of specific compounds like heptane, ammonium fluoride, and various surfactants.[97, 100, 101] The morphological characteristics of MSNs are influenced by the type and concentration of organoalkoxysilanes precursors, leading to different bonding and interactions between surfactant templates and organoalkoxysilanes.[102]

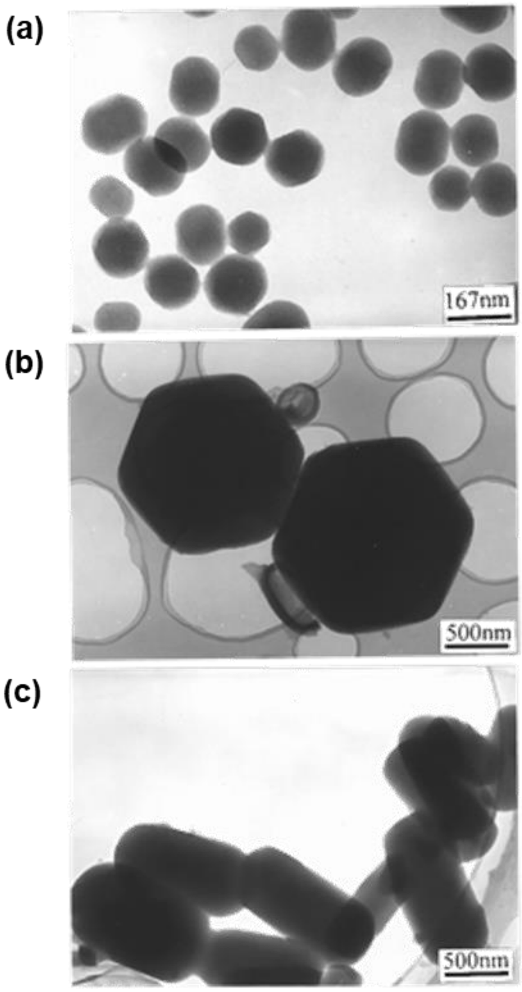

Figure 1. 10: TEM images depicting the controllable synthesis of MCM-41 silica particles with diverse morphologies in a basic medium, modified with permission from American Chemical Society (ACS) Publications.[95]

1.2.3.4 Surface modification

Surface modification and functionalisation of MSNs are critical for overcoming challenges related to premature drug release during drug delivery. These modifications aim to achieve specific properties such as controlled drug release, enhanced drug loading capacity, and reduced toxicity compared to free drugs.[103] Functionalising the surface of MSNs involves attaching various functional groups, including amino groups containing polymers like PEG and dendrimers, thiols, and organic phosphates, significantly impacting the interactions of nanocarriers with biological fluids.[104] The presence of silanol groups on the surfaces of MSNs allows for extensive modifications, which can be used to enhance biomedical applications, for example by controlling drug release under specific physiological conditions.[105]

Modifications on the hydroxyl groups of MSNs, with groups such as amine, thiols, or other organic chain modifications, play a crucial role in drug release under specific physiological conditions. These modifications also enhance the loading capacity for agents like Small interfering ribonucleic acid (siRNA) and Deoxyribonucleic acid (DNA), promoting targeted delivery of cytotoxic agents.[105] Moreover, capping of MSNs may involve immobilising molecular stalks covering the pores through covalent bonding, with reversible alterations in physiological conditions leading to drug release.[106] Various capping ligands such as inorganic nanoparticles, synthetic polymers, biomacromolecules, and peptides, have been introduced to trigger controlled drug release by modifying the MSN structure.[107-109]

1.2.4 Biomedical applications of MSNs

MSNs have gained significant attention as a highly promising approach for targeted and controlled drug delivery. They offer the potential to enhance the solubility of drugs that are otherwise insoluble, while also serving as effective carriers for dyes and contrast agents in diagnostic applications. Consequently, MSNs are widely employed in various capacities, including therapeutic drug delivery, diagnostic imaging, stimuli-responsive and the emerging field of theranostics (Figure 1. 11).[48]

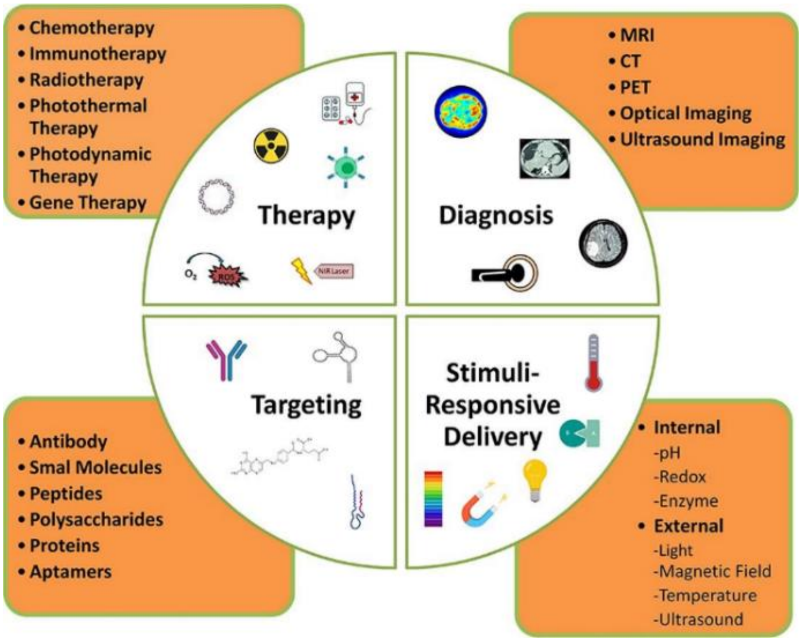

Figure 1. 11: Biomedical applications of MSNs, obtained with permission from Elsevier under the terms of the Creative Commons CC-BY license.[48]

1.2.4.1 Unleashing the therapeutic power of MSNs

Optimising drug delivery carriers is a pivotal challenge in pharmaceutical development, and recent research has turned its focus towards mesoporous silica materials for precisely delivering therapeutic agents within the human body. MSNs, characterised by their large surface area, high drug loading capacity, and ease of functionalisation, are emerging as promising candidates for the development of controlled and targeted drug delivery systems.[110]

Numerous studies have explored the therapeutic potential of MSNs. An illustrative study by Pishnamzi and colleagues stands out,[111] wherein they investigated the controlled release behaviour of paracetamol from MSNs post amine-functionalisation, aiming for enhanced oral drug delivery. KCC-1 MSNs were selected for this purpose, known for their distinctive properties such as high surface area, fibrous surface, dendritic structure, and mechanical robustness. The study compared the drug release dynamics of both unmodified and amino-functionalised KCC-1 MSNs. Impressively, the amino-functionalised MSNs displayed a considerably slower drug release, attributed to interactions between amino functional groups and hydroxyl groups in paracetamol, effectively impeding the rapid influx of phosphate buffer saline

(PBS) into the pores of the MSNs. This research underscores the potential of functionalised MSNs in crafting controlled drug delivery systems, especially for highly soluble drugs like paracetamol.[111]

In a similar approach, amino-functionalised MSNs were employed to control the release of sofosbuvir, an antiviral drug effective against the hepatitis C virus. This drug is known for its poor bioavailability and short half-life when orally administered. By decorating MSNs with aminopropyltriethoxysilane (APTES) and polyvinyl alcohol (PVA), high drug loading was achieved. Amino functionalisation was used to control drug release, resulting in a sustained release profile compared to non-functionalised MSNs. This approach significantly increased the bioavailability of sofosbuvir and prolonged its Tmax, the time it takes for a drug to reach the maximum concentration after administration, demonstrating the potential of MSNs for sustained drug delivery.[112]

MSNs also offer a promising avenue for targeted cancer therapy, allowing precise drug delivery and controlled release to overcome adverse effects. Li and colleagues developed dual-functionalised MSNs for efficient anticancer drug therapy.[113] The MSNs were modified with a hyperbranched polymer and a folic acid marker to achieve targeted delivery of tetrandrine. These multifunctional nanocarriers reduced drug cytotoxicity and enhanced delivery efficiency. The nanoengineered MSNs significantly increased drug loading efficiency and achieved sustained release, making them a promising platform for anticancer drug delivery.[113]

Surface-modified MSNs with nucleolin-targeting ligands have shown effectiveness in treating colorectal cancer. Co-delivery of camptothecin and short hairpin RNA (shRNA) to targeted sites using these MSNs resulted in controlled drug release and reduced tumour growth in a murine model, demonstrating their potential in colorectal cancer therapy.[114]

In addition, MSNs offer a potential solution for enhancing the solubility of poorly soluble active pharmaceutical ingredients (APIs),[115] leveraging their large pore volume and high surface area to improve the delivery of hydrophobic drugs. This unique characteristic of MSNs allows them to accommodate a higher quantity of drug molecules and efficiently disperse them, transforming the drug's crystalline form into an amorphous state. Notably, this amorphous state reduces lattice energy, ultimately boosting solubility.[116, 117] For instance, Resveratrol (RES), a drug with poor aqueous solubility, was successfully loaded into MCM-48, leading to a remarkable 95% improvement in RES's saturated solubility. Additionally, the *in vitro* release kinetics of RES-loaded MSNs exceeded those of pure RES. This enhancement is attributed to RES being confined within the mesochannels in a smaller and amorphous state, a conclusion supported by studies employing differential scanning calorimetry and X-Ray diffraction.[118]

Several drugs have similarly been loaded into MSNs to enhance their solubility, such as quercetin,[119] paclitaxel[120] and curcumin[121] by restricting their crystallisation inside the pore channels.[122] Encouragingly, research has progressed to oral administration in humans, such as MSNs loaded with poorly water-soluble drugs, demonstrating potential advancements in drug delivery.[123]

1.2.4.2 Shining a light: MSNs as a diagnostic agent

The early detection of cancerous tumours is paramount in lowering mortality rates and optimising treatment effectiveness. Various nanosystems, such as gold nanoparticles and quantum dots, have been used for early cancer cell diagnosis. However, they often lack efficiency and may entail toxic side effects.[124-126] In contrast, MSNs offer a safe, biodegradable, and effective alternative for early cancer diagnosis and monitoring drug efficacy.[124] Their distinct feature lies in the ability to exhibit three distinct domains - the silica framework, the internal pore walls, and the outer surface - each of which can be independently exploited or functionalised.[127] For instance, MSNs can be tailored for bio-imaging applications, encompassing optical imaging, magnetic resonance imaging (MRI), positron emission tomography (PET), computed tomography (CT), ultrasound imaging, and multimodal imaging, all aimed at achieving early diagnosis.[124]

In this thesis, our central focus revolves around enhancing the efficiency of MRI-active MSNs as a contrast agent, aiming to facilitate both the early detection of HCC and the monitoring of treatment progress.

1.2.4.2.1 The power of MRI: illuminating medical diagnostics

MRI has become widely embraced as a clinical diagnostic tool due to its powerful non-invasive capabilities, including remarkable soft tissue contrast, precise spatial resolution, and substantial depth of penetration.[128] Stemming from the principles of nuclear magnetic resonance (NMR), MRI exploits variations in the relaxation times of proton spins within water molecules found in different tissues. This distinction results in an image with varying contrast, enabling the diagnosis of diseases such as cancer, without the need for potentially damaging radiation.[129]

In 1971, an article by Raymond Damadian emphasised the use of magnetic resonance as a diagnostic tool to differentiate between normal and malignant tumourous tissue.[129] Over the following years, Paul Lauterbur and Peter Mansfield pioneered the development of MRI. The revolutionary concept involved using an external source to penetrate the body without disrupting cells, allowing for the identification and localisation of tumours. This groundbreaking work led to Lauterbur and Mansfield being awarded the 2003 Nobel Prize in Physiology or Medicine for their efforts.[130, 131]

1.2.4.2.2 Fundamental concepts of MRI

MRI relies on the imaging of spin half proton nuclei (^1H) where the application of an external magnetic field (B_0) leads to alignment of these spins with or against the direction of B_0 whilst they precess at the Larmour frequency, $\omega_{0,}$ (Equation 1.1).

Slightly more spins align with the B_0 than against, due to the favourable lower energy orientation, and this leads to the generation of a net magnetic moment (M_0) parallel with B_0 (precessing along the z-axis, M_z).

$$\omega_0 = \gamma B_0$$

Equation 1. 1

Where γ is the gyromagnetic ratio.

A radiofrequency pulse (RF) is required to perturb the net magnetisation out of equilibrium so that relaxation can be measured. An RF pulse oscillating close to the Larmor frequency is applied perpendicular to M_0, along the x-axis (B_1), creating resonance in this axis. This perturbation is sufficient to force the bulk magnetisation to precess in the xy-plane (M_{xy}) when the RF pulse is applied (Figure 1. 12a). Upon removal of the RF pulse, the protons relax back to their preferred equilibrated state along the z-axis (aligned with B_0) in a process called relaxation.

1.2.4.2.2.1 Mechanisms of relaxation

1.2.4.2.2.1.1 Transverse relaxation (T_2)

Following a 90-degree RF pulse at the Larmor frequency, the magnetised protons attain an initial phase coherence, resulting in maximal M_{xy}. The transverse magnetic field of the excited sample induces a signal in the receiver antenna coil by precessing at the Larmor frequency. This signal manifests as a damped sinusoidal electronic signal known as the free induction decay (FID), as depicted in Figure 1. 12c. Upon removal of the RF pulse, the decline in FID amplitude is attributed to the loss of M_{xy} phase coherence due to inherent micromagnetic inhomogeneities within the sample's structure.

In this context, protons within the bulk water and the hydration layer linked to macromolecules undergo precession at slightly different frequencies due to minor alterations in the local magnetic field strength, resulting from the structural irregularities. Over time, phase coherence diminishes exponentially, leading to a decay in the FID amplitude. The elapsed time from the peak transverse signal (e.g. immediately after the 90-degree RF pulse) to when the signal reaches 37% of its peak level (1/e) is defined as the T_2 relaxation time, as illustrated in Figure 1. 12e. Mathematically, this is expressed as shown in Equation 1. 2.

$$M_{xy}(t) = M_0 \, e^{\frac{-t}{T_2}}$$

Equation 1. 2

where $M_{xy}(t)$ is the transverse magnetic moment at time t for a sample that has M_0 transverse magnetisation at t = 0. When t = T_2, then $e^{-1} = 0.37$ and M_{xy} = 0.37 M_0.[132]

1.2.4.2.2.1.2 Longitudinal relaxation (T_1)

The restoration of longitudinal magnetisation initiates immediately after the B_1 excitation pulse, occurs simultaneously with transverse decay. However, the process of returning to equilibrium conditions has a longer duration. Spin-lattice relaxation refers to the phenomenon wherein energy is released back to the lattice (the molecular arrangement and structure of the hydration layer), leading to the regeneration of M_z. This occurs exponentially as shown in Equation 1. 3.

$$M_z\,(t) = M_0\,(1 - e^{\frac{-t}{T_1}})$$

Equation 1. 3

where M_z (t) is the longitudinal magnetisation at time t and T_1 is the time needed for the recovery of 63% of M_z after a 90-degree pulse (at t = 0, M_z = 0, and at t = T_1, M_z= 0.63 M_0), as shown in Figure 1. 12b and d.[132]

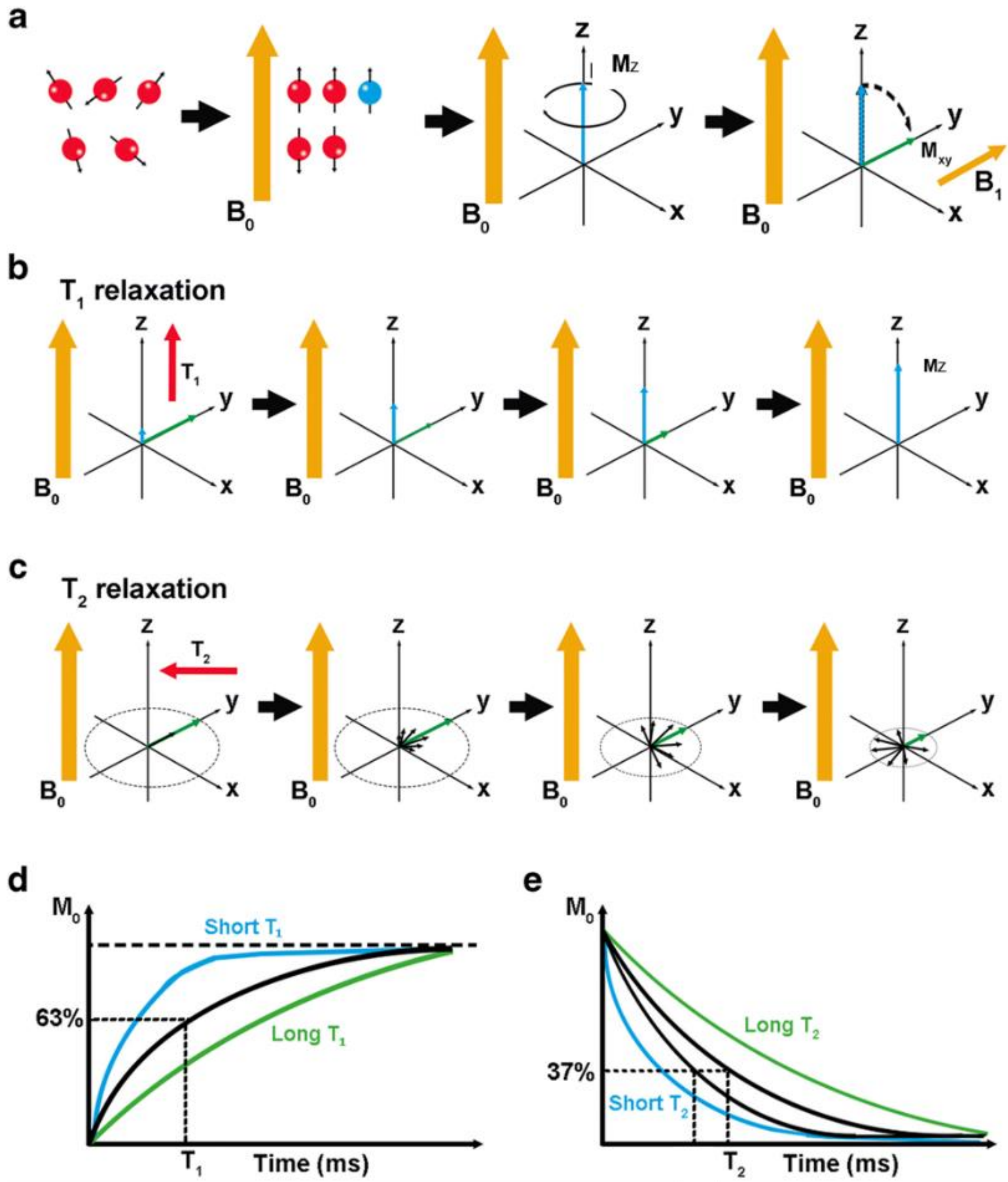

Figure 1. 12: Schematic illustration of the fundamental principles of MRI. Protons are symbolised as red balls, exhibiting spin behaviour. An external magnetic field (B_0, orange arrow) aligns protons in spin-up and spin-down orientations. The difference in alignment generates the MRI signal, represented by the blue ball. The resulting collective proton sum is depicted as the magnetisation vector (M_z, blue arrow). Introducing a perpendicular magnetic field (B_1) enables a 90° tilt of M_z along the x-y direction (M_{xy}, green arrow) as represented in (a). After B_1 is turned off, M_{xy} returns to equilibrium through T_1 and T_2 relaxation processes as represented in (b and c, respectively). T_1 relaxation is the time to achieve 63% of the original longitudinal magnetisation (M_0), represented by the blue curve and the green curve for tissues with short and long T_1 values, respectively as represented in (d). T_2 relaxation is defined as the time for dephasing up to 37% of the original value, with blue and green curves illustrating tissues with short and long T_2 values, respectively as shown in (e). This figure is adopted from Springer Nature with permission under the CC BY licence.[132]

1.2.4.2.3 MRI contrast agents: enhancing imaging insights

In order to enhance the sensitivity and contrast of MR images, nearly 40% of all MRI examinations use contrast agents (CAs) which have the ability to shorten the relaxation time of the nearby water protons through dipolar interactions. The contrast agents are classified as either T_1 or T_2 based on the mechanism by which they predominantly enhance the water proton relaxation. Clinically, gadolinium-based CAs are the most commonly used to yield a positive contrast (bright T_1-weighted images) unlike superparamagnetic iron oxide (SPIO) that yields a negative contrast (dark T_2-weighed images).[133] In this thesis, the primary focus will be on the commonly utilised positive contrast agents in clinical applications: those derived from Gd^{3+} complexes.

Gadolinium (III) contrast agents' popularity stems from its paramagnetic nature due to its 7 unpaired electrons in its 4f shell.[134-136] However, free Gd^{3+} is considered a toxic agent due to the similarity between its ionic radii and, that of calcium (II) which may lead to calcium replacement and nephrogenic systemic fibrosis (NSF).[137, 138] Consequently, gadolinium is always used in its FDA approved chelated form based on expansive macrocyclic ligands (e.g. DOTA: 1,4,7,10-tetraazacyclododecane-1,4,7,10-tetraacetic acid). These macrocyclic chelating agents typically coordinate with the Gd^{3+} ion in an 8-coordinated manner, allowing for one vacant site for water exchange. Several Gd-based contrast agents have gained clinical approval, as depicted in Figure 1. 13, such as Dotarem®. However, these agents exhibit low signal-to-noise ratios and are less efficient than free Gd^{3+} ions, necessitating higher doses and consequently elevating the risk of adverse side-effects.

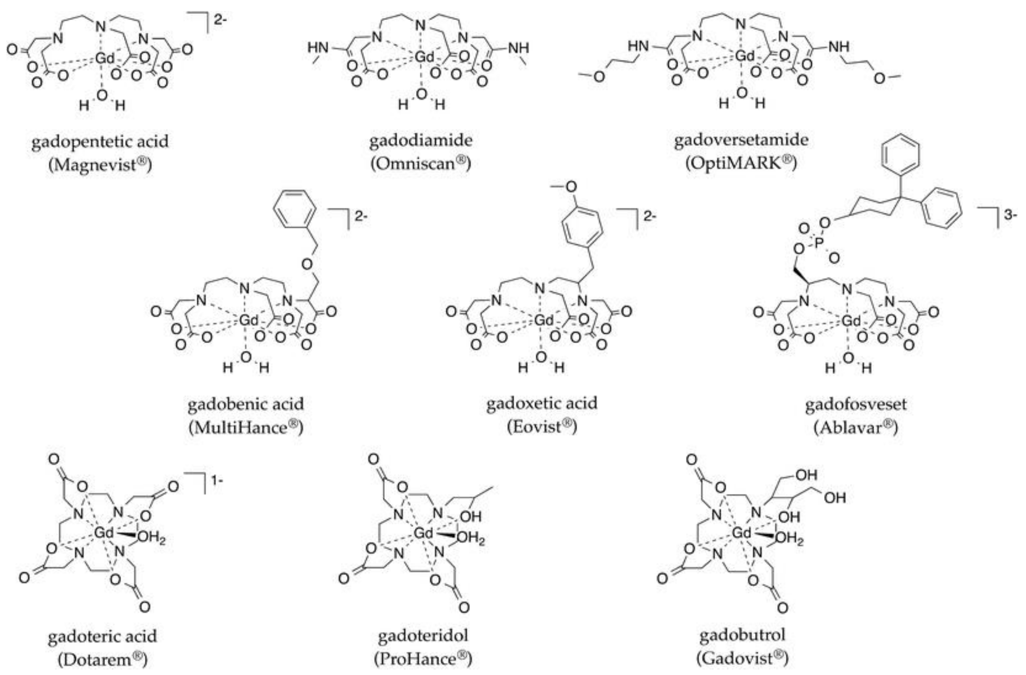

Figure 1. 13: Molecular structure and formal charge of the gadolinium-containing component present in the nine gadolinium-based contrast agents that have received approval from the U.S. Food & Drug Administration (proprietary names in parentheses), this figure was obtained with permission from Springer Nature.[139]

1.2.4.2.3.1 Efficacy of contrast agents

Contrast agents accelerate the relaxation rates, longitudinal or transverse, of protons in water molecules within tissues through dipole-dipole interactions that can be described by the Solomon-Bloembergen-Morgan (SBM) theory.[140, 141] The efficacy of these contrast agents is defined in terms of relaxivity (r_i where r_1 refers to longitudinal or r_2 for transverse, with units of $mM^{-1}\ s^{-1}$) which refers to the efficiency of a paramagnetic substance to enhance the relaxation rate of water protons ($1/T_i$) with respect to the concentration of contrast agent present. The relaxivity value can be calculated through Equation 1. 4.

$$\frac{1}{\mathrm{T_i}} = \frac{1}{\mathrm{T_{i,d}}} + r_i\ [Gd^{3+}]$$

Equation 1. 4

where i = 1, 2

$1/T_{i,d}$, the relaxation rate of the solvent (water) nuclei in the absence of a paramagnetic solute. $1/T_i$, the relaxation rate enhancement caused by the paramagnetic substance which is linearly proportional to the concentration of the paramagnetic species, [Gd^{3+}] in mM.[142]

The factors affecting the efficacy of gadolinium in enhancing the relaxivity can be summarised by their inner and outer sphere contribution. The inner sphere contribution is based on the direct interaction between Gd^{3+} ions and bound water while the outer sphere one depends on the diffusion of nearby water molecules. In some cases, the water molecules bonded to the chelating unit represent a second sphere effect.

In positive contrast agents, the inner sphere tends to have a relatively stronger influence on relaxivity. Hence, managing the parameters that control the inner sphere region is crucial to optimise a contrast agent's relaxivity. These parameters can be summarised as follows; the hydration number of water molecules directly coordinated to the central ion (e.g. Gd^{3+}) (q), electronic relaxation times of longitudinal and transverse (T_{ie}), rotational correlation time (τ_R), and the residence lifetime of bound water (τ_M).[134, 143] Increasing q, increasing τ_R and decreasing τ_M are common routes of boosting relaxation rate and hence MRI contrast signal (Figure 1. 14).[134, 143]

The outer sphere effects encompass contributions from the longitudinal electron spin relaxation time (T_{ie}) and the relative translational diffusion time (τ_D), which involves the exchange rate between bulk water and the magnetic species. The interaction between proton spins in water and the seven unpaired f electrons from Gd^{3+} is pivotal for these contributions, as the rate of diffusion between these interacting spins impacts the relaxation rate. Additionally, the exchange rate between a coordinated water molecule in the inner sphere and the bulk water molecules in the outer sphere significantly influences the relaxivity.[134, 143]

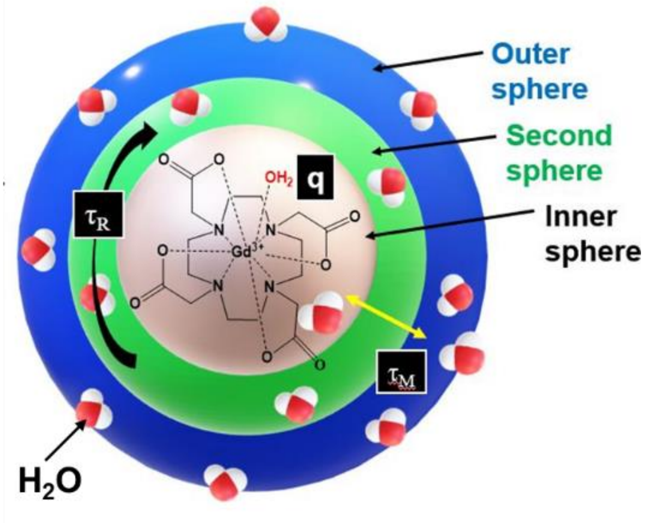

Figure 1. 14:Scheme illustrates the parameters influencing the relaxation efficiency of MRI contrast agent (Gd^{3+}) at the molecular level.

While molecular Gd-chelates lack outstanding contrast efficacy and sensitivity especially at the very early stages of cancer, the essential requirement for a notably improved alternative is paramount. Considering the factors influencing contrast agents' performance, nanomaterials present a promising avenue to augment sensitivity. By mitigating the rotational tumbling motion of Gd-chelates, nanomaterials facilitate an increase in relaxivity, consequently enhancing the contrast.[127]

1.2.4.2.3.2 MSNs as MRI contrast agent

In the realm of MRI nanomaterials, one of the most promising candidates is MSNs, known for their characteristics that significantly enhance sensitivity and overall imaging contrast performance. The enhancement of MRI contrast with MSNs is attributed to their large surface area, enabling high payloads of active magnetic centers.[144] Additionally, the mesopores within MSNs allow water molecules' protons easy access to the magnetic centres, leading to a significant reduction in the decay relaxation times.[145] Moreover, the relatively larger size of MSNs compared to molecular Gd^{3+}-chelates enhances interactions between neighbouring contrast agents by reducing the mobility of water molecules and limiting the potential rotation of CAs.[138, 146]

Several studies have investigated the development of MRI-active MSNs based on gadolinium paramagnetic centres. For instance, Taylor *et al.* coated the surface of MSNs with a Gd-Si-diethylenetriamine tetraacetic acid (DTTA) complex. On a 1 mM Gd basis, the Gd-Si-DTTA complex had an r_1 value of 28.8 mM^{-1} s^{-1} at 3 T and 10.2 mM^{-1} s^{-1} at 9.4 T due to the decrease in the tumbling rate and increased τ_R.[147] Although there is a clear positive effect of MSNs in enhancing the MRI contrast, a significant challenge in crafting optimised MRI probes lies in comprehending the intricate connections between the porous silica support and the relaxometric characteristics of the ultimate contrast agent. This vital aspect is frequently disregarded in current literature, where the primary emphasis is often placed on the sample's ability to deliver high MRI contrast in both *in vitro* and *in vivo* applications. However, this attention is given without due consideration to the chemical intricacies that underlie the relaxation mechanisms. For example, porosity can influence the binding of Gd^{3+} complexes within the pores and/or on the outer surface, consequently affecting the eventual relaxometric properties.

For example, the impact of porosity on relaxometric properties was investigated by Landry and co-workers in 2012.[148] Their study focused on utilising the imidodi(methanediphosphate) ligand, affixed to the internal surface of porous silica nanoparticles, serving as an efficient chelator for Gd^{3+} ions. In this research, three distinct mesoporous silica materials with varying specific surface areas and pore diameters (ranging from 3.6 to 5.5 nm) were appropriately functionalised with aminopropyl groups. Subsequently, the ligand molecules were introduced in the subsequent step. Longitudinal relaxivity values were measured at 1.4 T for all three samples and exhibited enhancements compared to the calculated values for typical commercial molecular Gd^{3+} chelates. This enhancement was attributed to the confinement effect on the tumbling motion of the chelates attached to the nanoparticle surface. However, a distinguishing behaviour was observed corresponding to the varying pore sizes in the samples. The optimal relaxometric performance was observed in the sample with a wider pore diameter (5.5 nm). This outcome was linked to the enhanced diffusion of water molecules through the larger pores, leading to superior propagation of paramagnetic relaxation throughout the bulk solvent.[148]

In certain instances, unexpected outcomes were observed. For example, Davis and co-workers investigated how the positioning of bonded Gd-DOTA chelates on the silica surface influenced the relaxation properties of the resulting samples.[149] The most impressive relaxometric performances, characterised by high relaxivity at a high magnetic field (7 T, 293 K), were achieved when the complexes were situated in close proximity to the entrance of the pores. This arrangement yielded r_1 values of 33.6 $mM^{-1}\ s^{-1}$. Conversely, a significant reduction in r_1, to 10.8 $mM^{-1}\ s^{-1}$, was noted for silica nanoparticles functionalised on the external surface with the same Gd^{3+} chelates at the same grafting densities.[149]

Furthermore, the relaxometric properties of paramagnetic conjugated systems can be significantly influenced by the chemical composition of the mesoporous support. Literature emphasises that the presence of reactive functionalities, such as silanol groups or neutral/positive species, in close proximity to attached paramagnetic chelates often leads to a notable decrease in relaxivity for the final solid. In another study, two hybrid materials were developed using MCM-41 as the MSN, initially activated with NH_3^+ groups, and then functionalised with negatively charged monohydrated GdDOTA-like chelates as well as bishydrated GdDO3A-like derivatives.[150] Contrary to expectations, the GdDO3A-based hybrid system exhibited notably low relaxation efficiency, believed to stem from the coordination of Si–OH groups to the metal centre, displacing one inner-sphere water molecule. A similar limited enhancement in relaxivity was observed for MSNs functionalised with [GdDOTAGA]. In this case, the lower-than-expected r_1 value was attributed to restricted water molecule accessibility to the metal centre due to a strong electrostatic interaction between the negatively charged complex and the NH_3^+ functionalities dispersed on the surface. To validate this hypothesis, the protonated amino groups were converted into neutral amides (Figure 1. 15). This modification significantly accelerated the bound-water chemical exchange process, resulting in a marked increase in relaxivity from 20.3 to 37.8 $mM^{-1}\ s^{-1}$ at 20 MHz and 310 K.

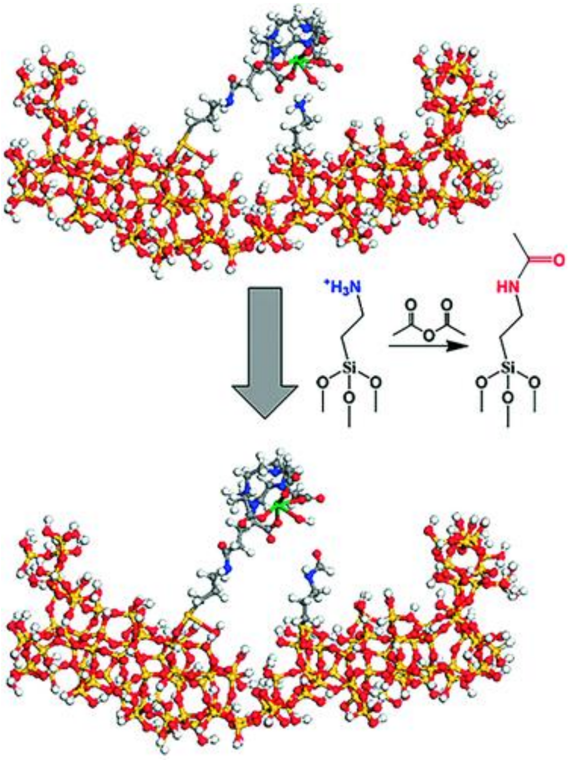

Figure 1. 15: Diagram illustrating [GdDOTAGA]– attachment to the silica surface both before and after ammonium functionalities acetylation, obtained with permission of John Wiley and Sons.[150]

Additionally, the modification of external silica surfaces can significantly influence the relaxometric properties of chelates. This was extensively studied by Davis *et al.* in 2013.[151] They functionalised mesoporous silica nanoparticles with a GdDOTA chelate inside the pores and attached biotin-BSA macromolecules on the surface using varying lengths of organic spacers (PEG molecules). The research demonstrated a strong correlation between relaxivity and the spacer's length between the MSN surfaces and the anchored biotin-BSA. Direct protein linking with a short spacer substantially reduced relaxivity by 78.5% compared to unmodified paramagnetic nanoparticles. This reduction was attributed to steric capping of silica mesopores, hindering water diffusion and access to internalised Gd^{3+} complexes (Figure 1. 16). Conversely, increasing the distance between the protein and the surface using a longer linker (PEG5000) led to a roughly 20% reduction in relaxivity.[151]

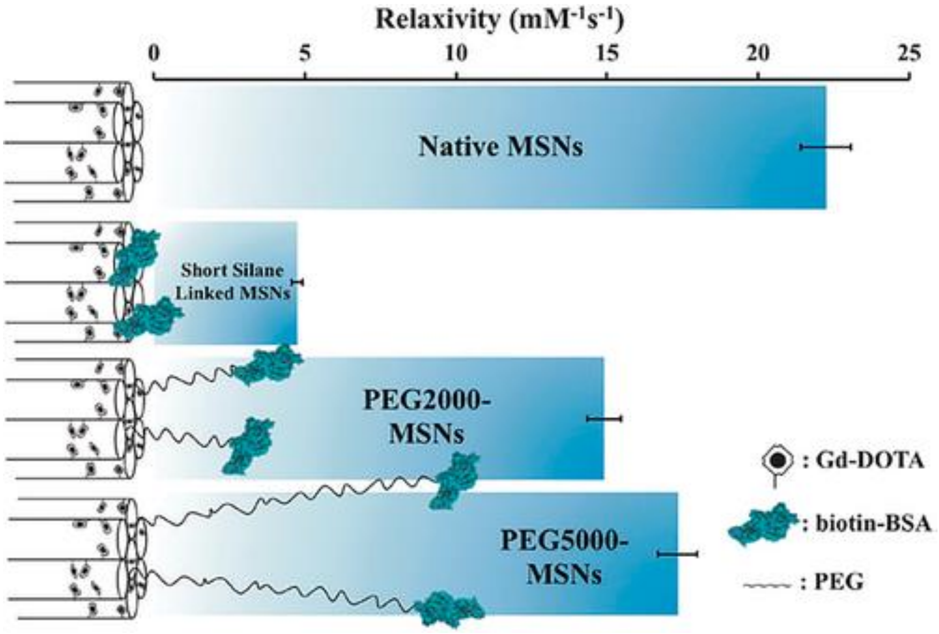

Figure 1. 16: Diagrammatic representation illustrating the relaxivity value (at 7 T and 20 °C) in relation to the varying lengths of spacers between the silica surface and the protein molecule, obtained. with permission from The Royal Society of Chemistry.[151]

In summary, the surface chemistry and pore size of mesoporous silica have a profound impact on the relaxometric properties of paramagnetic samples. This influence is crucial to consider when designing MRI probes, emphasising the need to carefully account for interactions among various functionalities on the silica surface to preserve overall effectiveness.

1.2.4.3 Multifunctional MSNs

1.2.4.3.1 Stimuli-responsive MSNs

As previously discussed, MSNs exhibit considerable promise for use as drug delivery systems as well as diagnostic tools. However, a major drawback of this system is the potential for premature drug release in the bloodstream before reaching the intended target tissues.[152]

To address this issue, controlled release of loaded cargos can be achieved by employing "gatekeepers" that respond to specific stimuli. Typically, these gatekeepers seal the drug molecules within the pores, and upon exposure to specific intracellular or extracellular stimuli (Figure 1. 17), the gatekeepers undergo changes in size, shape, conformation, or dissociate to release the drug.[153] This approach significantly enhances drug effectiveness while minimising damage to the entire body.

Tumour tissues possess a unique microenvironment with distinct physiological parameters compared to healthy tissues and cells.[154] Notably, the pH in the tumour microenvironment is weakly acidic (approximately 6.5−6.8), and endosome/lysosomal organelles have an even lower pH (about 4−6) compared to the relatively neutral pH (7.0−7.4) of cytoplasm, blood, and healthy tissues.[155] These variations can trigger the cleavage of acid-sensitive molecules. Additionally, tumours exhibit higher glutathione (GSH) levels and lower oxygen levels, providing favourable conditions for redox reactions. Tumour sites also feature a higher temperature (4–5 °C) than the normal tissues[156] as well as highly expressed enzymes, such as matrix metalloproteinases, proteinases K, cathepsin B, and hyaluronidase, which can specifically hydrolyse corresponding substrates.[157] Leveraging these endogenous stimuli is a promising strategy for the design of stimuli-responsive gated mesoporous silica systems.

In addition to endogenous stimuli, exogenous stimuli play a vital role and include heat, magnetic fields, ultrasonic waves, light, and more.[158, 159] Compared to endogenous stimulation, exogenous stimuli offer a safer and more effective means of achieving controlled release, overcoming variations due to individual differences. Utilising exogenous physical stimulations, the physicochemical changes in materials can accelerate drug release and enable spatiotemporal controlled manipulation. Exogenous stimuli not only prevent premature drug release and minimise side effects but can also induce additional therapeutic effects, such as photothermal therapy and photodynamic therapy.

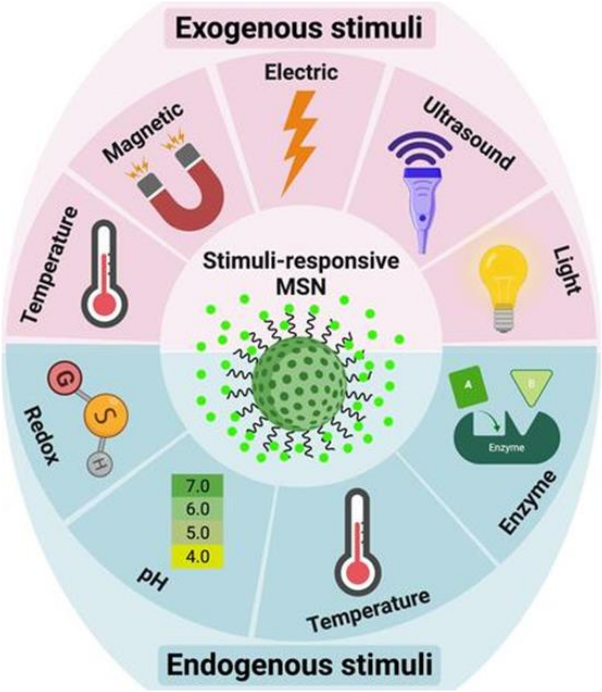

Figure 1. 17: Stimuli-responsive drug delivery systems based on MSNs, obtained with permission from Taylor & Francis Journal Permissions.[160]

Various studies have explored capping MSNs with responsive gatekeepers. For instance, sodium alginate-coated MSNs were developed for dual responsive controlled release of doxorubicin (Dox). The coating was facilitated *via* disulphide linkage, providing reduction-sensitive property, and inherent pH-responsive characteristics of alginate. Notably, over 60% of Dox was released at pH 5.0 in the presence of glutathione (10 mM), while less than 20% was released without stimuli. Blank nanocarriers exhibited high biocompatibility, with over 90% cell survivability in HeLa cells, whereas Dox-loaded MSNs exhibited 54% cell death.[161]

In another study, iron oxide core@shell MSNs coated with pH-responsive poly(ethyleneimine) (PEI) and folic acid were designed for effective erlotinib delivery. The iron oxide core enabled targeted magnetic resonance imaging, while PEI supported controlled drug release. Folic acid was conjugated to PEI for targeted delivery. These nanoparticles displayed higher toxicity in HeLa cell lines compared to free erlotinib. A 30% increase in drug release was observed at pH 5.5, attributed to reduced attraction between silica surface and PEI, enhancing drug release.[162]

Furthermore, Liu *et al.* utilised β-cyclodextrin coating on MSNs to regulate indocyanine green release from mesoporous silica-coated gold nanorods.[163] They incorporated a dual-functional RLA peptide for membrane penetration and mitochondrial targeting. Additionally, a charge-switchable and anti-fouling polymer was coated for biocompatibility and stability. Under the acidic tumour microenvironment, the interaction between the anti-fouling polymer and RLA peptide weakened, enhancing cellular internalisation and mitochondrial accumulation. Combined photodynamic and photothermal therapy demonstrated significant antitumour effects.[163] In addition, Tao *et al.* designed poly(acrylic acid) (PAA) coated MSNs loaded with arsenic trioxide for targeted and pH-triggered release in glioma. The MSNs were further encapsulated within liposomes coated with angioprep-2 as a targeting ligand, achieving improved cellular uptake and blood-brain barrier permeation. This hybrid nanocarrier exhibited remarkable antitumour activity in glioblastoma orthotopic rats, showcasing enhanced therapeutic efficacy compared to free arsenic trioxide or polymer-coated MSNs.[164]

In addition to drug release control, enveloping MSNs with stimuli-responsive materials can also serve as a gating system for water. These gatekeepers possess the capability to obstruct pore openings, regulating water access to an internalised paramagnetic species through stimuli-responsive behaviour, offering a novel avenue for tuneable MR imaging that can be switched “on” or “off”. Ensuring water accessibility is a crucial aspect in the design of MRI contrast agents to produce robust MRI signals. For instance, Pellico *et al.* explored Gd-DOTA loaded MSNs with a pH-responsive polymer on the particle surfaces, strategically positioning the Gd-DOTA species at the pore edges (designated as Gd-DOTA@MSNs), to investigate reversible water gating effects across different pH levels.[165] The polymer coating comprised poly(acrylic acid) (PAA), known to adopt a globular conformation at low pH (< 5.5) and an open conformation at higher pH (*e.g.*, pH 9). Their hypothesis was that in its globular state, the polymer would prevent or minimise water's accessibility to the pores, limiting interaction with the Gd-DOTA moieties. Conversely, in its uncoiled conformation at high pH, there would be less pore obstruction, enabling water to freely interact with the paramagnetic Gd^{3+} species and resulting in a higher longitudinal relaxivity. The study revealed a highly effective gating system during relaxometric measurements when varying the pH between 3 and 10. At low pH, the r_1 value was 9 $mM^{-1}s^{-1}$, while at pH 10, it experienced a 1.3x increase with a value of 20 $mM^{-1}s^{-1}$, highlighting the ability to trigger a relaxation change based on pH through water gating. This effect was reversible across pH, confirmed by cycling between pH 7 and 4, observing corresponding fluctuations in relaxivity.[165] As a result stimuli-responsive MSNs hold significant promise encompassing gated delivery and controllable imaging diagnostics.

In this thesis, our primary objective is to create a thermo-responsive polymer acting as a gatekeeper for MSNs. This gatekeeper aims to prevent early drug release and regulate water access to Gd^{3+} within the pores, enabling a switchable on/off drug release and MRI signal when exposed to stimuli at tumour tissues. This gatekeeper is specifically engineered to be highly sensitive to the subtle temperature difference between the standard physiological temperature of 37 °C and the elevated temperatures observed in cancerous tissues (38-42 °C) or hyperthermia treatment at 45 °C.[166, 167] This temperature differential poses a significant challenge, which we aim to address.

1.2.4.3.1.1 Thermo-responsive polymers

Thermo-responsive polymers are a unique class of materials that exhibit changes in solubility depending on the surrounding temperature. These alterations in solubility are accompanied by significant modifications in the polymer's molecular structure controlled by entropic changes in hydrogen bonding between neighbouring polymer chains. The temperature at which these changes occur is known as the transition temperature/cloud point, often referred to as the critical solution temperature.[168, 169]

Thermo-responsive polymers can be categorised into two main groups: those with an upper critical solution temperature (UCST) and those with a lower critical solution temperature (LCST).[168] The LCST polymers such as poly(N-isopropylacrylamide) (PNIPAAm) change from hydrophilic into hydrophobic upon increasing temperature, unlike UCST polymers such as poly(acrylamide-co-acrylonitrile) (poly(AAm-co-AN)) whose conformational changes from a hydrophilic to a hydrophobic state with decreasing temperature as shown in Figure 1. 18 and Figure 1. 19.

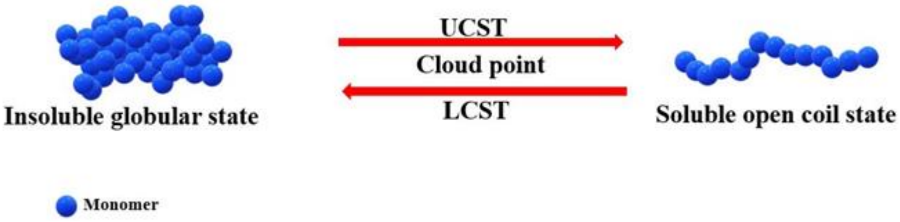

Figure 1. 18: Schematic representation of illustrating the change in UCST and LCST polymers conformation at the cloud point.

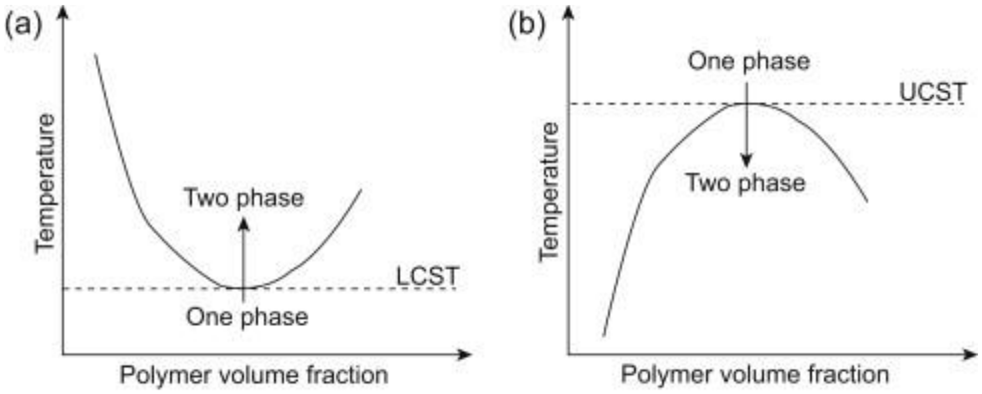

Figure 1. 19: Curves showing phase transition phenomenon. (a) Lower critical solution temperature (LCST) and (b) upper critical solution temperature (UCST) phase transition behaviours of thermo-responsive polymers in solution, obtained with permission from Science Direct.[170]

The cloud point of the polymer can be adjusted by modifying various factors to align with specific biomedical applications. For instance, altering the hydrophilic-hydrophobic balance of the building blocks can have a significant impact.[168, 169] An example of this is the inclusion of hydrophilic monomers, which enhances hydrogen bonding affinity with water, either reducing the UCST or elevating the LCST.[171] It was found that incorporating the hydrophilic monomer acrylamide with NIPAM at a molar ratio of 1:15 (acrylamide:NIPAM) resulted in an increase in LCST to 39 °C compared to PNIPAm alone whose LCST is 32°C.[172, 173]

In addition, changing the polymer chain length, concentration, and/or the solution components (salts or cosolvent) was also reported to affect the cloud point through changes in steric interactions between polymer chains, their hydrogen bonding behaviour or electrostatic interaction with the polymers.[171, 174] These unique properties render these polymers highly valuable in biomedical applications. Their solubility characteristics can be finely adjusted and utilised to target specific tumour tissues where the desired response is present.

Ideally, in order to achieve composites with biologically relevant responses for drug delivery, thermosensitive MSNs based on UCST and LCST polymers should retain their payload at body temperature (approximately 37 °C). Upon reaching the tumour site (38–42 °C), these polymers should facilitate rapid drug release. For instance, Hu *et al.* demonstrated an NIR-triggered drug release system based on thermo-responsive MSNs. They achieved this by grafting poly(N-acryloyl glycinamide-co-N-phenylacrylamide) (P(NAGAm-co-NPhAm)) UCST polymer onto hollow mesoporous silica nanoparticles (HMSNs) and then treating them with the photothermal conversion agent indocyanine green (ICG). The UCST polymers they prepared had a transition temperature of 45 °C, making them advantageous gatekeepers in the physiological environment at 37 °C. When exposed to NIR irradiation, the solution temperature surpassed the clearing point due to the presence of ICG, causing the UCST polymer chains to collapse and become more hydrophilic. As a result, the mesoporous channels of the HMSNs were exposed, enabling a rapid drug release.[175]

Moreover, Peralta *et al.*[176] introduced ferrous oxide (FeO) nanoparticles with mesoporous silica shells coated with poly(N-isopropyl acrylamide-co-3-(methacryloxypropyl) trimethoxysilane) (PNIPAM-co-MPS) for drug delivery applications (Figure 1. 20). Polymer contraction above the LCST (40 °C) led to pore opening, resulting in complete drug release within 24 hours. Conversely, below the LCST (25 °C), extended polymer state restricted drug release by obstructing the pores. In this case, temperature control could be achieved using the hyperthermic response of the iron oxide particles.

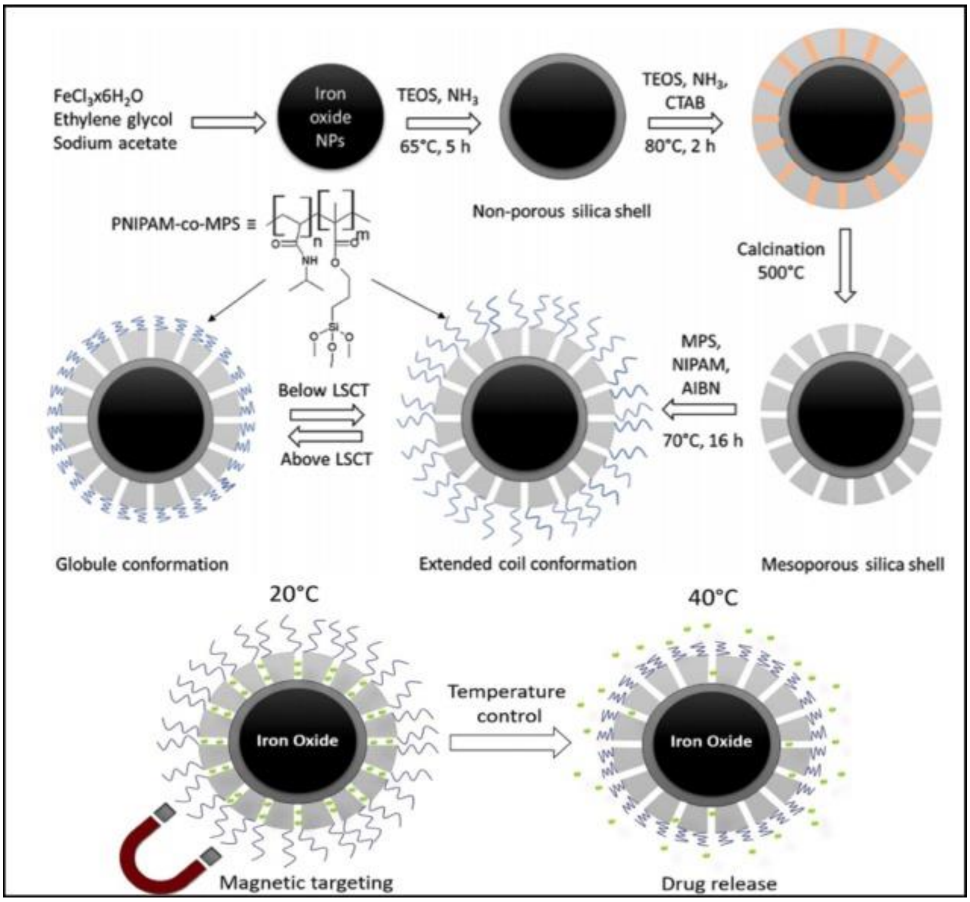

Figure 1. 20: Synthesis procedure for MMSNP–PNIPAM–co–MPS and graphical abstract, where MMSNP, TEOS, AIBN mean magnetic mesoporous silica nanoparticles, tetraethoxy orthosilicate, azobisisobuyrolnitirile, respectively, obtained with permission from Elsevier.[176]

1.2.4.3.1.2 Grafting of polymers onto the surface of MSNs

In order to bestow this thermo-responsive property onto nanoparticles, polymers must be covalently attached to the nanoparticle surfaces as shown in Figure 1. 21. This is carried out either by ‘grafting to’ or ‘grafting from’ as previously described in literature (Table 1. 1). In the ‘grafting to’ technique, a polymer with a suitable end-functionalised group is prepared first, before its immobilisation onto a reactive MSNs surface *via* a covalent bond.[177] This approach has the advantage of controlling the polymer molecular weight and its polydispersity, however the low grafting density as a result of the steric hindrance represents the main drawback.[178, 179] Silica surfaces are alternatively often modified using the ‘grafting from’ technique where surface-initiated polymerisation is followed.[180] The polymer chain can grow in this method directly on the MSNs surface, allowing higher density.[177, 179] However, the polymer molecular weight is more difficult to control and subsequently characterise.[177]

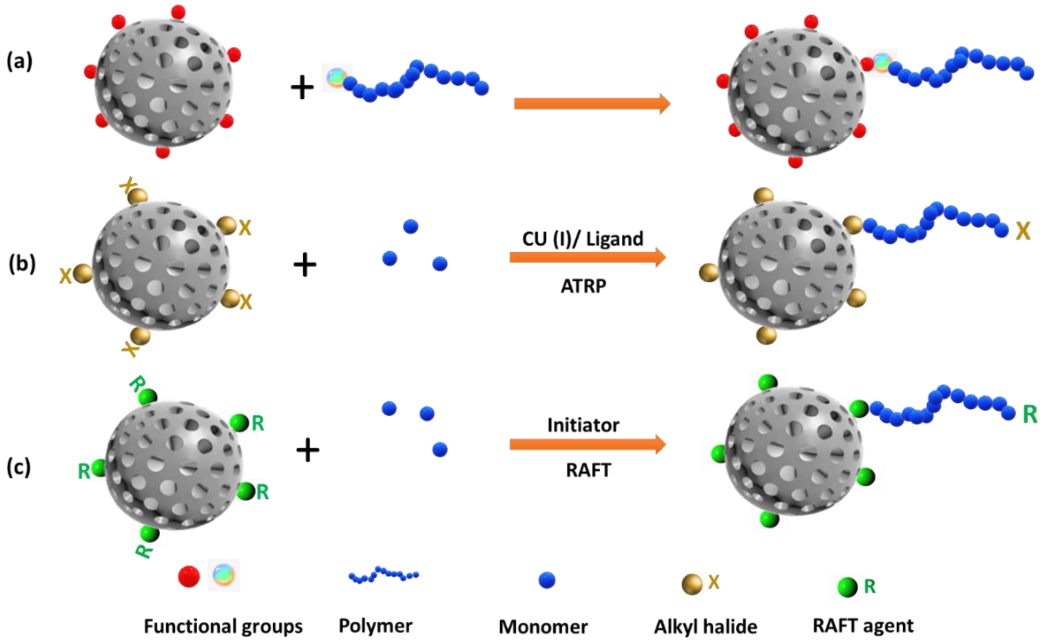

Figure 1. 21: Schematic representation of polymer immobilisation onto the surface of MSNs through (a) grafting to, (b) grafting from via ATRP, and (c) grafting from via RAFT.

Table 1. 1: Examples of thermo-responsive polymers grafted onto the surface of MSNs using different techniques.

Polymer	Type	Grafting technique	Function / nanocarrier	Refs
PNIPAm	**LCST**	**Graft from/ATRP**	**Control Rhodamine 6G release from MSNs**	177
PNIPAm		**Graft to/RAFT**	**Control uptake and release of fluorescein**	181
PNIPAm		**Graft from/RAFT**	**Thermo-responsive MSNS**	108, 182
Poly(NAGAm-co-NPhAm)	**UCST**	**Graft to/RAFT**	**Control Dox release from hollow MSNs**	175
Poly(AAm-co-AN)		**Graft to/radical polymerisation**	**Control Dox release from MSNs**	183

1.2.4.3.1.2.1 Controlled radical polymerisation

In order to control polymer grafting onto the silica surface, controlled radical polymerisation can be followed. Reversible addition fragmentation chain transfer (RAFT) and atom transfer radical polymerisation (ATRP) are the most popular polymerisation mechanisms where polymers of controlled molecular weight and narrow polydispersity can be prepared.[179]

1.2.4.3.1.2.1.1 Reversible addition fragmentation chain transfer (RAFT)

RAFT is a type of radical polymerisation where a chain transfer agent or RAFT agent is added to control the polymerisation reaction. RAFT agents mostly contain a thiocarbonylthio moiety (SC(Z)S-R) such as dithiocarboxylate.[179, 184] In this technique, a thermal initiator is used as free radical source ($I^\bullet$) ((*e.g.* azobisisobutyronitrile (AIBN)). It propagates the reaction *via* reacting with monomer molecules forming propagating radical ($P_n^\bullet$) as in the traditional radical polymerisation. The formed propagating radical is added to RAFT agent followed by fragmentation of $R^\bullet$ which re-initiates the reaction through reacting with other monomers, forming $P_m^\bullet$. The rapid equilibration between the propagating radical $P_m^\bullet$ and the dormant RAFT agent allows preparing polymers of similar chain length with narrow polydispersity, as shown in Figure 1. 22. In addition, an end-group functionalised polymer chain can be adjusted through selecting the RAFT agent.[177, 179, 184]

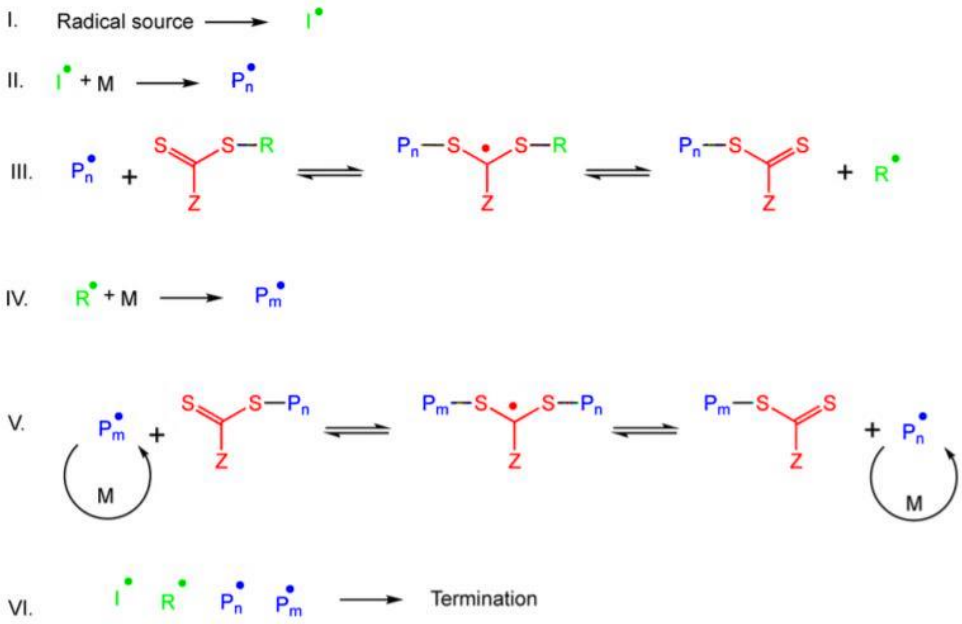

Figure 1. 22: The mechanism of RAFT polymerisation with permission of American Chemical Society (ACS) Publications under license CC-BY .[185]

In the 'grafting from' approach, the RAFT agent is covalently linked to silica surfaces *via* the R or Z group to initiate the polymerisation.[177] A sacrifice RAFT agent is added to the solution to allow polymerisation of free chains which can be separated and characterised.[179]

1.2.4.3.1.2.1.2 Atom transfer radical polymerisation (ATRP)

The components of this technique include an initiator as a radical source (alkyl halide), metal catalyst (*e.g.* copper halide (I)), ligand, and solvent. The initiator can be immobilised onto the MSNs for grafting the polymer from the surface (Figure 1. 23).[179, 186] Similar to RAFT, controlled molecular weight polymers with low polydispersity indexes (PDI), as well as easily end-group functionalised polymers can be prepared.[178, 179] However, using a metal catalyst may limit the biomedical application of such polymers since this can remain physisorbed to the particle surfaces and present potential toxicity. In order to characterise the grafted polymer in the case of grafting from, a sacrificial initiator is added to the medium to obtain a similar polymer in the chain length.[179, 187]

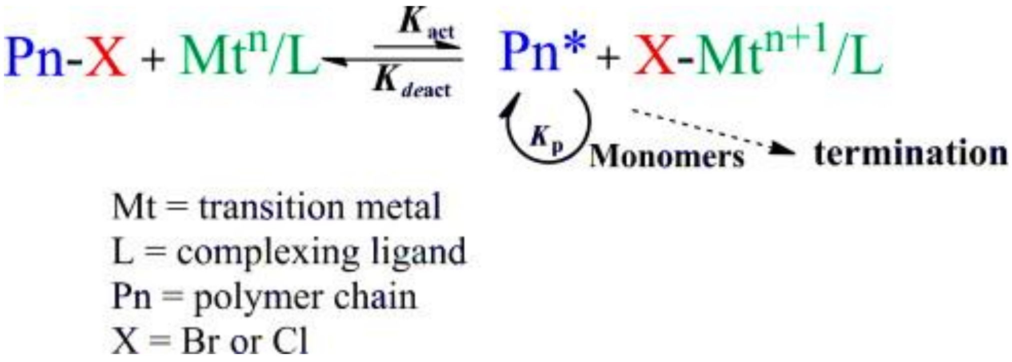

Figure 1. 23: The mechanism of ATRP, obtained with permission from Elsevier.[188]

1.2.4.3.2 Targeting approaches using MSNs in hepatocellular carcinoma

In addition to stimuli-responsive MSNs, various mechanisms for targeting HCC include both passive and active targeting strategies to selectively transport drugs to HCC tissues and cells. These strategies aim to overcome the limitations associated with conventional treatments and diagnostic approaches.[189, 190] The capability to specifically target the tumour not only enhances the efficacy of agents but also helps regulate dose-limiting side effects in other tissues. A well-optimised nanosystem consistently integrates multiple delivery strategies to achieve a substantial accumulation in the tumour.

1.2.4.3.2.1 Passive targeting

Liver tumours manifest extensive angiogenesis and flawed vascular structures, coupled with a compromised lymphatic drainage system.[191] This creates a scenario where the vascular networks in HCC exhibit increased permeability to circulating nanoparticles, while the lymphatic system experiences a diminished rate of disposal for internalised nanoparticles. Consequently, MSNs accumulate in the interstitial space of HCC. tumours,veraging the enhanced permeation and retention (EPR) effect as the foundational principle for achieving passive targeting in nanosystems.[192, 193]

The EPR effect's dynamics are significantly shaped by the size, shape, and surface chemistry of MSNs.[192, 194, 195] An illustrative study by Meng et al. revealed that 50 nm MSNs coated with a PEI-PEG copolymer achieved an intratumoral accumulation of approximately 12% of the total dose. This accumulation was notably superior to the 1% observed for 100 nm phosphonate-coated MSNs and 3% for 50 nm PEGylated MSNs. The introduction of an additional cationic polymer on the MSNs mitigated potential drawbacks associated with the PEG surface. Moreover, research from Harvard Medical School indicated that the combined use of radiation and cyclophosphamide could intensify tumour-associated vascular leakage, leading to a sixfold increase in nanoparticle accumulation in the tumour.[196]

1.2.4.3.2.2 Active targeting

Passive targeting, relying on EPR effect, often lacks specificity across different tumour tissues and stages of tumour development.[197] To enhance targeting efficiency, there has been a recent surge of interest in active targeting strategies.

Given the overgrowth and abnormalities in HCC, numerous receptors are typically upregulated on the surface of HCC cells compared to normal cells. This scenario provides an opportunity for smarter targeting approaches through the recognition of these receptors by specific ligands on MSNs. Various targeting ligands employed in MSN-based HCC theranostics include lactobionic acid,[198] folic acid,[199] arginine-glycine-aspartate (RGD),[200] transferrin,[201] hyaluronic acid,[202] low-density lipoprotein (LDL),[203] among others.

1.3 Unveiling nanocarrier dynamics: navigating the life cycle of nanoparticles in the human body for HCC delivery

Nanoparticles, especially MSNs, exhibit potential in overcoming obstacles associated with HCC. While intravenous administration of nanocarriers has been extensively studied in the context of HCC,[204-209] However, they still face challenges in achieving specificity, prolonged blood circulation, optimal cellular uptake, efficient intracellular release, and minimal clearance time.

1.3.1 Physiological hurdles in targeting HCC

Several physiological hurdles impede the penetration of nanoparticles into HCC tissues and cells in vivo. These obstacles encompass the formation of a serum protein corona upon contact with blood, clearance by the mononuclear phagocyte system (MPS), and interactions with the extracellular matrix and the membrane of HCC cells as shown in Figure 1. 24.[210]

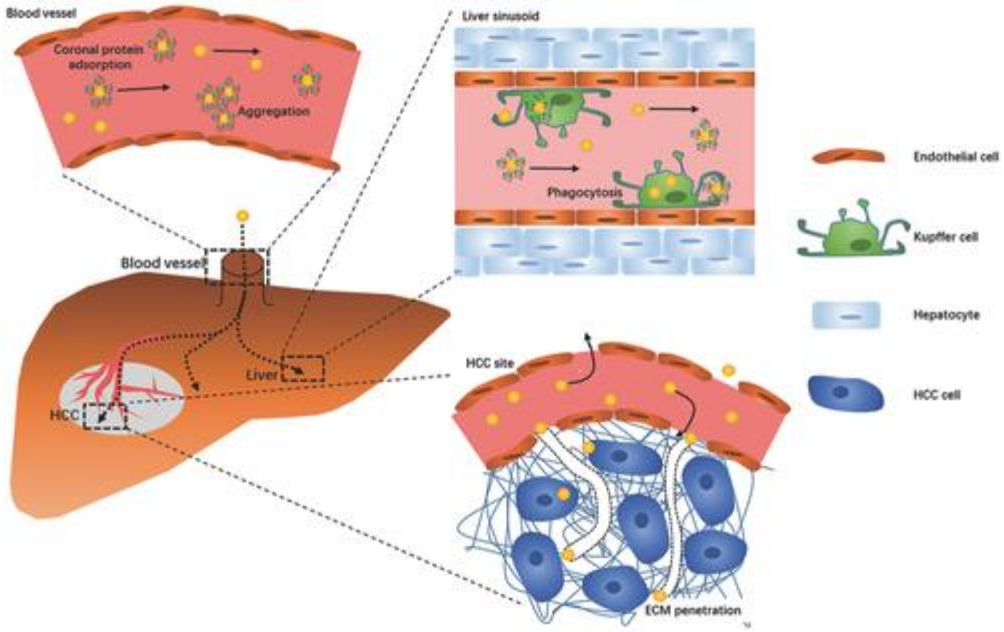

Figure 1. 24: The physiological barriers of nanoparticles for effective targeting in HCC, obtained with permission from John Wiley and Sons.[210]

1.3.1.1 Protein Corona Formation

The inevitability of protein corona formation on nanoparticles in a physiological environment has been well-established. Studies reveal that serum proteins bind to the surface of gold nanoparticles (AuNPs), irrespective of particle shape and surface charge.[211] Once the protein corona is formed, its interaction with nanoparticles can alter their size, surface charge, and aggregation state, potentially leading to detrimental aggregation. Additionally, the protein corona defines the biological identity of the nanoparticle, influencing its fate in vivo.[212] For instance, nanoparticles with an opsonin corona (e.g., immunoglobulin G (IgG), complement factors, and fibrinogen) tend to be recognised by the Mononuclear Phagocyte System (MPS) and are swiftly sequestered in the liver and spleen.[213] On the contrary, dysopsonin adsorption (e.g., albumin) results in prolonged blood circulation of nanoparticles.[214] In addition, He et al. emphasized the impact of PEGylation on MSNs, revealing that the grafting of PEG significantly reduced human serum albumin binding and cellular responses.[215] This study concluded that PEG modification substantially decreased protein binding to MSNs and mitigated macrophage uptake.[215]

1.3.1.2 Mononuclear Phagocyte System

The sequestration and elimination of nanomedicine in the liver and spleen constitute a crucial component of the body's self-defense mechanism. Prioritising well-crafted surface functionalisation of nanoparticles to diminish clearance from these protective mechanisms is imperative for the development of an efficient HCC targeting delivery system. Injected nanoparticles, particularly those attached by opsonin, are predominantly recognised by macrophages in the blood, spleen, and liver, leading to their subsequent phagocytosis and clearance.[216-219] The rate of sequestration in the spleen and liver heavily relies on the surface properties of the nanoparticles, including surface charge, ligand size, and relative chemical characteristics.[220] Notably, nanoparticles featuring highly cationic or anionic surface charges are prone to phagocytosis due to increased serum protein adsorption.[221]

Given that liver sequestration and clearance significantly impede the efficient delivery of nanoparticles to HCC,[222] it is crucial for nanoparticles to evade unspecific uptake by Kupffer cells before reaching the tumour site. Several strategies have been proposed to mitigate liver sequestration of nanoparticles, with PEGylation being a standard approach to enhance their escape. By impeding the interaction of the nanoparticle surface with opsonin, PEGylation effectively suppresses the likelihood of phagocytosis. Studies by Walkey et al. demonstrated the impact of PEG coating density and particle size of gold nanoparticles on uptake efficiency by macrophages.[221] It was observed that PEGylation significantly reduced the uptake of AuNPs of all sizes. With low PEG density coating, nanoparticles were susceptible to serum-dependent phagocytosis, whereas high PEG density coating rendered phagocytosis less efficient and serum-independent (Figure 1. 25).[221]

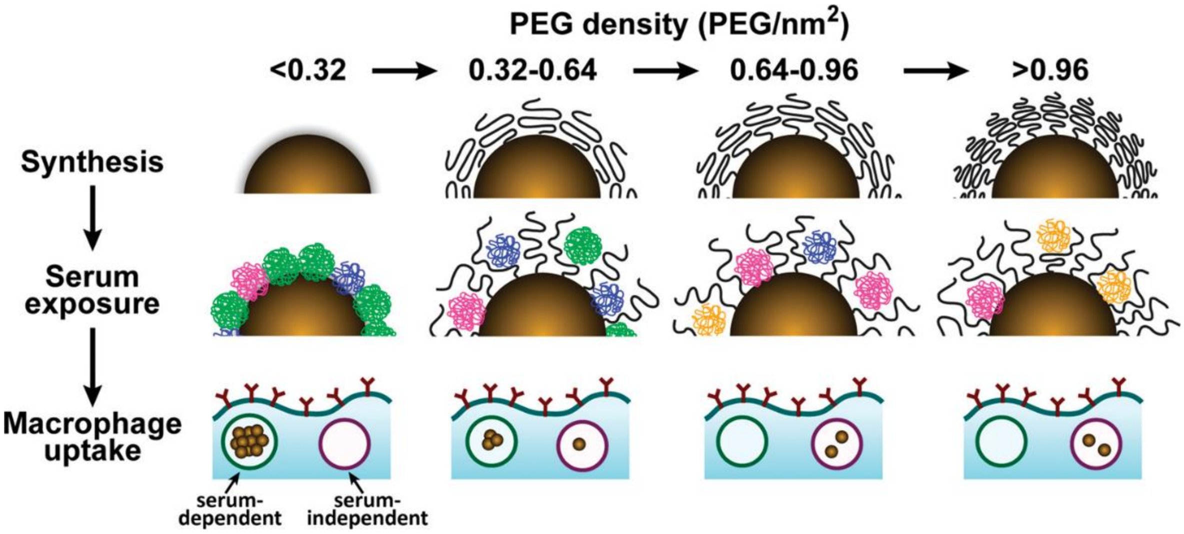

Figure 1. 25: Diagram demonstrating the impact of varying PEG density on the adsorption of serum proteins to gold nanoparticles and the consequent internalisation by macrophages, obtained with permission from American Chemical Society (ACS).[221]

1.3.1.3 Extracellular Matrix and Cell Membrane of HCC

After navigating through MPS clearance and circulating to the HCC tumour site, the Enhanced Permeability and Retention effect facilitates the accumulation of nanoparticles in the interstitial space. However, a significant hurdle remains as the nanoparticles need to penetrate the dense extracellular matrix (ECM) to reach tumour cells effectively.[210] For successful therapy, deep penetration into the central parenchyma of the HCC tumour is crucial. The normal ECM maintains a dynamic equilibrium of synthetic and degradative mechanisms, providing structural and biological support to cells through various components such as proteoglycans, hyaluronic acid, collagen, elastin, laminin, and other structural proteins.[223] In contrast, tumours exhibit a dense ECM characterised by the deregulated production of interconnected collagen fibers, large glycoproteins, and proteoglycans, impeding the diffusion of nanoparticles into deep HCC cells due to increased stiffness and reduced pore size of the matrix.[224-226] Additionally, high interstitial fluid pressure in the center of HCC further hinders nanoparticles from achieving deep penetration.

One effective strategy to enhance ECM penetration is the reduction of particle size. In a prior investigation, quantum dots with a size of 12 nm exhibited enhanced penetration when compared to larger quantum dot clusters of 60 nm and 125 nm in the tumour ECM.[227] Surface coating of nanoparticles with proteases, such as collagenase, gelatinase, and hyaluronidase, represents a more active approach to disrupt the dense ECM.[228, 229] For instance, Bromelain-mesoporous silica nanoparticles (Br-MSNs) coated with a mixture of nine different proteases demonstrated enhanced migration and ECM digestion in an animal model.[228, 229]

Following successful ECM penetration, the next challenge is the penetration of the HCC cell membrane for effective targeting. To comprehend this process and develop nanoparticles capable of delivering drugs to intracellular locations, understanding the interactions between nanoparticles and cell membranes is essential. Nanoparticles cannot freely permeate cell membranes; instead, their internalisation relies on endocytic processes such as pinocytosis, phagocytosis, or endocytosis.[230] The biophysical properties of the cell membrane and the physicochemical properties of nanoparticles play crucial roles in these interactions.[231, 232] For instance, surface charge influences nanoparticle internalisation by modulating the membrane potential.[233] Thus, modifying the surface of nanoparticles with a positively charged ligand has the potential to enhance HCC cell membrane penetration.

1.3.2 Optimising nanoparticle physicochemical properties for overcoming physiological barriers in HCC

Nanoparticles exhibit diverse physicochemical properties such as size, surface charge, geometry, and hydrophobicity, which impact HCC targeting by influencing protein adsorption, blood circulation half-life, renal clearance, extravasation, and endocytosis in numerous ways.

1.3.2.1 Particle size

Particle size stands out as a pivotal parameter determining the path of nanoparticles in drug delivery. Modulating nanoparticle size offers the potential to boost aggregation at the tumour site, influencing circulation half-lives and tumour extravasation/penetration. Smaller nanoparticles, evading MPS clearance, showcase prolonged circulation half-lives, augmenting the likelihood of tumour accumulation.[210] Optimal blood circulation half-life is achieved with nanoparticles within the 10–150 nm size range, while those smaller than 10 nm undergo rapid renal clearance.[234, 235] Larger nanoparticles tend to accumulate in the liver and spleen, while smaller counterparts, exceeding renal clearance thresholds, leverage EPR effect for superior tumour accumulation in analogous models.[236]

1.3.2.2 Surface charge

The surface charge of nanoparticles within a biological system is primarily determined by the charge of their surface ligands, a factor known to impact cellular internalisation and MPS clearance. Highly cationic or anionic surface charges make nanoparticles prone to phagocytosis, driven by elevated serum protein adsorption.[221] A previous study has indicated that positively charged particles may be more effective in antitumour therapy, as they are more readily taken up by proliferating cells.[237] Conversely, negatively charged particles may play a crucial role in scenarios requiring deep tissue delivery, benefiting from the rapid diffusion of particles.[237] In a study by Souris et al., highly positively charged, near-infrared fluorescent MSNs were synthesised for use as traceable drug delivery platforms with high capacity.[238] The MSNs were loaded with the near-infrared fluorescent dye indocyanine green (ICG) through covalent or ionic bonding, resulting in constructs with significantly different net surface charges. In vivo fluorescence imaging and subsequent analysis revealed distinct uptake and elimination behaviours, indicating that the highly charged moieties were rapidly excreted from the liver into the gastrointestinal tract, while less charged moieties remained sequestered within the liver.[238] These observations suggest that charge-dependent adsorption of serum proteins plays a crucial role in facilitating hepatobiliary excretion of silica nanoparticles, offering a potential avenue for regulating nanoparticle residence time in vivo through surface charge manipulation.

1.3.2.3 Geometry

Following successful evasion of the MPS and circulation to the tumour vasculature, nanoparticles must migrate toward the blood vessel wall to enter the HCC extracellular matrix through the pores of leaky vasculature.[239] Therefore, nanoparticles exhibiting higher drift velocity in blood flow have a greater likelihood of blood vessel penetration and increased tumour accumulation. In a normal blood vessel, spherical nanoparticles tend to follow the flow streamlines and exhibit no preference in margination due to balanced forces driving translational and rotational motions.[240] In contrast to spherical nanoparticles, those with different aspect ratios may experience lateral drift due to uneven forces driving their rotational motion.[194] For instance, discoidal (aspect ratio (AR) = 0.5), hemispherical, and ellipsoidal particles (AR = 0.5) have been demonstrated to possess higher drift velocities than spheres.[194] Chauhan and colleagues have shown that rod-shaped nanoparticles pass through porous media more rapidly than spherical ones of the same hydrodynamic size (34–36 nm).[241]

1.3.2.4 Hydrophobicity

As most nanoparticles are enveloped with a layer of surface ligand to ensure optimal performance in vivo, the hydrophobic nature of these surface ligands plays a pivotal role in determining the overall hydrophilicity/hydrophobicity of the final nanoparticles. Surface hydrophobicity significantly influences serum protein adsorption and cellular uptake of nanoparticles.[242] Hydrophobic nanoparticles tend to attract opsonins, leading to swift recognition and phagocytosis.[242] In a study by Moyano and colleagues, zwitterionic nanoparticles with adjustable hydrophobicity were synthesised, allowing control over protein adsorption at moderate levels of serum protein and preventing the formation of hard coronas at physiological serum concentrations.[243] However, it is noteworthy that, in terms of cellular internalisation, hydrophobic nanoparticles are more readily taken up by cells.[244]

1.4 Aims and objectives

This thesis endeavours to offer a robust solution to the multifaceted challenges encountered in both advanced-stage treatment and the early diagnosis of hepatocellular carcinoma. This will be accomplished by crafting a multifunctional thermo-responsive system using mesoporous silica nanoparticles (MSNs) as the foundational platform. These MSNs will be meticulously loaded with active pharmaceutical ingredients (doxorubicin HCl and sorafenib tosylate), strategically augmented with the inclusion of Gd-DOTA chelate - an essential element for MRI. Surface grafting with thermo-responsive polymers will permit fine control over the drug release and

concomitant water entry to internalised MRI active Gd species, resulting in signal changes reflective of cargo release. This innovative approach aims to deliver a comprehensive and effective solution for the management of HCC, encompassing advanced treatment options with minimal side effects, improved bioavailability, and precise early-stage diagnostics.

Chapter 2 focuses on enhancing the drug-loading capacity of mesoporous silica nanocarriers for both the hydrophilic drug doxorubicin and the hydrophobic drug sorafenib tosylate. We plan to achieve this by optimising various elements, such as the surface chemistry of pore channels, the loading method, solvent selection based on polarity, and pore size. By thoroughly investigating these aspects, we aim to optimise the nanocarriers' ability to encapsulate drugs with differing solubilities. Ultimately, this endeavour aims to develop more efficient drug delivery systems with improved therapeutic effectiveness.

In Chapter 3, the main goal is to create Gd-DOTA MRI-active theranostic mesoporous silica nanoparticles. The investigation delves into the influence of several factors on the MRI signal, including the localisation of paramagnetic chelates, surface chemistry, pore size, as well as variations in media and temperature. Additionally, the study explores the effect of hydrophilic and hydrophobic drug loading and the subsequent release of doxorubicin and sorafenib on MRI signal. Overall, this research aims to advance the development of efficient MRI contrast agents based on MSNs, catering both non-invasive imaging and targeted drug delivery.

Chapter 4 focuses on creating thermo-responsive polymers, poly(AAm-co-AN) and PNIPAm, that respond to elevated temperatures typical of hepatocellular carcinoma tissues or hyperthermia treatment (38-45 °C). The challenge is precise tuning of the UCST of poly(AAm-co-AN) within the applicable temperature range, necessitating exploration of polymer synthesis strategies and optimisation through Design of Experiments (DoE). Similarly, for LCST PNIPAm, the goal is to achieve a homogenous polymer with a tuned cloud point and appropriate end groups for future grafting onto MSNs. Thermo-responsive behaviour validation will employ turbidimetry and dynamic light scattering techniques. The objective is to provide well-characterised UCST and LCST polymers for grafting onto MRI-active and drug loaded MSNs, enabling water gating and controlled drug release in Chapter 5.

In Chapter 5, our aim is to create a versatile thermo-responsive theranostic system that can both regulate drug release and modulate MRI signals in response to temperature shifts, utilising an MRI-active MSN framework. We begin the process by examining the effects of polymer grafting density, linker/spacer chain length, and polymer molecular weight through various techniques such as turbidimetry, dynamic light scattering (DLS), and relaxivity studies. Subsequently, we aim to develop two thermo-responsive systems: one with UCST poly(AAm-co-AN) and the other with LCST PNIPAm polymers previously developed in Chapter 4 on MSN surfaces. These systems were designed to incorporate doxorubicin and sorafenib, respectively, along with a positive MRI contrast agent covalently linked to internal MSN surfaces. The thermo-responsive behaviour of these systems will be confirmed using DLS, and drug release at different temperatures will be determined. Finally, we will assess the effectiveness and safety of the developed theranostic systems through nuclear magnetic relaxation dispersion (NMRD), clinical phantom MRI, and *in vitro* cytotoxicity studies.

In summary, this work aims to shed light on the critical role of MSNs in addressing HCC challenges. It emphasises the creation of highly effective MRI contrast agents for early diagnosis, curative treatment, and improved drug bioavailability and safety, achieved through localised drug release and controlled MRI signal modulation.

1.5 References

1. https://gco.iarc.fr/, (accessed 25/09/2023, 2023).
2. H. Zhang, W. Zhang, et al., Biomarker Research, 2022, **10**, 3.
3. J. D. Yang, P. Hainaut, et al., Nature Reviews Gastroenterology & Hepatology, 2019, **16**, 589-604.
4. K. Tarao, A. Nozaki, et al., Cancer Med, 2019, **8**, 1054-1065.
5. A. Desai, S. Sandhu, et al., World J Hepatol, 2019, **11**, 1-18.
6. A. Jindal, A. Thadi, et al., J Clin Exp Hepatol, 2019, **9**, 221-232.
7. E. Kim and P. Viatour, Experimental & Molecular Medicine, 2020, **52**, 1898-1907.
8. M. S. Gallaway, S. J. Henley, et al., MMWR Surveillance Summaries, 2018, **67**, 1.
9. P. Rawla, T. Sunkara, et al., Contemp Oncol (Pozn), 2018, **22**, 141-150.
10. S. Tellapuri, P. D. Sutphin, et al., Indian J Gastroenterol, 2018, **37**, 481-491.
11. L. Liu, H. Chen, et al., PLoS One, 2014, **9**, e91124.
12. A. Forner, M. Reig, et al., Medicina Clínica (English Edition), 2016, **146**, 511.e511-511.e522.
13. M. Maida, E. Orlando, et al., World J Gastroenterol, 2014, **20**, 4141-4150.
14. X. He, J. Wu, et al., PLoS One, 2018, **13**, e0191095.
15. F. Kanwal and A. G. Singal, Gastroenterology, 2019, **157**, 54-64.
16. K. Lang, N. Danchenko, et al., Journal of hepatology, 2009, **50**, 89-99.
17. Y. Imai, K. Katayama, et al., Liver cancer, 2017, **6**, 349-359.
18. P. Tabrizian, G. Jibara, et al., Ann Surg, 2015, **261**, 947-955.
19. G. Sapisochin and J. Bruix, Nat Rev Gastroenterol Hepatol, 2017, **14**, 203-217.
20. A. Forner, M. Gilabert, et al., Nature Reviews Clinical Oncology, 2014, **11**, 525-535.
21. M. Le Grazie, M. R. Biagini, et al., World J Hepatol, 2017, **9**, 907-920.
22. J. Bruix, S. Qin, et al., Lancet, 2017, **389**, 56-66.

23. M. Kudo, R. S. Finn, et al., Lancet, 2018, **391**, 1163-1173.
24. G. K. Abou-Alfa, T. Meyer, et al., N Engl J Med, 2018, **379**, 54-63.
25. A. X. Zhu, Y. K. Kang, et al., Lancet Oncol, 2019, **20**, 282-296.
26. V. Chew, L. Lai, et al., Proc Natl Acad Sci U S A, 2017, **114**, E5900-e5909.
27. A. B. El-Khoueiry, B. Sangro, et al., Lancet, 2017, **389**, 2492-2502.
28. FDA grants accelerated approval to nivolumab and ipilimumab combination for hepatocellular carcinoma

https://www.fda.gov/drugs/resources-information-approved-drugs/fda-grants-accelerated-approval-nivolumab-and-ipilimumab-combination-hepatocellular-carcinoma, (accessed 25/09/2023, 2023).
29. R. S. Finn, S. Qin, et al., N Engl J Med, 2020, **382**, 1894-1905.
30. J. M. Llovet, S. Ricci, et al., N Engl J Med, 2008, **359**, 378-390.
31. A. L. Cheng, Y. K. Kang, et al., Lancet Oncol, 2009, **10**, 25-34.
32. Z. Ren, K. Zhu, et al., Journal of Clinical Oncology, 2015, **33**, 894-900.
33. A. Bailey and S. A. Shah, J Surg Oncol, 2019, **120**, 847-850.
34. S. Usman, L. Smith, et al., Radiography (Lond), 2018, **24**, e109-e114.
35. J. Li, J. Wang, et al., Eur Radiol, 2019, **29**, 6519-6528.
36. M. Li, W. Zhang, et al., Int J Nanomedicine, 2016, **11**, 5645-5669.
37. A. Raza and G. K. Sood, World J Gastroenterol, 2014, **20**, 4115-4127.
38. A. Vogel and A. Saborowski, Cancer Treat Rev, 2020, **82**, 101946.
39. R. Feynman, in Feynman and computation, CRC Press, 2018, pp. 63-76.
40. J. Jeevanandam, A. Barhoum, et al., Beilstein J Nanotechnol, 2018, **9**, 1050-1074.
41. J. N. Tiwari, R. N. Tiwari, et al., Progress in Materials Science, 2012, **57**, 724-803.
42. R. T. Stiepel, E. Duggan, et al., Bioengineering & Translational Medicine, 2023, **8**, e10421.
43. R. Awasthi, A. Roseblade, et al., Curr Drug Targets, 2018, **19**, 1696-1709.
44. X. Jin, J. Zhao, et al., Front Oncol, 2023, **13**, 1192597.
45. E. D. Mohamed Isa, H. Ahmad, et al., Pharmaceutics, 2021, **13**.

46. S. Jafari, H. Derakhshankhah, et al., Biomed Pharmacother, 2019, **109**, 1100-1111.
47. F. Tang, L. Li, et al., Advanced Materials, 2012, **24**, 1504-1534.
48. F. Ahmadi, A. Sodagar-Taleghani, et al., International Journal of Pharmaceutics, 2022, **625**, 122099.
49. A. Watermann and J. Brieger, Nanomaterials (Basel), 2017, **7**.
50. V. Chiola, J. Ritsko, et al., US 3556725D A filed on, 1971.
51. B. Hanns and K. Gottfried, US 3493341D A filed on January, 1967, **23**, 1967.
52. G. Kallrath and H. Biegler, Google Patents, 1968.
53. C. T. Kresge, M. E. Leonowicz, et al., Nature, 1992, **359**, 710-712.
54. J. S. Beck, J. C. Vartuli, et al., Journal of the American Chemical Society, 1992, **114**, 10834-10843.
55. M. Vallet-Regí, ISRN Materials Science, 2012, **2012**, 608548.
56. B. Siddiqui, A. u. Rehman, et al., International Journal of Pharmaceutics: X, 2022, **4**, 100116.
57. M. Vallet-Regi, A. Rámila, et al., Chemistry of Materials, 2001, **13**, 308-311.
58. G. Øye, J. Sjöblom, et al., Advances in Colloid and Interface Science, 2001, **89-90**, 439-466.
59. D. Zhao, J. Feng, et al., science, 1998, **279**, 548-552.
60. Y. Tozuka, A. Wongmekiat, et al., Chemical and Pharmaceutical Bulletin, 2005, **53**, 974-977.
61. T. Heikkilä, J. Salonen, et al., International Journal of Pharmaceutics, 2007, **331**, 133-138.
62. A. B. D. Nandiyanto, S.-G. Kim, et al., Microporous and Mesoporous Materials, 2009, **120**, 447-453.
63. W. Stöber, A. Fink, et al., Journal of Colloid and Interface Science, 1968, **26**, 62-69.
64. X. Wang, Y. Zhang, et al., Chemistry of Materials, 2016, **28**, 2356-2362.
65. S.-H. Feng and G.-H. Li, in Modern inorganic synthetic chemistry, Elsevier, 2017, pp. 73-104.
66. S.-H. Wu, C.-Y. Mou, et al., Chemical Society Reviews, 2013, **42**, 3862-3875.

67. J. J. Corbalan, C. Medina, et al., International journal of nanomedicine, 2012, 631-639.
68. M. M. Adnan, A. R. M. Dalod, et al., Polymers, 2018, **10**, 1129.
69. A. E. Danks, S. R. Hall, et al., Materials Horizons, 2016, **3**, 91-112.
70. M. Grün, I. Lauer, et al., Advanced Materials, 1997, **9**, 254-257.
71. C. Bharti, U. Nagaich, et al., International journal of pharmaceutical investigation, 2015, **5**, 124.
72. M.-A. Shahbazi, B. Herranz, et al., Biomatter, 2012, **2**, 296-312.
73. S. M. Egger, K. R. Hurley, et al., Chemistry of Materials, 2015, **27**, 3193-3196.
74. P. Yang, S. Gai, et al., Chemical Society Reviews, 2012, **41**, 3679-3698.
75. Q. Yu, J. Hui, et al., Nanoscale, 2012, **4**, 7114-7120.
76. K. Kettler, K. Veltman, et al., Environ Toxicol Chem, 2014, **33**, 481-492.
77. Z.-A. Qiao, L. Zhang, et al., Chemistry of Materials, 2009, **21**, 3823-3829.
78. K. Moeller, J. Kobler, et al., Advanced Functional Materials, 2007, **17**, 605-612.
79. Y.-D. Chiang, H.-Y. Lian, et al., The Journal of Physical Chemistry C, 2011, **115**, 13158-13165.
80. J. Gu, W. Fan, et al., Small, 2007, **3**, 1740-1744.
81. N. I. Vazquez, Z. Gonzalez, et al., Boletín de la Sociedad Española de Cerámica y Vidrio, 2017, **56**, 139-145.
82. N. A. Zainala, S. Shukor, et al., Chem. Eng, 2013, **32**, 432-444.
83. K. Ma, U. Werner-Zwanziger, et al., Chemistry of Materials, 2013, **25**, 677-691.
84. Á. A. Beltrán-Osuna, J. L. Gómez Ribelles, et al., Journal of Nanoparticle Research, 2017, **19**, 1-14.
85. N. Varga, M. Benkő, et al., Microporous and Mesoporous Materials, 2015, **213**, 134-141.
86. L. Xiong, X. Du, et al., Journal of Materials Chemistry B, 2015, **3**, 1712-1721.
87. Y. He, J. Li, et al., Journal of Non-Crystalline Solids, 2017, **457**, 9-12.

88. J. Zhang, X. Li, et al., Journal of Colloid and Interface Science, 2011, **361**, 16-24.
89. T. Kimura, Y. Sugahara, et al., Chemical Communications, 1998, 559-560.
90. J. L. Blin and B. L. Su, Langmuir, 2002, **18**, 5303-5308.
91. D. Shao, M.-m. Lu, et al., Acta biomaterialia, 2017, **49**, 531-540.
92. B. G. Trewyn, J. A. Nieweg, et al., Chemical Engineering Journal, 2008, **137**, 23-29.
93. X. Huang, L. Li, et al., ACS nano, 2011, **5**, 5390-5399.
94. W. Zhang, N. Zheng, et al., Pharmaceutics, 2018, **11**, 4.
95. Q. Cai, Z.-S. Luo, et al., Chemistry of materials, 2001, **13**, 258-263.
96. L. Han, Y. Zhou, et al., Journal of materials science, 2013, **48**, 5718-5726.
97. E. M. Björk, F. Söderlind, et al., Langmuir, 2013, **29**, 13551-13561.
98. X. Pang, J. Gao, et al., Journal of non-crystalline solids, 2005, **351**, 1705-1709.
99. S. Shen, T. Gu, et al., Chemistry of Materials, 2012, **24**, 230-235.
100. B. C. Chen, H. P. Lin, et al., Advanced Materials, 2004, **16**, 1657-1661.
101. X. Cui, S.-W. Moon, et al., Materials letters, 2006, **60**, 3857-3860.
102. S. Huh, J. W. Wiench, et al., Chemistry of materials, 2003, **15**, 4247-4256.
103. A. B. Nik, H. Zare, et al., Microporous and Mesoporous Materials, 2020, **299**, 110115.
104. D. Tarn, C. E. Ashley, et al., Accounts of chemical research, 2013, **46**, 792-801.
105. S. K. Natarajan and S. Selvaraj, RSC advances, 2014, **4**, 14328-14334.
106. L. Pan, Q. He, et al., Journal of the American Chemical Society, 2012, **134**, 5722-5725.
107. S. Giri, B. G. Trewyn, et al., Angewandte chemie International edition, 2005, **44**, 5038-5044.
108. C.-Y. Hong, X. Li, et al., The Journal of Physical Chemistry C, 2008, **112**, 15320-15324.
109. Z.-Y. Li, Y. Liu, et al., ACS Applied Materials & Interfaces, 2014, **6**, 14568-14575.

110. Y. Wang, Q. Zhao, et al., Nanomedicine, 2015, **11**, 313-327.
111. M. Pishnamazi, H. Hafizi, et al., Scientific reports, 2021, **11**, 535.
112. Y. Mehmood, I. U. Khan, et al., European journal of pharmaceutical sciences, 2020, **143**, 105184.
113. Y. Li, S. Wang, et al., Colloids and Surfaces A: Physicochemical and Engineering Aspects, 2020, **590**, 124470.
114. M. Babaei, K. Abnous, et al., European Journal of Pharmaceutics and Biopharmaceutics, 2020, **156**, 84-96.
115. W. Xu, J. Riikonen, et al., International journal of pharmaceutics, 2013, **453**, 181-197.
116. N. Biswas, European Journal of Pharmaceutical Sciences, 2017, **99**, 152-160.
117. M. Thomas, I. Slipper, et al., international Journal of Pharmaceutics, 2010, **387**, 272-277.
118. N. Summerlin, Z. Qu, et al., Colloids and Surfaces B: Biointerfaces, 2016, **144**, 1-7.
119. A. Sarkar, S. Ghosh, et al., Biochim Biophys Acta, 2016, **1860**, 2065-2075.
120. Y. He, S. Liang, et al., Mater Sci Eng C Mater Biol Appl, 2017, **78**, 12-17.
121. J. Wang, Y. Wang, et al., ACS Appl Mater Interfaces, 2016, **8**, 26511-26523.
122. K. E. Bremmell and C. A. Prestidge, Drug Dev Ind Pharm, 2019, **45**, 349-358.
123. K. Bukara, L. Schueller, et al., European Journal of Pharmaceutics and Biopharmaceutics, 2016, **108**, 220-225.
124. Y. Feng, N. Panwar, et al., Coordination Chemistry Reviews, 2016, **319**, 86-109.
125. T. Zheng, N. Pierre-Pierre, et al., ACS Applied Materials & Interfaces, 2015, **7**, 6819-6827.
126. P. Pericleous, M. Gazouli, et al., Int J Cancer, 2012, **131**, 519-528.
127. F. Carniato, L. Tei, et al., European Journal of Inorganic Chemistry, 2018, **2018**, 4936-4954.

128. J. Estelrich, M. J. Sánchez-Martín, et al., Int J Nanomedicine, 2015, **10**, 1727-1741.
129. R. Damadian, Science, 1971, **171**, 1151-1153.
130. P. C. Lauterbur, Clin Orthop Relat Res, 1989, 3-6.
131. P. Mansfield and P. K. Grannell, Journal of Physics C, Solid State Physics, 1973, **6**, L422-L426.
132. S. Mastrogiacomo, W. Dou, et al., Molecular Imaging and Biology, 2019, **21**, 1003-1019.
133. L. Zhang, R. Liu, et al., Nanoscale, 2016, **8**, 10491-10510.
134. A. Narmani, B. Farhood, et al., Journal of Drug Delivery Science and Technology, 2018, **44**, 457-466.
135. M. Colilla, B. González, et al., Biomaterials Science, 2013, **1**, 114-134.
136. S. Saroj and S. J. Rajput, Journal of Drug Delivery Science and Technology, 2018, **44**, 349-365.
137. M. Rogosnitzky and S. Branch, Biometals, 2016, **29**, 365-376.
138. F. Lux, L. Sancey, et al., Nanomedicine, 2015, **10**, 1801-1815.
139. E. M. Gale, P. Caravan, et al., Pediatric Radiology, 2017, **47**, 507-521.
140. I. Solomon, Physical Review, 1955, **99**, 559.
141. N. Bloembergen and L. Morgan, The Journal of Chemical Physics, 1961, **34**, 842-850.
142. E. Toth, L. Helm, et al., The chemistry of contrast agents in medical magnetic resonance imaging, 2013, 25-81.
143. Y. Cao, L. Xu, et al., Journal of Materials Chemistry B, 2017, **5**, 3431-3461.
144. W. J. Rieter, J. S. Kim, et al., Angewandte Chemie International Edition, 2007, **46**, 3680-3682.
145. N. Wartenberg, P. Fries, et al., Chemistry – A European Journal, 2013, **19**, 6980-6983.
146. B. Godin, E. Tasciotti, et al., Accounts of Chemical Research, 2011, **44**, 979-989.
147. K. M. L. Taylor, The University of North Carolina at Chapel Hill, 2009.
148. A. K. Duncan, P. J. Klemm, et al., J Am Chem Soc, 2012, **134**, 8046-8049.
149. J. J. Davis, W. Y. Huang, et al., J Mater Chem, 2012, **22**, 22848-22850.

150. F. Carniato, L. Tei, et al., Chemistry, 2010, **16**, 10727-10734.
151. W.-Y. Huang, G.-L. Davies, et al., Chemical Communications, 2013, **49**, 60-62.
152. P. Huang, D. Lian, et al., Chinese Chemical Letters, 2021, **32**, 3696-3704.
153. J. Wen, K. Yang, et al., Chemical Society Reviews, 2017, **46**, 6024-6045.
154. X. Lu, X. Guo, et al., Sheng wu Gong Cheng xue bao= Chinese Journal of Biotechnology, 2020, **36**, 1723-1731.
155. G. Helmlinger, F. Yuan, et al., Nature medicine, 1997, **3**, 177-182.
156. S. Mura, J. Nicolas, et al., Nature Materials, 2013, **12**, 991-1003.
157. J. Jiang, N. Shen, et al., Advanced Materials, 2019, **31**, 1904278.
158. C. R. Thomas, D. P. Ferris, et al., Journal of the American Chemical Society, 2010, **132**, 10623-10625.
159. Z. Zhang, L. Wang, et al., Advanced materials, 2012, **24**, 1418-1423.
160. S. Porrang, S. Davaran, et al., International Journal of Nanomedicine, 2022, **17**, 1803-1827.
161. W. Feng, W. Nie, et al., ACS Applied Materials & Interfaces, 2014, **6**, 8447-8460.
162. N. Avedian, F. Zaaeri, et al., Journal of Drug Delivery Science and Technology, 2018, **44**, 323-332.
163. J. Liu, H. Liang, et al., Biomaterials, 2018, **157**, 107-124.
164. J. Tao, W. Fei, et al., Molecular Pharmaceutics, 2019, **16**, 786-797.
165. J. Pellico, C. M. Ellis, et al., Chemical Communications, 2019, **55**, 8540-8543.
166. B. Chen, W. Dai, et al., Theranostics, 2017, **7**, 538-558.
167. Y. Song, Y. Li, et al., Int J Nanomedicine, 2017, **12**, 87-110.
168. M. I. Gibson and R. K. O'Reilly, Chemical Society Reviews, 2013, **42**, 7204-7213.
169. T. Kang, F. Li, et al., Biomaterials, 2017, **136**, 98-114.
170. A. K. Teotia, H. Sami, et al., in Switchable and Responsive Surfaces and Materials for Biomedical Applications, ed. Z. Zhang, Woodhead Publishing, Oxford, 2015, DOI: https://doi.org/10.1016/B978-0-85709-713-2.00001-8, pp. 3-43.

171. D. Roy, W. L. A. Brooks, et al., Chemical Society Reviews, 2013, **42**, 7214-7243.

172. S. A. Shah, M. H. Asdi, et al., Materials Chemistry and Physics, 2012, **137**, 365-371.

173. Z. Tian, X. Yu, et al., Microporous and Mesoporous Materials, 2018, **256**, 1-9.

174. Z. Zhang, H. Li, et al., Angewandte Chemie International Edition, 2019, **58**, 7866-7872.

175. W. Hu, X. Bai, et al., Journal of Materials Chemistry B, 2019, **7**, 5789-5796.

176. M. E. Peralta, S. A. Jadhav, et al., Journal of Colloid and Interface Science, 2019, **544**, 198-205.

177. S. Schmidt, Niedersächsische Staats-und Universitätsbibliothek Göttingen, 2018.

178. S. Edmondson, V. L. Osborne, et al., Chemical society reviews, 2004, **33**, 14-22.

179. G. Conzatti, S. Cavalie, et al., Colloids and Surfaces B: Biointerfaces, 2017, **151**, 143-155.

180. M. Ma, S. Zheng, et al., Journal of Materials Chemistry B, 2014, **2**, 5828-5836.

181. Y.-Z. You, K. K. Kalebaila, et al., Chemistry of Materials, 2008, **20**, 3354-3359.

182. P. W. Chung, R. Kumar, et al., Advanced Functional Materials, 2008, **18**, 1390-1398.

183. M. Hei, J. Wang, et al., Journal of Materials Chemistry B, 2017, **5**, 9497-9501.

184. D. Taton, M. Destarac, et al., Handbook of RAFT polymerization, 2008, 373-421.

185. S. Perrier, Macromolecules, 2017, **50**, 7433-7447.

186. M. Klein Gunnewiek, A. Di Luca, et al., Israel Journal of Chemistry, 2012, **52**, 339-346.

187. N. Ayres, C. D. Cyrus, et al., Langmuir, 2007, **23**, 3744-3749.

188. J. Ran, L. Wu, et al., Progress in Polymer Science, 2014, **39**, 124-144.

189. Y. Tao, J. Wang, et al., Frontiers in Bioengineering and Biotechnology, 2020, **8**.

190. K. H. Bae, H. J. Chung, et al., Molecules and cells, 2011, **31**, 295-302.

191. A. X. Zhu, D. G. Duda, et al., Nature reviews Clinical oncology, 2011, **8**, 292-301.

192. H. Maeda, H. Nakamura, et al., Advanced drug delivery reviews, 2013, **65**, 71-79.

193. H. Maeda, J. Wu, et al., Journal of controlled release, 2000, **65**, 271-284.

194. S.-Y. Lee, M. Ferrari, et al., Nanotechnology, 2009, **20**, 495101.

195. L. Li, T. Liu, et al., Journal of Nanoscience and Nanotechnology, 2016, **16**, 6766-6772.

196. M. A. Miller, R. Chandra, et al., Science translational medicine, 2017, **9**, eaal0225.

197. A. A. Natfji, D. Ravishankar, et al., Journal of pharmaceutical sciences, 2017, **106**, 3179-3187.

198. L. Zhang, T. Wang, et al., Chemistry–A European Journal, 2012, **18**, 12512-12521.

199. C. Chen, W. Yao, et al., International journal of biological macromolecules, 2019, **122**, 1090-1099.

200. Q.-Y. Chen, G.-P. Tao, et al., Spectrochimica Acta Part A: Molecular and Biomolecular Spectroscopy, 2012, **96**, 284-288.

201. W. Hao, Y. Shen, et al., RSC advances, 2017, **7**, 851-860.

202. D. Lee, S. Beack, et al., Advanced Functional Materials, 2018, **28**, 1800941.

203. M. Ao, X. Xiao, et al., Brazilian Journal of Medical and Biological Research, 2018, **51**.

204. M. Xie, Y. Xu, et al., International Journal of Pharmaceutics, 2014, **474**, 223-231.

205. X. Sheng, T. Huang, et al., Oncol Lett, 2017, **14**, 6163-6169.

206. W. Fei, Y. Zhang, et al., International Journal of Pharmaceutics, 2017, **519**, 250-262.

207. Q. Wang, Y. Sun, et al., Biomaterials, 2015, **56**, 229-240.

208. S. Pranatharthiharan, M. D. Patel, et al., Drug Delivery, 2017, **24**, 20-29.

209. Z. Ding, D. Wang, et al., International Journal of Nanomedicine, 2020, **15**, 8383-8400.

210. J. Lu, J. Wang, et al., Small, 2018, **14**, 1702037.

211. S. P. Boulos, T. A. Davis, et al., Langmuir, 2013, **29**, 14984-14996.

212. F. Alexis, E. M. Pridgen, et al., Drug delivery, 2010, 55-86.

213. P. Camner, M. Lundborg, et al., Journal of Applied Physiology, 2002, **92**, 2608-2616.

214. K.-i. Ogawara, K. Furumoto, et al., Journal of controlled release, 2004, **100**, 451-455.

215. Q. He, J. Zhang, et al., Biomaterials, 2010, **31**, 1085-1092.

216. D. Dutta, S. K. Sundaram, et al., Toxicological Sciences, 2007, **100**, 303-315.

217. S. Nagayama, K.-i. Ogawara, et al., International journal of pharmaceutics, 2007, **342**, 215-221.

218. D. O. Adams and T. A. Hamilton, Annual review of immunology, 1984, **2**, 283-318.

219. S. A. MacParland, K. M. Tsoi, et al., ACS nano, 2017, **11**, 2428-2443.

220. S. Ye, G. Marston, et al., Advanced Functional Materials, 2015, **25**, 2117-2127.

221. C. D. Walkey, J. B. Olsen, et al., Journal of the American Chemical Society, 2012, **134**, 2139-2147.

222. M. Longmire, P. L. Choyke, et al., 2008.

223. T. Achilleas, S. Spyros, et al., Adv Drug Deliv Rev, 2016, **97**, 4-27.

224. D. E. Ingber, J. A. Madri, et al., Proceedings of the National Academy of Sciences, 1981, **78**, 3901-3905.

225. K. Kessenbrock, V. Plaks, et al., Cell, 2010, **141**, 52-67.

226. Q. Xiao and G. Ge, Cancer microenvironment, 2012, **5**, 261-273.

227. Z. Popović, W. Liu, et al., Angewandte Chemie, 2010, **122**, 8831-8834.

228. T. Lammers, F. Kiessling, et al., Nano-Enabled Medical Applications, 2020, 159-203.

229. M. R. Kano, Y. Bae, et al., Proceedings of the National Academy of Sciences, 2007, **104**, 3460-3465.

230. L. M. Bareford and P. W. Swaan, Advanced drug delivery reviews, 2007, **59**, 748-758.
231. C. Peetla, S. Vijayaraghavalu, et al., Advanced drug delivery reviews, 2013, **65**, 1686-1698.
232. C. Peetla, R. Bhave, et al., Molecular pharmaceutics, 2010, **7**, 2334-2348.
233. J. B. Rothbard, T. C. Jessop, et al., Advanced drug delivery reviews, 2005, **57**, 495-504.
234. H.-H. Jeong, E. Choi, et al., Journal of Materials Chemistry B, 2019, **7**, 3480-3496.
235. N. Hoshyar, S. Gray, et al., Nanomedicine (Lond), 2016, **11**, 673-692.
236. E. A. Sykes, J. Chen, et al., ACS Nano, 2014, **8**, 5696-5706.
237. B. Kim, G. Han, et al., Nat Nanotechnol, 2010, **5**, 465-472.
238. J. S. Souris, C.-H. Lee, et al., Biomaterials, 2010, **31**, 5564-5574.
239. R. Toy, P. M. Peiris, et al., Nanomedicine, 2014, **9**, 121-134.
240. E. Gavze and M. Shapiro, International Journal of Multiphase Flow, 1997, **23**, 155-182.
241. V. P. Chauhan, Z. Popović, et al., Angewandte Chemie International Edition, 2011, **50**, 11417-11420.
242. A. Vonarbourg, C. Passirani, et al., Biomaterials, 2006, **27**, 4356-4373.
243. D. F. Moyano, K. Saha, et al., ACS nano, 2014, **8**, 6748-6755.
244. F. Zhao, Y. Zhao, et al., small, 2011, **7**, 1322-1337.

Chapter 2.

Optimisation of hydrophilic and hydrophobic drug loading into mesoporous silica nanoparticles

2.1 Introduction

Mesoporous silica nanoparticles (MSNs) hold great promise as controlled drug delivery systems. Their distinct properties allow for customisation of interior and exterior surface characteristics, enabling selective loading of hydrophobic or hydrophilic drugs of interest.[1-3] Moreover, these materials offer a plethora of advantages, including durability in various solvents for hydrophobic drug loading, biocompatibility, high drug loading capacity, biodegradability, zero premature release, and ease of functionalisation. These features position MSNs as highly promising candidates for drug delivery.[4, 5]

Numerous pivotal factors significantly impact drug loading into mesoporous MSNs, as evidenced in literature.[6-12] One such factor is the chemistry of the internal pores, which has been reported to exert a substantial effect on drug loading.[6] For instance, Gou *et al.* demonstrated the development of carboxyl-functionalised MSNs for the controlled release of nonsteroidal anti-inflammatory drugs (NSAIDs) such as nimesulide and indomethacin. Carboxyl functionalisation enhanced the dissolution profile of these drugs by modifying the pore chemistry and structure of MSNs.[6] Furthermore, the influence of surface area on drug loading was also evaluated using two mesoporous structures with identical symmetry but differing surface areas: MCM-41 (surface area = 1157 m^2/g) and SBA-15 (surface area = 719 m^2/g). Experimental results revealed that MCM-41 exhibited higher alendronate drug loading compared to SBA-15 due to the larger contact surface area with alendronate.[7]

In another study, the effect of pore size on drug adsorption and release was investigated. MCM-41 with varying pore diameters was obtained using diverse structural directing agents with different alkyl chain lengths, ranging from 12 to 16 carbons.[8] These MCM-41 matrices were thoroughly evaluated as ibuprofen delivery systems, unveiling that pore diameter strongly influences the release rate of molecules into the delivery medium. Specifically, MCM-41 with a larger pore size exhibited a higher release of ibuprofen molecules compared to materials with smaller pore sizes.[9] Additionally, the choice of solvent in the drug loading process plays a pivotal role, as reported in prior studies. The choice of loading solvent depends on the drug's solubility, where polar drugs like amoxicillin[10] or gentamicin[11] necessitate a polar solvent such as water, while non-polar drugs like ibuprofen require a non-polar solvent like hexane to achieve optimum drug loading.[8]

Over the last decade, a plethora of techniques for loading drugs into MSNs have been developed. These methods encompass melt processes, solvent adsorption method, and evaporation method.[13] The impact of the loading technique on drug loading has been investigated. For instance, the loading efficiency of carvedilol (CAR) into MSNs was found to be considerably low at 7.9% using the solvent adsorption method. However, the solvent evaporation method, which differs from solvent adsorption, which involves a continuous drug loading process alongside solvent evaporation. This approach led to higher loading efficiency for MSNs when compared to adsorption.[12]

Therefore, the objective of this chapter is to explore various aspects such as the choice of solvent, surface modification of MSNs, and adjustments in pore size/volume. The goal is to enhance the drug loading efficiency of both hydrophilic drug doxorubicin HCl and hydrophobic drug sorafenib tosylate within MSNs.

2.2 Aims

In this chapter, the primary goal is to enhance the drug loading capacity of mesoporous silica nanocarriers for both the hydrophilic drug doxorubicin and the hydrophobic drug sorafenib tosylate. This enhancement is crucial for developing more efficient drug delivery systems with improved therapeutic efficacy. To achieve this objective, mesoporous silica nanoparticles (MSNs) were synthesised using the modified Stöber method. The internal pore chemistry was tailored by incorporating and functionalising with a hydrophobic group using phenyltrimethoxy silane (PhTMS) to investigate the effect of pore chemistry on drug loading. Additionally, various pore sizes of MSNs were synthesised by adjusting the ratio of the swelling agent to the micelle template. The porosity of the resulting MSNs was characterised using transmission electron microscopy (TEM) before exploring the impact of pore size on drug loading.

Furthermore, the effect of solvent polarity and the loading method (evaporation or adsorption) on the loading process was examined, especially concerning the challenge of loading the hydrophobic drug sorafenib tosylate into MSNs. Another critical aspect investigated was the effect of the initial drug concentration for both doxorubicin and sorafenib. A range of techniques, including dynamic light scattering (DLS), TEM, Fourier-transform infrared spectroscopy (FTIR), X-ray diffraction (XRD), high-performance liquid chromatography (HPLC), and ultraviolet/visible spectroscopy (UV/Vis), were employed for thorough investigation and analysis. By comprehensively studying these factors, the aim is to optimise the nanocarriers' ability to encapsulate drugs with varying solubilities, ultimately enhancing their drug delivery efficiency and therapeutic impact.

2.3 Experimental

2.3.1 Materials

All chemicals were used as received without further modification. Cetyl trimethylammonium bromide (CTAB), tetraethyl orthosilicate (TEOS), triethanolamine, trimethoxyphenylsilane (PhTMS), 1,3,5- trimethylbenzene (TMB), hydrochloric acid (HCl, 37%), and trifluoroacetic acid (TFA) were purchased from Sigma-Aldrich or Fisher Scientific, UK. Doxorubicin hydrochloride (Dox) as well as sorafenib tosylate (Sor) were obtained from LEAPChem, *China.*

HPLC grade solvents of dimethylformamide (DMF), dichloromethane (DCM), methanol (MeOH), ethanol (EtOH), tetrahydrofuran (THF), chloroform, toluene, acetone, acetonitrile, hexane, and dimethyl sulfoxide (DMSO) were used as received and sourced from Fisher Scientific or Sigma-Aldrich, UK. An Elga PureLab system operated at 16.0 MΩ or a Merck Milli-Q Direct water purification system operated at 18.2 MΩ provided the ultrapure water.

2.3.2 Methodology

2.3.2.1 Preparation of hydrophilic mesoporous silica nanoparticles (HMSNs)

MSNs were prepared using hydrolysis and condensation reactions where a surfactant is used as a template.[14, 15] Briefly, cetyltrimethylammonium bromide (CTAB, 0.64 g, 1.75 mmol) was dissolved in a mixture of ethanol (1.84 mL, 0.03 mol) and ultrapure water (16.02 mL, 0.89 mmol) before heating to 80 °C. Triethanolamine (1.03 g, 6.90 mmol) was added whilst stirring followed by dropwise addition of tetraethoxysilane (TEOS, 1.454 mL, 6.5 mmol). The reaction mixture was stirred for two hours at 80 °C. After preparing the nanoparticles, CTAB was removed by washing three times using acidified ethanol 13.1 M (hydrochloric acid: ethanol, 3 mL : 20 mL) using centrifugation and sonication treatment (Figure 2. 1a). Particles were neutralised by washing with ethanol using centrifugation (15300 rpm for 30 minutes, each sample was washed at least 7 times). Finally, the obtained particles were dispersed in ethanol for storage at room temperature for further characterisation.

2.3.2.2 Preparation of hydrophobic mesoporous silica nanoparticles (HPMSNs)

The same procedure was followed as described before for the hydrophilic nanoparticles. However, in the case of hydrophobic mesoporous silica nanoparticles (HPMSNs), 4.5 µl of a mixture of 1:1 molar ratio of TEOS: PhTMS (33 µl: 35 µl) was added after 10, 30 and 60 minutes (a total volume added of 13.5 µl) in addition to an initial TEOS concentration (1.441 mL, 6.497 mmol) as displayed in Figure 2. 1b. The delayed and multiple additions ensured that the hydrophobic groups were distributed across the internal pore surfaces of the MSNs achieving a final concentration of 0.45 mol% of the total added silica precursors. The reaction mixture was stirred at 80 °C for a total of two hours. The same washing using acidified ethanol to remove CTAB and ethanol for neutralisation was followed before storing the samples in ethanol at room temperature.

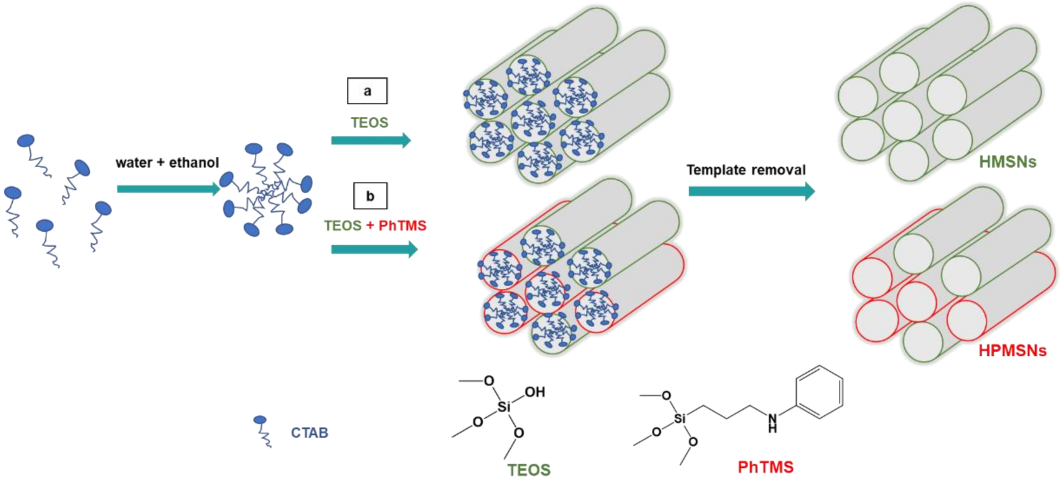

Figure 2. 1: Schematic representation of MSNs synthesis by sol-gel chemistry, (a) synthesis of HMSNs, (b) synthesis of HPMSNs.

2.3.2.3 Preparation of mesoporous silica nanoparticles of different pore sizes

In order to prepare varying pore sizes of both hydrophilic MSNs and hydrophobic MSNs, 1,3,5-trimethylbenzene (TMB) was added simultaneously with CTAB in a molar ratio of 2:1 (0.42 g, 3.5 mmol : 0.64g, 1.75 mmol, TMB : CTAB) or 3:1 (0.63 g, 5.25 mmol: 0.64 g, 1.75 mmol, TMB: CTAB) to prepare swollen HMSNs (HMSNs S2:1 and HMSNs S3:1, Figure 2. 2a) and swollen HPMSNs (HPMSNs S2:1 and HPMSNs S3:1, Figure 2. 2b). All other steps of the methodology are as described in Sections 2.3.2.1 and 2.3.2.2 for hydrophilic and hydrophobic silica particles, respectively. In this way, MSNs with two additional pore sizes were produced.

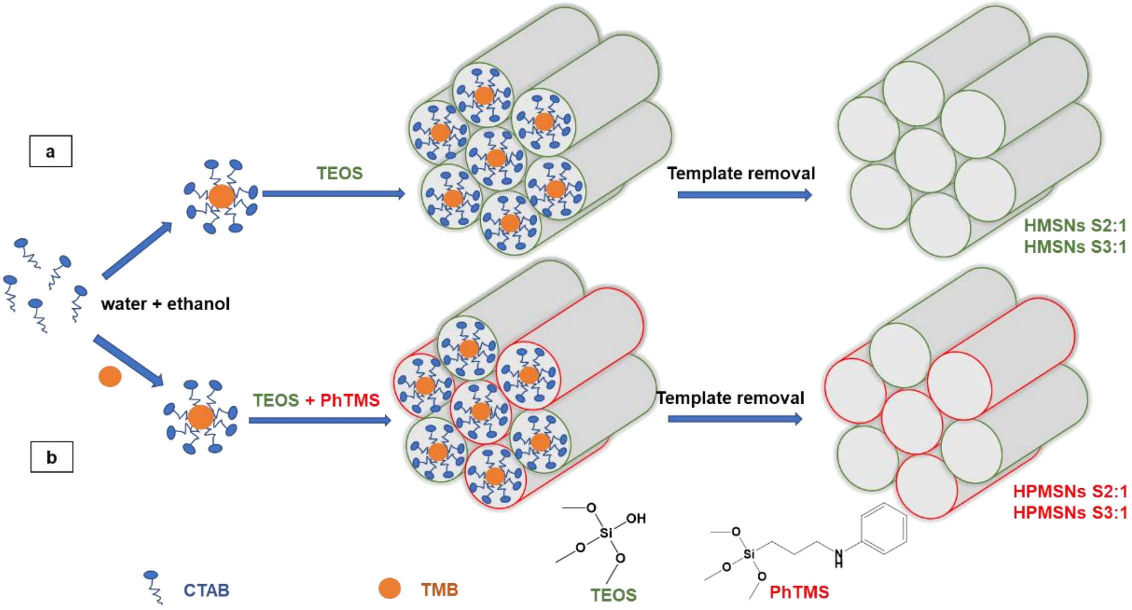

Figure 2. 2: Schematic representation of large pore size MSNs synthesis by sol-gel chemistry using the swelling agent (TMB), (a) preparation of HMSNs S2:1 and HMSNs S3:1, (b) preparation of HPMSNs S2:1 and HPMSNs S3:1.

2.3.2.4 Drug loading into mesoporous silica nanoparticles

2.3.2.4.1 Hydrophilic drug (doxorubicin HCl)

The adsorption method (Figure 2. 3a) was followed to load doxorobucin HCl (Dox) into both hydrophilic and hydrophobic MSNs with different pore chemistry and sizes as prepared in Sections 2.3.2.1, 2.3.2.2 and 2.3.2.3. To achieve the loading of MSNs, MSNs were dispersed into a concentrated aqueous solution of Dox (5 mg/ml) at a ratio of 1:1 or 2:1 Dox:MSNs (w/w), respectively. The dispersions were left to stir overnight at room temperature, and the unloaded free drug was subsequently separated via centrifugation for 10 minutes at 15300 rpm, followed by the removal of the supernatant. The loaded MSNs@Dox were then washed twice with 50% aqueous ethanolic solution before being dispersed in 50% aqueous ethanolic solution for storage.

2.3.2.4.2 Hydrophobic drug (sorafenib tosylate)

The same adsoption method was followed for the loading of sorafenib tosylate (Sor) as in Figure 2. 3a, however different factors were investigated to maximise the drug loading capacity as well as the entrapment efficiency.

First, MSNs were mixed with concentrated sorafenib solutions in solvents with different polarities (hexane, toluene, chloroform, DMSO, DMF, DCM, THF, ethanol, and acetone) with a mass ratio of 1:1 w/w. The resulting dispersions were stirred overnight at room temperature, followed by centrifugation for 10 minutes at 15300 rpm to separate the unloaded free drug in the supernatant. The loaded MSNs@Sor were then washed twice with 100% ethanol before being dispersed in a 100% ethanolic solution for storage.

To evaluate the effect of loading method on drug loading, the evaporation method was compared to the adsorption method. The evaporation method involved using 1:1 (w/w) HMSNs@Sor in THF, where the dispersion was heated at 60 ^{o}C to evaporate the solvent until about 1 ml of the solvent remained before separating the free unloaded drug by centrifugation for 10 minutes at 15300 rpm (Figure 2. 3b).

To assess the influence of the initial drug concentration on the loading capacity, various ratios of Sor: MSNs in THF were examined through the use of the adsorption method (1:4, 1:2, and 1:1 Sor: MSNs (w/w), respectively).

Finally, the chosen optimised factors of solvent, initial drug concentration, and loading method were employed to analyse the impact of pore sizes and chemistry on both loading capacity and entrapment efficiency.

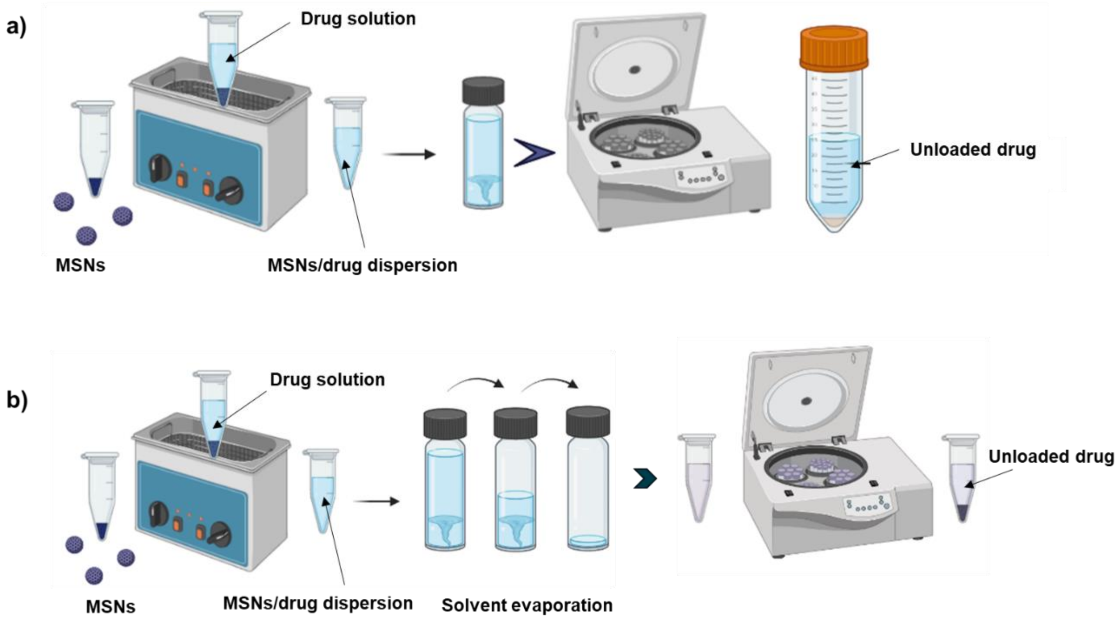

Figure 2. 3: Schematic representation of drug loading methods of adsorption (a), and evaporation (b). This figure was produced using Biorender.

2.3.2.5 Evaluation of drug loading capacity and entrapment efficiency

To assess the drug loading and entrapment efficacy in compliance with Equation 2. 1 and Equation 2. 2, both free doxorubicin HCl and sorafenib tosylate were measured using UV-vis spectrophotometer or high-performance liquid chromatography (HPLC), respectively, from previously analysed calibration curves (Figure S2. 1 and Figure S2. 2).

In the case of doxorubicin HCl, the supernatant drug concentration was measured using a Cary 60 UV-Vis spectrophotometer at 480 nm.

For sorafenib tosylate, HPLC with UV detection at 264 nm was utilised, using the Agilent 1260 Infinity HPLC system. Based on a previously reported method,[16] the chromatographic conditions were modified. Separation was performed on an ACE 5 C18-AR column (4.6 x 150 mm, 5 µm particle size)

(Avantor, Radnor Township), employing an isocratic mobile phase with a flow rate of 1.0 mL/min comprising a methanol and 0.1% TFA aqueous solution mixture (70:30, v/v). The HPLC system was conducted at room temperature (25 ± 1 °C), and the sample solution had an injection volume of 10 μL. All samples were filtered using a 0.45 μm PTFE membrane filter from Millipore, and measurements were in triplicate.

$$Drug\ loading\ capacity\ (\%) = \frac{weight\ of\ encapsulated\ drug}{weight\ of\ MSNs} \times 100$$

Equation 2. 1

$$Encapsulation\ efficiency\ (\%) = \frac{weight\ of\ encapsulated\ drug}{weight\ of\ total\ added\ drug} \times 100$$

Equation 2. 2

2.3.2.6 Physicochemical characterisation

Hydrodynamic size, size distribution and zeta potential of MSNs were determined by dynamic light scattering technique (DLS) and zeta potential analysis, respectively, using a Malvern Zetasizer Nano ZS equipped with He-Ne laser (λ= 632.8nm) at 173 ^{o}C scattering angle and temperature of 25 ^{o}C for MSNs. The data was analysed using Zetasizer software (version 7.12).

Fourier-transform infrared spectroscopy (FTIR) spectra were collected on a Shimadzu IRTracer-100 spectrometer operated by LabSolutions IR (version 2.10). At least 32 scans of the samples were evaluated over the spectra region of 400 cm^{-1} to 4000 cm^{-1}.

Transmission electron microscopy (TEM) was performed using a JEOL 2100 TEM operating at 200kV. The samples were diluted to 1 mg/mL in water before drop-casting onto formvar coated 300 mesh copper TEM grids (EM Resolutions). The diameter of the nanoparticles was determined as a mean of at least 100 different particles using ImageJ (Version 1.52). X-ray diffraction (XRD) analysis was performed using a Rigaku Miniflex 600 diffractometer with

Cu Kα radiation (λ = 1.5418 Å). Patterns were collected over the 2θ range of at least 2–50°, at 40 kV and 15 mA.

2.3.2.7 Statistical analysis

The data were expressed as mean values with their respective standard deviations. Statistical analysis was conducted employing Prism 7.0 software (GraphPad Software). An unpaired t-test was employed to compare two groups, while *two-way ANOVA* followed by *Sidak's* or Tukey's multiple comparison test was used to compare more than two groups and their interaction. Statistical significance was defined as p-values below 0.05.

2.4 Results and discussion

To optimise drug-loaded nanoparticles, mesoporous silica nanoparticles (MSNs) were tailored by varying their hydrophobicity and pore size. Hydrophilic MSNs were synthesised through a standard hydrolysis and condensation reaction using a surfactant to generate the porous network.

Conversely, hydrophobic MSNs were crafted by grafting phenyltrimethoxysilane (PhTMS) into the internal surface of the pore channel, employing a delayed hydrolysis and co-condensation reaction as shown in Figure 2. 1. Additionally, pore size adjustments were made in both hydrophilic and hydrophobic MSNs by introducing a swelling agent (TMB). The swelling agent facilitated the expansion of CTAB micelles, resulting in a larger pore size after template removal, as depicted in Figure 2. 2.

2.4.1 Characterisation of prepared mesoporous silica nanoparticles

To validate the synthesis and porosity of both hydrophilic and hydrophobic MSNs, transmission electron microscopy (TEM) was employed. The TEM images exhibited a consistent, porous, and spherical morphology for all the synthesised MSNs particles, showcasing average diameters of 44.4 ± 3.8, 38.3 ± 5.8, and 45.5 ± 5.8 nm in case of hydrophilic MSNs HMSNs,

HMSNs S2:1 and HMSNs S3:1 as displayed in Figure 2. 4 a, b and c, respectively. In addition, the size of hydrophobic MSNs, non-swollen HPMSNs, HPMSNs S2:1 and HPMSNs S3:1 were 42.4 ± 5.3, 44.4 ± 5.1, and 43.7 ± 6.7 nm (Figure 2. 4 d, e and f), respectively. The observed sizes were in close proximity, demonstrating an anticipated level of uniformity.

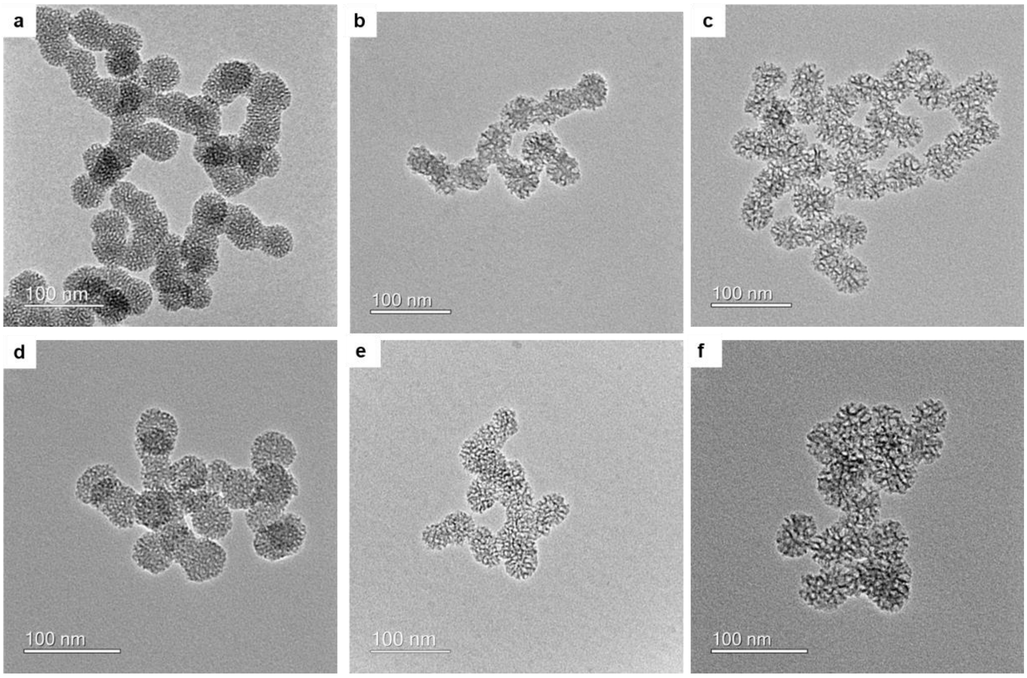

Figure 2. 4: TEM images of hydrophilic MSNs (top row); HMSNs, HMSNs S2:1, and HMSNs S3:1 as well as hydrophobic MSNs (bottom row); HPMSNs, HPMSNs S2:1, and HPMSNs S3:1 represented as a, b, c, d, e and f, respectively.

The measured surface zeta potential showed a negative value for all prepared MSNs which was attributed to the silanol groups on the external surface indicating colloidal stability.[17] The average hydrodynamic diameter of swollen MSNs was larger than non-swollen nanoparticles where non-swollen HMSNs and HPMSNs were 157.3 ± 1.7 and 181.4 ± 1.4, respectively. Upon employing TMB as a swelling agent during the synthesis, the diameter of HMSNs S2:1 and S3:1 increased to 268.9 ± 3.2 nm and 252.7 ± 3.3, respectively. Additionally, for HPMSNs S2:1 and S3:1, the diameters expanded to 266.9 ± 0.4 and 201.9 ± 2.7, respectively, as shown in Table 2. 1. These values match the literature where larger particles tend to be formed upon inserting a swelling agent.[18] The polydispersity index (PdI) represents the uniformity of particle size distribution within a sample. Low values of 0.3 or less indicate the homogeneity and colloidal stability of all prepared MSNs as shown in Table 2. 1.[19]

Table 2. 1: DLS measurements in water at 25 °C as well as size as determined by TEM.

Formula	**Particle size (D_H)[a]* (nm)**	**Polydispersity index (PdI)[b]***	**ζ-potential (mV)***	**TEM size (nm)[c]**
HMSNs	157.3 ± 1.7	0.2 ± 0.01	-25.0 ± 0.2	44.4 ± 3.8
HMSNs S2:1	268.9 ± 3.2	0.3 ± 0.01	-28.0 ± 0.8	38.3 ± 5.8
HMSNs S3:1	252.7 ± 3.3	0.3 ± 0.03	-26.4 ± 0.4	45.5 ± 5.8
HPMSNs	181.4 ± 1.4	0.2 ± 0.01	-27.0 ± 0.6	42.4 ± 5.3
HPMSNs S2:1	266.9 ± 0.4	0.3 ± 0.03	-38.2 ± 0.9	44.4 ± 5.1
HPMSNs S3:1	201.9 ± 2.7	0.2 ± 0.01	-33.8 ± 0.5	43.7 ± 6.7

[a] Hydrodynamic diameter extracted by cumulant analysis of the data.
[b] Polydispersity index from cumulant fitting.
[c] TEM particle size analysis of at least 100 nanoparticles using Image J.
* All values represent mean ± standard deviation (n=3).

The variation in size measurements of MSNs is dependent on the chosen technique, either TEM or DLS. In TEM, images are taken of nanoparticles after they have been dried onto a surface; DLS, on the other hand, is carried out on samples in suspension. DLS is influenced by any hydrogen bonding and van der Waals interactions between the particles and surrounding solvent molecules which affect the Brownian motion of the particles. Due to these effects, the DLS results measure the hydrodynamic diameter of the particles in liquid and hence show a larger value for the nanoparticles' diameter. In addition, DLS weighs the size distribution by intensity that correlates to the particle radius to power six (r^6) while the TEM weighs the size as number average, as a result the presence of any large particle affects DLS measurements dramatically.[20]

Consequently, the hydrodynamic size determined by DLS usually exceeds the TEM size by a few nanometers. Nonetheless, the difference observed between DLS and TEM data suggests the possibility of aggregation or fusion of MSNs. This concurrence between DLS observations and corresponding findings in TEM images underscores the significance of taking into account the impact of the experimental technique on size measurements and the interpretation of nanoparticle characteristics.

FTIR spectra confirmed the complete removal of CTAB template as the C-H stretching vibration at (2922 and 2855 cm^{-1}) and tertiary amine $RN(CH_3)_3^+$ vibrations at (961 and 1472 cm^{-1}) were absent in all prepared mesoporous silica nanoparticles. The absorption bands of silica appeared in all types of the synthesised MSNs at 1072, 450 and 950 cm^{-1} for Si-O-Si asymmetric stretching vibration, Si-O-Si symmetric stretching vibration and Si-OH stretching vibration, respectively (Figure 2. 5). The presence of phenyl groups in the hydrophobic MSNs was confirmed with absorption peaks at 2000-1660 cm^{-1}, 1450-1300 cm^{-1} and 900-650 cm^{-1}.[21] However, a future investigation using the Brunauer-Emmett-Teller (BET) physisorption technique—widely employed to measure the specific surface area of materials through the physical adsorption of gas molecules onto their surfaces—would offer robust confirmation of both the absence of batch-to-batch variation and the complete removal of cetyltrimethylammonium bromide (CTAB) from within the pores. However, such validation was unattainable due to the lack of resources during the research period.

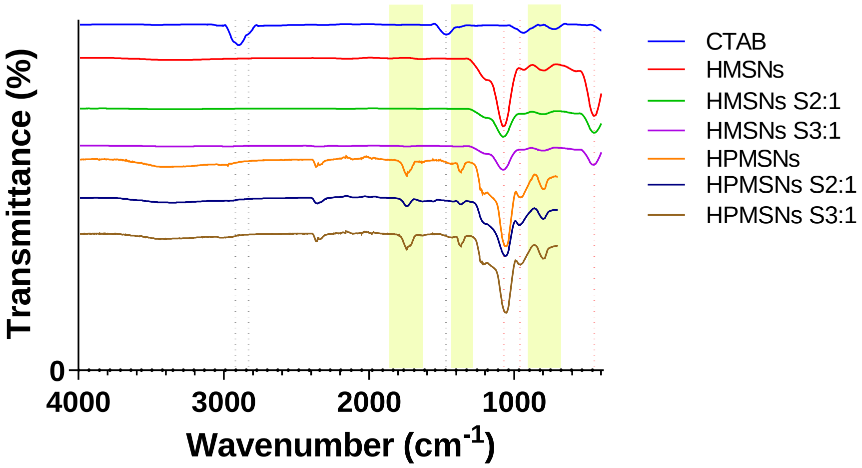

Figure 2. 5:FTIR spectra of cetyltrimethyl ammonium bromide (CTAB), hydrophilic MSNs (HMSNs), swollen hydrophilic MSNs (HMSNs S2:1), swollen hydrophilic MSNs (HMSNs S3:1), hydrophobic MSNs (HPMSNs), swollen hydrophobic MSNs (HPMSNs S2:1), swollen hydrophobic MSNs (HPMSNs S3:1). The dotted lines indicate the stretching vibrations of both CTAB (black lines) and silica (pink lines) while the yellow bands represent aromatic phenyl groups.

2.4.2 Drug loading optimisation

2.4.2.1 Hydrophilic drug (doxorubicin. HCl)

To explore how drug/MSNs mass, hydrophobicity, and pore size impact the loading of a hydrophilic drug (Dox), hydrophilic non-swollen MSNs were used to study the drug/MSNs mass ratios of 1:1 and 2:1 (w/w) initially to establish the optimal initial drug concentration for subsequent experiments throughout the thesis. Furthermore, a range of pore sizes in both hydrophilic and hydrophobic MSNs were investigated to evaluate the effects of chemistry and pore size on drug loading. The drug was loaded into the nanoparticles using the adsorption method across all cases.

2.4.2.1.1 Drug/MSNs mass ratio

Following the adsorption method of incorporating Dox into hydrophilic MSNs, it was found that the higher the initial ratio of drug:MSNs w/w, the higher the loading capacity. For hydrophilic MSNs, the obtained drug loading capacity increased significantly from 104.6 ± 0.9 to 164.1± 0.5 % when double the amount of drug was added (p-value 0.0002), however, the entrapment efficiency decreased slightly from 79. 4 ± 0.3 to 77.9 ± 0.4 % in the case of 1:1 and 2:1 Dox:MSNs (w/w), respectively (Figure 2. 6). This could be explained by reaching the maximum drug encapsulation which could not be improved by increasing the initial drug added.[22] As a result, 2:1 Dox:MSNs (w/w) was selected for further study of the effect of the pore size and chemistry on doxorubicin loading.

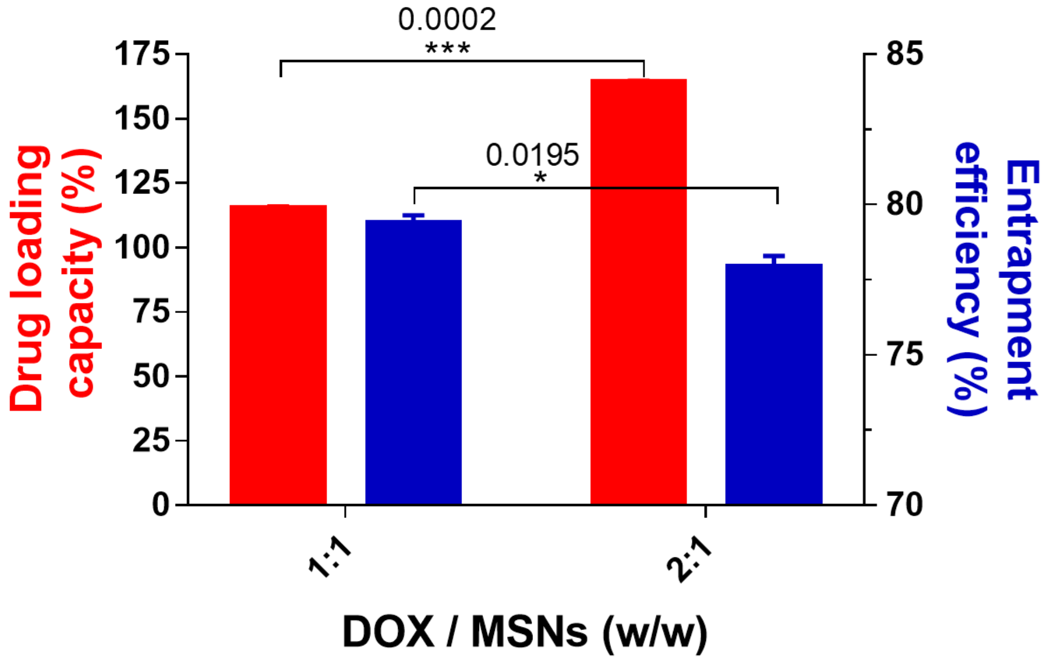

*Figure 2. 6: Effect of doxorubicin/MSNs mass ratio on drug loading capacity (indicated by red bars) and entrapment efficiency (indicated by blue bars). All the values are expressed as mean ± standard deviation; n = 3, *** $p < 0.001$, and * $p < 0.05$ based on unpaired t-test.*

2.4.2.1.2 Silica hydrophobicity and pore size effect

In exploring the influence of hydrophobicity on drug loading capacity and entrapment efficiency, it was evident that hydrophilic MSNs (HMSNs) exhibited higher but not significant drug loading at 42.2% and entrapment efficiency at 22.1%. Conversely, hydrophobic MSNs (HPMSNs) displayed slightly lower drug loading at 33.9% and entrapment efficiency at 19.8% (Figure 2. 7).

Numerous theories have been proposed to elucidate the loading of doxorubicin HCl into silica nanoparticles. Among these, hydrogen bonding is considered the most probable form of interaction between doxorubicin and silica. Consequently, the observed behaviour regarding the impact of silica's hydrophobicity can be attributed to the presence of phenyl groups in HPMSNs. These phenyl groups hinder the formation of hydrogen bonding sites between the silanol groups of MSNs and doxorubicin, introducing steric hindrance when compared to HMSNs.[23]

On the other hand, the effect of pore size on drug loading was significant within MSNs. In hydrophilic MSNs, larger pore sizes reduced drug loading significantly due to a decrease in the comparative number of silanol (Si-OH) groups available for hydrogen bond interactions from 42.2% in the case of HMSNs to 39.9% and 34.6% in the case of HMSNs S2:1 and HMSNs S3:1, with p values of 0.0462 and 0.0481, respectively (Figure 2. 7).[24] Conversely, in hydrophobic MSNs, increasing the pore size initially enhanced doxorubicin loading significantly from 33.9% for HPMSNs to 41.8% for HPMSNs S2:1 (p-value 0.0348) because of reducing steric hindrance and increasing available pore volume for loading. However, beyond a certain threshold, a negative impact on drug loading was observed due to a reduction in the number of silanol groups available for interaction (36.0%; HPMSNs S3:1) as displayed in Figure 2. 7. This duality in pore size effects, depending on hydrophobicity, plays a pivotal role in optimising the drug loading and entrapment efficiency in MSNs. Regarding entrapment efficiency, it followed a similar pattern to drug loading when changing the pore size or hydrophobicity of the nanoparticles. However, the change was more gradual due to the higher amount of drug added than MSNs (Dox:MSNs 2:1 w/w). [24]

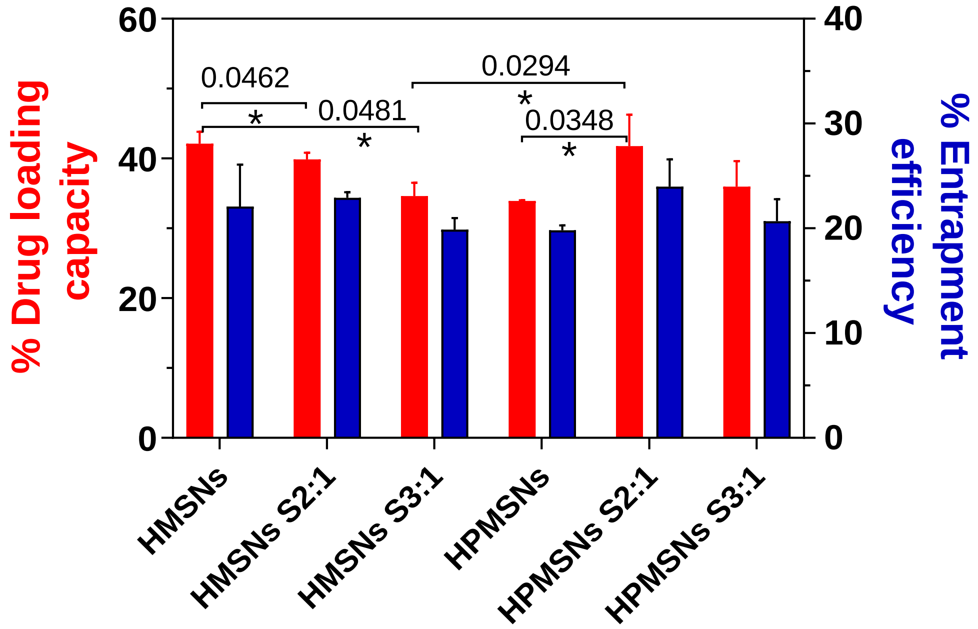

*Figure 2. 7: Effect of silica hydrophilicity and pore size on drug loading capacity (indicated by red bars) and entrapment efficiency (indicated by blue bars). All the values are expressed as mean ± standard deviation; n = 3, * $p < 0.05$ based on two-way ANOVA. Variations from HMSNs data in Figure 2. 6 are due to differences in the reaction scale.*

2.4.2.2 Hydrophobic drug (sorafenib tosylate)

Sorafenib demonstrates marked hydrophobicity and lipophilicity, clearly reflected in its elevated LogP value of 3.8.[25] The partition coefficient (P), evaluates the differential solubility of a compound in water and lipids/organic solvents. In addition, LogP categorises compounds into hydrophilic (negative LogP), lipophilic (positive LogP), or neutral (zero LogP). Sorafenib's LogP value underscores its lipophilic nature, potentially influencing both bioavailability and systemic distribution within the organism.

To tackle the challenges associated with loading the hydrophobic drug sorafenib tosylate into MSNs, we explored various factors aiming to optimise both the drug's loading capacity and entrapment efficiency within the MSNs. Initially, we delved into the impact of solvent polarity, utilising different solvents but maintaining the same adsorption method for loading, to determine the most suitable solvent for subsequent loading processes. Subsequently, we conducted a comparative analysis of the drug loading and entrapment efficiency between the evaporation loading method and the adsorption method. Lastly, we investigated the influences of drug/MSNs mass ratio, silica hydrophobicity, and pore size, leveraging the previously fine-tuned solvent and loading method.

2.4.2.2.1 Solvent polarity

To address the effect of solvent polarity on sorafenib loading into MSNs using adsorption method and the same Sor/MSNs mass ratio of 1:1 w/w, variable solvents of different polarity were used including hexane, toluene, chloroform, DMF, DCM, THF, ethanol, acetone and DMSO as shown in Table 2. 2.[26]

Table 2. 2: Solvents' polarity parameters.[26]

Solvent	**Polarity Index**	**Dipole moment**	**Dielectric Constant (ε)**
Hexane*	0.1	0.08	1.89
Toluene*	2.4	0.31	2.38
Tetrahydrofuran	4.0	1.75	7.58
Chloroform*	4.1	1.15	4.81
Dichloromethane*	3.1	1.14	8.93
Acetone	5.1	2.69	20.7
Ethyl Alcohol	5.2	1.66	24.55
N,N-DimethylFormamide*	6.4	3.86	36.71
Dimethyl Sulfoxide	7.2	4.1	46.68
Water	10.2	1.87	80.1

* Solvents show fair solubility of sorafenib tosylate

It was observed that sorafenib showed negligible solubility in toluene, hexane, chloroform, DCM, and DMF, which are among the least polar solvents, thus restricting their utility in drug loading where a solution of the drug is required.[27]

For THF, acetone, and ethanol, the solubility of sorafenib was limited to about 1 mg/mL. In the case of DMSO, the solubility was slightly higher at approximately 2 mg/mL. This determination was initially made using a literature search, as well as by dissolving a specified amount of the drug into a defined volume of solvent until reaching a state of supersaturation, from which the solubility was deduced visually.[27, 28]

Figure 2. 8 illustrates both drug loading capacity (DLC) and entrapment efficiency of sorafenib tosylate using THF, EtOH, or acetone as the solvent in the adsorption loading method. For THF, DLC% and EE% were comparable across hydrophilic and hydrophobic MSNs with different pore sizes. DLC% ranged from 6.8-4.4% and 5.7-4.0%, while EE% ranged from 8.6-5.6 and 7.2-5.1%, in the case of different pore size of hydrophilic and hydrophobic MSNs respectively. For EtOH, DLC% and EE% were slightly higher in hydrophobic MSNs (2.5-4.0 and 2.4-3.8%, respectively), compared to the hydrophilic ones (1.9-2.5% and 1.0-2.5%, respectively). Conversely, in the case of acetone, DLC% and EE% ranged from 0.8-1.8% and 1.6-3.4%, respectively in hydrophilic MSNs, while the loading was undetectable by HPLC in hydrophobic MSNs. The limited detectability of the loaded drug was also observed with DMSO; consequently, we excluded the data from the figure.

The findings revealed a negative correlation between solvent polarity, indicated by higher dielectric constants denoting greater polarity as illustrated in Table 2.2, and the drug loading capacity (DLC%) and entrapment efficiency (EE%) of the hydrophobic drug sorafenib within mesoporous silica nanoparticles (MSNs). A comparison of dielectric constants for the three solvents showed that THF had the lowest value at 7.58, indicating lower polarity, while ethanol and acetone had values of 24.55 and 20.7, respectively, making them more polar solvents (Table 2. 2).

The variance in solvent polarity elucidates the differences in drug loading, wherein hydrogen bonding of the drug with Si-OH groups play vital roles in the loading process. Consequently, the higher the solvent's polarity, the greater the competition with drug molecules for the active silanol groups, resulting in reduced drug loading and entrapment. This behaviour aligns with observations made in previous studies.[29-32]

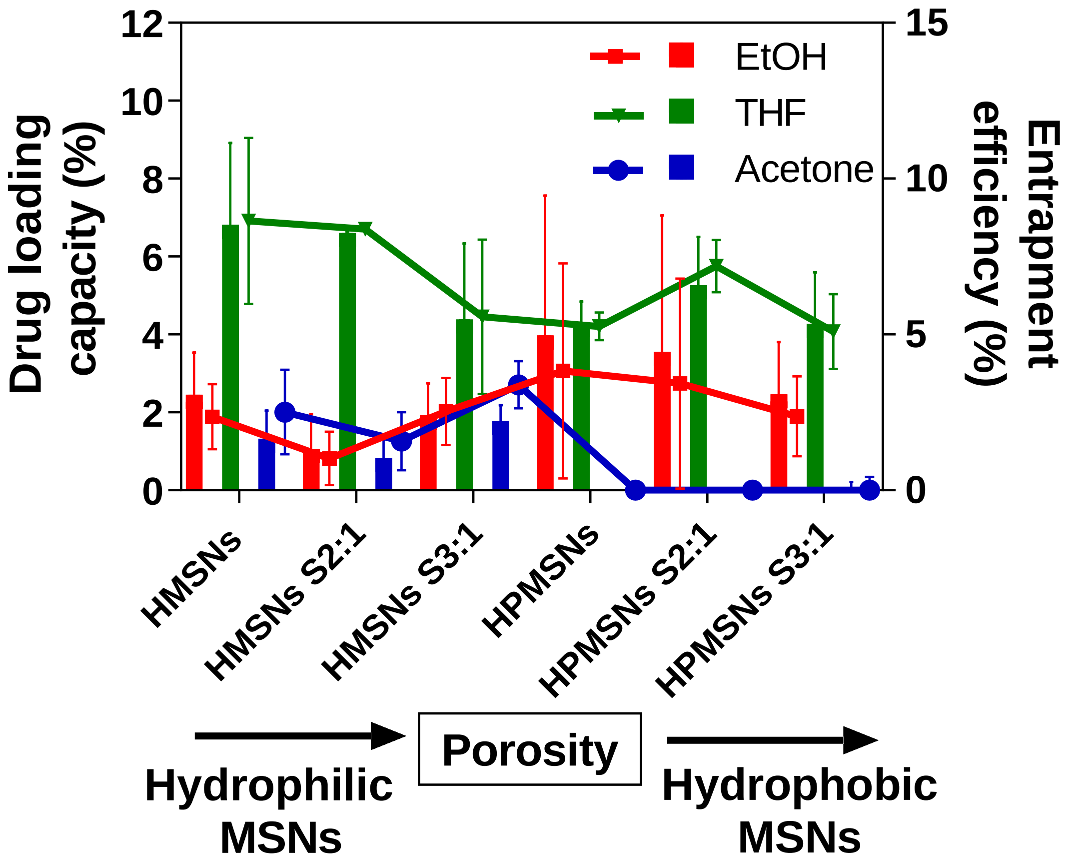

Figure 2. 8: Effect of solvent polarity on drug loading capacity (indicated by bars) and entrapment efficiency (indicated by lines) of sorafenib tosylate into both hydrophilic and hydrophobic MSNs of different pore sizes using EtOH, THF and acetone. All the values are expressed as mean ± standard deviation; n = 3.

One of the significant challenges encountered in loading a hydrophobic drug into MSNs is determining the appropriate localisation within the particles. Loading within the nanopores can enhance drug solubility and bioavailability by restricting drug crystallinity, whereas loading on the external surface might limit both solubility and the total amount of drug that can be loaded. When the pore capacity of mesoporous silica particles is surpassed, it raises concerns regarding potential drug recrystallisation on the surface of MSNs.[33-35] This phenomenon occurs when the quantity of loaded drug exceeds the maximum loading capacity of the pores, posing a risk of drug crystallisation that could affect formulation stability and performance.

The X-ray diffraction analysis of various types of mesoporous silica nanoparticles (MSNs) in Figure 2. 9 confirms the formation of amorphous

MSNs in the absence of drugs. The diffraction pattern exhibits a broad peak at 25°, which corresponds to the characteristic peaks of silica as indicated before.[36] On the other hand, the X-ray diffraction pattern of the free sorafenib tosylate drug reveals sharp diffractions at 4.4° and 13.11°, along with several other reflections.[37] However, when sorafenib is loaded into MSNs using the adsorption method with different organic solvents, the drug's crystallisation is effectively inhibited. In these cases, only the broad peak associated with mesoporous silica is observed, suggesting the successful amorphisation of the drug within the MSNs. As a result, THF was selected for further studies of sorafenib loading into MSNs.

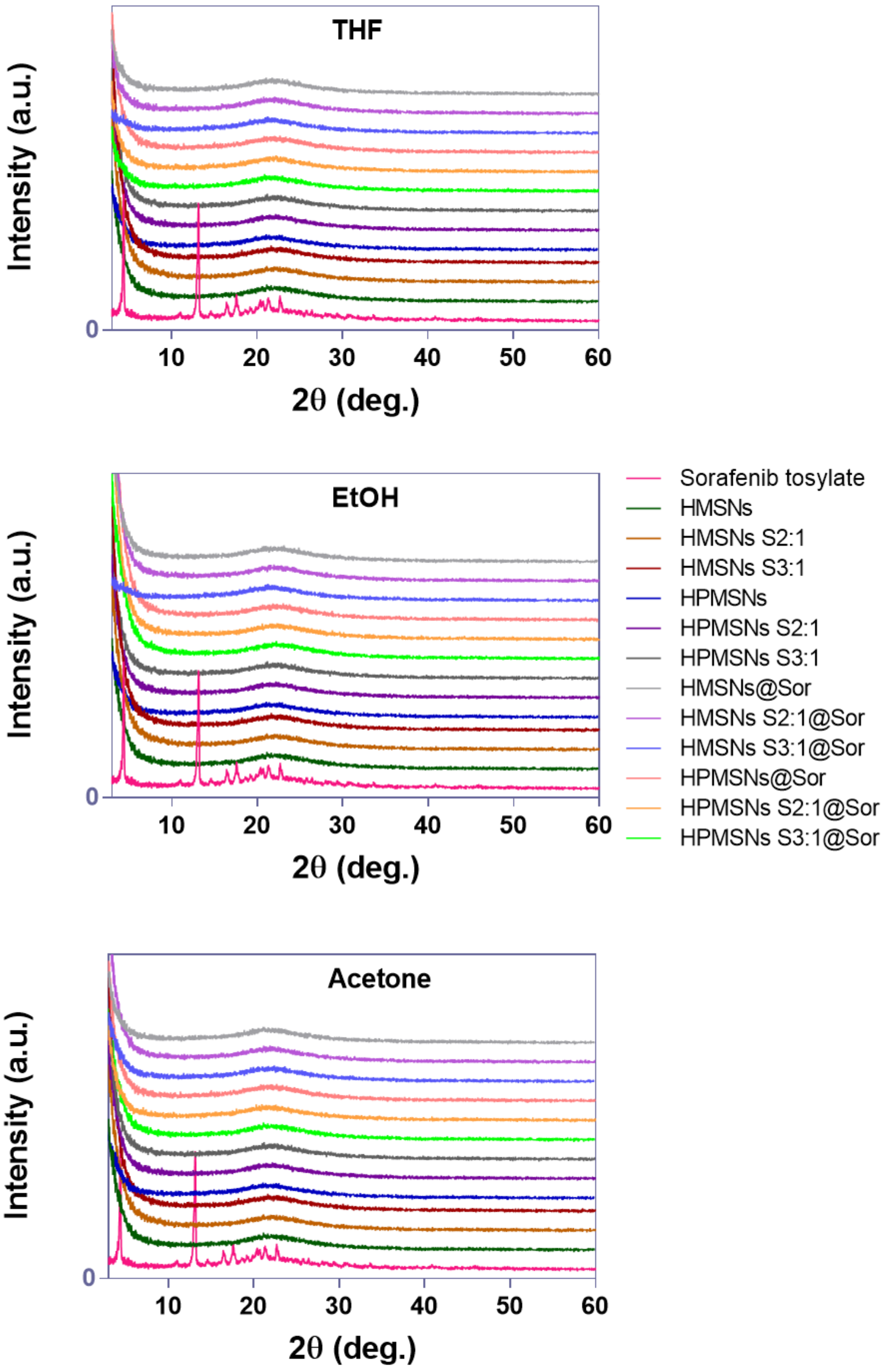

Figure 2. 9:X-ray diffraction patterns illustrating hydrophilic and hydrophobic sorafenib-loaded mesoporous silica nanoparticles (MSNs) with diverse pore sizes. The nanoparticles were prepared using the adsorption method and solvents EtOH, THF, and acetone.

2.4.2.2.2 The loading method

To explore the influence of the drug loading method on sorafenib loading, a comparative analysis was conducted between the traditional adsorption method and the evaporation method. The same THF solvent, as determined in Section 2.4.2.2.1, was employed. Additionally, a 1:1 w/w ratio of Sor/MSNs mass was used to load sorafenib into non-swollen hydrophilic MSNs (HMSNs), serving as an initial investigation into the effect of the drug loading method.

Figure 2. 10 illustrates the Drug Loading Capacity (DLC%) and Entrapment Efficiency (EE%) of sorafenib tosylate using two distinct loading methods: adsorption and evaporation. When employing the evaporation method, the DLC% notably increased to 20.1% compared to 13.5% with the adsorption method. Similarly, the EE% demonstrated a significant enhancement, reaching 18.9% with the evaporation method in contrast to 13.1% with the adsorption method as shown in Figure 2. 10.

The observed improvements in both DLC% and EE% with the evaporation method can be attributed to the gradual solvent evaporation, creating a concentration gradient. This gradient facilitates the inward movement of the drug into the silica pore channels through capillary forces.[38]

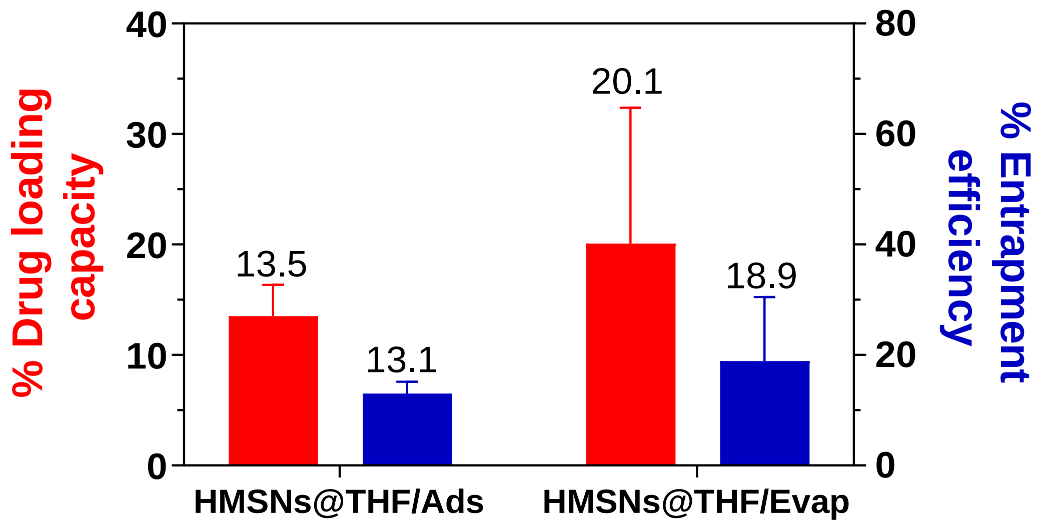

Figure 2. 10: Comparison between the adsorption and evaporation methods on sorafenib tosylate loading capacity (indicated by red bars) and entrapment efficiency (indicated by blue bars) into HMSN using equal Sor: MSNs mass ratio. All the values are expressed as mean ± standard deviation; n = 3. Note: Variations from HMSNs data in Figure 2. 8 are due to differences in the reaction scale.

Before validating the evaporation method as a default for sorafenib loading the impact of the loading method on the state of sorafenib crystallinity and localisation within the pores was determined by XRD. The results revealed that both loading methods effectively prevented the crystallisation of sorafenib tosylate and the adsorption of crystals onto the surface of MSNs, as evidenced by the absence of sharp reflection peaks corresponding to sorafenib at 4.4° and 13.1° in the XRD patterns as shown in Figure 2. 11.[37] Henceforth, the evaporation method utilising THF as a solvent for sorafenib loading into MSNs has been adopted for the remainder of this chapter.

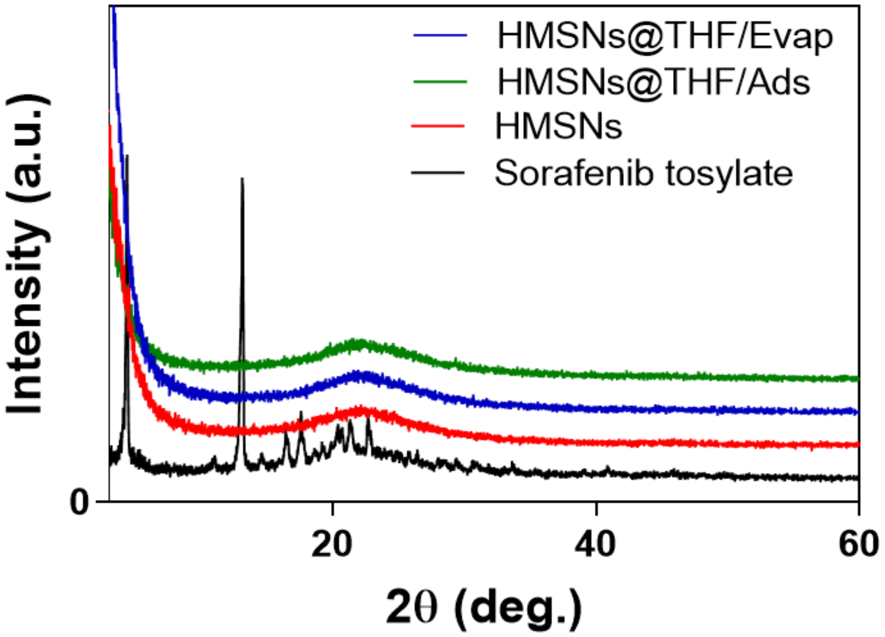

Figure 2. 11: X-ray diffraction patterns illustrating the effect of the loading methods of adsorption and evaporation on sorafenib loading into non-swollen hydrophilic MSNs (HMSNs@Sor) with diverse pore sizes. The nanoparticles were prepared using the same Sor:MSNs ratio and THF as a solvent.

2.4.2.2.3 Initial drug concentration

In a similar approach to the Dox loading optimisation discussed in Section 2.4.2.1.1, we examined how the initial Sor concentration impacts DLC% and EE%. Various amounts of sorafenib tosylate were introduced to a fixed quantity of MSNs, resulting in mass ratios of 1:4, 1:2, and 1:1 (Sor:MSN, w/w). This investigation into the initial drug concentration involved both non-swollen hydrophilic and hydrophobic MSNs. For this study, the evaporation method of loading using THF, as previously determined in Sections 2.4.2.2.1 and 2.4.2.2.2, was used.

The results presented in Figure 2. 12 reveal that higher initial drug concentrations led to an increase in DLC% for both hydrophilic and hydrophobic MSNs. The optimal drug loading was observed at a 1:1 MSNs:Sor weight ratio, with HMSNs achieving 15.7% and HPMSNS achieving 16.5%. In the case of hydrophilic MSNs, decreasing the drug concentration to 50% and 25% of MSNs resulted in reduced DLC% to 9.2% and 7.0%, respectively. Similar behaviour was observed with HPMSNs, where the 2:1 and 4:1 MSNs:Sor w/w ratios decreased the loading to 5.7% (p-value 0.0027) and 4.5% (p-value 0.0011), respectively. Consequently, increasing the initial concentration of sorafenib in relation to MSNs proportionally enhances the loading, as was also observed with doxorubicin in Section 2.4.2.1.1.[32]

The decreased DLC% values observed in HPMSNs at 2:1 and 4:1 ratio compared to HMSNs can be ascribed to steric hindrance caused by the phenyl groups of PhTMS. These groups may potentially push the drug toward the external surface, partially blocking the pores and thereby restricting drug loading.

In terms of entrapment efficiency, hydrophobic mesoporous silica exhibited a relatively consistent EE% irrespective of the drug-to-silica ratio. At ratios of 1:1, 2:1, and 4:1 MSNs:Sor, EE% were recorded at 16.1%, 11.2%, and 17.9%, respectively. Conversely, in hydrophilic mesoporous silica, a significant decrease in EE% was observed upon increasing the initial drug concentration, reducing from 26.8% at 4:1 MSNs:Sor to 15.3% (p-value 0.0139) at 1:1 w/w as displayed in Figure 2. 12. This trend is understandable as it indicates reaching the maximum drug encapsulation capacity that cannot be further enhanced by increasing the initial drug added. Additionally, it highlights the decline in entrapment efficiency as the initial drug concentration is elevated relative to the loaded amount.

In summary, since 1:1 MSNs:Sor achieved the highest drug loading, subsequent investigations will employ this ratio as the optimal initial concentration of sorafenib.

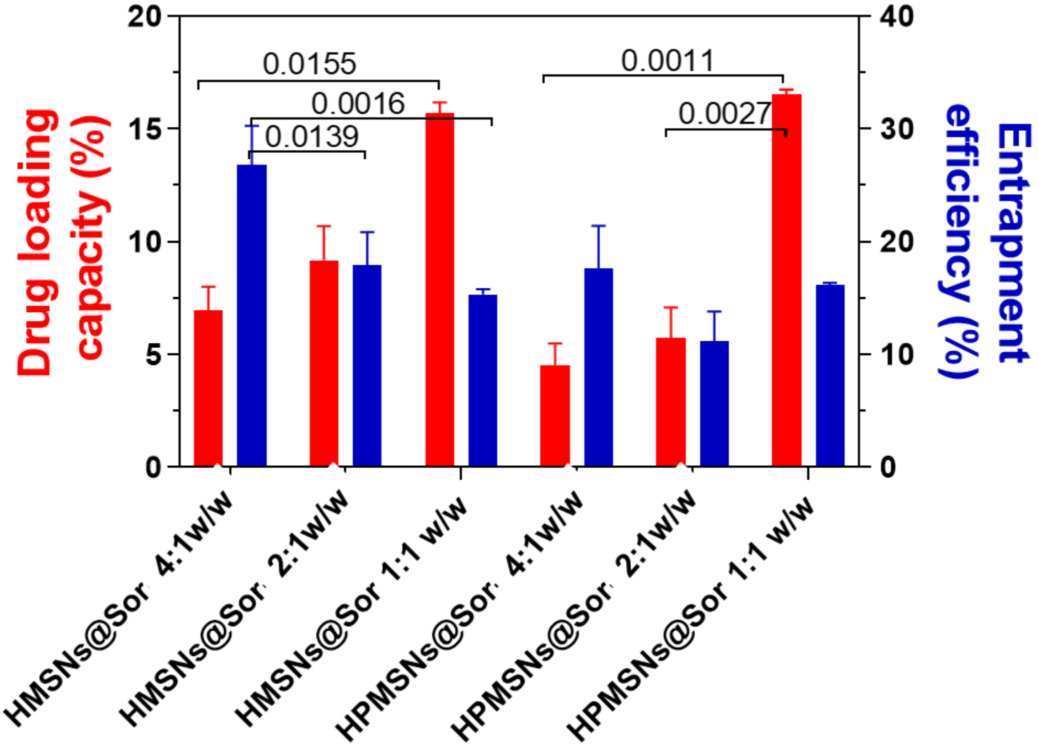

Figure 2. 12: Effect of initial sorafenib concentration on drug loading capacity (indicated by red bars) and entrapment efficiency (indicated by blue bars) into both non-swollen HMSNs and HPMSNs. All the values are expressed as mean ± standard deviation; n = 3, p-values based on two-way ANOVA.

2.4.2.2.4 Pore size

To explore the impact of pore size on sorafenib loading, hydrophilic and hydrophobic MSNs with varying pore sizes were employed to load sorafenib using the evaporation method in THF with the initial sorafenib concentration of 1:1 MSNs:Sor w/w, determined as the optimal conditions for maximum loading in the previous Sections (2.4.2.2.1, 2.4.2.2.2, and 2.4.2.2.3).

Hydrophilic MSNs showed a decrease in both DLC% and EE% upon increasing the pore size. Specifically, HMSNs with a S3:1 pore size exhibited a significant decrease in DLC% and EE% compared to regular HMSNs (with P-values of 0.0211 and 0.0277, respectively) as shown in Figure 2. 13.

In contrast, in the hydrophobic MSNs, increasing the pore size resulted in a significant increase in both drug loading and entrapment efficiency by 3 folds, aligning with the values obtained from the hydrophilic MSNs, as presented in Figure 2. 13

This can be attributed to the decreased steric hindrance imposed by the phenyl groups in the hydrophobic MSNs when the pore size is increased. In contrast, in the hydrophilic MSNs, the increase in pore size leads to a reduction in the available surface area for drug loading through hydrogen bonding interactions. These findings aligned with the influence of pore size observed in Dox loading. However, in the case of sorafenib, the effect of pore size on both DLC% and EE% was more pronounced for hydrophobic MSNs. Increasing the pore size became crucial to facilitate improved sorafenib loading into the sterically hindered pore channels with the presence of phenyl groups of PhTMS.[24, 39]

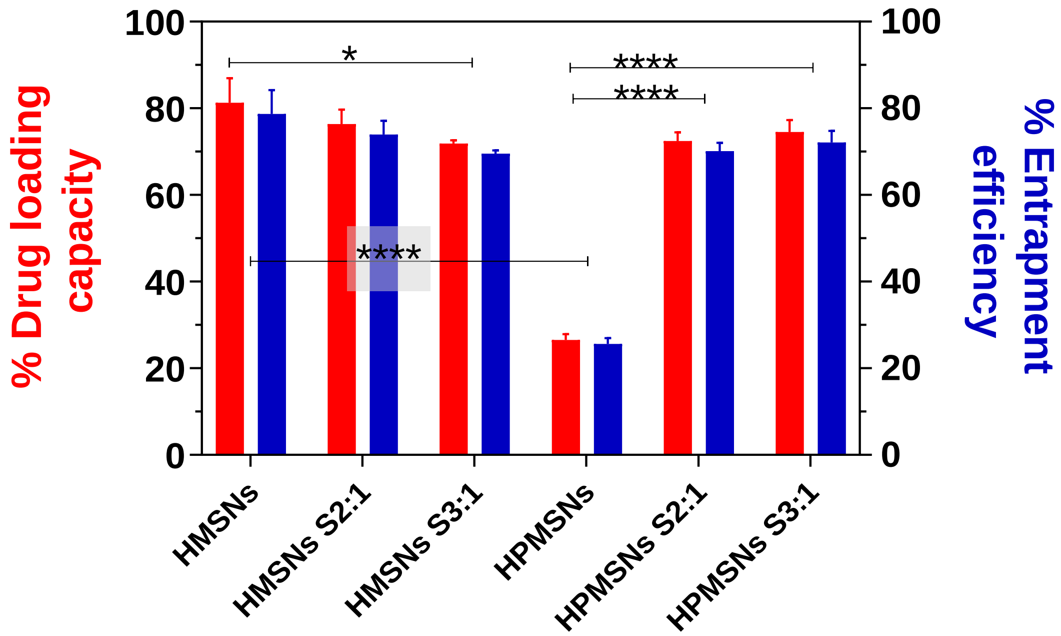

*Figure 2. 13: Effect of pore size on sorafenib loading capacity (indicated by red bars) and entrapment efficiency (indicated by blue bars) into hydrophilic and hydrophobic MSNs. All the values are expressed as mean ± standard deviation; n = 3, **** $p < 0.0001$ and * $p < 0.05$ based on two-way ANOVA.*

Finally, to assess the distribution and confinement of sorafenib within the pores of MSNs and determine if the loaded amount is mainly internalised rather than adsorbed on the surface, X-ray diffraction (XRD) analysis was performed on MSNs@Sor samples of different pore sizes. The obtained XRD results indicated that the sorafenib tosylate molecules were loaded in an amorphous form, as evidenced by the absence of distinct crystalline peaks attributed to sorafenib tosylate. Instead, only broad peaks corresponding to the silica nanoparticles were observed in the XRD pattern, suggesting the successful encapsulation of sorafenib within the mesoporous structure of the MSNs as displayed in Figure 2. 14.

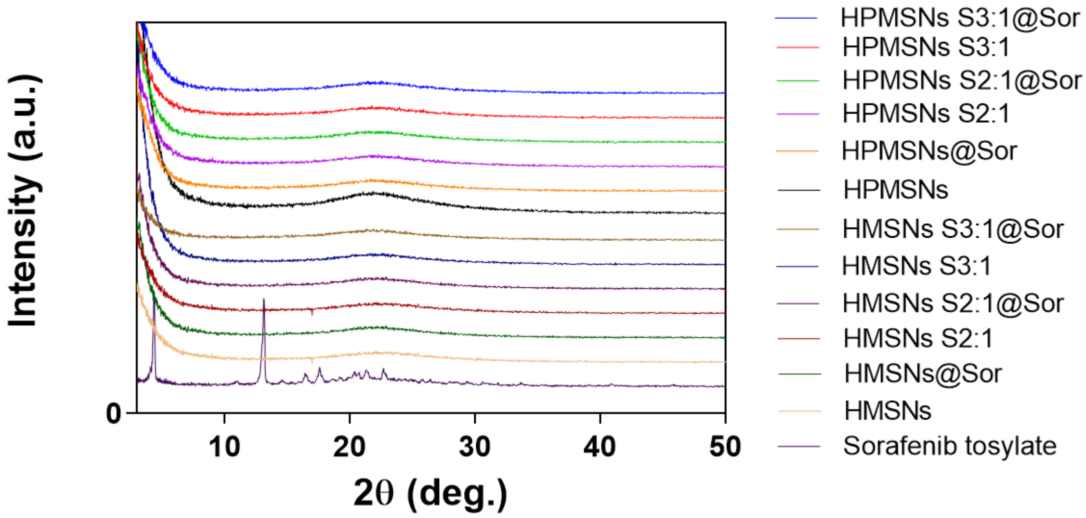

Figure 2. 14: X-ray diffraction patterns illustrating the effect of pore size on sorafenib loading into hydrophilic and hydrophobic MSNs of different pore size. The nanoparticles were prepared using the same Sor: MSNs 1:1 w/w mass ratio and evaporation method in THF as a solvent.

In future investigations seeking to confirm the influence of varying pore sizes on drug loading, utilizing BET physisorption to evaluate surface area and pore size distribution is advisable. This becomes crucial because discerning whether the differences in loading capacity among MSNs with distinct pore diameters arise from steric hindrance or simply mirror variations in surface area presents a challenging task. Unfortunately, it should be noted that this technique was not available for use in the current study.

2.5 Conclusions

In this chapter, we thoroughly investigated variables influencing the loading of doxorubicin HCl (hydrophilic) and sorafenib tosylate (hydrophobic) into MSNs. These variables encompassed initial drug concentration, pore size, MSNs surface hydrophobicity, loading method, and solvent polarity. The key findings revealed that the optimal loading capacities were achieved using hydrophilic mesoporous silica nanoparticles (HMSNs) and hydrophobic mesoporous silica nanoparticles (HPMSNs S2:1), specifically at weight ratios of 2:1 and 1:1 (drug to silica, w/w) for doxorubicin and sorafenib, respectively.

For subsequent preparation and characterisation, we carefully selected methods: an adsorption loading technique employing an aqueous doxorubicin solution and an evaporation method using tetrahydrofuran (THF) as the solvent for sorafenib tosylate. This method selection aimed to enhance drug loading by capitalising hydrogen bonding and concentration gradient differences, particularly with THF, a non-polar solvent that minimised competition with sorafenib for binding sites on Si-OH. These careful choices were made to ensure efficient drug loading into mesoporous silica nanoparticles, laying the foundation for the promising development of theranostic MSNs in Chapter 3.

2.6 References

1. X. Chen and Z. Liu, Journal of Materials Chemistry B, 2016, **4**, 4382-4388.
2. M. Vallet-Regí, F. Balas, et al., Angewandte Chemie International Edition, 2007, **46**, 7548-7558.
3. M. Manzano and M. Vallet-Regí, Journal of Materials Chemistry, 2010, **20**, 5593-5604.
4. Z. Li, J. C. Barnes, et al., Chemical Society Reviews, 2012, **41**, 2590-2605.
5. Y. Fang, G. Zheng, et al., Angewandte Chemie International Edition, 2014, **53**, 5366-5370.
6. K. Gou, Y. Wang, et al., Acta Biomaterialia, 2021, **134**, 576-592.
7. F. Balas, M. Manzano, et al., Journal of the American Chemical Society, 2006, **128**, 8116-8117.
8. M. Vallet-Regi, A. Rámila, et al., Chemistry of Materials, 2001, **13**, 308-311.
9. P. Horcajada, A. Rámila, et al., Microporous and Mesoporous Materials, 2004, **68**, 105-109.
10. M. Vallet-Regí, J. C. Doadrio, et al., 2004.
11. A. L. Doadrio, E. M. B. Sousa, et al., Journal of Controlled Release, 2004, **97**, 125-132.
12. C. Han, H. Huang, et al., Molecules, 2019, **24**, 1770.
13. K. B. Seljak, P. Kocbek, et al., Journal of Drug Delivery Science and Technology, 2020, **59**, 101906.
14. W. Stöber, A. Fink, et al., Journal of Colloid and Interface Science, 1968, **26**, 62-69.
15. J. J. Davis, W.-Y. Huang, et al., Journal of Materials Chemistry, 2012, **22**, 22848-22850.
16. Y. Ke and C. Xiang, Int J Nanomedicine, 2018, **13**, 8339-8354.
17. A. Yildirim, E. Ozgur, et al., Journal of Materials Chemistry B, 2013, **1**, 1909-1920.

18. S. A. Jadhav, I. Miletto, et al., PHYSICAL CHEMISTRY: AN INDIAN JOURNAL, 2017, **1**, 102-112.
19. M. Danaei, M. Dehghankhold, et al., Pharmaceutics, 2018, **10**, 57.
20. T. G. Souza, V. S. Ciminelli, et al., 2016.
21. Y. Lv, J. Li, et al., International journal of nanomedicine, 2017, 4361-4370.
22. Y. Wang, X. Ding, et al., Biomaterials, 2016, **101**, 207-216.
23. N. V. Roik, L. A. Belyakova, et al., Adsorption Science & Technology, 2017, **35**, 86-101.
24. J. Li, S. Shen, et al., RSC Advances, 2018, **8**, 24633-24640.
25. H. Raut, C. Jadhav, et al., OpenNano, 2022, **8**, 100103.
26. Polarity parameters of different solvents, https://people.chem.umass.edu/xray/solvent.html, (accessed 10/10/2023, 2023).
27. Y. Wu, Q. Guo, et al., Journal of Chemical & Engineering Data, 2021, **66**, 4286-4292.
28. Sorafenib tosylate, https://www.sigmaaldrich.com/GB/en/product/sigma/sml2633, (accessed 10/10/2023, 2023).
29. K. Trzeciak, A. Chotera-Ouda, et al., Pharmaceutics, 2021, **13**.
30. M. Mohseni, K. Gilani, et al., Iran J Pharm Res, 2015, **14**, 27-34.
31. S. Egodawatte, S. Dominguez, et al., Microporous and Mesoporous Materials, 2017, **237**, 108-116.
32. Y. He, S. Liang, et al., Materials Science and Engineering: C, 2017, **78**, 12-17.
33. K. Letchmanan, S.-C. Shen, et al., Colloids and Surfaces B: Biointerfaces, 2017, **155**, 560-568.
34. S. Jambhrunkar, Z. Qu, et al., Journal of Colloid and Interface Science, 2014, **434**, 218-225.
35. M. V. Speybroeck, V. Barillaro, et al., Journal of Pharmaceutical Sciences, 2009, **98**, 2648-2658.
36. J. Liu, S. Liu, et al., RSC Adv, 2019, **9**, 40835-40844.
37. G. Wiergowska, A. Stasiłowicz, et al., Pharmaceutics, 2021, **13**, 384.
38. S. Shawky, A. Abo-AlHassan, et al., Journal, 2016.

39. L. Jia, J. Shen, et al., International Journal of Pharmaceutics, 2012, **439**, 81-91.

2.7 Supplementary information

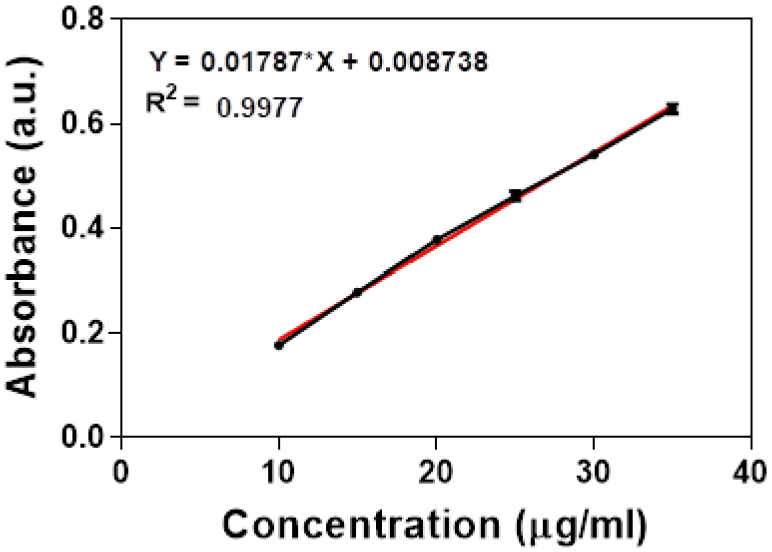

Figure S2. 1: Calibration curve of doxorubicin HCl using UV/Vis at 480 nm in water. The red line represents linear regression analysis of the data represented by black line. (n=3)

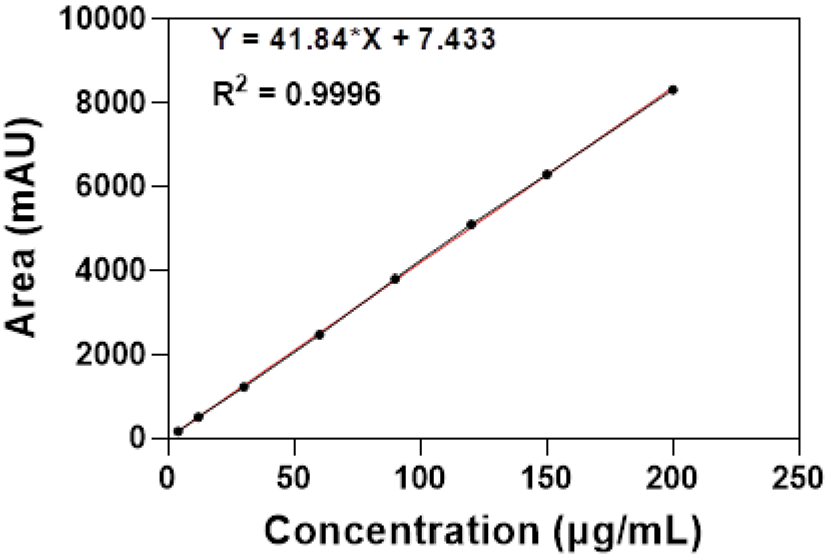

Figure S2. 2: Calibration curve of sorafenib tosylate using HPLC with UV detection at 264 nm prepared in mobile phase. The red line represents linear regression analysis of the data represented by black line. (n=3)

Chapter 3.

Optimisation of MRI-active theranostic MSNs: influence of variables on signal intensity

3.1 Introduction

Magnetic resonance imaging (MRI) is a powerful non-invasive imaging technique widely used in clinical and research settings for visualising internal structures and functions of the human body. Over the last two decades, significant progress has been made in the development and investigation of nanostructured T_1 magnetic resonance imaging (MRI) contrast agents (CAs).[1] These nanostructured agents show great promise in dramatically enhancing the sensitivity of MRI, addressing limitations associated with traditional MRI probes composed of small paramagnetic metal chelates such as Gd^{3+} or Mn^{2+}. These conventional probes have inherent shortcomings, including limited sensitivity, efficiency, and lack of tissue specificity. To overcome the sensitivity limitations of traditional MRI probes and achieve highly efficient contrast agents, a promising strategy involves the use of nanosized carriers that incorporate Gd-chelates onto or into nanocarriers or integrate Gd^{3+} ions as part of the inorganic nanostructure.[1] This approach allows for a higher loading of active paramagnetic centres, leading to improved contrast efficiency. The increased size of these nanosized carriers, compared to molecular species, results in a significant reduction in the global tumbling motion (τ_R) of the system, thereby leading to higher relaxivity, especially within the optimal magnetic field range of 0.5 – 2.0 T. Researchers have extensively explored a diverse array of nanosystems, encompassing both organic hosts (proteins, polymers, dendrimers, micelles, liposomes) and inorganic/organic hybrid matrices based on metal oxides, zeolites, and mesoporous silicas (MSNs).[2-5]

This chapter investigates the development and optimisation of efficient multifunctional theranostic MSNs as MRI contrast agents. MSNs offer a unique platform for immobilising paramagnetic centres, which can be achieved through efficient functionalisation using chelating agents with active NHS-ester groups. These agents react with organic functionalities, such as $-NH_2$ groups, previously anchored on the silica surface. The covalent conjugation of Gd^{3+} chelates to MSNs prevents the release of free Gd^{3+} ions from the nanoparticle. The use of chelated Gd^{3+} is essential to restrict free Gd^{3+} ions as they are known to be toxic and can act as an antagonist of calcium channels at low concentrations.[6] The versatility of MSNs also allows drug molecules to be loaded into the pores and thus facilitates drug delivery applications, making them promising candidates for theranostic applications, where both therapeutic and imaging functionalities are combined to enable precise imaging of drug delivery systems in blood and specific organs, providing detailed pharmacokinetic and drug delivery data.[7, 8]

One significant challenge in designing optimised MRI probes lies in achieving optimal localisation of paramagnetic chelates within MSNs. Recent studies have highlighted the pivotal role of the mesoporous support in determining the physio-chemical properties of the final material and its impact on relaxometric properties. Distinct MSN types, such as SBA-15 and nanosized MCM-41, have shown varying behaviours in hosting Gd^{3+} complexes. Several studies have shown that SBA-15 primarily hosts Gd^{3+} complexes inside the channels, while MCM-41 predominantly attaches them to the external surface.[9, 10] These localisation differences significantly influence the relaxivity of the MRI probes, with Gd^{3+} complexes primarily located on the external surface exhibiting higher longitudinal relaxivity due to improved accessibility of water molecules to the paramagnetic centres.[11] In contrast, another study has observed optimal relaxometric performance when Gd-DOTA chelates are near the pores' entrance, leading to high relaxivity at high magnetic fields attributed to confinement mediated changes in water exchange. However, functionalising silica nanoparticles on its external surface with the same Gd^{3+} chelates resulted in decreased relaxivity.[6]

Another critical factor often investigated in the literature is the role of porosity in determining the relaxometric properties of paramagnetic-immobilised MSNs. A study conducted by C. C. Landry and co-workers in 2012 explored the influence of porosity on the relaxometric properties of porous silica nanoparticles with Gd^{3+} chelators. They attached the imidodi(methanediphosphate) (NDP2) ligand to the internal surface of three different mesoporous silica samples with varying specific surface areas and pore diameters, serving as an efficient chelator for Gd^{3+} ions.[12] The longitudinal relaxivity values measured at 1.4 T for all three samples showed significant improvement compared to commercial molecular Gd^{3+} chelates due to restricted tumbling motion of the attached chelates within the silica nanoparticles. Interestingly, the nanoparticles with the widest pore diameter (5.5 nm) demonstrated the best relaxometric performance. This was attributed to the enhanced diffusion of water molecules through the larger pores, resulting in a more efficient propagation of paramagnetic relaxation to the bulk solvent.[12]

Surface properties and chemistry play a significant role in determining the relaxometric properties of paramagnetic conjugated systems within mesoporous supports. Studies indicate that the presence of reactive functionalities on the surface, such as silanol groups or neutral/positive species, in close proximity to the attached paramagnetic chelates can lead to a pronounced decrease in relaxivity.[13] In addition, the correlation between relaxivity and spacer length, observed when linking biotin-BSA macromolecules on the MSN surface with different lengths of organic spacers polyethylene glycol (PEG), illustrates the sensitivity of relaxometric properties to the chemical environment. Direct protein linking with a short spacer led to a significant relaxivity decrease due to steric capping, hindering water diffusion

and access to internalised Gd^{3+} complexes. Conversely, using a longer linker (PEG5000) reduces relaxivity by approximately 20%.[14]

Furthermore, when considering using such materials for theranostics, the impact of the introduction of the therapeutic species must also be considered, since it is not necessarily inert with respect to the effect of the relaxometric properties of a Gd-modified MSN species. For example, MSNs with a stable and neutral Gd-DOTA chelate immobilised while containing ibuprofen molecules inside the pores, has been studied. This work highlighted the significant impact of interactions between ibuprofen and the Gd^{3+}-chelates attached to the surface near the edges of the channels on the relaxometric properties of the probe.[15] The relaxivity of the sample was notably affected by the presence of the drug, exhibiting a substantial increase upon the partial release of ibuprofen. This was attributed to dynamics of the Gd-DOTA chelates which were influenced by strong electrostatic and H-bonding interactions with nearby drug molecules, leading to changes in water exchange rate and improved local mobility of the complex upon drug release.[15]

As a result, the objective of this study is to explore how different variables, including Gd-chelate location within pore channels, porosity, surface chemistry, dispersion media, temperature, and drug loading, influence the relaxometric properties of the final theranostic MSNs. Understanding these critical factors is essential for the rational design of highly efficient MRI-active systems with theranostic capabilities.

3.2 Aims

The breadth of work in this area in the literature has highlighted that various parameters can individually impact the MRI properties of Gd-modified MSNs. In this chapter, we seek to combine the knowledge gained from the literature to produce MSNs which are optimised in terms of their relaxometric properties and drug loading characteristics, with a focus on doxorubicin and sorafenib tosylate drugs. This chapter emphasises the importance of understanding the localisation of paramagnetic chelates in MSNs, along with the surface chemistry and drug loading and release, in the optimisation of relaxometric properties of multifunctional theranostic MSNs.

To accomplish this, a range of MRI-active MSNs with varying pore sizes and surface chemistries was synthesised. The MRI signals of these MSNs were measured in aqueous suspensions and phosphate-buffered saline (PBS) at temperatures of 25 °C and 42 °C, in anticipation of using these species for thermally-controlled biologically-relevant drug release. In addition, the impact of the location of Gd-chelates within the MSN pores, whether at the edge or core of the pore channel, on the MRI signal was thoroughly examined, to ensure that optimal species are ultimately produced. In addition, the influence of drug loading and release on the MRI signal were investigated using single-field relaxometry and nuclear magnetic resonance dispersion (NMRD), as well as phantom imaging.

By exploring these key factors, this chapter aims to elucidate the most favourable conditions and configurations for optimising the relaxometric properties of theranostic MSNs. The outcomes of this research hold great promise in advancing the field of MRI contrast agents, contributing to the development of more efficient and versatile systems for non-invasive imaging and targeted drug delivery in biomedical applications.

3.3 Experimental

3.3.1 Materials

All chemicals were used as received without further modification. (3-aminopropyl)triethoxysilane (APTES), gadolinium(III) chloride, and triethylamine were purchased from Sigma-Aldrich or Fisher Scientific. 2,2',2''-(10-(2-((2,5- dioxopyrrolidin-1-yl)oxy)-2-oxoethyl)-1,4,7,10-

tetraazacyclododecane-1,4,7- triyl)triacetic acid (DOTA-NHS-ester) was purchased from CheMatech. A ten-element custom mix ICP standard was purchased from QMX Laboratories, containing Gd (100 mgL^{-1}) in 5% nitric acid (HNO_3) (100 mL). Anhydrous dimethylformamide (DMF) and anhydrous tetrahydrofuran (THF) were used as received and sourced from Fisher Scientific or Sigma-Aldrich, UK. All other chemicals and solvents were as described in Chapter 2, Section 2.3.1.

3.3.2 Methodology

3.3.2.1 Synthesis of aminated mesoporous silica nanoparticles (MSNs-NH_2)

To synthesise aminated MSNs (MSNs-NH_2), the same procedure described in Sections 2.3.2.1, 2.3.2.2 and 2.3.2.3 for hydrophilic and hydrophobic silica particles synthesis of different pore sizes was followed.

However, in the case of aminated MSNs, a slight modification was introduced. After the addition of TEOS (1.45 mL, 6.49 mmol), a mixture of TEOS and APTES in a 1:1 molar ratio (4.7 µL) was added either after a 10-minute interval to create core-located amino groups (referred to as core MSNs-NH_2, with a short delay co-condensation), or after one hour to generate edge-located amino groups (referred to as edge MSNs-NH_2, with a long delay) according to a previously published method.[6] Subsequently, the samples were washed by acidified ethanol to eliminate CTAB, followed by ethanol for neutralisation, and finally stored in ethanol at room temperature, as previously described in Sections 2.3.2.1, 2.3.2.2 and 2.3.2.3.

3.3.2.2 Synthesis of MRI-active MSNs (MSNs-NH_2@Gd^{3+}- DOTA)

Aminated MSNs (edge and core) (100 mg) as prepared in 3.3.2.1 were dispersed into anhydrous N,N-dimethylformamide (DMF, 16 mL) and stirred vigorously at room temperature overnight with 2,2’,2”- (10-(2-((2,5-dioxopyrollidin-1-yl)oxy)-2-oxoethyl)-1,4,7,10-tetraazacyclododecane-1,4,7-triyl)triacetic acid (DOTA-NHS ester, 4 mg, 5 µmol) and triethylamine (200 µl). After this time, the nanoparticles were washed three times with ethanol using centrifugation and redispersed into ethanol (10 mL). $GdCl_3$ (2.6 mg, 10 µmol) was added and the mixture was stirred vigorously at room temperature for 24 h. The excess Gd^{3+}-ions were removed using dialysis (3.5 K MWCO, 35 mm) against ultrapure water for two hours while changing the water regularly every 20 minutes. Finally, the nanoparticles were washed five times with ethanol using centrifugation at 15,300 rpm for 30 minutes (each sample was washed at least 7 times) before storing in ethanol.

3.3.2.3 Preparation of MRI-active theranostic MSNs

According to the findings presented in Chapter 2, Section 2.4.2, optimal drug loading capacities of doxorubicin and sorafenib tosylate were successfully achieved using both non-swollen hydrophilic MSNs (HMSNs) and moderate swollen hydrophobic MSNs (HPMSNs S2:1). As a result, we proceeded with the synthesis of MRI-active mesoporous silica nanoparticles

(HMSNs@Gd and HPMSNs S2:1@Gd), as described in detail in Section 3.3.2.2 to prepare the theranostic nanocarriers.

3.3.2.3.1 Hydrophilic drug (doxorubicin HCl)

To achieve the loading of the hydrophilic drug doxorubicin (Dox) into the MRI-active diagnostic MSNs (HMSNs@Gd and HPMSNs S2:1@Gd), 80 mg of MSNs (large scale in comparison to Section 2.3.2.4.1 in Chapter 1 where 10 mg MSNs were used) were dispersed in a concentrated aqueous solution of doxorubicin (5 mg/ml) at a weight ratio of 2:1 (Dox: MSNs), following the procedure outlined in Section 2.3.2.4.1. The dispersions were stirred overnight at room temperature, enabling the successful loading of doxorubicin into the MSNs.

To eliminate any unbound or free doxorubicin, the dispersions were centrifuged at 15,300 rpm for 10 minutes, and the supernatant was carefully removed. The resulting loaded HMSNs@Gd/Dox and HPMSNs S2:1@Gd/Dox were then subjected to two washes using a 50% aqueous ethanolic solution at 15,300 rpm for 10 minutes. Finally, the loaded nanoparticles were dispersed in a 50% aqueous ethanolic solution for storage.

3.3.2.3.2 Hydrophobic drug (sorafenib tosylate)

To prepare theranostic sorafenib-loaded MSNs, 80 mg of MSNs (HMSNs@Gd or HPMSNS S2:1@Gd) (large scale in comparison to Section 2.3.2.4.2 in Chapter 1 where 10 mg MSNs were used) were mixed with a concentrated sorafenib solution in tetrahydrofuran (THF, 1 mg/mL) at a ratio of 1:1 (Sor:MSNs, w/w). The resulting dispersion was stirred overnight at room temperature. The solvent was then gradually evaporated at 60 °C until approximately 2 mL of solvent remained. The dispersion was subjected to centrifugation for 10 minutes at 15,300 rpm to separate the unloaded free drug in the supernatant.

Following centrifugation, the loaded HMSNs@Gd/Sor and HPMSNs S2:1@Gd/Sor were washed twice with 100% ethanol using centrifugation at 15,300 rpm for 10 minutes to remove any residual unbound sorafenib. Finally, the loaded nanoparticles were dispersed in a 100% ethanolic solution for storage, as described in Section 2.3.2.4.2.

3.3.2.4 Drug loading and release kinetics of MSNs@Gd/drug

Equation 3. 1 and Equation 3. 2 were used to measure the drug loading capacity and entrapment efficacy, where both free doxurubicin HCl and sorafenib tosylate were quantified based on pre-determined calibration curves recorded using HPLC and UV/Vis, respectively, as mentioned in Section 2.3.2.5 according to the calibration curves in Figure S3. 1 and Figure S3. 2.

$$Drug\ loading\ capacity\ (\%) = \frac{weight\ of\ encapsulated\ drug}{weight\ of\ MSNs} \times 100$$ Equation 3. 1

$$Encapsulation\ efficiency\ (\%) = \frac{weight\ of\ encapsulated\ drug}{weight\ of\ total\ added\ drug} \times 100$$ Equation 3. 2

To determine the drug release kinetics from HMSNs and HPMSNs S2:1, the loaded MSNs@Gd/Dox or MSNs@Gd/Sor equivalent to 4.4 mg of Dox or 27 μg of Sor were suspended in 2 mL of release medium to achieve sink conditions (PBS, pH 7.4, with 1 w/w % Tween 80) and incubated at 37 °C with constant agitation of 200 rpm. At predetermined time points, the suspension was centrifuged at 10,000 rpm for 10 min at room temperature to separate MSNs pellets and supernatants. The sampled supernatant was analysed immediately using UV/Vis for doxorubicin or stored frozen for subsequent HPLC analysis of sorafenib, using the analysis methods described in Section 2.3.2.5. To study the mechanism of drug release, both Weibull and Korsmeyer-Peppas models were applied. The Korsmeyer–Peppas model describes the kinetics of drug release from the matrices as described in Eqation 3. 3.[16]

$$\frac{M_t}{M_\infty} = Kt^n$$

Equation 3. 3

where M_t and M_∞ denote the cumulative mass of drug released at time t and at infinite time, respectively; k is a kinetic constant characteristic of the drug–carrier system; and n is an exponent that characterises the mechanism of drug release.

Despite not having a kinetic basis, the Weibull model has the ability to dampen abrupt changes in the release profile curves using α as a reaction rate constant and β as the behaviour index (Equation 3. 4).[17, 18]

$$\frac{M_t}{M_\infty} = 1 - e^{-\alpha t \beta} \qquad \textit{Equation 3. 4}$$

where α is a scale parameter, and β is the curve shape factor.

3.3.2.5 Relaxivity and MRI studies

An Oxford Instruments MQC+ benchtop NMR analyser with a resonant frequency of 23.4 MHz (single-field relaxometry) was used to determine the relaxivity (r_1 and r_2) of Gd^{3+}-loaded nanoparticles for at least four different concentrations of suspended MSNs in water, PBS, or release media at 25, 37 or 42 ^oC. The relaxation rates R_1 and R_2 were determined as the reciprocal of the relaxation time T_1 and T_2 (s). By plotting the values of R_1 or R_2 (s^{-1}) against Gd^{3+} concentrations (mM, as calculated from ICP-OES data), relaxivity (mM^{-1} s^{-1}, the slope of the best fit line) was obtained. The measurement of T_1 used the standard inversion-recovery method. The T_2 values were measured using the Carr-Purcell-Meiboom-Gill (CPMG) method. Each measurement was evaluated using 4 scans.

The nuclear magnetic resonance dispersion (NMRD) profiles were measured on an HTS-110 3T Magnet System for magnetic fields from 0.01 MHz to 128 MHz (Fast-Field Cycling Relaxometry). NMRD profiles were recorded at 25 and 37 °C to avoid issues with heating throughout the measurements. Samples were dispersed in 1 mL of ultrapure water and were carefully sonicated prior to measurement. The NMRD profiles were recorded by Prof. Mauro Botta and Dr. Fabio Carniato from the University of Eastern Piedmont.

In addition, T1-weighed MR images of hydrophilic MSNs (HMSNs@Gd) and hydrophobic MSNs (HPMSNs S2:1@Gd) with and without drug (Dox or Sor) were acquired using a 3 T Philips Ingenia CX MRI scanner (Philips Healthcare) using a 3D T1-weighted gradient−echo sequence where repetition time (TR = 7 ms), echo time (TE = 3.5 ms), field of view (FOV)= 200 x 200 x 60 mm^3, resolution = 600 x 600 µm, slice thickness = 0.6 mm. Dispersions of polymer grafted MSNs in ultrapure water with Gd^{3+} concentration of 0.05 mM were measured at three different temperature 23, 39, 48 °C. The phantom imaging were recorded by Prof Geoff JM Parker and Dr. Mina Kim from the Centre for Medical Image Computing, University College London.

3.3.2.6 Physicochemical characterisation

Hydrodynamic size, size distribution and zeta potential of MSNs were determined by dynamic light scattering technique (DLS) and zeta potential analysis using Malvern Zetasizer Nano ZS equipped with a He-Ne laser (λ= 632.8 nm) at 173 ^oC scattering angle and a temperature of 25 ^oC. The data were analysed using the Zetasizer software (version 7.12). Fourier-transform infrared spectroscopy (FTIR) spectra were collected on a Shimadzu IRTracer-100 spectrometer operated by LabSolutions IR software (version 2.10). At least 32 scans of the samples were evaluated over the spectral region of 400 cm^{-1} to 4000 cm^{-1}. Transmission electron microscopy (TEM) was performed using a JEOL 2100 TEM operating at 200kV. The samples were diluted to 1 mg/mL in water before drop-casting onto formvar coated 300 mesh copper TEM grids (EM Resolutions). The diameter of the nanoparticles was determined as a mean of at least 100 different particles using ImageJ (Version 1.52).

Inductively coupled plasma optical emission spectroscopy (ICP-OES) was used to determine the concentration of gadolinium. The process involved preparing samples for ICP-OES by digesting 3 mg of MSNs in 1 mL of ultrapure water with hot nitric acid (70% w/w). The resulting solution was then diluted to 25 mL in a volumetric flask. ICP-OES analysis was carried out using an Agilent Varian 720-ES instrument, running at 1 kW power with a 40 MHz radiofrequency argon plasma. The plasma gas flow was maintained at 15

L/min, while the nebulizer flow rate was set to 0.75 L/min. The spectral lines used for gadolinium were 335 nm, 336 nm, and 342 nm. To ensure accuracy, the concentrations were determined by averaging the results from these three spectral lines. For calibration purposes, a range of standards from 2 – 8 ppm was generated. This calibration was created using an initial gadolinium (III) concentration of 100 mg/L in 5% HNO_3, a standard provided by QMX Laboratories.

Thermogravimetric analysis (TGA) was performed at a heating rate of 10 ^oC/min under nitrogen (40 mL/min). TGA data were recorded and analysed by the Trios software (version 4.5.1). X-ray diffraction (XRD) X-ray diffraction analysis was performed using a Rigaku Miniflex 600 diffractometer with Cu Kα radiation (λ = 1.5418 Å). Patterns were collected over the 2θ range of at least 2–50°, at 40 kV and 15 mA.

3.4 Results and discussion

3.4.1 MRI-active MSNs

3.4.1.1 Synthesis and characterisation

Aminated hydrophilic MRI-active nanoparticles (HMSNs-NH_2) were initially synthesised to investigate the impact of Gd-chelate location within the pore channel, solvent composition, and temperature on the signal intensity in MRI. To achieve this, amino groups were immobilised on the internal pore surfaces through a delayed hydrolysis and co-condensation reaction. APTES groups were subsequently introduced at two different time points (10 minutes or 1 hour) during a two-hour reaction, resulting in the formation of aminated-core HMSNs or aminated-edge HMSNs, respectively (Section 3.3.2.4) as illustrated in Figure 3. 1.

The short and long delay co-condensation is a well-known approach and is consistent with previously published studies,[19, 20] for example, Cauda and colleagues conducted a study on the selective functionalization of the inner and outer surfaces of MSNs using different trialkoxysilanes through a delayed co-condensation approach.[20] They prepared MSNs with distinct functional groups positioned either on the outer shell or within the inner core of the particle. The identification and localization of these functional groups were determined through various techniques, including zeta potential, nitrogen sorption measurements, and fluorescence spectroscopy. Fluorescence experiments using FITC-labeled MSNs revealed that fluorescence quenching of gold nanoparticles, of higher diameter than the pores, occurred only when FITC was positioned on the outer surface, not in the inner core. This study demonstrated the controlled localization of functional groups within the nanometer space of MSNs, providing the opportunity to synthesize bifunctional mesoporous nanoparticles with precise localization of different functional groups in either the inner core or on the outer shell through a multistep co-condensation strategy.

To attach Gd^{3+}-chelates, DOTA-NHS ester was first conjugated to these internal amino groups using carbodiimide chemistry. Then, Gd^{3+} ions were loaded onto the nanoparticles as described in Section 3.3.2.2 (Figure 3. *1*).[6]

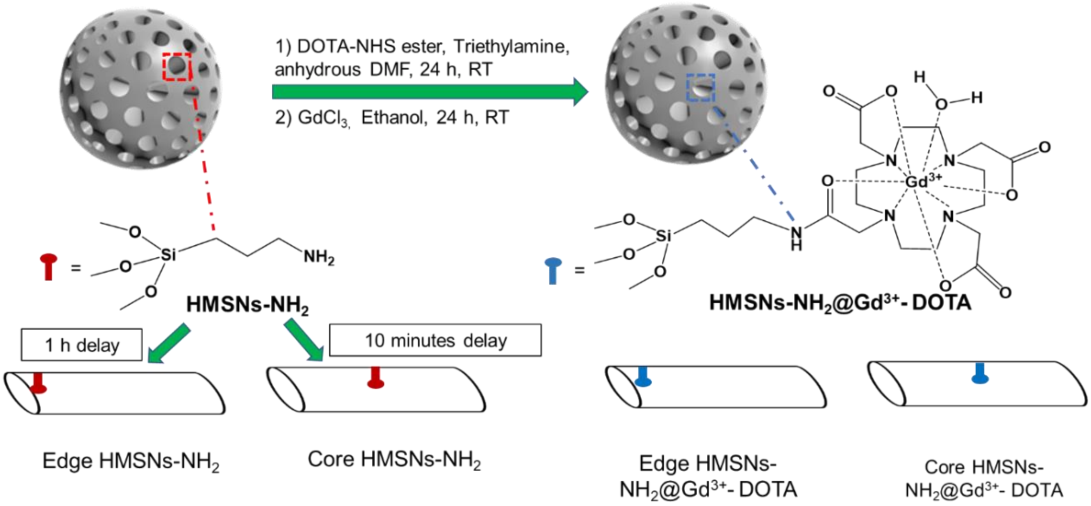

Figure 3. 1: Schematic representation of the synthesis of MRI-active gadolinium chelate-loaded HMSNs from HMSNs-NH_2 in different pore locations (edge or core).

The TEM images showed a uniform, porous and spherical morphology of all the synthesised MSNs particles with average diameters ranging from 40.9 ± 5.1 nm to 44.4 ± 3.8 nm (Figure 3. 2). All sizes were within error of one another due to low grafting densities, as expected. This is important to note to ensure that any changes identified by relaxometry are as a result of designed parameters, and not changes in τ_R due to size differences.

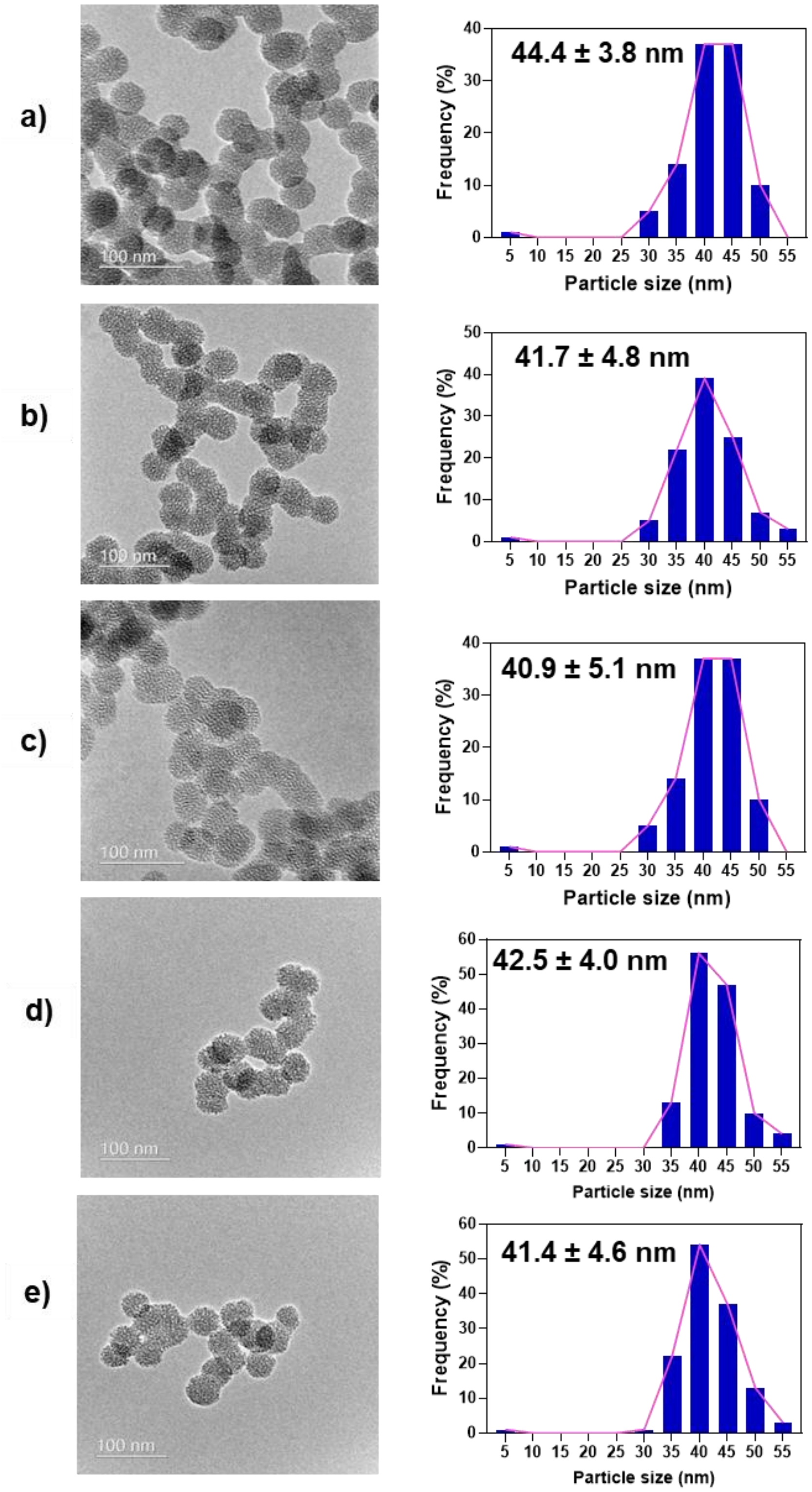

Figure 3. 2: Transmission electron microscope (TEM) images (left column) and the corresponding size distribution histograms (right column) of a) HMSNs, b) core HMSNs-NH_2, c) edge HMSNs-NH_2, d) core HMSNs-NH_2@Gd^{3+}-DOTA and e) edge HMSNs-NH_2@Gd^{3+}-DOTA.

The average hydrodynamic diameter of MSNs measured by dynamic light scattering (DLS) was 157.3 ± 1.7 nm for plain HMSNs and became slightly larger upon functionalisation (Table 3. 1). In addition, PdI values were less than 0.3 confirming the homogeneity of the synthesised nanoparticles. The surface zeta potential showed a negative value for plain MSNs which was attributed to the silanol groups on the external surface (-25.0 ± 0.2 mV). The aminated MSNs (both core and edge) showed a change in surface zeta potential towards positive potentials (-11.4 ± 0.3 and -10.2 ± 0.5 mV, respectively), due to the covalent grafting of the positively charged amino groups. Upon loading Gd^{3+}-DOTA chelates in both core and edge MSNs, more negative potentials were observed, as some of these amino groups have been used in the carbodiimide reaction (-16.3 ± 0.1 and -14.0 ± 0.4 mV, for Gd-DOTA-MSNs edge and core loaded, respectively), as shown in Table 3. 1.

The size measurements of MSNs vary depending on the technique used, namely TEM or DLS. TEM captures images of nanoparticles dried onto a surface, while DLS analyses samples in suspension. DLS is influenced by hydrogen bonding and van der Waals interactions with solvent molecules, affecting particle Brownian motion. Consequently, DLS reports a larger diameter for nanoparticles due to hydrodynamic radius measurement in liquid. Moreover, DLS quantifies size distribution by intensity, correlating to particle radius to the power of six, while TEM measures size as a number average, making DLS highly sensitive to large particle presence.[21] In addition, TEM data suggests the possibility of aggregation or fusion of MSNs as observed and discussed in Section 2.4.1.

Table 3. 1: Particle size, polydispersity index, and zeta potential measured by DLS and TEM.

Formulae	**Particle size (D_H)^{a*} (nm)**	**Polydispersity index (PdI)^{b*}**	**ζ-potential (mV)***	**TEM size (nm)^c**
HMSNs	157.3 ± 1.7	0.2 ± 0.01	-25.0 ± 0.2	44.4 ± 3.8
Core HMSNs-NH$_2$	163.6 ± 2.1	0.2 ± 0.03	-11.4 ± 0.3	41.7 ± 4.8
Edge HMSNs-NH$_2$	177.7 ± 1.2	0.2 ± 0.02	-10.2 ± 0.5	40.9 ± 5.1
Core HMSNs@Gd^{3+}-DOTA	164.5 ± 6.0	0.17 ± 0.08	-16.3 ± 0.1	42.5 ± 4.0
Edge HMSNs@Gd^{3+}-DOTA	159.7 ± 0.4	0.2 ± 0.02	-14.0 ± 0.4	41.4 ± 4.6

[a] Hydrodynamic diameter extracted by cumulant analysis of the data.
[b] Polydispersity index from cumulant fitting.
[c] TEM particle size analysis of at least 100 nanoparticles using Image J.
[*] All values represent mean ± standard deviation (n=3).

3.4.1.2 Relaxivity measurements

3.4.1.2.1 Gd-chelate location

The synthesised core and edge HMSNs-NH$_2$@Gd^{3+}-DOTA showed r$_1$ relaxivity values of 39.6 ± 0.7 and 34.0 ± 1.9 mM^{-1} s^{-1} and r$_2$ relaxivity values of 45.7 ± 0.7 and 43.1 ± 1.5 mM^{-1} s^{-1}, respectively, at 23 MHz (0.47 T) (Figure 3. 3). The obtained relaxivity values (r$_1$) are 11.6 (core) and 10 (edge) times higher values than the commercially available molecular Gd-DOTA chelate (Dotarem©), which has r$_1$ of 3.4 mM^{-1} s^{-1} at 1 T. [22] The enhanced contrast effect can be primarily attributed to the loading of Gd-chelate into the MSNs which provides a higher rotational correlation time (τ_R), longer water proton residence lifetime (τ_M) and increased diffusional time (τ_D). This behaviour has been previously noted in the literature for materials produced in this way.[6, 23] The data showed higher relaxivity values of the core HMSNs-NH$_2$@Gd^{3+}-DOTA in comparison with the edge loaded system, which contradicts a previously published study (Figure 3. 3).[6] The Gd^{3+} concentration calculated by ICP-OES in Gd-loaded edge MSNs samples was found to be slightly higher than that of Gd-loaded core MSNs (0.35 and 0.2 mM, respectively). The high concentration of Gd^{3+} at the pores' edge may result in a steric blocking of the pores, especially upon using a short spacer such as APTES, which may restrict water accessibility to the internalised Gd-DOTA chelate beneath the outer molecules, unlike the core loaded Gd-DOTA chelate where water exchange and diffusion is more feasible as the lower amounts of Gd-DOTA do not prevent water access to the internalised chelates.[14] As a result, core located Gd-chelate, HMSNs-NH_2@Gd^{3+}-DOTA, was selected as the optimum system with which to further study the effect of both temperature and solvent (water and PBS) on relaxivity values.

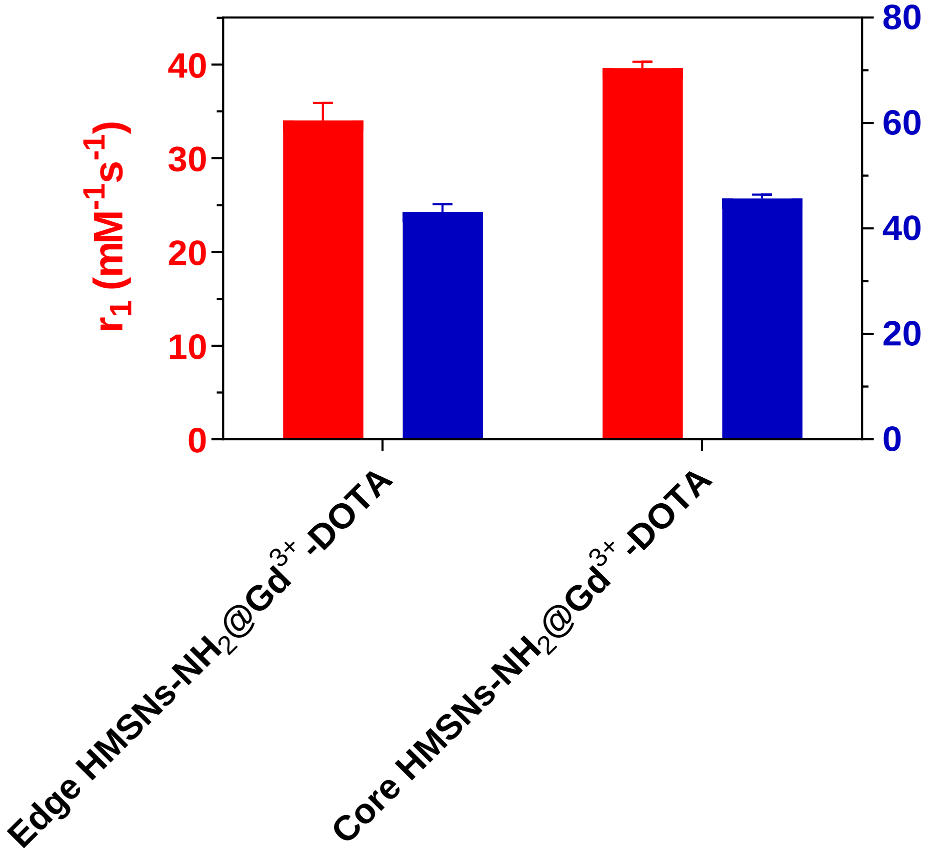

Figure 3. 3: ^1H r_1 and r_2 relaxivity values of Gd-loaded core MSNs and Gd-loaded edge MSNs measured at 0.47 T and 25 °C. All values represent mean ± standard deviation (n=3 independent syntheses).

3.4.1.2.2 Effect of dispersion media and temperature

To study the effect of solvent as well as temperature on MRI signal, core HMSNs-NH_2@Gd^{+3}-DOTA were dispersed in either water or PBS and the relaxivity values were evaluated at two different temperatures (25 and 42 °C).

Upon increasing the temperature, a slight reduction in relaxivity values (r_1 and r_2) was observed in both dispersion media (Table 3. 2), due to changes in Brownian motion of particles and water causing a decrease in the *water residency time* (τ_M), *an increase in relaxation time (*τ_{ie}*), and* a decrease in rotation correlation time (τ_R), hence leading to acceleration of relaxation time and reduction in relaxivity.[24] This is a commonly reported phenomenon in the literature.

When dispersing Gd-loaded core MSNs into different media, we found a more marked effect on relaxivity. For instance, the relaxivity values decreased from $r_1 = 39.6 \pm 0.7$ mM^{-1} s^{-1} in water to $r_1 = 9.6 \pm 0.6$ mM^{-1} s^{-1} in PBS, and from $r_2 = 45.7 \pm 0.7$ mM^{-1} s^{-1} in water to $r_2 = 12.4 \pm 1.5$ mM^{-1} s^{-1} in PBS, as presented in Table 3. 2. This drastic reduction in relaxivities upon using PBS can be explained by the tendency of phosphate anions to displace water molecules in the Gd inner sphere, however the relaxivity values remain high enough for these to be useful biologically.[25, 26]

Table 3. 2: ^{1}H r_1 and r_2 relaxivity values of Gd-loaded core hydrophilic MSNs measured at 0.47 T in water and PBS at 25 °C and 42 °C.

Temperature	**25 (°C)**		**42 (°C)**	
Dispersion medium	**r_1 (mM^{-1} s^{-1})**	**r_2 (mM^{-1} s^{-1})**	**r_1 (mM^{-1} s^{-1})**	**r_2 (mM^{-1} s^{-1})**
Water	39.6 ± 0.7	45.7 ± 0.7	35.0 ± 1.0	44.4 ± 3.2
PBS	9.6 ± 0.6	12.4 ± 1.5	8.9 ± 2.2	12.3 ± 3.0

3.4.1.2.3 Effect of pore size and chemistry on relaxivity

In an initial investigation, we explored how pore size and chemical composition affect MRI signal. To achieve this, we synthesised a variety of aminated hydrophilic and hydrophobic mesoporous silica nanoparticles (MSNs) with varying pore sizes. The hydrophobic MSNs were synthesised following the procedure outlined in Chapter 2 (Section 2.3.2.2), incorporating PhTMS during MSN synthesis to create hydrophobic internal pore surfaces. Different pore sizes were achieved by incorporating the swelling agent TMB during the preparation process (Chapter 2, Section 2.3.2.3). Following the synthesis, Gd-chelate was loaded into the core of these MSNs, as these were previously found optimum in terms of MRI signal enhancement (Section 3.4.1.2.1). The MSNs were then dispersed in water, and their relaxivity values were evaluated at 25 °C for each MSN type (Table 3. 3).

Notably, the relaxivity of hydrophobic MSNs fell within the range of values seen in hydrophilic ones, suggesting that this alteration in surface chemistry does not immediately impact relaxivity (Table 3. 3). In contrast, it is evident that porosity significantly influences relaxivity. In the case of the hydrophilic MSNs (HMSNs), r_1 increased with increasing pore size from narrow to medium in HMSNs @Gd^{3+}-DOTA and HMSNs S2:1@Gd^{3+}-DOTA, respectively, but the large pore size of HMSNs S3:1@Gd^{3+}-DOTA gave a dramatic decrease in r_1 (r_1 values of 39.6, 45, and 33.7 $mM^{-1}s^{-1}$, respectively). On the contrary, the hydrophobic MSNs showed a consistent increase of relaxivity with an increase in pore size, and the maximum r_1 was achieved in HPMSNs-NH_2 S3:1@Gd^{3+}-DOTA of 45.8 $mM^{-1}s^{-1}$ (Table 3. 3). In previous studies, it was established that the diffusion of water within mesopores slows down as the pore size decreases. This phenomenon results in a prolonged residence time for protons within smaller mesopores, leading to extended interactions with the contrast agent and allowing for multiple water molecules to be coordinated with each Gd centre, decreasing Gd rotation within the framework and hence increased relaxivities.[27-29]

As a result, increasing the pore size should positively affect the relaxivity until a threshold is reached, in which the size of the pore channel allows fast diffusion of water and so less interactions with Gd-chelate and lower relaxivity. This was observed in the hydrophilic MSNs where r_1 increased from 39.6 to 45.4 $mM^{-1}s^{-1}$ in small and medium pores, respectively, before it decreased to 33.7 $mM^{-1}s^{-1}$ in large pores. In the case of the large pore size in the hydrophobic MSNs, the presence of phenyl groups seems to continue to restrict the water diffusion and thus allow better relaxivity. As a result, the relaxivity increased from 41.4 to 43.1 $mM^{-1}s^{-1}$ in small and medium size pores finally reaching 45.8 $mM^{-1}s^{-1}$ at the large pore size hydrophobic nanoparticles.

Table 3. 3: ^1H r_1 relaxivity values of MSNs of different pore sizes measured at 0.47 T in water at 25 °C.

Formulae	**r_1 (mM-1s^{-1})**
HMSNs@Gd^{3+}- DOTA	39.6 ± 0.7
HMSNs S2:1@Gd^{3+}- DOTA	45.4
HMSNs S3:1@Gd^{3+}- DOTA	33.7
HPMSNs @Gd^{3+}- DOTA	41.9
HPMSNs S2:1@Gd^{3+}- DOTA	43.1
HPMSNs S3:1@Gd^{3+}- DOTA	45.8

3.4.2 MRI-active theranostic MSNs

To prepare theranostic MSNs of both maximum drug loading capacity and suitable MRI contrast, both hydrophilic MSNs (HMSNs) and hydrophobic MSNs (HPMSNs S2:1) were selected based on the data deduced from Chapter 2. First, the contrast agent Gd-chelate was incorporated into the core location of the pores to achieve efficient enhanced MRI contrast capabilities as discussed in Section 3.4.1.2. Subsequently, the hydrophilic drug doxorubicin HCl or the hydrophobic drug sorafenib tosylate were loaded into these MSNs separately (Section 3.3.2.3).

The size and morphology of the drug loaded hydrophilic and hydrophobic particles were evaluated using DLS and TEM. Porous and spherical nanoparticles with different pore sizes and similar particle sizes were observed as shown in Figure 3. 4. There was no apparent change in structure or morphology upon loading drugs.

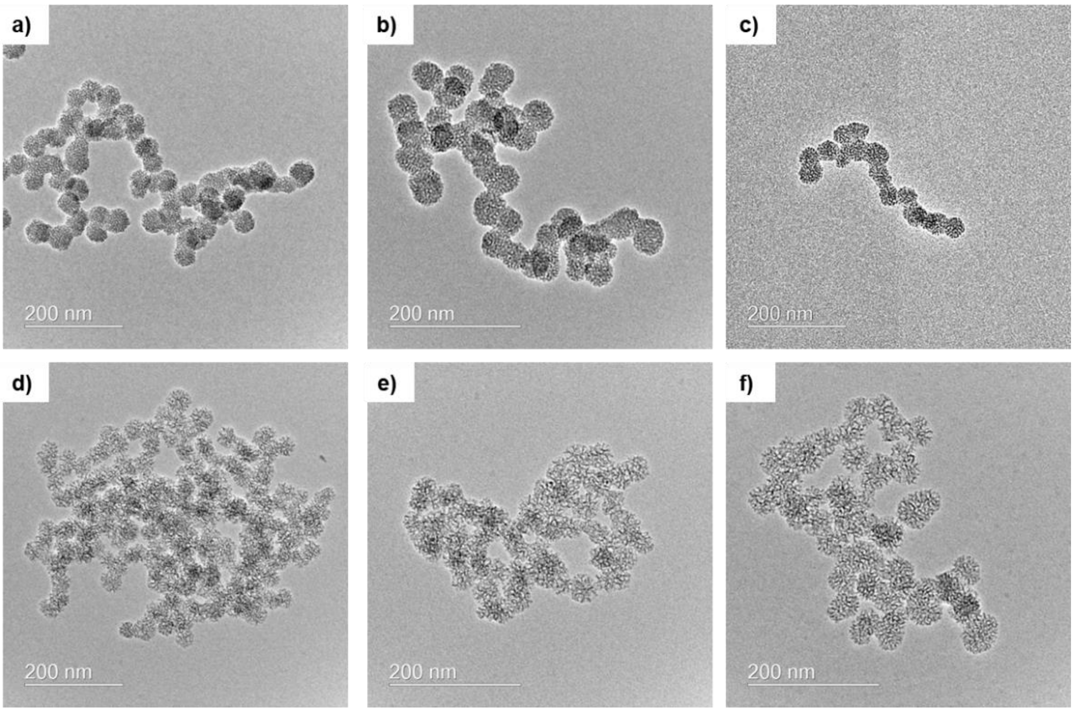

Figure 3. 4: TEM images of hydrophilic MSNs (upper row) showing a) HMSNs-NH_2@Gd^{3+}-DOTA, b) core HMSNs@Gd/Dox and c) core HMSNs@Gd/Sor; hydrophobic MSNs (lower row) with d) HPMSNs-NH_2@Gd^{3+}-DOTA, e) core HPMSNs@Gd/Dox and f) core HPMSNs@Gd/Sor.

DLS (Table 3. 4) revealed monodispersed negatively charged particles before and after drug loading of PdI less than 0.3 and z-potential in the range of -14.5 ± 1.0 to -23.9 ± 1.8. In addition, a small increase in size was observed after loading (to ~200 nm) which is reported to allow prolonged circulation, resisting excretion and enhancing cell internalisation.[30, 31]

Table 3. 4: Particle size, polydispersity index, and zeta potential measured by DLS and TEM.

Formulae	Particle size (D_{H})[a]* (nm)	Polydispersity index (PdI)[b]*	ζ-potential (mV)*	TEM size (nm)[c]
Core HPMSNs S2:1-NH$_2$	181.70 ± 15.6	0.2 ± 0.04	-19.4 ± 2.2	
Core HPMSNs S2:1@Gd^{3+}- DOTA	164.8 ± 9.6	0.2 ± 0.01	-14.5 ± 1.0	41.0 ± 6.3
Core HPMSNs S2:1@Gd/Dox	213.0 ± 3.7	0.2 ± 0.02	-20.1 ± 3.5	40.4 ± 4.3
Core HPMSNs S2:1@Gd/Sor	208.9 ± 3.4	0.2 ± 0.07	-20.2 ± 0.2	42.5 ± 5.3
Core HMSNs@Gd/Dox	221.8 ± 8.5	0.2 ± 0.03	-17.1 ± 3.1	44.3 ± 6.3
Core HMSNs@Gd/Sor	202.1 ± 8.1	0.2 ± 0.06	-23.9 ± 1.8	43.4 ± 4.9

[a] Hydrodynamic diameter extracted by cumulant analysis of the data.
[b] Polydispersity index from cumulant fitting.
[c] TEM particle size analysis of at least 100 nanoparticles using Image J.
* All values represent mean ± standard deviation (n=3).

3.4.2.1 Drug loading and release kinetics of MSNs@Gd/drug

To study the effect of the incorporation of Gd-chelate contrast agent into the pore channels on the drug loading capacity and entrapment efficacy (Equation 3. 1 and Equation 3.2) were determined. The DLC% and EE% of sorafenib into hydrophobic MSNs of medium pore size (HPMSNs S2:1@Gd/Sor, 22.1 and 21.2 %, respectively) were half in comparison with the hydrophilic nanoparticles with small pores (HMSNs@Gd/Sor, 46.3 and 44.7 %, respectively) as shown in Table 3. 5. The same pattern was observed in case of doxorubicin; however the loading capacity and entrapment efficiency of doxorubicin was only half that of sorafenib (24.2 and 11.4 %, in case of hydrophilic MSNs and 14.2 and 7.3 % in case of hydrophobic MSNs, respectively) (Table 3. 5). This pattern of hydrophilic particles demonstrating higher drug loading and entrapment efficiency can be explained as a result of the steric hindrance caused by the incorporation of phenyl groups as well as the presence of the Gd-chelate, which restrict the available space to accommodate the drug molecule into the hydrophobic MSNs pore channels, regardless of the nature of the drug. In addition, previous studies showed that the larger the surface area (smaller pore diameter), the higher the drug loading capacity, as is the case of the hydrophilic MSNs here.[32, 33]

Table 3. 5: The drug loading capacity and entrapment efficiency of both sorafenib and doxorubicin into different MSNs (n=3).

Formulae	DLC (%)	EE (%)
HMSNs@Gd/Sor	46.3 ± 2.0	44.7 ± 1.9
HPMSNs S2:1@Gd/Sor	22.1 ± 7.2	21.2 ± 6.9
HMSNs@Gd/Dox	24.2 ± 5.6	11.4 ± 2.6
HPMSNs S2:1@Gd/Dox	14.2 ± 4.0	7.3 ± 2.0

The drug loading was confirmed using TGA where a weight loss was recorded at the temperature range of 230-330 ˚C in the case of doxorubicin and 170-270 ˚C for sorafenib. This arises due to thermal degradation of the drug within the pores (Figure 3. 5). However, FTIR spectra (Figure 3. 6) could not confirm the drug loading, which may be as a result of the incorporation of the drug into the centre of the pores away from the pore edges or the low sensitivity of this technique. However, FTIR has confirmed the complete removal of the template surfactant by the absence of the C-H stretching vibration (2922 and 2855 cm^{-1}) and tertiary amine $RN(CH_3)_3^+$ vibrations (961 and 1472 cm^{-1}) of CTAB in all prepared mesoporous silica nanoparticles (Figure 3. 6), meaning that the pores were available for drug loading. As previously mentioned in Section 2.4.2.2.4, subsequent studies employing BET to confirm the complete removal of CTAB and to validate the impact of diverse pore sizes on drug loading will be necessary. Unfortunately, it should be noted that BET was not available for use in this context.

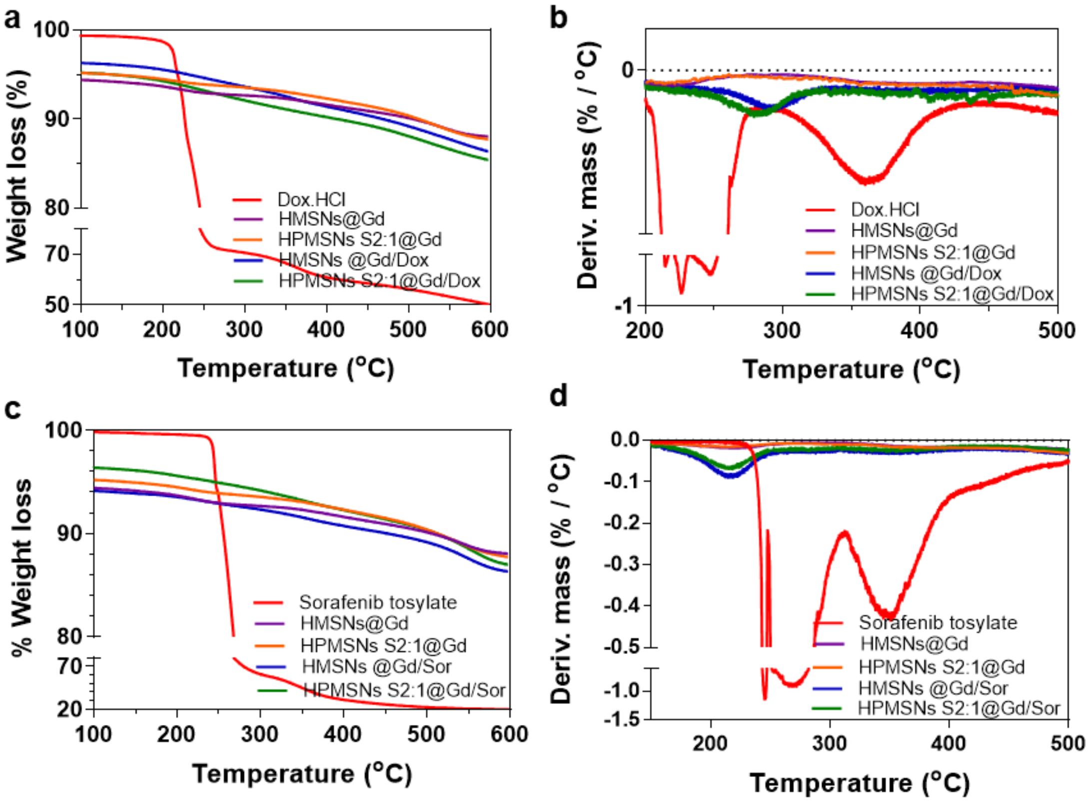

Figure 3. 5: TGA of hydrophilic (HMSNs@Gd) and hydrophobic MSNs (HPMSNs S2:1@Gd) with and without doxorubicin (as represented in a and b) or sorafenib tosylate (as represented in c and d).

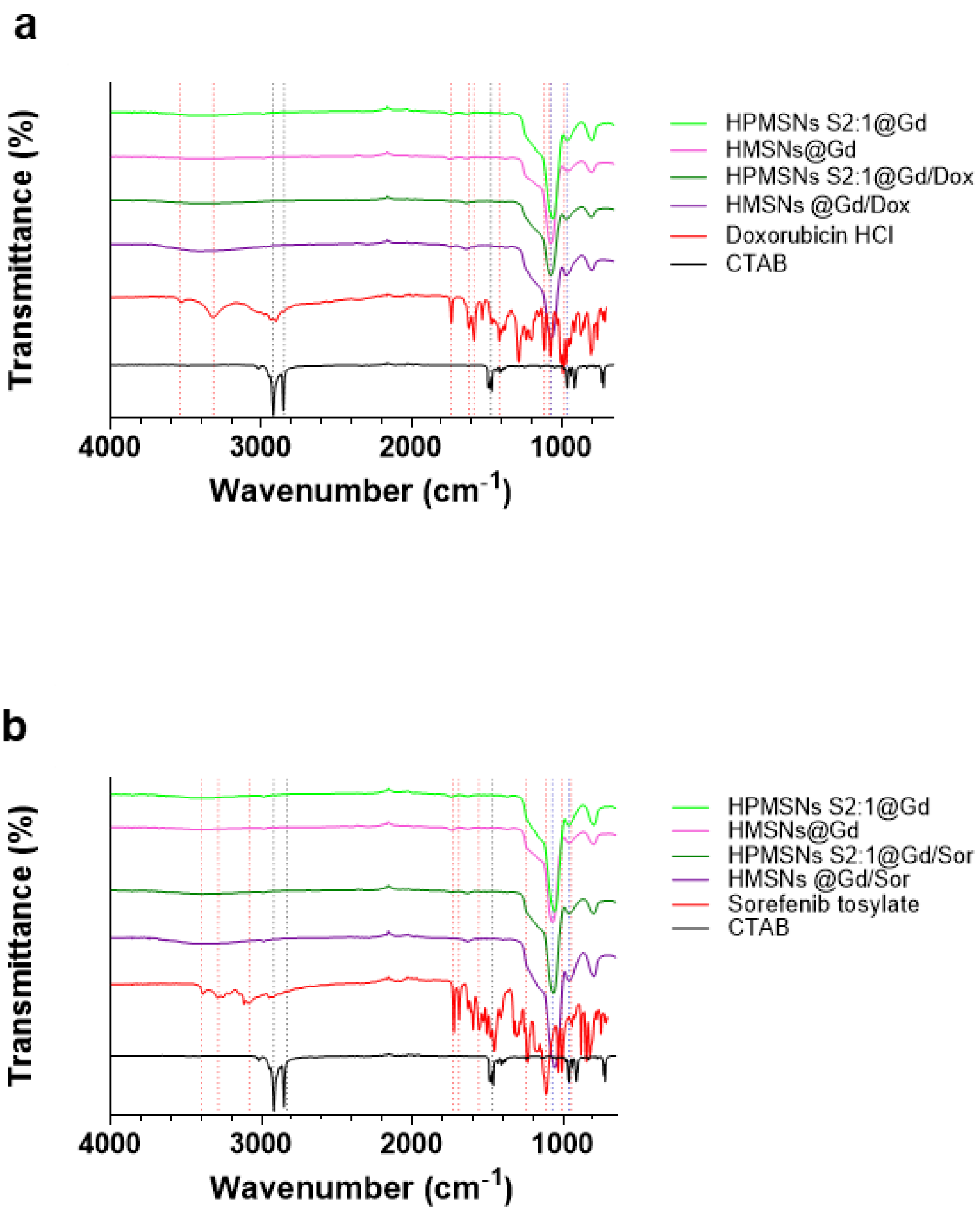

Figure 3. 6: FTIR spectra of hydrophilic and hydrophobic MSNs with or without the loaded drug (doxorubicin, represented in (a) and sorafenib represented in (b)). The dotted lines indicate the stretching vibrations of CTAB (black lines), silica (blue lines), and the drug (red lines).

X-ray diffraction analysis has provided confirmation of the amorphous form of both drugs within the pores of MSNs. The distinct peaks observed at 5–30° in the X-ray diffraction pattern of free Dox·HCl and Sor have disappeared in the case of drug-loaded silica. Instead, drug-loaded MSNs exhibited a broad peak at 25°, which is a characteristic feature for silica (Figure 3. 7).[34]

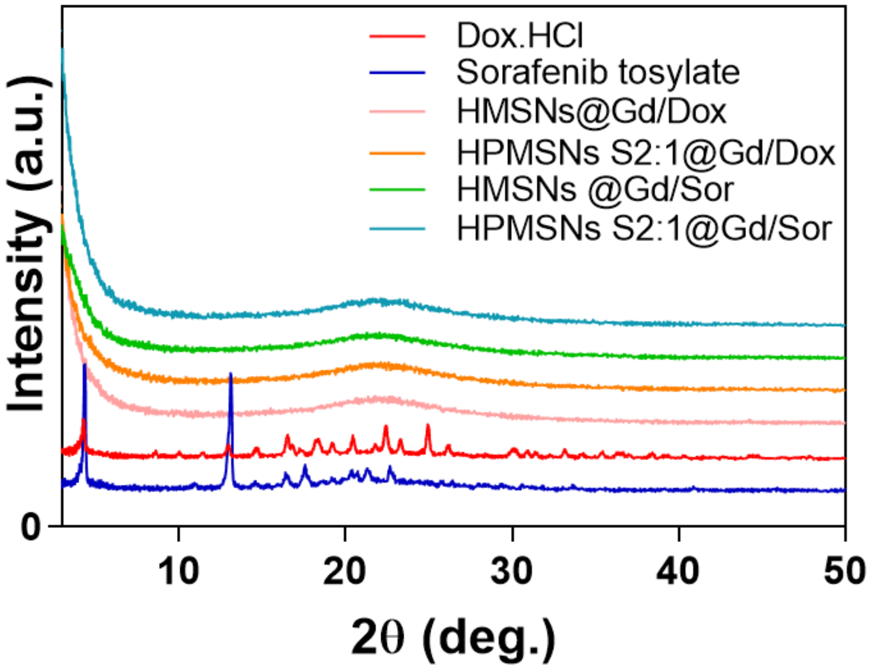

Figure 3. 7: X-ray diffraction patterns of hydrophilic and hydrophobic mesoporous silica nanoparticles with and without drug.

To study the pattern of the drug release, drug loaded MSNs were incubated at 37 °C and shaken at 200 rpm. Samples were collected at different time intervals and the amount of the drug released determined. Figure 3. 8 showed higher cumulative doxorubicin release (15%) in case of hydrophilic MSNs (HMSNs) in comparison with lower release (5%) seen in case of the hydrophobic MSNs (HPMSNs S2:1@Gd) after 24 hours (Figure 3. 8). The difference is attributed to both the difference in the drug loading capacity as well as restriction in the release process caused by the sterically hindered pores of HPMSNs due to the presence of both DOTA and phenyl groups.

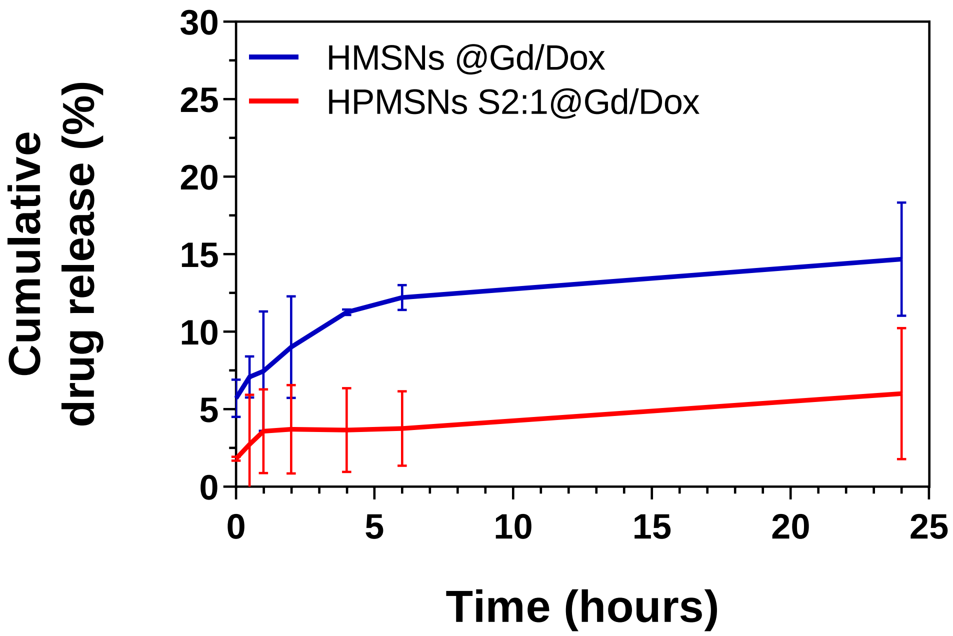

Figure 3. 8: Cumulative drug release profile of doxorubicin HCl from HMSNs@Gd and HPMSNs S2:1@Gd (n=3).

In the case of sorafenib, the overall drug release was lower than for Dox, but the drug release rate was higher with the hydrophobic MSNs (HPMSNs S2:1) than the hydrophilic ones (HMSNs). Although the difference in the release percentage was slight (range of 2-4%) in 24 hours (Figure 3. 9). This can be explained where larger pore sizes of these (hydrophobic HPMSNs S2:1) particles potentially facilitate improved diffusion of the dissolution medium into the mesopores and/or faster diffusion of the drug from the pores. However, the smaller pore size of the non-swollen hydrophilic HMSNs would restrict the diffusion of such a large molecule as sorafenib, thus aiding in controlled release.[35]

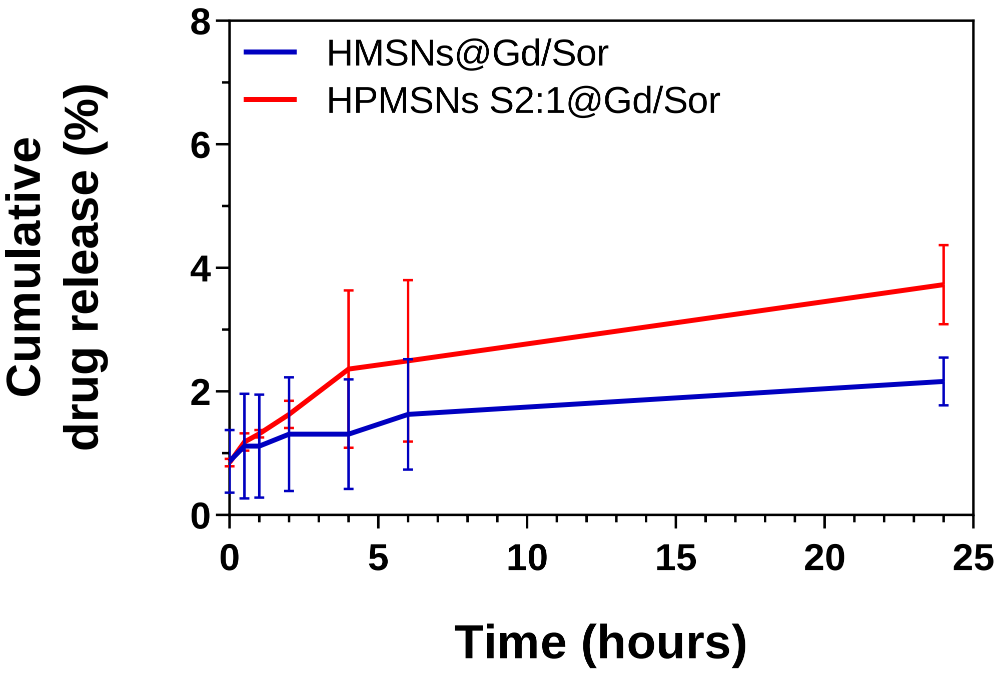

Figure 3. 9: Cumulative drug release profile of sorafenib tosylate from HMSNs@Gd and HPMSNs S2:1@Gd (n=3).

To understand the process and mechanism of drug release, we have employed two mathematical kinetic models, the Korsmeyer-Peppas and Weibull models. The Weibull model showed the best fit for HMSNs@Gd/Dox and HPMSNs S2:1@Gd/Sor, whereas the Korsmeyer-Peppas model demonstrated the best fitting for HPMSNs S2:1@Gd/Dox and HMSNs@Gd/Sor (as presented in Table 3. 6), the difference in R^2 between the two models was negligible, allowing us to use both models in evaluating the drug release mechanism (Figure 3. 10 and Table 3. 6).[36, 37]

Within the Weibull model, two parameters, namely α and β, were used to characterise the time dependence and shape of the drug release curve, respectively. The β parameter describes the shape of the curve as exponential (β = 1), sigmoid, S-shaped, (β > 1), or parabolic, with a higher initial slope followed by a consistent exponential trend (β < 1). In our observations, the latter case fits where β < 1. This release profile was associated with Fickian diffusion (Table 3. 6).[36, 38]

The Korsmeyer-Peppas model is well-suited to describe drug release from polymeric matrices or in cases where the release involves multiple kinetic mechanisms. To determine the transport mechanism of the drug, we estimated the exponent of diffusion (n) using the Korsmeyer-Peppas model, with n representing the fitting parameter, and k representing the rate constant. For spherical carriers as MSNs, distinct ranges of n indicated different release mechanisms: $n \leq 0.43$ suggested a consistent Fick diffusion mechanism, $0.43 < n < 0.89$ indicated a non- Fickian diffusion mechanism, and $n = 0.89$ signified a mechanism dominated by zero order release. In our case, $n \leq 0.43$ in all different formulations, suggesting Fickian diffusion (Table 3. 6).

The application of both Korsmeyer-Peppas and Weibull models offered valuable insights into the drug release processes from the different MSN formulations, shedding light on their underlying mechanisms and kinetics. The two mathematical models imply the drug release behaviour followed Fickian diffusion, described by Fick's laws, as suggested by diffusion occurring in the absence of boundaries and the release mechanism may be driven by two processes: first, the solvent diffuses into the pores of the mesoporous silica to dissolve the drug and second, the dissolved drug molecules diffuse out of the pore. The water diffusion is restricted in case of the hydrophobic MSNs which explains the low rate of doxorubicin release in case of HPMSNs S2:1@Gd/Dox, however in the case of sorafenib tosylate, the hydrophobicity of the pore channel as well as the steric hindrance enhance its solubility and hence the release as suggested before upon codelivery of doxorubicin in the presence of hydrophobic drugs into MSNs.[16, 39]

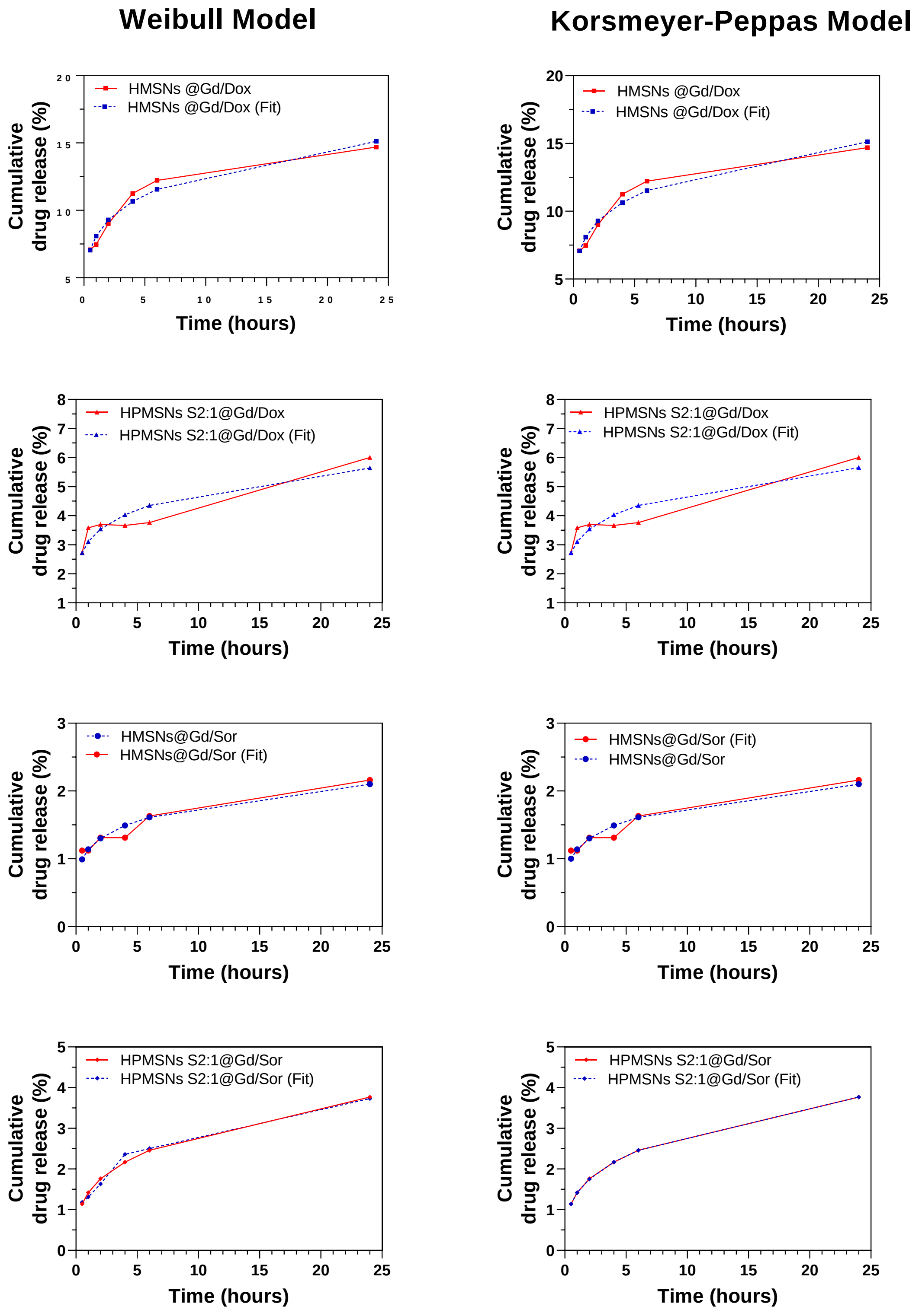

Figure 3. 10: Drug release data fitted to the Korsmeyer-Peppas and Weibull models.

Table 3. 6: Fitted kinetic parameters for the drug release from MSNs.

Formulae	**Weibull model**				**Korsmeyer-Peppas Model**			
	A	β	R^2	AIC	kKP	n	R^2	AIC
HMSNs @Gd/Dox	11.851	0.209	0.9668	6.2629	8.104	0.197	0.9651	6.5690
HPMSNs S2:1@Gd/Dox	31.726	0.192	0.8550	3.1615	3.102	0.189	0.8562	3.1109
HMSNs@Gd/Sor	87.393	0.195	0.9356	-13.8102	1.138	0.193	0.9359	-13.8390
HPMSNs S2:1@Gd/Sor	70.115	0.312	0.9855	-12.3017	1.417	0.308	0.9853	-12.2231

3.4.2.2 Relaxivity studies and MRI phantom imaging

To understand the effect of drug loading and release on the MRI signal, single-field relaxometry at 23 MHz (0.47 T) and fast-field cycling relaxometry in the range of (0.01-120 MHz) were studied using hydrophilic MSNs only to avoid any interference of the phenyl group of PhTMS with either the loaded drug or the paramagnetic centre.

In single-field relaxometry, drug-loaded MSNs with the same porosity and chemistry were dispersed in a release medium at 37 °C to isolate the drug release effect from other parameters influencing relaxivity (Figure 3. 11). Initially, doxorubicin-loaded MSNs exhibited the highest r_1 values compared to the parent MSNs which suggests an interaction between the Gd-DOTA chelate and the drug is affecting the local tumbling rate (τ_{RL}). The release of doxorubicin from MSNs was monitored over 24 hours by measuring r_1 values. A rapid decrease in relaxivity was observed during the first 2-4 hours, followed by a plateau. This release profile corresponds to the behaviour observed in Figure 3. 8, where the drug release rate was faster in the initial 4 hours, possibly restricting water access to Gd-chelate in the core of the channel. Once the release rate slowed down and reached a plateau, a constant water diffusion through the pores ensued, resulting in a steady MRI signal. On the other hand, sorafenib showed a steady decrease in r_1 values over the 24 hour period, indicating a lower percentage of drug released, as also shown in Figure 3. 9. This behaviour suggests a more sustained and controlled drug release from MSNs compared to the doxorubicin-loaded ones. The parent particles showed steady MRI relaxivities over 24 h, with all values within error of one another.

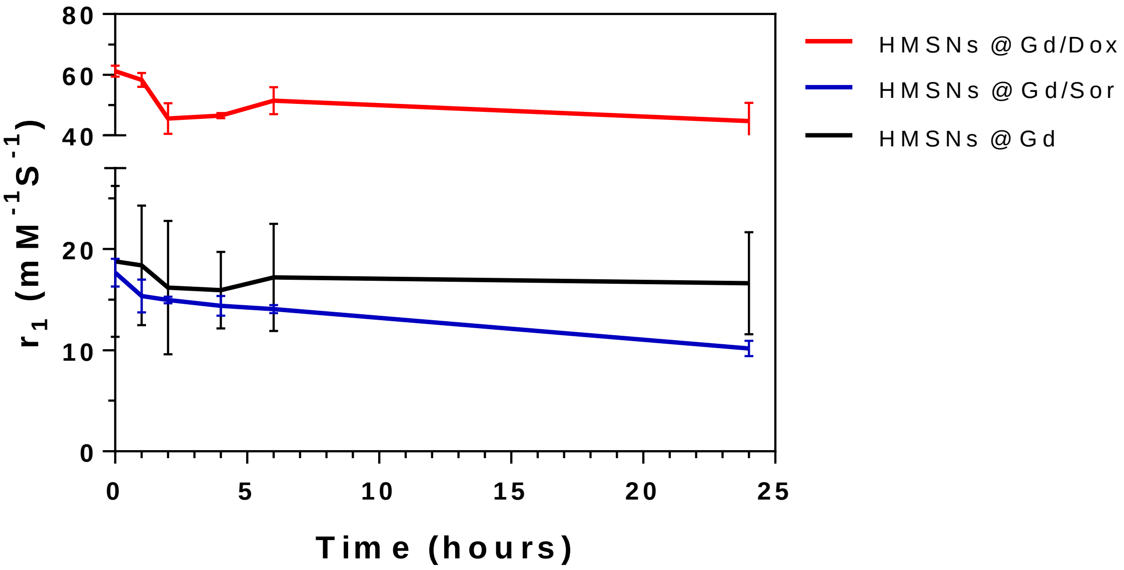

Figure 3. 11: ^{1}H r_1 relaxivity profiles of hydrophilic MSNs with/or without drug measured at 0.47 T and 37 ˚C. All values represent average ± standard deviation (n=3 independent syntheses).

Nuclear Magnetic Resonance Dispersion (NMRD) studies were conducted to gain deeper insights into the performance of drug loaded MSNs at different magnetic field strengths, ranging from 0.01 to 105 MHz at 25 and 37 °C in water. This investigation used fast-field cycling nuclear magnetic resonance (FFC-NMR), a technique that probes the magnetic environments of nanomaterials and their interactions with water. By measuring the rate of longitudinal relaxation, FFC-NMR generates NMRD plots, allowing us to study the behaviour of the contrast agent species and provide information about the major parameters impacting relaxation, such as τ_R, τ_M, etc. Typically, Gd-chelate loaded nanoparticles exhibit relaxivity peaks at high field strengths >10 MHz, followed by a dispersion plateau at low field strengths.[2, 40] This pattern is a characteristic feature of positive paramagnetic chelate-based contrast agents immobilised onto nanoparticles and has been observed in previous studies.[2, 40] The maximum of this peak is of much interest to us as it can be interpreted by local and global tumbling rate (τ_{RL} and τ_{RG}). The recorded NMRD profiles were evaluated by Prof. Mauro Botta and Dr. Fabio Carniato from the University of Eastern Piedmont.

In the case of hydrophilic MSNs (HMSNs), doxorubicin loaded nanoparticles showed a peak maxima of 14.8 $mM^{-1}s^{-1}$ at 22 MHz and 298 K while sorafenib tosylate showed a maxima of 23.2 $mM^{-1}s^{-1}$ at 42 MHz and 298 K (Figure 3. 12). The profiles for HMSNs@Gd/Sor are very typical for MSNs of this type. Shifting of the peak maximum to higher frequencies coupled with decreased r_1 values is typically indicative of higher mobility of the Gd-chelate species on the MSNs, which is not what is observed here for the doxorubicin-loaded particles, where the peak maximum shifts to lower frequencies, indicating lower mobility. This behaviour can be attributed to the effect of doxorubicin directly on the gadolinium-chelate motion inside the pore channel of MSNs. It is postulated that this decrease in mobility may be attributed to the interaction between the planar doxorubicin and DOTA may affect τ_{RL} as well as restricting the water diffusion. In addition, Figure 3. 12 showed the effect of temperature on longitudinal relaxation. Usually, increased temperature results in overall lower r_1 values across all field strengths. This is observed for HMSNs@Gd/Sor (20.8 $mM^{-1}s^{-1}$, 42 MHz), however a higher relaxivity was achieved for HMSNs@Gd/Dox at higher temperatures (18.8 $mM^{-1}s^{-1}$, 10 MHz). This can be explained by the lower drug release rate from hydrophilic silica in the case of the hydrophobic drug sorafenib, while the higher rate of doxorubicin release will allow the water diffusion and interaction with the paramagnetic Gd-chelate which supersedes the effect of heating on the water exchange rate.

In terms of the hydrophobic silica with medium pore size (HPMSNs S2:1), the same behaviour was observed as with hydrophilic silica. However, at 298 K, higher relaxivity values of both peak maxima of (18.8 $mM^{-1}s^{-1}$, 22 MHz) and (29.6 $mM^{-1}s^{-1}$, 52 MHz) for doxorubicin and sorafenib, respectively, were achieved. The increase in the relaxivity is attributed to the bigger pore size which allows a higher hydration layer and easy water access to the contrast agent (Figure 3. 12). At 318 K, a higher increase in r1 values compared to the hydrophilic HMSNs as a result of the additive drug release effect as well as the bigger pore sizes where HPMSNs@Gd/Sor showed (25.8 $mM^{-1}s^{-1}$, 42 MHz) while HPMSNs showed a relaxivity value of (24.6 $mM^{-1}s^{-1}$, 22 MHz).

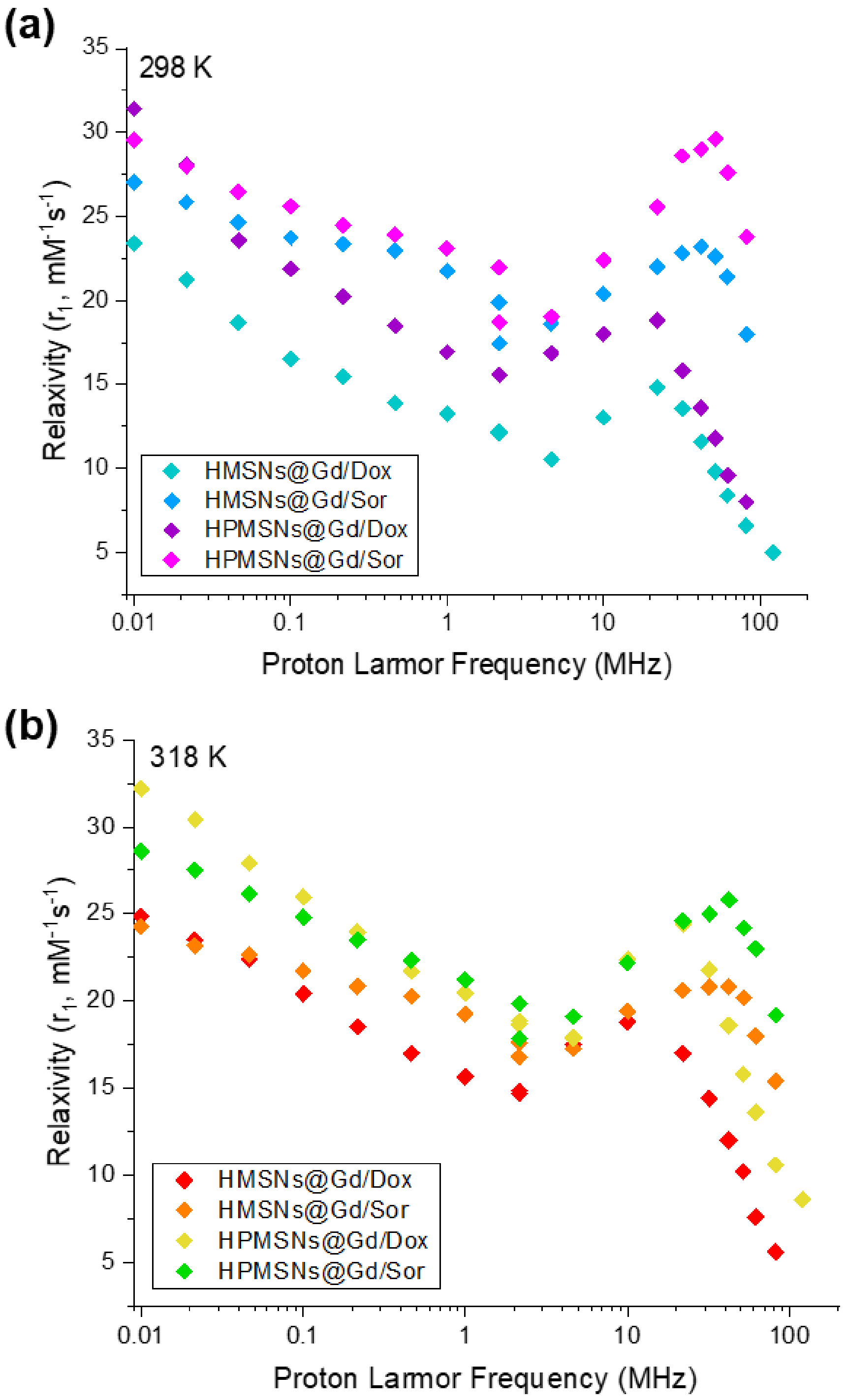

Figure 3. 12: ^{1}H NMRD profiles of HMSNs@Gd and HPMSNs@Gd with either Dox or Sor at 298 represented by (a) and 318 K represented by (b).

T_1 -weighted images were obtained using a volume coil with a 3-tesla MRI scanner. The T_1 relaxation times became longer upon heating, however parent samples without drug (HMSNs@Gd and HPMSNs S2:1@Gd) showed a shorter time, followed by sorafenib loaded samples, while doxorubicin loaded MSNs gave the longest relaxation time at all different temperatures as shown in Figure 3. 13 and Figure 3. 14. NMRD profiles at high field strength as shown in (Figure 3. 12) are similar to the obtained T1 weighed values, again suggesting the direct interaction of doxorubicin with Gd-chelate which affects the water access and decreases rotational correlation time of the Gd-chelate, resulting in decreased relaxivity.[41]

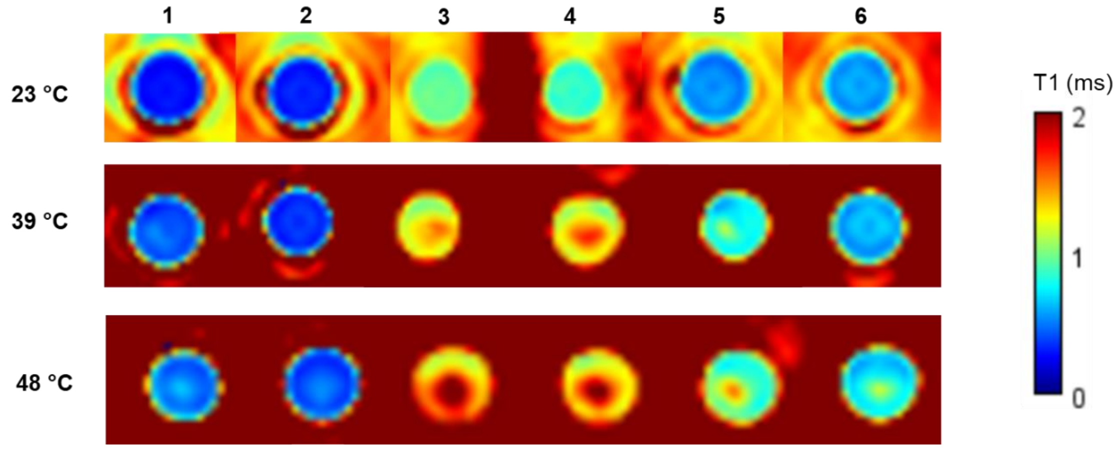

Figure 3. 13: T_1-weighed maps (0-2 ms scale) recorded at 3T and 23, 39 and 48 °C; where 1) HMSNs@Gd, 2) HPMSNs S2:1@Gd, 3) HMSNs@Gd/Dox, 4) HPMSNs S2:1@Gd@Dox, 5) HMSNs@Gd/Sor, and 6) HPMSNs S2:1@Gd/Sor.

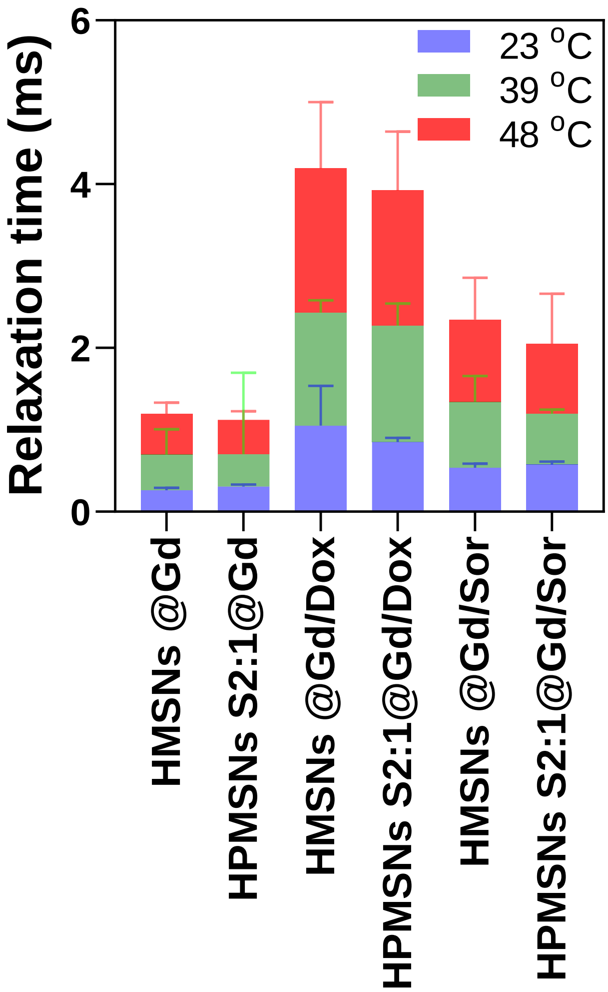

Figure 3. 14: T_1-weighed from phantom imaging recorded at 3T and 23, 39 and 48 °C.

3.5 Conclusions

In this chapter, we have undertaken a comprehensive investigation into various factors crucial for optimising a theranostic system. Among the factors explored, the location of the Gd-chelate within the porous channel of the silica nanoparticles, and the presence of the drug have emerged as particularly significant elements influencing the system's performance. Our findings clearly indicate that the precise location of the Gd-chelate within the nanoparticle's pore plays a pivotal role in the system's ability to act as an effective theranostic agent. Although this trend is slightly different to previously reported works,[15, 42] it is clear that our system differs due to different amounts of grafted

Gd, leading to the different behaviour observed. By strategically placing the Gd-chelate, we can enhance the contrast agent's interaction with the surrounding environment, leading to a more accurate and sensitive MRI signal. Moreover, our research has highlighted the interplay between the drug and the contrast agent in the theranostic system. The presence of the drug can modulate the MRI signal intensity at different field strengths, which can be harnessed to monitor the drug's distribution and assess the effectiveness of the treatment.

A key takeaway from our investigation is the importance of isolating and studying individual factors when examining their impact on the MRI signal intensity. To understand the effect of a particular factor, it is essential to keep other parameters fixed to ensure accurate and reliable results. Furthermore, the development of a theranostic system is a complex process that demands careful consideration of its potential effects on the MRI signal. Changes in the system, such as drug release, can introduce variability in the MRI signal, necessitating a thorough understanding of these alterations to accurately interpret imaging data. As we progress towards the subsequent chapters, we will continue to build upon these findings, seeking to further refine the theranostic system and enhance its potential applications in medical diagnostics and treatment monitoring.

3.6 References

1. P. Caravan, Chemical Society Reviews, 2006, **35**, 512-523.
2. F. Carniato, L. Tei, et al., European Journal of Inorganic Chemistry, 2018, **2018**, 4936-4954.
3. W. Zhang, J. A. Peters, et al., The Journal of Physical Chemistry C, 2015, **119**, 5080-5089.
4. T. D. Schladt, K. Schneider, et al., Dalton Transactions, 2011, **40**, 6315-6343.
5. A. J. Villaraza, A. Bumb, et al., Chem Rev, 2010, **110**, 2921-2959.
6. J. J. Davis, W.-Y. Huang, et al., Journal of Materials Chemistry, 2012, **22**, 22848-22850.
7. M. Vallet-Regi, A. Rámila, et al., Chemistry of Materials, 2001, **13**, 308-311.
8. Y. Chen, H. Chen, et al., Adv Mater, 2013, **25**, 3144-3176.
9. H. Skår, A. M. Bienfait, et al., Zeitschrift für anorganische und allgemeine Chemie, 2014, **640**, 604-615.
10. H. Skår, Y. Liang, et al., Microporous and Mesoporous Materials, 2013, **175**, 125-133.
11. F. Carniato, L. Tei, et al., Chemical Communications, 2009, DOI: 10.1039/B820591D, 1246-1248.
12. A. K. Duncan, P. J. Klemm, et al., J Am Chem Soc, 2012, **134**, 8046-8049.
13. F. Carniato, L. Tei, et al., Chemistry – A European Journal, 2010, **16**, 10727-10734.
14. W.-Y. Huang, G.-L. Davies, et al., Chemical Communications, 2013, **49**, 60-62.
15. F. Carniato, M. Muñoz-Úbeda, et al., Dalton Transactions, 2015, **44**, 17927-17931.
16. Q. Liu, J. Zhang, et al., International Journal of Nanomedicine, 2012, **7**, 999-1013.
17. M. K. Marwah, S. Shehzad, et al., Journal of Experimental Nanoscience, 2022, **17**, 197-213.

18. B. Brauner, C. Schuster, et al., ACS Omega, 2020, **5**, 9013-9022.
19. J. J. Davis, W. Y. Huang, et al., J Mater Chem, 2012, **22**, 22848-22850.
20. V. Cauda, A. Schlossbauer, et al., Journal of the American Chemical Society, 2009, **131**, 11361-11370.
21. S. Mourdikoudis, R. M. Pallares, et al., Nanoscale, 2018, **10**, 12871-12934.
22. K. N. Raymond and V. C. Pierre, Bioconjugate Chemistry, 2005, **16**, 3-8.
23. K. M. Taylor-Pashow, J. Della Rocca, et al., Nanomaterials (Basel), 2012, **2**, 1-14.
24. V. Jacques, S. Dumas, et al., Investigative Radiology, 2010, **45**.
25. R. M. Supkowski and W. D. Horrocks, Inorganic Chemistry, 1999, **38**, 5616-5619.
26. N. Kuźnik and M. M. Tomczyk, Beilstein Journal of Nanotechnology, 2016, **7**, 1086-1103.
27. J. Zhang, J. M. Rosenholm, et al., ChemPhysChem, 2012, **13**, 2016-2019.
28. R. Schmidt, M. Stöcker, et al., in Studies in Surface Science and Catalysis, eds. L. Bonneviot and S. Kaliaguine, Elsevier, 1995, vol. 97, pp. 149-156.
29. Z. Li, J. Guo, et al., Front Chem, 2022, **10**, 837032.
30. A. Panariti, G. Miserocchi, et al., Nanotechnol Sci Appl, 2012, **5**, 87-100.
31. P. Foroozandeh and A. A. Aziz, Nanoscale Research Letters, 2018, **13**, 339.
32. C. G. Bavnhøj, M. M. Knopp, et al., International Journal of Pharmaceutics: X, 2019, **1**, 100008.
33. J. Andersson, J. Rosenholm, et al., Chemistry of Materials, 2004, **16**, 4160-4167.
34. P. B. Sarawade, J.-K. Kim, et al., Journal of Hazardous Materials, 2010, **173**, 576-580.
35. A. K. Meka, A. Gopalakrishna, et al., Molecular Pharmaceutics, 2023, **20**, 2966-2977.
36. F. Langenbucher, J Pharm Pharmacol, 1972, **24**, 979-981.

37. R. W. Korsmeyer, R. Gurny, et al., International Journal of Pharmaceutics, 1983, **15**, 25-35.
38. N. Vilaça, A. F. Machado, et al., RSC advances, 2017, **7**, 13104-13111.
39. L. Ahmed, R. Atif, et al., 2019, **8**, 52-56.
40. C. J. Meledandri and D. F. Brougham, Analytical Methods, 2012, **4**, 331-341.
41. J. Zhu, Z. Xiong, et al., RSC Advances, 2015, **5**, 30286-30296.
42. K. He, J. Li, et al., Journal of Materials Chemistry B, 2019, **7**, 6840-6854.

3.7 Supplementary information

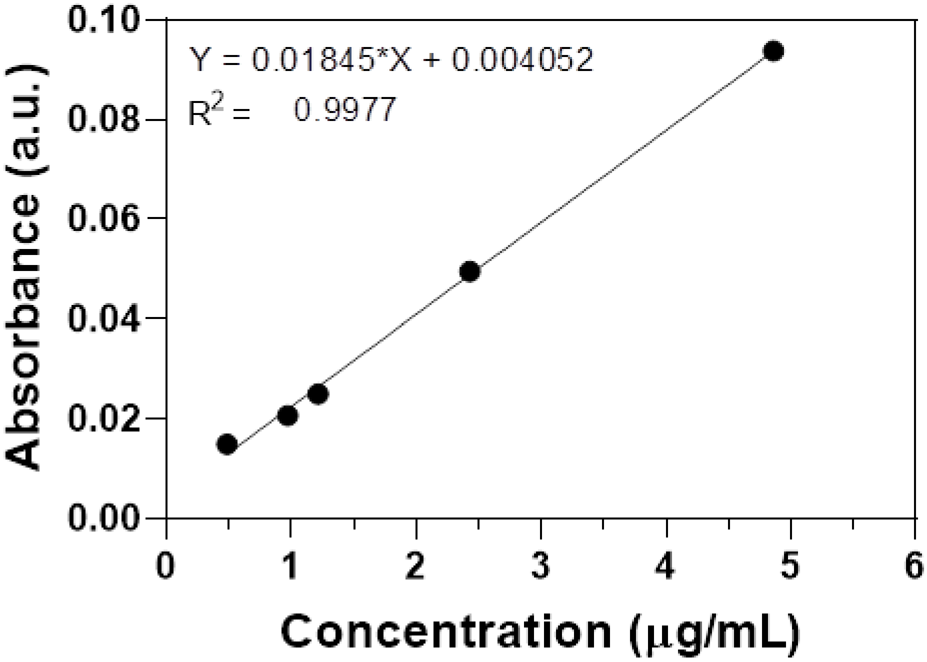

Figure S3. 1: Calibration curve of doxorubicin HCl using UV/Vis at 480 nm in PBS 7.4 release medium. (n=3)

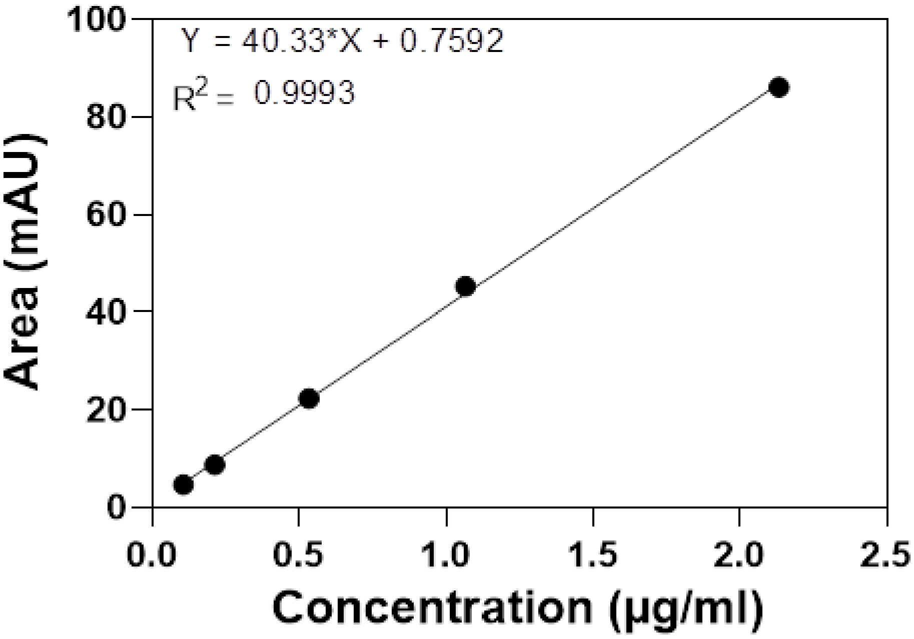

Figure S3. 2: Calibration curve of sorafenib tosylate using HPLC at 264 nm in PBS 7.4 with 1 % w/w tween 80 release medium. (n=3)

Chapter 4.

Development of thermo-responsive UCST and LCST polymers

4.1 Introduction

Conventional cancer therapy suffers from undesirable toxic side effects, highlighting the necessity for the development of localised, controlled-release, drug delivery systems. One promising approach involves the utilisation of a responsive system that reacts to either internal or external stimuli.[1] Among these, temperature emerges as a straightforward trigger that can be harnessed either through the elevated temperature inherent to tumour tissues or externally through the application of mild to moderate hyperthermia (ranging from 39 to 45 °C).[2] Hence, the development of thermo-responsive polymers holds significant promise for controlled drug release. These polymers have the ability to undergo a conformational change, transitioning from a soluble coil state to an insoluble globular form, at a specific temperature known as the "cloud point" or "transition point". This characteristic has garnered immense interest for its potential in biomedical applications.[1, 2]

There are two main types of thermo-responsive polymers. The first present a lower critical solution temperature (LCST), while the second possess an upper critical solution temperature (UCST), as shown in Figure 4.1.[1-3] Among the former, the polymer polyisopropylacrylamide (PNIPAm) has LCST at approximately 32 °C.[2] Since its discovery in 1968, PNIPAm has been extensively investigated for numerous applications, particularly in the biomedical field.[4]

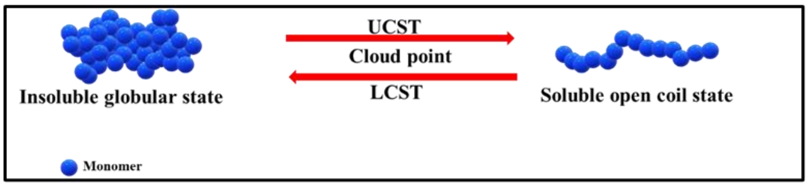

Figure 4. 1: Schematic representation of the conformational changes of thermo-responsive polymers at UCST and LCST.

A number of studies have explored the grafting of PNIPAm and related polymers onto mesoporous silica nanoparticles (MSNs) to control the drug release. For instance, Chen *et al.* introduced a novel approach, covalently functionalising silica nanoparticles with PNIPAm *via* reversible addition-fragmentation chain transfer before grafting it to the surface of MSNs using click chemistry.[5] The LCST responsive behaviour of the PNIPAm polymer layer, triggered by changes in temperature, serves as a switch to precisely control the release of cargo from MSNs. In addition, Tang and co-workers demonstrated the grafting of poly(N-isopropylacrylamide-co-N-hydroxymethyl acrylamide) (P(NIPAm-co-NHMA)) onto gold nanorod@mesoporous silica structures to enable precise doxorubicin release.[6] Guisasola *et al*., on the other hand, developed thermo-sensitive P(NIPAM-co-NHMA) polymer coated magnetic mesoporous silica, harnessing magnetic fields to trigger drug release at temperatures of 43 °C.[7]

UCST polymers are less widely investigated despite their thermo-responsive behaviour being perhaps more intuitive for biomedical applications, as they are fully soluble above the UCST and insoluble below it, rendering them a useful capping agent below the responsive temperature.[8] In 2013, Roy *et al.* compiled a review on thermo-responsive polymers, highlighting 57 LCST polymers and merely 5 UCST polymers.[9] Despite the publication of over 5000 papers concerning LCST polymers, the emergence of research on UCST polymers has lagged behind, with just over 1000 papers by 2020.[10]

A primary challenge in exploring UCST polymers stems from the difficulty of fine-tuning their UCST to align with specific applications. This tuning process is significantly influenced by a range of factors that intricately impact intermolecular and intramolecular hydrogen bonding, such as polymer chain length, hydrophilic-hydrophobic balance, concentration, and others.[8, 11]

An illustrative example of a non-ionic UCST polymer is poly(acrylamide-co-acrylonitrile) (poly(AAm-co-AN)), which exhibits reversible hydrogen bonding between copolymer chains below the UCST and with surrounding water above it.[11] Numerous endeavours have been made to tailor the UCST of poly(AAm-co-AN). For instance, Zhang *et al.* investigated the UCST under various pH conditions, revealing only a slight change in UCST of approximately 2 °C over pH 3 to 10.[12] Another study by Zhao involved the creation of three distinct block copolymers by coupling poly(AAm-co-AN) with hydrophobic polystyrene or hydrophilic poly(dimethyl acrylamide) or poly(N,N-dimethylaminoethylmethacrylate). These variations led to phase transitions occurring at temperatures of 48 °C, 14 °C, and 20 ˚C, respectively.[13] Furthermore, investigations into altering the acrylonitrile content in poly(AAm-co-AN) resulted in its UCST ranging from 5.5 °C to 56.5 ˚C.[14]

Only a limited number of studies have explored the development of UCST-grafted mesoporous silica nanoparticles.[15, 16] For example, Hei and colleagues developed three UCST-type polymers, namely TRP1, TRP2, and TRP3, by copolymerising acrylamide and acrylonitrile in varying ratios.[16] These polymers exhibited cloud points at 32 °C, 42 °C, and 50 °C, respectively. They then created a dual-responsive delivery system by grafting TRP2 onto the surface of mesoporous silica nanoparticles (MSN-TRP2) using disulfide bonds. This delivery system demonstrated controlled and extended release of hydrophobic drugs, responding to temperature changes and reducing agents. Loading the system with Dox enabled intracellular delivery and cargo release upon temperature changes and exposure to reducing agents. In another study by Hu *et al.*, a near infrared -responsive drug delivery system was developed by grafting UCST poly(N-acryloyl glycinamide-co-N-phenylacrylamide) onto hollow mesoporous silica nanoparticles (HMSNs) using the photothermal conversion agent indocyanine green (ICG). Under normal conditions (37 °C), the grafted UCST polymers acted as gatekeepers, blocking drug release. When exposed to NIR irradiation, UCST chains become well-hydrated, allowing drug release from the HMSNs' mesoporous channels. The system demonstrated excellent cytocompatibility, effective cell uptake, and burst drug release in response to NIR irradiation.[15]

In addition to free polymer chains in solution, an alternative structures known as star-shaped and amphiphilic polymers, each possessing distinctive properties are designed to act as thermos-responsive polymers. Star polymers are formed by covalently anchoring at least three polymer chains around a core, restricting chain mobility and exhibiting thermos-responsive characteristics.[17, 18] The arms of the star polymer interact with the solvent, leading to thermo-induced swelling. Combining thermos-responsive and nonresponsive polymers enables the modulation of the star polymer's corona, resulting in intermolecular micellisation.[19] In contrast to free polymer chains, star polymers display enhanced segmental density, resembling the hard sphere model, and exhibit unique physicochemical properties such as low viscosity, high density of polymer segments, and a smaller hydrodynamic radius with a larger diffusion coefficient.[20]

Moreover, the amphiphilic copolymers, composed of hydrophilic and hydrophobic units, spontaneously form micelle structures through self-assembly above a critical concentration.[21, 22] When corona blocks are large compared to core-forming blocks, these structures typically adopt a star-shaped configuration, composed of multiple individual chains held together by noncovalent interchain interactions. In polar solvents like water, the hydrophobic block forms an anhydrous core, while the hydrophilic chains extend into the solvent in the form of a swollen corona. Micelle size, shape, and dynamics can be fine-tuned by adjusting the absolute length of the block copolymer and the relative length of the blocks, as well as the glass transition temperature. Introduction of a thermos-responsive polymer block allows for alterations in amphiphilic character and self-assembly behaviour based on temperature changes, resulting in a reversible switching of the micelle's structure and shape.[20]

For example, Fazlalizadeh et al. have designed a smart anti-cancer drug delivery system using a thermal-responsive star-shaped amphiphilic block copolymer known as poly(N-isopropylacrylamide-block-[poly(ε-caprolactone)]$_2$ (PNIPAAm-b-PCL$_2$).[23] The synthesised PNIPAAm-b-PCL$_2$ exhibits a lower critical solution temperature in the range of 39–41°C. The drug

delivery system demonstrates promising loading and encapsulation capacities for doxorubicin hydrochloride, measured at 62 ± 3% and 75 ± 4%, respectively. Moreover, the drug release profile reveals values of up to 46.5% over 40 hours at 37°C, and a higher release of up to 88% at 40°C, highlighting its potential as an effective drug delivery platform.[23]

This chapter focuses on an in-depth study of free polymers, specifically poly(AAm-co-AN) and PNIPAm. These polymers were chosen for their suitability for grafting onto the surface of MSNs and the abundance of existing literature data to address and overcome any challenges associated with these polymers and design comprehensive responsive nanocarriers.

4.2 Aims

The primary objective of this thesis chapter is to design and fabricate thermo-responsive polymers, specifically poly(AAm-co-AN) and PNIPAm. These polymers are intended to exhibit a transition in response to the elevated temperatures characteristic of hepatocellular carcinoma tissues or hyperthermia treatment (38-45 ^{o}C).

The main challenge in this pursuit involves precisely tuning the UCST of poly(AAm-co-AN) within a temperature range suitable for the intended application. This necessitates a thorough exploration of polymer synthesis strategy, including applying free radical and RAFT polymerisation techniques. Additionally, it involves the application of Design of Experiments (DoE), optimising variables such as monomer ratios and polymerisation time, aiming to create a homogeneous polymer with an ideal transition temperature. This also includes the design of a polymer with a readily graftable end group for effective attachment to MSN surfaces.

Similarly, for the LCST PNIPAm polymer, the objective is to generate a polymer with excellent homogeneity tuned cloud point, and appropriate end groups that facilitate straightforward grafting onto the external surface of MSNs. To achieve this, a range of PNIPAm-NHS ester derivatives of different degrees of polymerisation has been synthesised.

To validate the thermo-responsive behaviour of both polymers, turbidimetry and dynamic light scattering techniques will be employed as well as gel permeation chromatography (GPC) to evaluate the polymer homogeneity. In this chapter, a range of well characterised UCST and LCST polymers will be presented. These polymers will feature suitable end groups and precisely adjusted cloud points, specifically designed for grafting onto MSNs. This grafting is intended for applications involving gating, controlled release, and MRI signal alterations (Chapter 5).

4.3 Experimental

4.3.1 Materials

All chemicals were used as received without further modification. Acrylonitrile (AN), acrylamide (Aam), 3-mercaptopropionic acid, azobisisobutyronitrile (AIBN),1,3,5-trimethylbenzene4-cyano-4-[(dodecylsulfanyl-thiocarbonyl) sulfanyl]pentanoic acid, N-Isopropylacrylamide (NIPAm), 2,2'-azobis(2-methylpropionitrile) (ACVA), and1,4-dioxane were purchased from Fisher Scientific or Sigma-Aldrich, UK. N-hydroxysuccinimide ester of 2-propanoic acid butyl trithiocarbonate (PABTC-NHS) was prepared previously by Dr. Pratik Gurnani. All other chemicals and solvents were as described in Chapter 2, Section 2.3.1.

4.3.2 Methodology

4.3.2.1 Synthesis of UCST polymer by free radical polymerisation

In order to prepare UCST poly(AAm-co-AN), acrylamide and acrylonitrile monomers were polymerised *via* the free radical method where monomers were dissolved in 50 mL DMSO at different ratios as shown in Table 4. 1, before adding the reaction initiator azobisisobutyronitrile (AIBN).[24] The reaction mixture was stirred and purged with nitrogen for at least 30 minutes before heating at 60 ^oC. After one or two hours, a N_2 purged solution of 3-mercaptopropionic acid (35 µl) in DMSO (1 mL) was added and the reaction was stopped after a varied period (3, 3.5, and 4 hours) by cooling in an ice bath and opening the flask to air (Figure 4. 2, Table 4. 1). The polymer was precipitated using excess cold methanol (500 mL) before separation by filtration under vacuum through 80 µm filters and washing using methanol. To remove any DMSO traces, the polymer was suspended again in methanol and washed 3 times using centrifugation at 8000 rpm for 10 minutes. Finally, the product, obtained by filtration of the resuspended polymer in methanol, was dried using a rotary evaporator under vacuum at 70 ^{o}C for 2 hours. ^{1}H (700 MHz, DMSO-d6, 25 °C): δ = 6.7, 2.3-3.1, 2.0-2.7, 1.2-2 ppm.

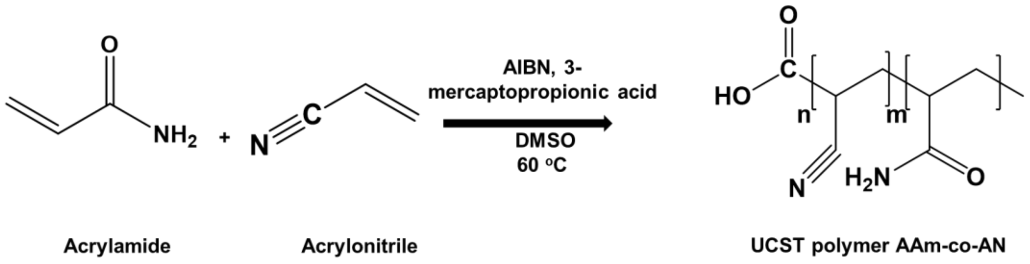

Figure 4. 2: Free radical polymerisation of acrylamide and acrylonitrile under nitrogen at 60 ^{o}C to produce the UCST poly(AAm-co-AN) polymer.

Table 4. 1 Free radical polymerisation of AAm and AN with 3-mercaptopropionic acid and AIBN as initiator.

Chemicals/reaction conditions	**UP1-F**	**UP2-F**	**UP3-F**	**UP4-F**	**UP5-F**
Acrylamide (AAm) (mmol)	40.5	40.5	40.5	40.5	40.5
Acrylonitrile (AN) (mmol)	9.5	9.5	9.5	9.5	10
AIBN (mmol)	0.24	0.24	0.24	0.24	0.24
3-mercaptopropionic acid (mmol)	0.4	0.4	0.4	0.4	0.4
Total polymerisation time (hours)	4	3	3	3.5	3
3-mercaptopropionic acid addition (hours)	2	1	2	1	1

4.3.2.2 Synthesis of UCST polymer by reversible addition−fragmentation chain-transfer polymerisation

Poly(AAm-co-AN) was prepared *via* RAFT polymerisation following a previously published method.[14] In brief, different molar ratios (see Table 4. 2) of acrylamide and acrylonitrile (total amount 74 mmol) were dissolved in DMSO (25 mL) before adding a constant number of moles of both AIBN and 4-cyano-4-[(dodecylsulfanyl- thiocarbonyl)sulfanyl]pentanoic acid (RAFT agent) (see Table 4. 2). After 30 minutes of N_2 purging, the mixture was heated at 65 ˚C for 16 hours; after this time, the reaction was stopped by opening the flask to air and cooling in an ice bath (Figure 4. 3, Table 4. 2). The polymer was obtained through precipitation in cold methanol (300 mL) followed by filtration through 80 µm filters under vacuum. For purification, the obtained product was dissolved in 100 mL ultrapure water at 70 ºC and dialysed against water overnight at 65 ºC (MWCO 3500). Finally, the product was dried using freeze-drier for 48 hours. ^{1}H (700 MHz, DMSO-d6, 25 °C): δ = 6.9, 2.3-3.0, 2.0-2.6, 1.29-1.9 ppm.

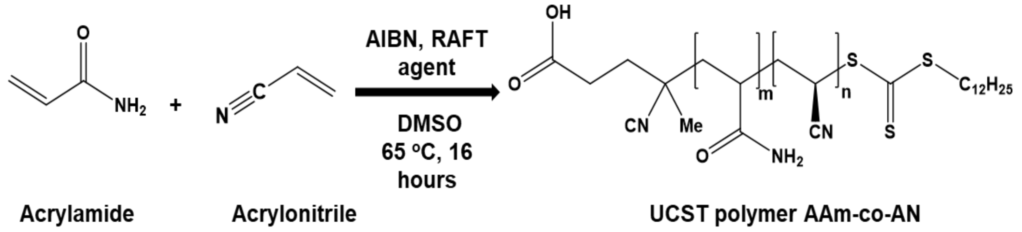

Figure 4. 3: RAFT polymerisation of acrylamide and acrylonitrile to produce poly(AAm-co-AN) under nitrogen at 65 ºC using 4-cyano-4- [(dodecylsulfanyl- thiocarbonyl) sulfanyl] pentanoic acid as RAFT agent and AIBN as initiator.

Table 4. 2: RAFT polymerisation of acrylamide and acrylonitrile.

Chemicals (mmol)	UPL1-R	UPL2-R	UPL3-R
Acrylamide	60	56	51
Acrylonitrile	14	18	23
AIBN	0.02	0.02	0.02
RAFT agent	0.15	0.15	0.15

4.3.2.3 Modified RAFT synthesis of UCST polymer using Design of Experiments (DoE)

A response surface design employing a two-factor Central Composite Design (CCD) was applied using JMP® Pro software (version 17.0.0) to optimise the synthesis of poly(AAm-co-AN) through RAFT polymerisation. The same procedure as in Section 4.3.2.2 was used for synthesis, where the two independent variables included the monomer molar ratio (1:1, 1.5:1 and 2:1 AAm: AN) and the polymerisation time (16, 20 and 24 hours). The same amounts of both AIBN and RAFT agent were maintained in the different runs (Table 4. 3). The two response dependent variables, cloud point and molecular weight, were evaluated in a total of nine experiments generated by the CCD where one centre, 4 axial and 4 factorial points were carried out in randomised order.

Following the completion and characterisation of the experimental runs, regression analysis was carried out for each of the response variables. To determine the fitting extent of experimental data, the regression coefficient R^2 along with predicted and adjusted R^2 were determined. Analysis of Variance (ANOVA) was performed, and the P-value with 95% confidence interval was evaluated to determine the significance of the independent variables' effects. In order to visualise the interaction effects of the variables on the responses, three-dimensional response surface plots were prepared.

The response surface behaviour was assessed using a polynomial model as represented in Equation 4. 1:

$$\mathrm{Y_i} = \beta_0 + \beta_1 A + \beta_2 B + \beta_3 AB + \beta_4 A^2 + \beta_5 B^2$$

Equation 4. 1

Where, Y_i represents the predicted response, β_0 is a constant, and β_1 to β_2 are estimated coefficients for the corresponding factors A and B.

Table 4. 3: Randomised Response Surface design of (poly (AAm-co-AN)) by RAFT.[*]

Code	**AAm (mmol)**	**AN (mmol)**	**Experimental independent variables**		**Response dependent variables**	
			AAm:AN (molar ratio)	**Time (hours)**	**Cloud point (ºC)**	**Molecular weight [**] (g/mol)**
UP1-R	44.4	29.6	1.5:1	24	36.5	120500
UP2-R	44.4	29.6	1.5:1	16	39.8	100300
UP3-R	49.33	24.7	2:1	16	31.7	85600
UP4-R	44.4	29.6	1.5:1	20	37.3	84600
UP5-R	49.33	24.7	2:1	20	37	121100
UP6-R	37	37	1:1	24	27.5	125300
UP7-R	37	37	1:1	20	30.6	122300
UP8-R	49.33	24.7	2:1	24	32.9	164100
UP9-R	37	37	1:1	16	30.5	134300

[*] All runs have same amount of AIBN (0.02 mmol) and RAFT agent (0.15 mmol)

[**] The molecular weight values were evaluated using GPC performed by Dr. Pratik Gurnani, School of Pharmacy, University of Nottingham following the method in section 4.3.2.5.

4.3.2.4 Synthesis of LCST polymer by RAFT polymerisation

Three poly(N-isopropylacrylamide) N-hydroxysuccinimide ester (PNIPAm-NHS ester) samples with different degrees of polymerisation (DP, the average number of monomer units, 10, 120, and 400) were prepared under identical conditions. For instance, the synthesis of PNIPAm with a DP of 10 proceeded as follows: NIPAm (0.5 g), the RAFT agent or chain transfer agent N-hydroxysuccinimide ester of 2-propanoic acid butyl trithiocarbonate (PABTC-NHS, 148 mg), and the initiator 2,2'-azobis(2-methylpropionitrile) (ACVA, 2.06 mg or 413 µL from a 5 mg/mL stock solution in 1,4-dioxane), were dissolved in 1.06 mL of 1,4-dioxane (Figure 4. 4). The solution was then stirred and deoxygenated by purging it with argon gas for 10 minutes. Subsequently, the solution was immersed in a pre-heated oil bath at 70 °C for 4 hours. After completion of the polymerisation, the system was exposed to air and cooled down. The resulting polymers were isolated by precipitating them twice in diethyl ether from 1,4-dioxane. Detailed information on reaction parameters is provided in Table 4. 4. The same set of procedures was followed for synthesising PNIPAm with DPs of 120 and 400. ^{1}H (700 MHz, DMSO-d6, 25 °C): δ = 7.2, 3.8, 1.9, 1.47, 1.03 ppm.[25] These polymers were synthesised by Dr. Pratik Gurnani.

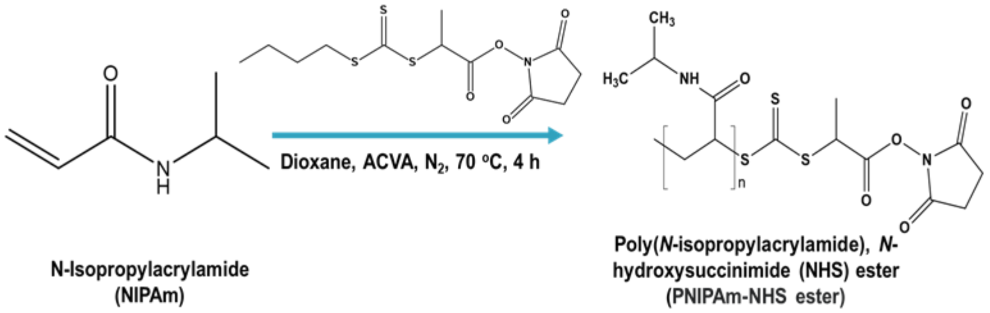

Figure 4. 4: PNIPAm-NHS ester synthesis scheme by RAFT polymerisation (polymers were provided by Dr. Pratik Gurnani, School of Pharmacy, University of Nottingham).

Table 4. 4: List of synthesised PNIPAm-NHS ester samples.

Sample	NIPAm/g	PABTC-NHS/ g*	ACVA/ mg	Dioxane / mL	PABTC-NHS / ACVA
PNIPAm-001	0.5	0.148	2.06	1.06	60
PNIPAm-002	3	0.074	6.2	8.5	10
PNIPAm-003	5	0.037	6.2	13.5	3

*PABTC-NHS was synthesised according to previously published protocol.[26-28]

4.3.2.5 Physicochemical characterisation

Several techniques have been applied to characterise the prepared polymers. Fourier-transform infrared spectroscopy (FTIR) spectra were collected on a Shimadzu IRTracer-100 spectrometer operated by LabSolutions IR (version 2.10). ^{1}H NMR (700 MHz) spectra in d6-DMSO were recorded at room temperature on a Bruker Avance Neo 700.

The cloud point of the polymer was determined in water or phosphate buffered saline (PBS, pH = 7.4) using turbidimetry as well as dynamic light scattering (DLS). Turbidimetry analysis was carried out using an Agilent Cary 60 UV-Vis Spectrophotometer equipped with Quantum Pro unit for temperature control. Transmittance was measured in the temperature range of 10-70 ˚C, with 0.1 ˚C temperature intervals and a 2 ˚C/min heating/cooling rate, at 670 nm. Experiments were performed using 10 mg/mL of poly(AAm-co-AN) prepared by free radical polymerisation or 25 mg/mL of poly(AAm-co-AN) prepared *via* literature-based RAFT polymerisation. The same conditions were used except for measurement at 500 nm for PNIPAm-NHS ester (10 mg/mL). The data were analysed using the Cary WinUV ADL Shell Application software (version 5.0.0.1008).

For the DoE experiment, the turbidity of the polymers was read over the range 25-45 ºC at 670 nm. Here, a 24 well plate was employed for measurements (each well containing 1 mL of aqueous polymeric solution of 10 mg/mL), which were collected using a SpectraMax M2e microplate reader (Molecular Devices). To ensure the reproducibility of the cloud point, at least two cycles of cooling and heating in water or PBS were undertaken.

Hydrodynamic size and size distribution were also determined by dynamic light scattering (DLS) at varied temperature of 20-60 ˚C with 0.5 ˚C temperature interval using a Malvern Zetasizer Nano ZS instrument equipped with a He-Ne laser (λ= 632.8 nm) at 173˚ scattering angle. The data was analysed using Zetasizer software (version 7.12).

Gel permeation chromatography (GPC) was performed by Dr. Pratik Gurnani using a Polymer Labs PL50+ system equipped with a differential RI detector and autosampler. This instrument used Agilent Plgel mixed-D (300 x 7.5 mm) + Plgel (5 mm) guard columns. For LCST PNIPAm-NHS ester, DMF containing 0.1% w/v lithium bromide was used as the mobile phase, with a flow rate of 1 mL/min at 50 ºC. For the UCST polymers a DMSO mobile phase was used with the same flow rate at 50 ºC. Calibration was performed using polymethylmethacrylate (PMMA) standards (Agilent EasyVials) between 2,220,000 – 700 g/mol. Measurements were performed using 100 µL injection volume. PMMA is often considered a more valid standard for GPC due to its well-defined and narrow molecular weight distribution. The narrow dispersity of PMMA standards contributes to the accuracy and reproducibility of GPC results, making it a preferred choice in polymer analysis and characterisation. In addition to the suitability in both mobile phases of DMF as well as DMSO.[29]

4.4 Results and discussion

Towards creating all-in-one stimuli-responsive MSNs with dual capabilities of preventing premature drug release and controlling the MRI signal, UCST and LCST thermo-responsive polymers have been synthesised and fully characterised in this chapter. Both types of polymer were carefully developed to be grafted onto the external surface of silica nanoparticles (Chapter 5).

4.4.1 UCST (poly(AAm-co-AN)

In order to synthesise a UCST polymer based on acrylamide and acrylonitrile monomers with a carboxylic end group enabling the grafting on the surface of aminated silica, free radical and RAFT polymerisation were followed.[14, 24]

4.4.1.1 Free radical polymerisation

To produce a small family of UCST polymers with different chain lengths and hence transition temperatures, parameters including the time of polymerisation and the time of addition of 3-mercaptopropionic acid were varied as shown in (Section 4.3.2.1*).* The synthesis of poly(AAm-co-AN) was confirmed by both FTIR and ^{1}H NMR. In FTIR, both the absorption bands of the nitrile functional group of acrylonitrile (in the range 2250 to 2000 cm^{-1}) and the amide group of acrylamide at 1650 cm^{-1}, 3200 cm^{-1} and 3400 cm^{-1} were observed for all prepared polymers (Figure 4. 5).[30]

^{1}H NMR confirmed successful polymer synthesis, with peaks at 1.2-2.0 ppm (polymer backbone, $-CH_2-$), 2.0-2.7 ppm (polymer backbone, -CH-CO-), 2.3-3.1 ppm (polymer backbone, -CH-CN), and 6.7 ppm ($-NH_2$) were noted (Figure 4. 6).[11]

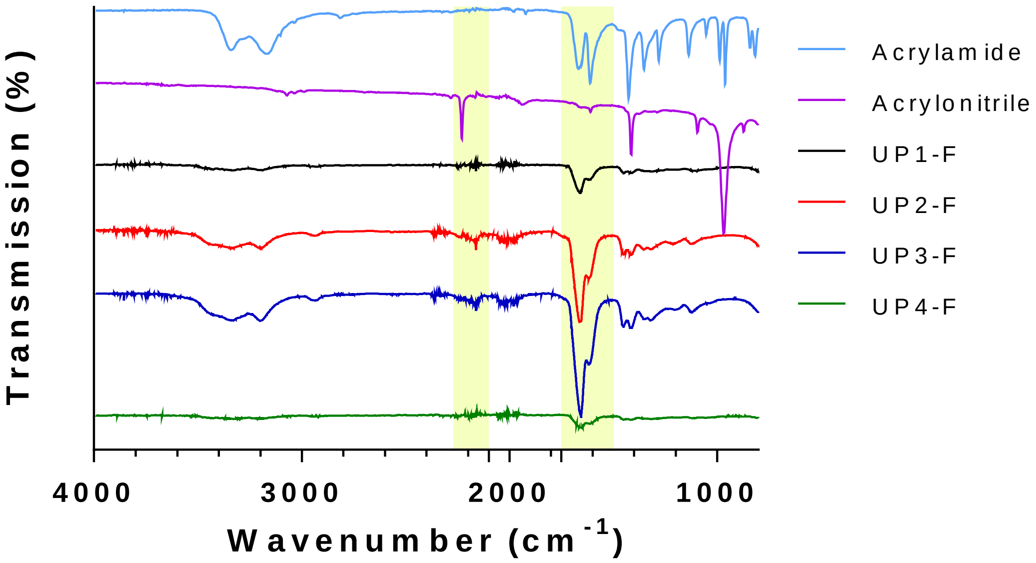

Figure 4. 5: FTIR spectra of poly(AAm-co-AN) prepared via *free radical polymerisation, and the constructing monomers acrylamide and acrylonitrile. The yellow bands represent acrylonitrile and the acrylamide absorption peaks.*

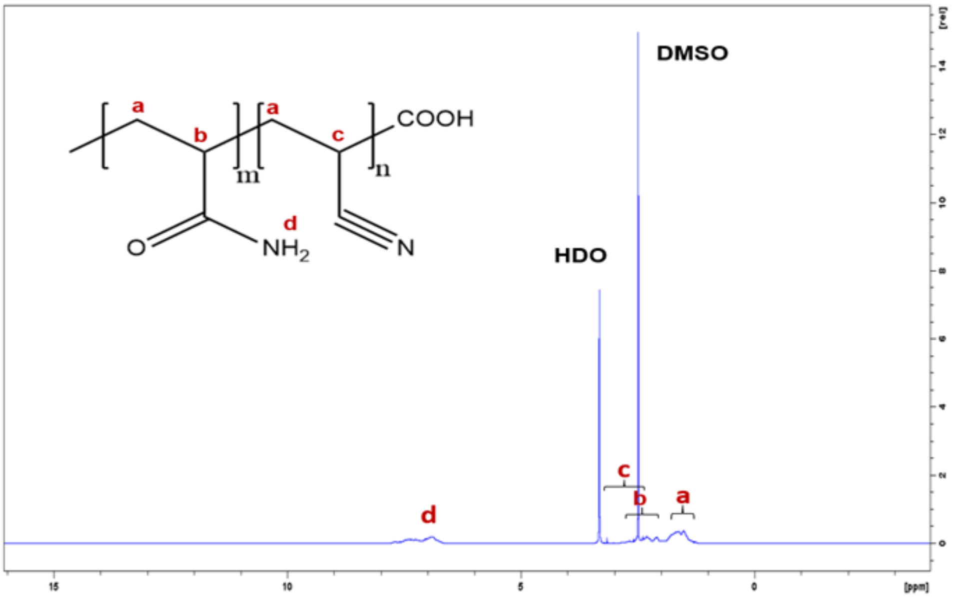

Figure 4. 6: ^{1}H NMR spectrum of poly(AAm-co-AN) prepared by free radical polymerisation, recorded in DMSO-d6 at 700 MHz.

To assess the thermo-responsive characteristics of the prepared polymers, both turbidimetry and DLS were employed. These methods can monitor alterations in turbidity, hydrodynamic diameter, and PdI induced by temperature variations. These changes arise from the transition of the polymer from an insoluble collapsed globule state to a soluble open coil conformation upon heating through the UCST.[11, 14] In turbidimetry, the temperature at which the transmittance dropped by 50% was identified as the cloud point, a key parameter reflecting the transition (Figure 4. 7).[11, 31]

Through turbidimetry analysis, it was observed that UP1-F and UP4-F showed higher cloud points in water compared to UP2-F and UP3-F, with transitions seen at 53.5 °C, 51.1 °C, 37.1 °C, and 37.3 °C, respectively, as shown in Figure 4. 7 and Table 4. 5. This behaviour may be attributed to the higher dispersity (PdI) of UP2-F and UP3-F than the other polymers (Table 4. 5). GPC showed that the polymer dispersity (M_w/M_n) was quite different for all samples, and clearly plays an important role in the resulting cloud points. The greater the polymer uniformity, the stronger the intermolecular and intramolecular hydrogen bonding within the polymer matrix. Consequently, a higher thermal threshold is necessary to disrupt these bonds, resulting in elevated temperatures required for the transition.[11, 14, 31]

Hysteresis was observed between the cooling and heating cycles. This is a common phenomenon, attributed to the increased energy needed for the hydrophobic-to-hydrophilic conformational change, due to intra- and intermolecular bonds in the phase-separated state requiring higher energy to disrupt. A lower energy is therefore required when transitioning in the opposite direction. The hysteresis has been reported previously with thermo-responsive polymers such as poly(N-acryloyl glycinamide-co-styrene) and poly(Aam-co-AN).[11, 14]

To evaluate the effect of the dispersion medium on the transition temperature, the same polymer concentrations were measured in PBS. All prepared samples have showed a lower cloud point in PBS compared to water (Table 4. 5). This can be explained by the salt effect, which has been studied previously for both LCST and UCST polymers. Increasing the salt concentration leads to a decrease in the critical solution temperature as a result of the higher ionic strength interfering with the polymer inter- and intramolecular hydrogen bonding (Figure 4. 7).[11, 32, 33]

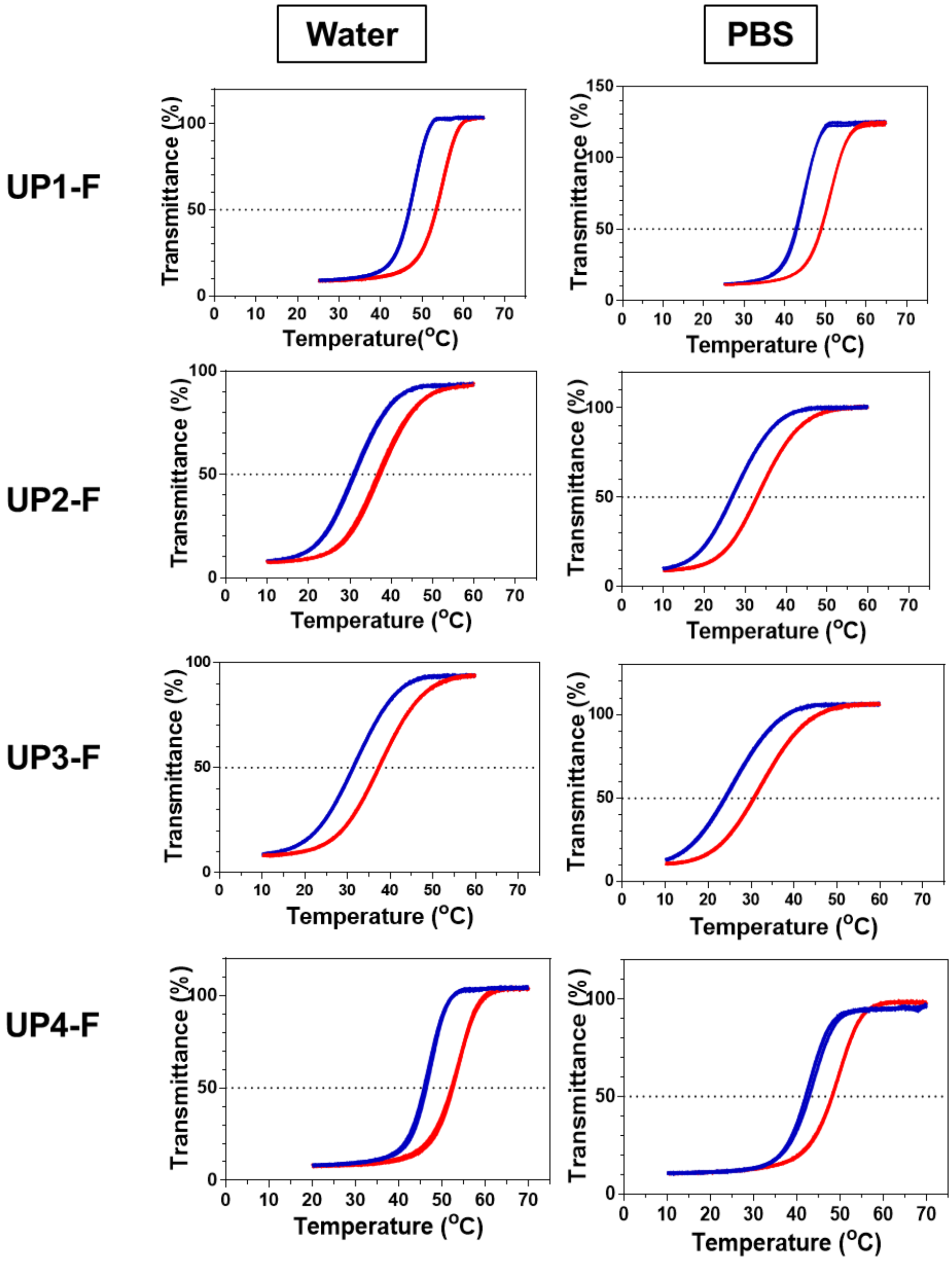

Figure 4. 7: Turbidimetry plots of poly(Aam-coAN) prepared by free radical polymerisation in water and PBS (10 mg/mL), measured at 670 nm in at least three heating (red) and cooling (blue) cycles.

Table 4. 5: GPC data and cloud points of free-radical synthesised poly(AAm-co-AN) in water and PBS.

Dispersion medium	**Water**		**PBS**		**M_w (g/mol)**	**M_n (g/mol)**	**Dispersity (Đ)**
Polymers	**Heating***	**Cooling***	**Heating***	**Cooling***			
UP1-F	53.4 °C	46.9 °C	48.9 °C	42.8 °C	107709	38260	2.82
UP2-F	37.1 °C	31.1 °C	32.9 °C	26.8 °C	114280	29733	3.84
UP3-F	37.3 °C	31.3 °C	30.6 °C	23.9 °C	103623	26307	3.94
UP4-F	51.1 °C	44.7 °C	48.2 °C	42.4 °C	107867	35321	3.05

*The data represent the mean of three different cycles of heating and cooling.

In DLS, the polymer transition was evaluated by the change in hydrodynamic diameter and PdI. The globular insoluble polymer turns into soluble micelles upon heating, followed by a plateau once the transition is completed. Consequently, an approximate estimation of the cloud point can be inferred through DLS analysis. For instance, in Figure 4. 8, phase shifts were observed at temperatures of 51 °C, 43 °C, and 44 °C where the corresponding sizes reached 35 nm, 123 nm, and 52 nm, instead of sizes in thousands of nanometres, while PdI reduced from 1 to 0.35, 0.21, and 0.35 for UP1-F, UP2-F, and UP3-F, respectively. Notably, the transition temperatures determined *via* DLS exhibit slight variation from those obtained through turbidimetry. This divergence arises because DLS measurements rely on measuring the fluctuations in scattered light intensity due to diffusing particles, whereas turbidimetry depends on the analysis of absolute mean intensity.[34]

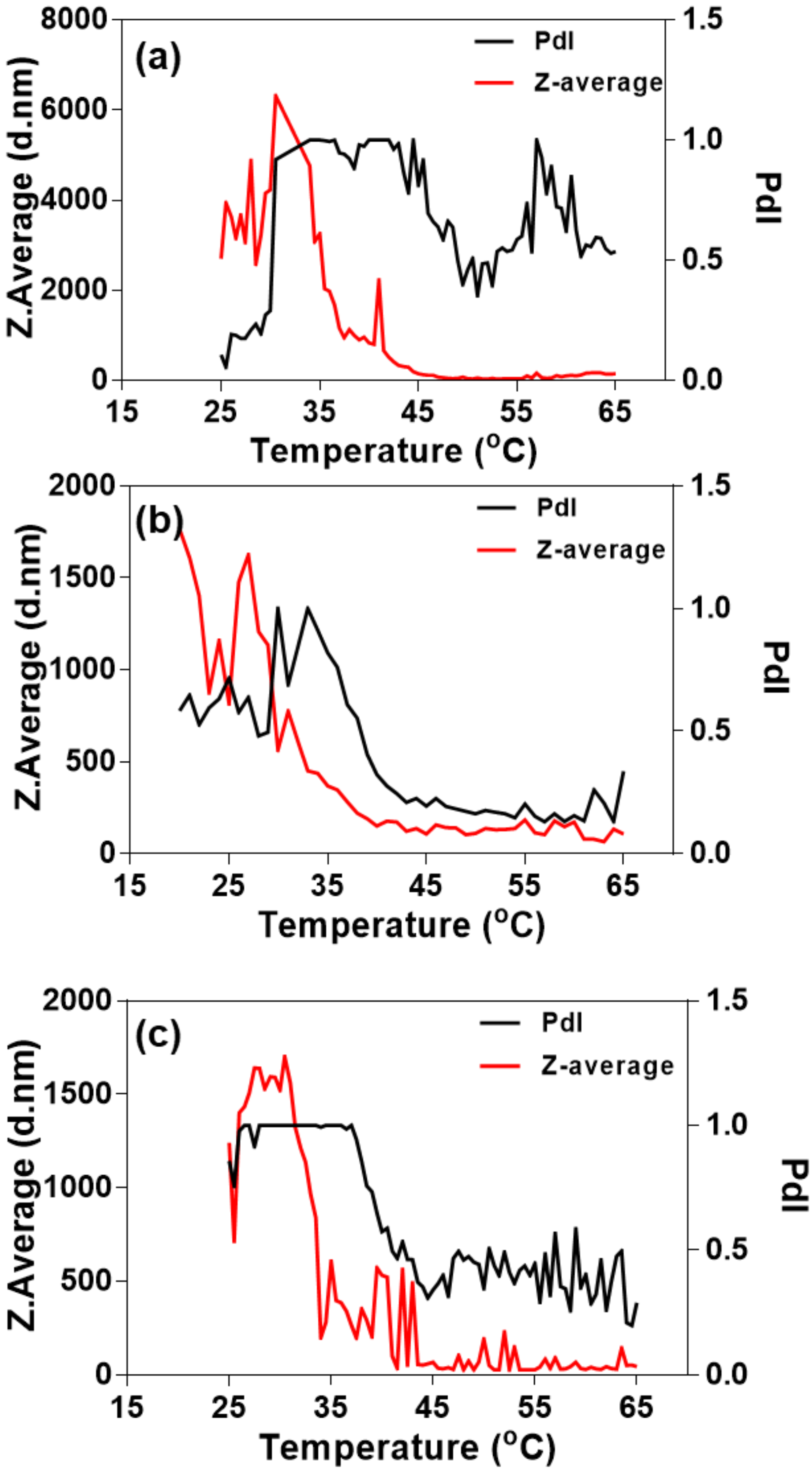

Figure 4. 8: Temperature-dependant DLS data in water for UP1-F (a), UP2-F (b), and UP3-F (c), prepared by free radical polymerisation (10 mg/mL). Note: UP4-F yield was insufficient for DLS analysis.

4.4.1.2 RAFT polymerisation

In order to design monodispersed homogenous polymers, we opted for RAFT polymerisation due to its ability to create polymers with uniform chain lengths and low polydispersity. Moreover, RAFT enables precise control over the end-group functionality of polymer chains by choosing the appropriate RAFT agent.[35-37]

4.4.1.2.1 Literature-based method

In order to prepare poly(AAm-co-AN) of different transition temperatures using RAFT polymerisation, an established method was followed, increasing the concentration of hydrophobic acrylonitrile (14, 18, and 23 mmol to prepare UPL1-R, UPL2-R, and UPL3-R, respectively) while keeping a constant total monomer amount (74 mmol) as in Table 4. 2.[14] This aimed to produce polymers with increasing relative hydrophobicity, leading to varying cloud points.

The synthesis of the prepared polymers was confirmed using FTIR and ^{1}H NMR. In FTIR, the characteristic absorption bands of the nitrile functional group of acrylonitrile monomer at 2200 cm^{-1} and amide group of acrylamide monomer at 1650 cm^{-1}, 3200 cm^{-1} and 3400 cm^{-1} were observed for all prepared polymers (bands highlighted in yellow in Figure 4. 9).[30] The chemical shifts of ^{1}H NMR peaks were 1.29-1.9 ppm (polymer backbone, -CH$_2$-), 2.0-2.6 ppm (polymer backbone, -CH-CO-NH$_2$), 2.3-3.0 ppm (polymer backbone, -CH-CN), and 6.9 ppm (-NH$_2$) (all peaks as labelled in Figure 4. 10).[11]

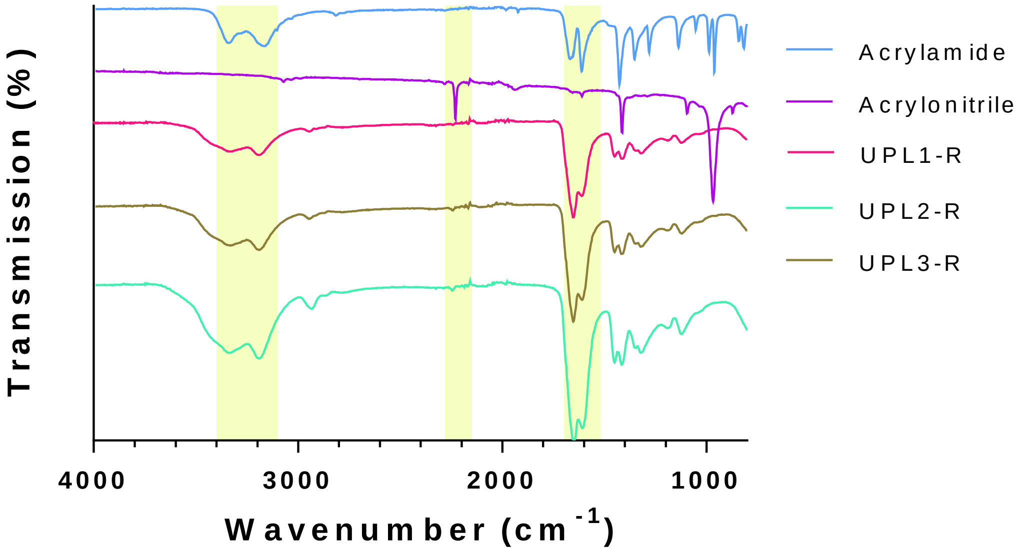

Figure 4. 9: FTIR spectra of UCST poly(AAm-co-AN) prepared via literature-based RAFT, and the constructing monomers acrylamide and acrylonitrile. The yellow bands represent acrylonitrile and the acrylamide absorption peaks.

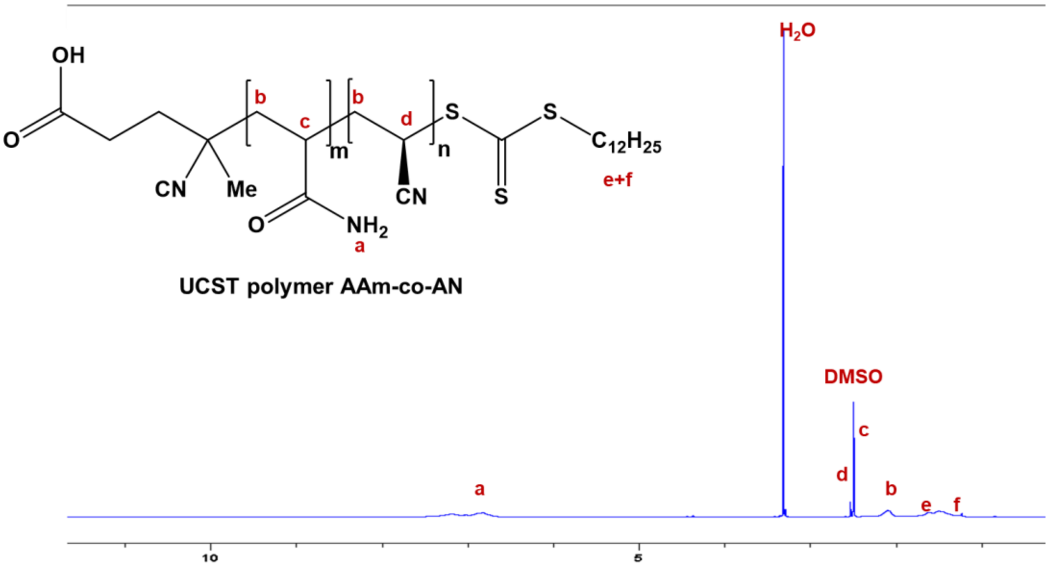

Figure 4. 10: ^{1}H NMR spectrum of poly(AAm-co-AN) prepared by literature-based RAFT, recorded in DMSO-d6 at 700 MHz.

Turbidity measurements were evaluated on aqueous solutions of the prepared polymers with concentrations ranging from 5 to 25 mg/mL to ensure the responsive behaviour. Surprisingly, these measurements did not reveal any thermo-responsive characteristics within the temperature range of 20 to 60 °C (as depicted in Figure 4. 11). Nonetheless, the analysis of GPC data provided evidence of successful RAFT synthesis of uniform polymers with well-controlled chain lengths and low dispersity, unlike the free radical method (Table 4. 6).[38] The absence of UCST behaviour could potentially be explained by the domination of acrylamide groups, which constitute the hydrophilic monomers in the synthesised polymer chains. This dominance might lead to a reduction in the UCST value, causing it to fall below the experimental temperature range.[14]

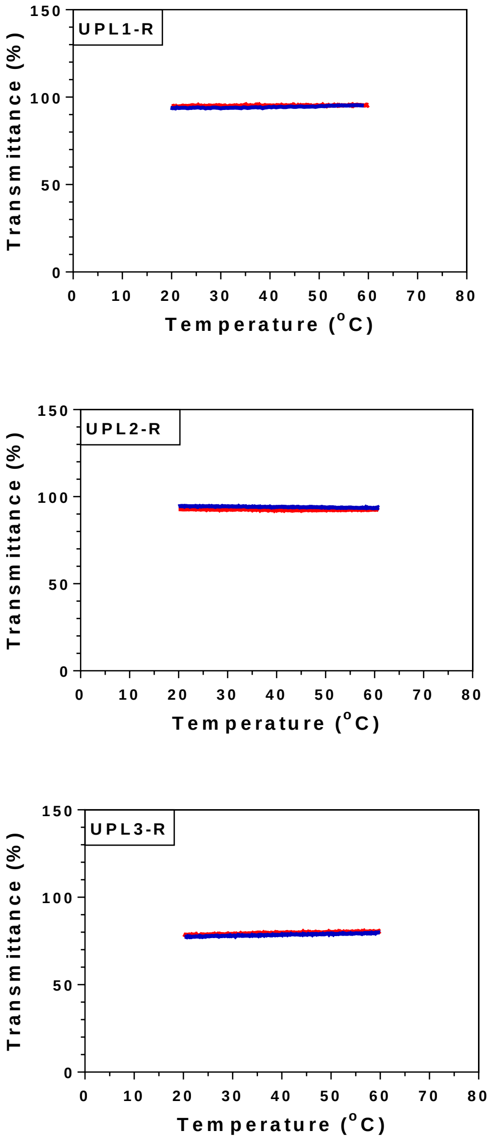

Figure 4. 11: Turbidimetry plots of UPL1-R, UPL2-R, and UPL3-R (25mg/mL in water) measured at 670 nm in at least two heating (red) and cooling (blue) cycles.

Table 4. 6: GPC data of different poly (AAm-co-AN) prepared by RAFT polymerisation.

Dispersion medium	M_w (g/mol)	M_n (g/mol)	Dispersity (Đ)
UPL1-R	23800	16600	1.43
UPL2-R	20200	13100	1.54
UPL3-R	26200	19600	1.34

4.4.1.2.2 Design of Experiment synthetic approach

The high polydispersity observed in the UCST polymers synthesised through free radical polymerisation in Section 4.4.1.1, along with the absence of thermo-responsive behaviour in the homogeneous monodisperse polymers prepared by RAFT in Section 4.4.1.2.1, led us to explore the Design of Experiments approach. Our goal was to create a model that can predict the polymer transition temperature and molecular weight generated through the use of RAFT polymerisation parameters. To achieve this, we employed a response surface design using a two-factor Central Composite Design (CCD). The variables chosen for this design were the monomer molar ratio (AAm: AN) at three levels (1:1, 1.5:1, and 2:1) and the polymerisation time (16, 20, and 24 hours) through modified RAFT polymerisation (Table 4. 7). These selections were based on both our preliminary investigation of UCST synthesis and the existing literature on the influence of monomer ratio and molecular weight on determining the transition temperature.[14, 31, 39]

To validate the synthesis of poly(AAm-co-AN), we evaluated the samples using FTIR and ^{1}H NMR spectroscopy. The results from these analyses confirmed the desired polymer structure where FTIR showed the characteristic absorption peaks of acrylonitrile and acrylamide in the synthesised polymers (Figure 4. 12), as previously described, as well as the chemical shifts from ^{1}H NMR (Figure S4. 2).[11] The GPC results confirmed the exceptional uniformity of the polymers. Evident homogeneity was observed, displaying a single peak in GPC, in contrast to the multiple peaks associated with varying molecular weights in free radical polymerisation as shown in (Figure S4. 1, Figure S4. 3 and Table 4. 7). Furthermore, the molecular weights ranged from 84,600 to 164,100 g/mol, aiming to achieve a spectrum of transition temperatures (Table 4. 7). [40, 41] It is worth noting that these molecular weights are significantly higher compared to those obtained in the previous Section (4.4.1.2.1).

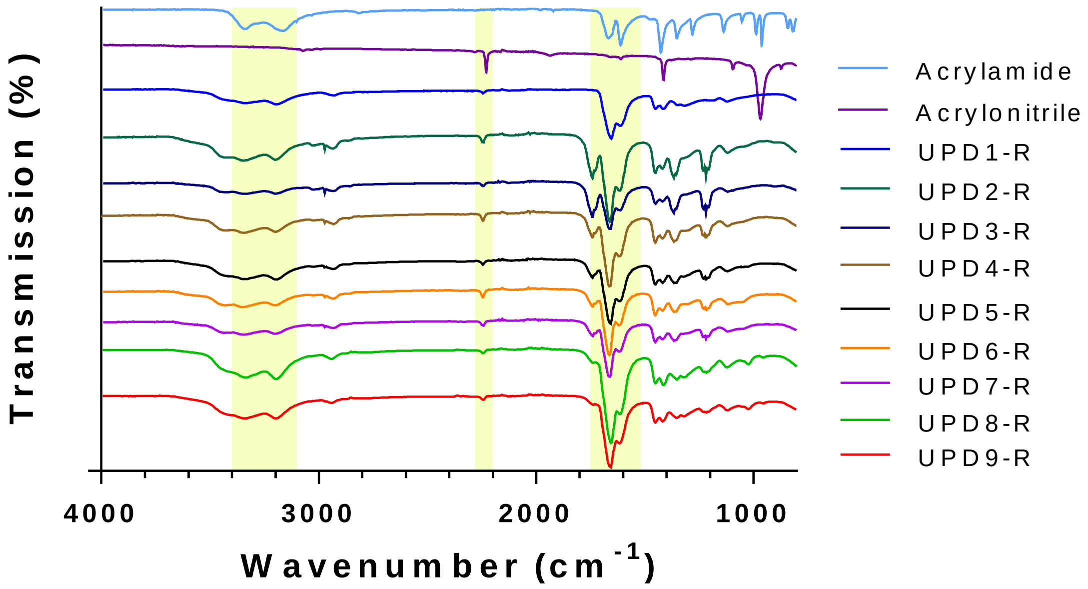

Figure 4. 12: FTIR spectra of poly(AAm-co-AN) prepared via DoE-based RAFT, and the constructing monomers acrylamide and acrylonitrile. The yellow bands represent acrylonitrile and the acrylamide absorption peaks.

Table 4. 7: Parameters varied and GPC data of poly (AAm-co-AN) prepared by RAFT polymerisation.

GPC	Monomer ratio	Time (h)	M_n (g/mol)	M_w (g/mol)	Dispersity (Đ)	Transition temperature (°C)
UPD1-R	1.5:1	24	107700	120500	1.12	36.5
UPD2-R	1.5:1	16	88700	100300	1.13	39.9
UPD4-R	1.5:1	20	74500	84600	1.14	34
UPD8-R	2:1	24	138200	164100	1.19	27.9
UPD3-R	2:1	16	75300	85600	1.14	37.2
UPD5-R	2:1	20	107300	121100	1.13	33.6
UPD6-R	1:1	24	100200	125300	1.25	31
UPD7-R	1:1	20	103600	122300	1.18	33
UPD9-R	1:1	16	110700	134300	1.21	30.5

In order to assess the thermo-responsive characteristics, a solution containing 10 mg/mL of UCST polymers was prepared in warm water to obtain clear solution. Subsequently, the turbidity of each polymer was measured in triplicate using a plate reader at 670 nm. This turbidimetry was conducted within the temperature range 25 to 45 °C. It was found that the transition points vary between 27.9 °C and 39.9 °C as shown in Table 4. 7. These variations occurred as a result of altering both the monomer molar ratio and the duration of polymerisation (Figure 4. 13).

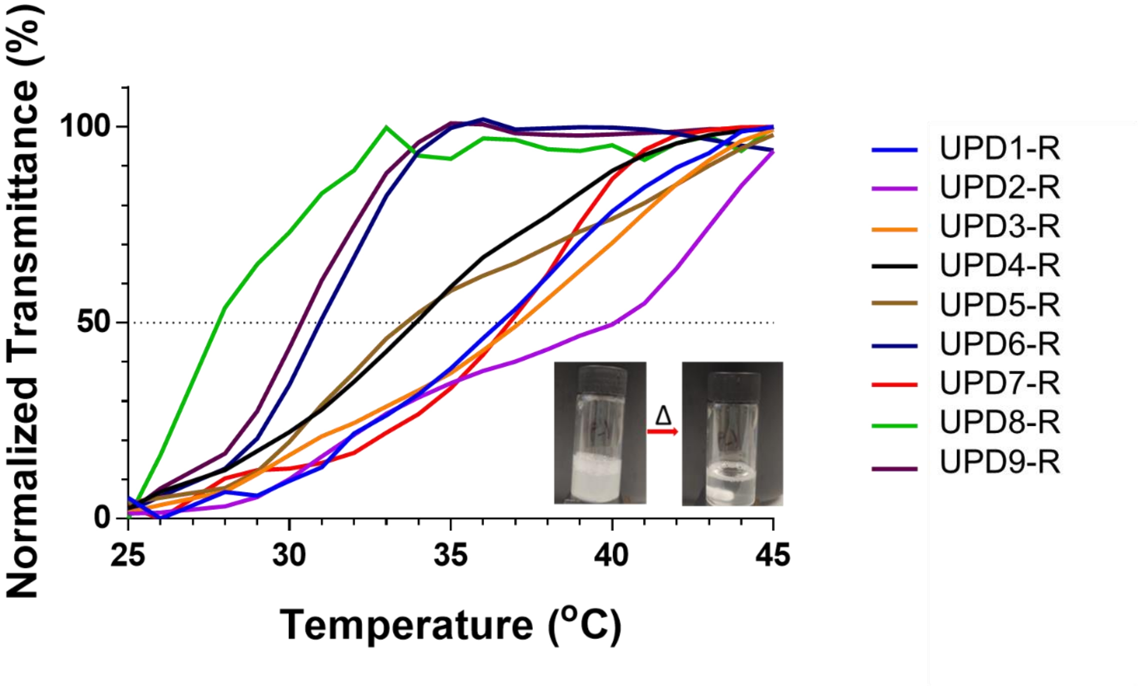

Figure 4. 13: Turbidimetry plots of poly(AAm-co-AN) (10mg/mL in water) measured at 670 nm using a microplate reader in at least three heating cycles. The inset figure shows the visual change in the turbidity of UCST polymer upon heating.

To test our model and to ascertain the trend of parameter impact on the generated polymer characteristics of polymer molecular weight (from GPC) and cloud point as determined by turbidimetry, regression analysis of variance for all response variables has been evaluated. The effect of both independent variables (ratio of AAm:AN and reaction time) was non-significant in predicting the cloud point (p = 0.16 and R^2 value of 0.85, Figure 4. 14, Table 4. 8), but the model could predict the molecular weight successfully (p = 0.04, R^2 = 0.95; Figure 4. 14, Table 4. 8).

Table 4. 8: Results of regression analysis of variance for all response variables.

Response	Mean	R^2	RMSE	p-value	F-ratio
Cloud point (˚C)	33.74	0.85	2.33	0.16	3.52
Mw (g/mol)	117566.70	0.95	9240.45	0.04	11.01

R^2 is the ratio of sum of squares describing the proportion of variation explained by the model. The F-ratio is the ratio between explained error and unexplained error.

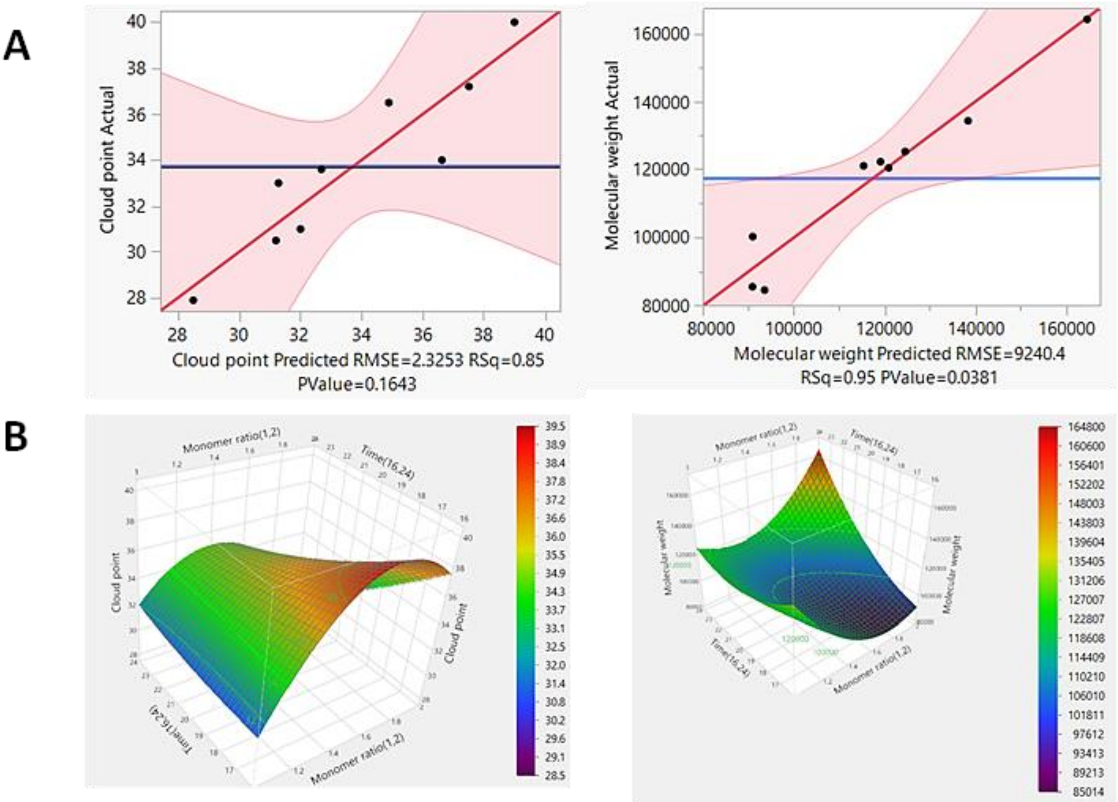

Figure 4. 14: Regression analysis of cloud point (left) and molecular weight (right) responses. (A) Actual vs. predicted scatter plot where the black markers are the treatment populations, the blue line is the mean population, the red line is the line of fit, and the light pink bands are 0.05 significance curve, and (B) 3D response surface plots of experimental design for the optimisation of response versus polymerisation time and monomer ratio.

The parameter estimates that were deemed to be active in affecting the molecular weight were calculated from the regression analysis and used in the prediction expression. Time, monomer ratio-time interaction and monomer ratio-monomer ratio interaction were found significant, with p-values of 0.0287, 0.0179, and 0.0393, respectively (Table 4. 9).

Table 4. 9: Parameter estimates of molecular weight response calculated from the regression analysis.

Response	Parameter	Estimate	Std Error	t Ratio	p-value
Molecular weight response	Intercept	93566.67	6887.42	13.59	0.0009
	Monomer ratio	-1850	3772.40	-0.49	0.6575
	Time	14950	3772.40	3.96	0.0287*
	Monomer ratio*time	21875	4620.22	4.73	0.0179*
	Monomer ratio * monomer ratio	23650	6533.98	3.62	0.0363*
	Time*Time	12350	6533.98	1.89	0.1551

*Significant p-value <0.05

A prediction model equation for molecular weight has been modified to only involve the statistically significant parameters (p <0.05; time, monomer ratio * time interaction and monomer * monomer ratio interaction) as shown in Equation 4. 2.

$$Y = 93566.7 + 1450 \times (Time - 20)/4 + (Monomer\ ratio - 1.5)/0.5 \times (Time - 20)/4 \times 21875 + (Monomer\ ratio - 1.5)/0.5 \times (Monomer\ ratio - 1.5)/0.5 \times 23650$$

Equation 4. 2

Since the model could not predict the cloud point of the prepared polymers based on monomer ratio and polymerisation time change, a more detailed full factorial design could be performed to elucidate this behaviour more clearly. Expanding the range of monomer ratios and introducing additional factors like the AIBN/RAFT agent ratio, stirring rate, and time of N_2 purging could enhance the accuracy of predictions. Moreover, incorporating a greater number of replicates, particularly for the central data points, would contribute to the development of a more effective predictive model.[42-44] To process to the next chapter, UPD1-R was selected to be the gatekeeper for our all-in-one theranostic system. A comprehensive Design of Experiments (DoE) study was deemed unnecessary since the initial experiment provided a diverse range of UCST values, one of which closely matched the physiological transition range. Specifically, the UCST of UPD1-R was identified as 36.5 °C. It is anticipated to experience a slight increase upon grafting onto the surface of MSNs in Chapter 5, aligning it with the desired UCST.

4.4.2 LCST PNIPAm-NHS ester

To facilitate the formation of LCST PNIPAm with an end group suitable for linking to aminated MSNs, Dr. Pratik Gurani from the University of Nottingham developed the PABTC-NHS RAFT agent.[26-28] Following this, a series of three distinct LCST polymers was synthesised through RAFT polymerisation. Different ratios of PABTC-NHS to ACVA (Table 4. 4) were employed in the synthesis process to yield LCST polymers with varying chain lengths and degree of polymerisation, each terminated with an NHS end group. The synthesis of PNIPAm-NHS ester was confirmed using both FTIR and ^{1}H NMR. In IR, PNIPAm-NHS ester displays absorption peaks at 3300, 1650, 1630, and 1540 cm^{-1} corresponding to N–H stretching, C=O stretching, C=C stretching and N-H bending, respectively. In addition, the vinyl double bonds peaks of the monomer has dispersed in the synthesised polymers of =C-H, C=C and stretching of vinyl double bonds at 3150-3000 cm^{-1}, 1630-1600 cm^{-1} and 610-990 cm^{-1}, respectively (Figure 4. 15).[45, 46]

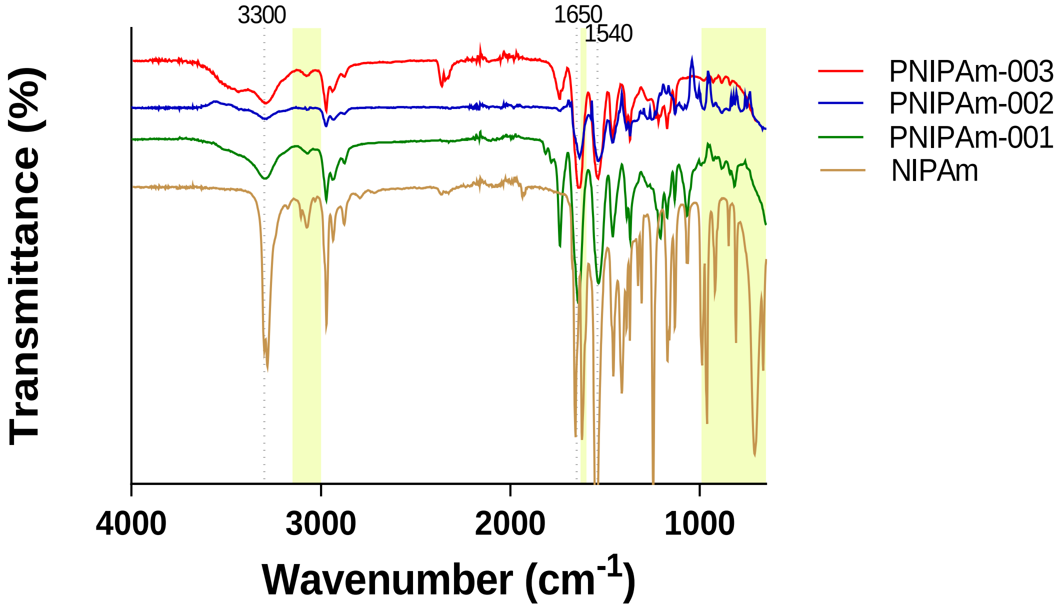

Figure 4. 15: FTIR spectra of PNIPAm-NHS esters of different molecular weight and the monomer NIPAm. Dotted lines express the peaks of the polymer while the yellow bands express the monomer ones.

^{1}H-NMR confirmed the chemical structure of the polymer, with signals at 1.03 ppm (-CH_3), 1.47 ppm (polymer backbone, -CH_2-CH), 1.9 ppm (polymer backbone, -CH-CH_2-), 3.8 ppm (-CH isopropyl) and 7.2 ppm (-NH-) (Figure S4. 5).[25] GPC analysis demonstrated that all the polymers synthesised through RAFT exhibited minimal dispersity, with molecular weights of 2,200, 18,900, and 59,500 g/mol for PNIPAm-001, PNIPAm-002, and PNIPAm-003, respectively (Table 4. 10).

Table 4. 10: Gel permeation chromatography (GPC) data of different PNIPAm prepared by RAFT polymerisation.

Sample	**DP_{target}**	**Conversion (%)**	**$M_{n,SEC}$**	**$M_{w,SEC}$**	**Đ**
PNIPAm-001	10	>99	2200	2400	1.07
PNIPAm-002	120	>99	18900	20300	1.08
PNIPAm-003	400	>99	59500	68000	1.14

The turbidimetric analyses of the prepared LCST polymers in water (10 mg/mL) show transition temperatures of 36.4 °C, 32.9 °C and 34.6 °C upon heating and 30.4 °C, 24.3 °C, and 29.2 °C upon cooling for PNIPAm-001, 002 and 003, respectively (Figure 4. 16). The impact of molecular weight on the cloud point was evident mainly in PNIPAm-001 and PNIPAm-002, consistent with previously reported literature. The literature suggests that the LCST of this polymer remains relatively unaffected by polydispersity and molecular weight, as long as the polymer's molecular weight exceeds 50,000 g/mol.[47] However, an additional factor influencing the cloud point is the nature of the end group. In our case, the NHS-ester end group fosters more hydrogen bonds with the surrounding water, requiring higher energy for transition into the insoluble form.[47]

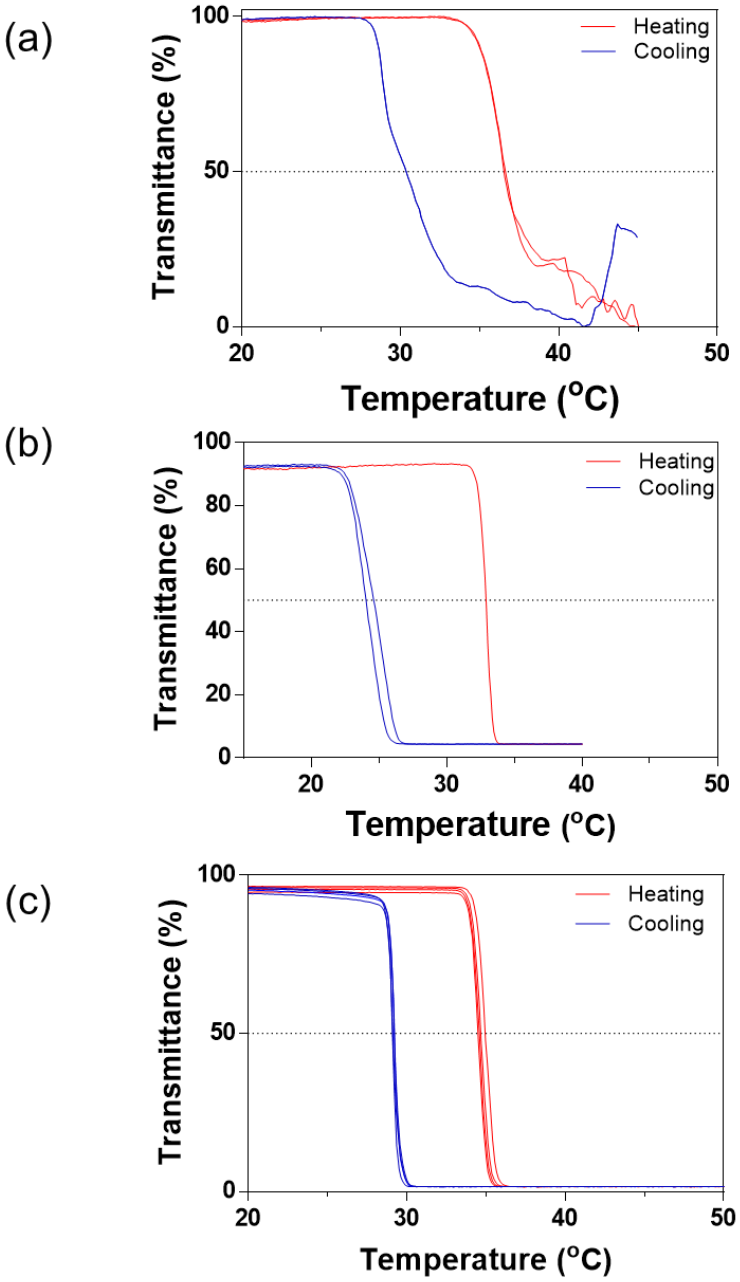

Figure 4. 16: Turbidimetry plots of (a) PNIPAm-001, (b) PNIPAm-002, and (c) PNIPAm-003 (10 mg/mL in water) measured at 500 nm in at least two heating and cooling cycles.

DLS data showed the same trend as turbidimetry. Both z-average and PdI increased markedly in the temperature order PNIPAm-001 > PNIPAm-003 > PNIPAm-002, at 44 °C, 26 °C, and 30 °C respectively (Figure 4. 17).

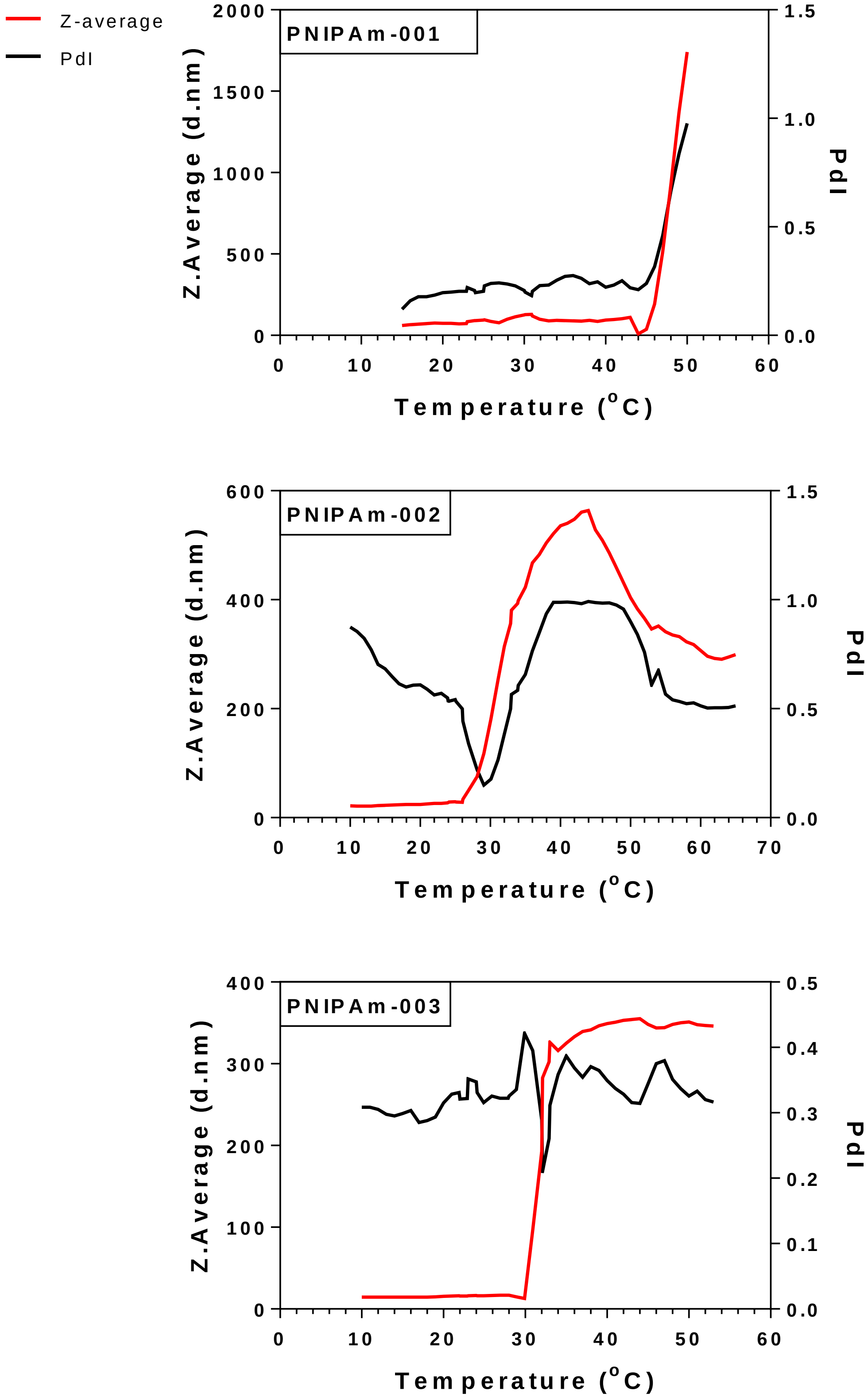

Figure 4. 17: Temperature-dependant DLS data for PNIPAM-NHS esters prepared by RAFT in water (10 mg/mL).

4.5 Conclusions

In conclusion, this chapter emphasises the importance and success of tuning the transition temperature of UCST poly(AAm-co-AN) to suit biomedical applications by manipulating the monomer molar ratio (1:1, 1.5:1 and 2:1 of AAM: AN) and polymerisation time (16, 20, and 24 hours). Utilising Design of Experiments (DoE), we could develop a model to successfully predict the molecular weight of the product polymer, with statistically significant parameters related to time, the interaction between time and monomer ratio, and the interaction between monomer ratios. A range of UCSTs were obtained, from 27.9 °C and 39.9 °C. Of these, polymer UPD1-R with UCST 36.5 °C has a suitable transition temperature for biomedical applications and so will be taken forward in future work.

For PNIPAm, employing RAFT synthesis to give NHS ester end groups could result in materials with varying degrees of polymerisation (10, 120 and 400) and a range of molecular weights (2,400-68,000 g/mol). The polymers are marked by low dispersity and exceptional homogeneity as demonstrated by very low dispersity values. Our findings indicate a limited shift in LCST (32.9-36.4 ˚C) despite a significant increase in molecular weight, in agreement with existing literature. Consequently, both PNIPAm-002 and PNIPAm-003 exhibit suitable molecular weights (20300 and 68000 g/mol, respectively) for potential application in future LCST polymer grafting endeavors, when compared to the molecular weights of the linker ligands.

4.6 References

1. M. A. Ward and T. K. Georgiou, Polymers, 2011, **3**, 1215-1242.
2. A. Gandhi, A. Paul, et al., Asian Journal of Pharmaceutical Sciences, 2015, **10**, 99-107.
3. L. Klouda and A. G. Mikos, European Journal of Pharmaceutics and Biopharmaceutics, 2008, **68**, 34-45.
4. M. Heskins and J. E. Guillet, Journal of Macromolecular Science: Part A - Chemistry, 1968, **2**, 1441-1455.
5. J. Chen, M. Liu, et al., ACS Applied Materials & Interfaces, 2011, **3**, 3215-3223.
6. H. Tang, S. Shen, et al., Journal of Materials Chemistry, 2012, **22**, 16095-16103.
7. E. Guisasola, A. Baeza, et al., Langmuir, 2015, **31**, 12777-12782.
8. Y. Nan, C. Zhao, et al., Macromolecular Rapid Communications, **n/a**, 2300261.
9. D. Roy, W. L. A. Brooks, et al., Chemical Society Reviews, 2013, **42**, 7214-7243.
10. Y. Kotsuchibashi, Polymer Journal, 2020, **52**, 681-689.
11. J. Seuring and S. Agarwal, Macromolecules, 2012, **45**, 3910-3918.
12. H. Zhang, S. Guo, et al., Macromolecules, 2016, **49**, 1424-1433.
13. H. Zhang, X. Tong, et al., Langmuir, 2014, **30**, 11433-11441.
14. A. Asadujjaman, B. Kent, et al., Soft Matter, 2017, **13**, 658-669.
15. W. Hu, X. Bai, et al., Journal of Materials Chemistry B, 2019, **7**, 5789-5796.
16. M. Hei, J. Wang, et al., Journal of Materials Chemistry B, 2017, **5**, 9497-9501.
17. D. Kuckling and A. Wycisk, Journal of Polymer Science Part A: Polymer Chemistry, 2013, **51**, 2980-2994.
18. J. M. Ren, T. G. McKenzie, et al., Chemical Reviews, 2016, **116**, 6743-6836.
19. Z. Wu, H. Liang, et al., Macromolecules, 2010, **43**, 5699-5705.

20. P. Flemming, A. S. Münch, et al., Beilstein Journal of Organic Chemistry, 2021, **17**, 2123-2163.
21. X. L. Sun, P. C. Tsai, et al., Journal of Materials Chemistry B, 2015, **3**, 814-823.
22. N. S. Vishnevetskaya, V. Hildebrand, et al., Macromolecules, 2017, **50**, 3985-3999.
23. F. Farnaz, B. Massoumi, et al., Polymer Science, Series B, 2020, **62**, 540-549.
24. M. Hei, J. Wang, et al., J Mater Chem B, 2017, **5**, 9497-9501.
25. S. Jadhav, Journal of Applied Polymer Science, 2016, **In press**.
26. H. Li, A. P. Bapat, et al., Polymer Chemistry, 2011, **2**, 323-327.
27. N. Vanparijs, S. Maji, et al., Polymer Chemistry, 2015, **6**, 5602-5614.
28. J. E. Petch, P. Gurnani, et al., ACS Applied Materials & Interfaces, 2021, **13**, 19230-19243.
29. Polymethylmethacrylate Standards, https://www.agilent.com/en/product/gpc-sec-columns-standards/gpc-sec-standards/polymethylmethacrylate-standards, (accessed 28/12/2023, 2023).
30. S. N. A. M. Jamil, M. Khairuddin, et al., e-Polymers, 2015, **15**, 45-54.
31. J. Seuring and S. Agarwal, ACS Macro Letters, 2013, **2**, 597-600.
32. F. Liu, J. Seuring, et al., Polymer Chemistry, 2013, **4**, 3123-3131.
33. L. Lu, Z. Wang, et al., Journal of Wuhan University of Technology-Mater. Sci. Ed., 2012, **27**, 285-289.
34. K. Kogej, D. Božič, et al., Int J Mol Sci, 2021, **22**.
35. S. Schmidt, Niedersächsische Staats-und Universitätsbibliothek Göttingen, 2018.
36. G. Conzatti, S. Cavalie, et al., Colloids and Surfaces B: Biointerfaces, 2017, **151**, 143-155.
37. D. Taton, M. Destarac, et al., Handbook of RAFT polymerization, 2008, 373-421.
38. R. Whitfield, K. Parkatzidis, et al., Chem, 2020, **6**, 1340-1352.
39. M. A. Abou-Shamat, J. L. Stair, et al., Molecular Systems Design & Engineering, 2020, **5**, 1538-1546.
40. K. Kanta Sharker, Y. Ohara, et al., Polymers (Basel), 2019, **11**.

41. D. G. Lessard, M. Ousalem, et al., Canadian Journal of Chemistry, 2001, **79**, 1870-1874.
42. C. L. G. Harman, N. Mac Fhionnlaoich, et al., Materials Advances, 2022, **3**, 6007-6018.
43. T. Eckert, F. C. Klein, et al., Polymers, 2021, **13**, 3147.
44. T. Eckert, Staats-und Universitätsbibliothek Hamburg Carl von Ossietzky, 2022.
45. J.-H. Park, J.-W. Jang, et al., International Journal of Polymer Science, 2019, **2019**, 3824207.
46. J. Hu, X. Liu, et al., Biomacromolecules, 2023, **24**, 1345-1354.
47. S. Furyk, Y. Zhang, et al., Journal of Polymer Science Part A: Polymer Chemistry, 2006, **44**, 1492-1501.

4.7 Supplementary information

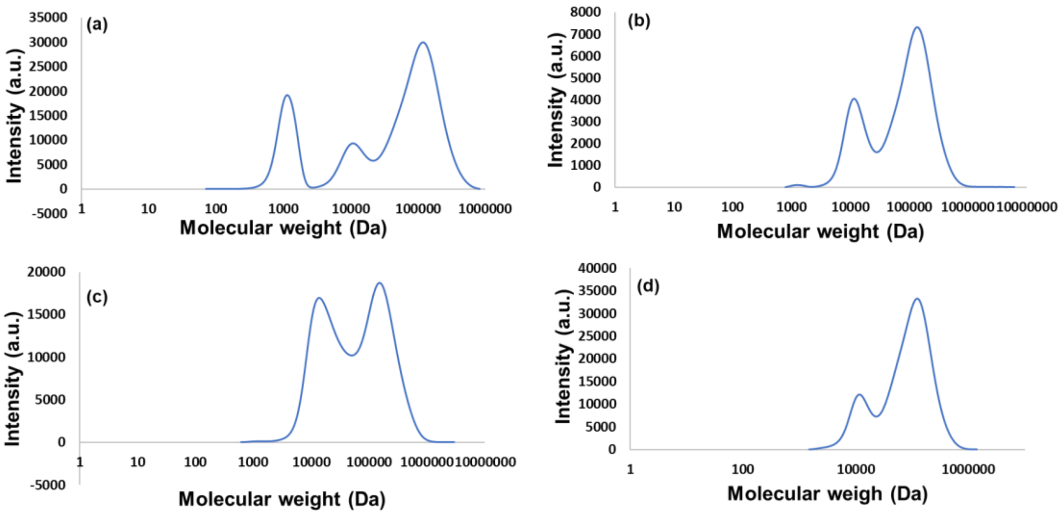

Figure S4. 1:GPC traces of (a) UP1-F,(b) UP2-F, (c) UP3-F, and (d) UP4-F prepared by free radical polymerisation.

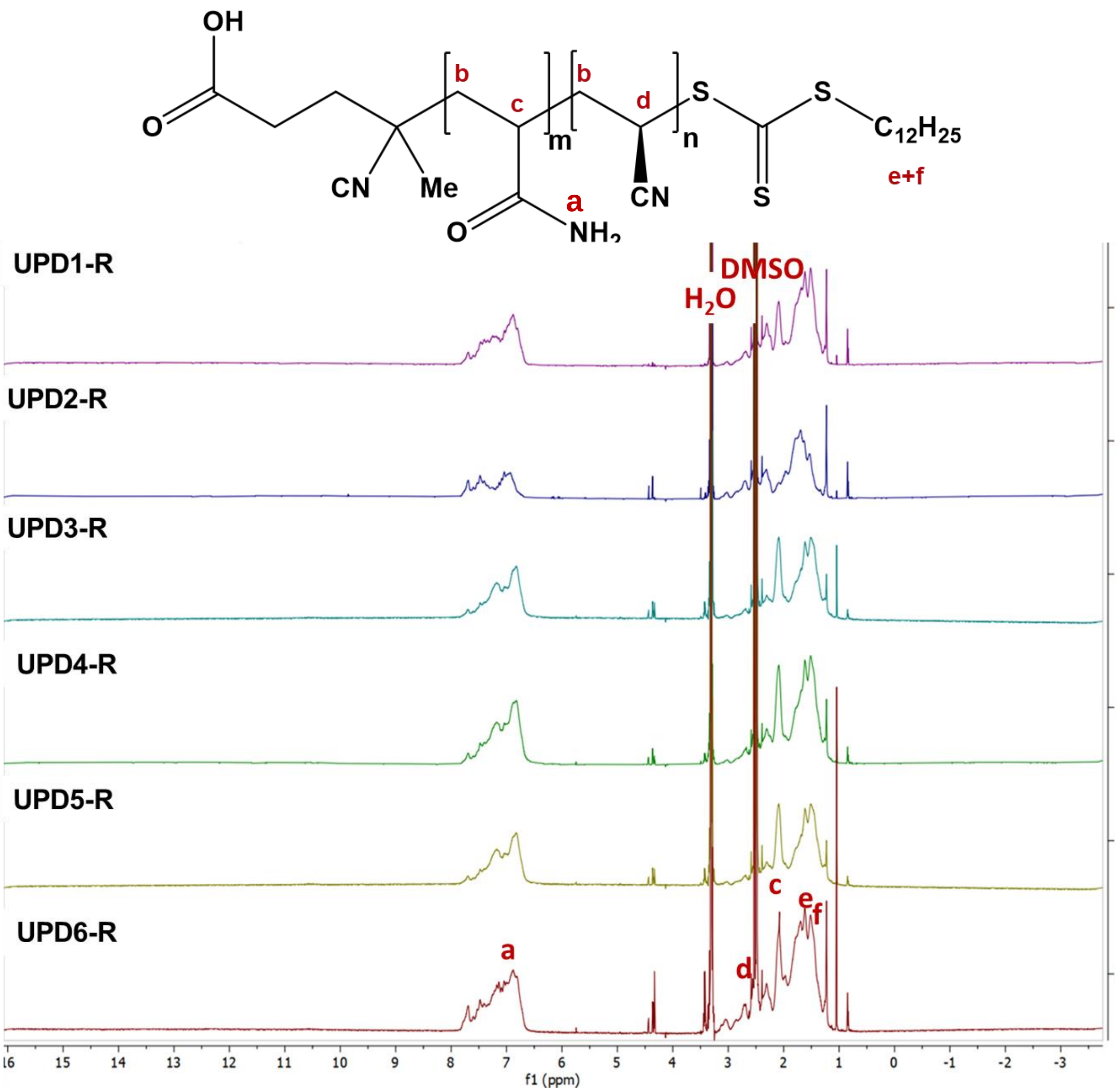

Figure S4. 2: ^{1}H NMR spectra of poly(AAm-co-AN) systems prepared by DoE-based RAFT, recorded in DMSO-d6 at 700 MHz.

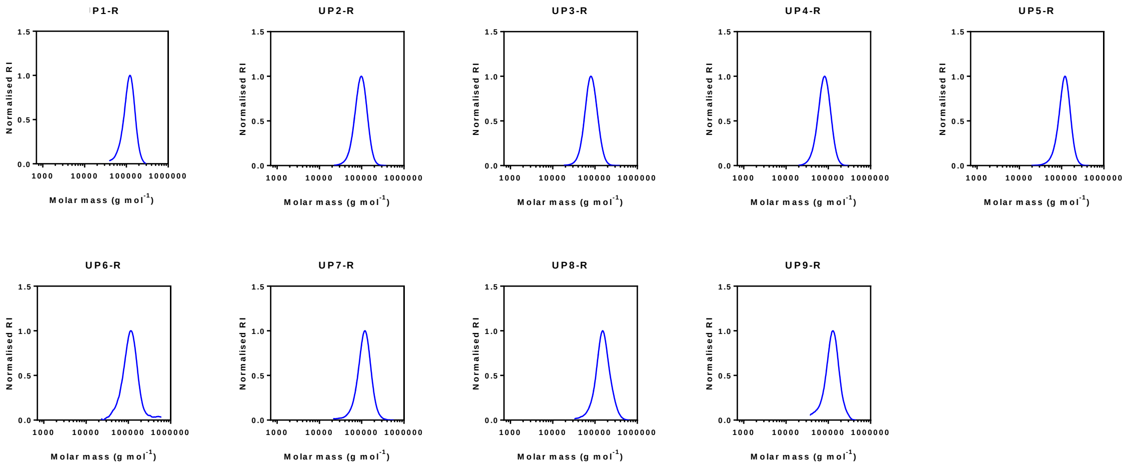

Figure S4. 3: GPC of poly(Aam-co-AN) prepared by RAFT polymerisation using DoE.

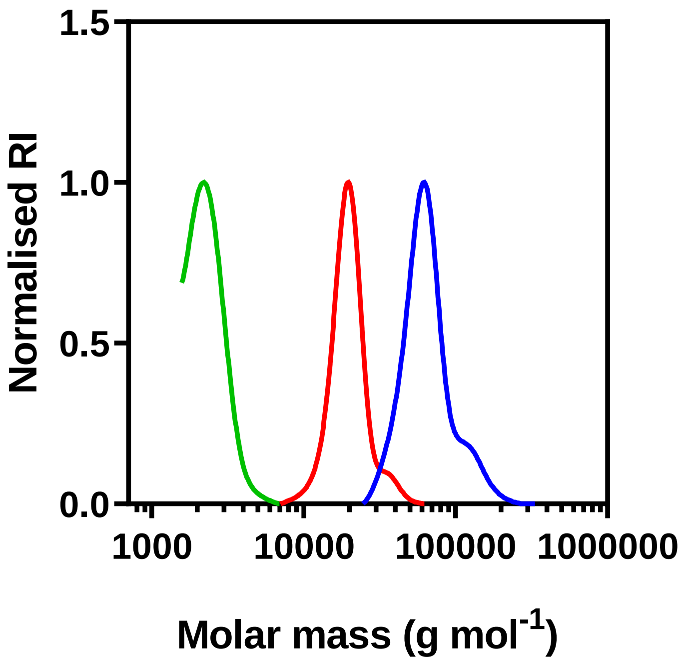

Figure S4. 4: GPC data of PNIPAm-NHS esters prepared by RAFT polymerisation, where green represents PNIPAm001, red represents PNIPAm-002 and blue represents PNIPAm-003.

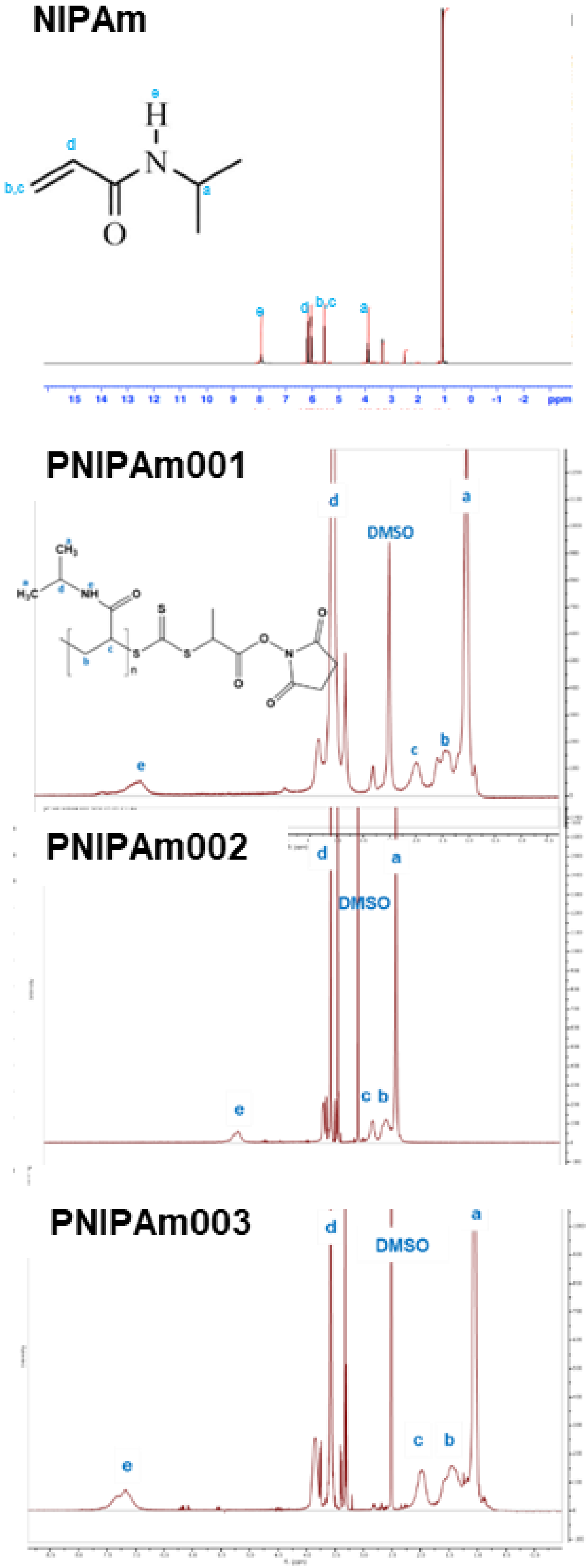

Figure S4. 5: 700 MHz ^{1}H NMR spectrum of LCST PNIPAm esters in DMSO-d6.

Chapter 5.

Development of all-in-one thermo-responsive theranostic MSNs

5.1 Introduction

Hepatocellular carcinoma (HCC) is a major contributor to cancer-related deaths worldwide, with a rising rate of incidence.[1] Unfortunately, most patients are diagnosed at an advanced stage, and even those who undergo surgery face a high recurrence rate. Traditional chemotherapy is challenging due to limited drug delivery to the tumour and high toxicity to healthy tissues, resulting in minimal clinical benefits.[2] Thus, there is a critical need for an effective drug delivery system targeting HCC, to enhance treatment efficacy and reduce systemic side effects. Utilising the ability to modify the external surface of MSNs with responsive materials, the development of stimuli-responsive theranostic MSNs is one approach to target and localise drug release within cancerous liver tissues, mitigating side effects while maintaining and monitoring the treatment efficiency.[3]

Numerous studies have reported the development of stimuli-responsive MSNs. These systems can be triggered by various stimuli, whether internal or external, such as changes in pH,[3] redox conditions,[4] temperature,[5] light,[6] enzymes,[7] or magnetic field.[8] Furthermore, hyperthermia, a technique involving the controlled elevation of temperature in the range of 38-45 °C, has demonstrated clinical effectiveness as a radiosensitiser and chemosensitiser without causing harmful side effects.[9, 10] This highlights the potential of employing temperature-responsive polymers to precisely control and localise drug release.

While nanoparticles grafted with poly(ethylene glycol) (PEG) are prevalent in non-responsive systems, nanoparticles based on poly(N-isopropylacrylamide) (PNIPAm) dominate the realm of thermo-responsive nanoparticles. Various approaches have been proposed to synthesise PNIPAm-modified MSNs, with the ultimate goal of the polymer molecules acting as gatekeepers, enabling the controlled opening and closing of pores through thermal stimulation. This is achieved by the polymer transitioning between soluble coil chains and insoluble globules, thereby regulating drug release.[11] Organic/inorganic composite synthesis generally involves surface activation, initiators, chain transfer agents, or other methods for post-synthesis functionalisation of MSNs.

A recent investigation has disclosed the successful development of temperature-controlled drug release from hollow MSNs decorated with lower critical solution temperature (LCST) poly(N-isopropylacrylamide-co-N-hydroxymethyl acrylamide) (P(NIPAm-co-NHMA)).[12] This system also demonstrated enhanced biocompatibility and stability. In another study, responsive MSNs using the LCST copolymer poly(N-isopropylacrylamide-co-methacrylic acid) (P(NIPAm-co-MAA)) have been developed and loaded with doxorubicin. The resulting nanoparticles demonstrated the ability to release drug in response to changes in temperature. Notably, these nanoparticles showed low cytotoxicity and were effectively internalised by HeLa cells.[13]

However, despite intensive research on PNIPAm/MSNs systems, the utilisation of UCST (upper critical solution temperature) functionalised MSNs remains relatively unexplored. These polymers hold significant promise in drug delivery due to their unique ability to transition to a soluble form during hyperthermia, allowing for controlled and targeted drug release.

Hei *et al.* developed dual-responsive MSNs for breast cancer using UCST poly(AM-co-AN) linked by disulfide bonds. This system demonstrated the ability to consistently release doxorubicin, and its release rate could dynamically adjust in response to changes in temperature and exposure to reducing agents.[14] Recently, Ramezanian *et al.* created UCST MSNs using poly(dimethylaminoethyl methacrylate) (PDMAEMA) via atom transfer radical polymerisation (ATRP). This system demonstrated responsiveness in cancerous tissues, and the use of high molecular weight PDMAEMA effectively regulated drug release, reducing leakage in physiological conditions and healthy cells.[15]

In this chapter, we synthesised thermo-responsive theranostic MSNs and conducted a comprehensive analysis of the functional performance of the all-in-one system. Our primary objective is to examine the impact of integrating temperature-responsive polymers on the release of both hydrophilic and hydrophobic drugs, as well as the accessibility of water to Gd-chelate anchored within the mesopores of MSNs. It is imperative to conduct a thorough investigation into how factors such as grafting density, polymer molecular weight, and grafting methodology influence the thermo-responsive characteristics of the entire system. Additionally, we will evaluate the effectiveness and cytocompatibility of this integrated responsive system.

5.2 Aims

In this chapter, our objective is to design a comprehensive theranostic system that can simultaneously regulate drug release and modulate MRI signals in response to temperature changes, based on an MRI active MSN scaffold. To achieve this goal, we conducted preliminary investigations into the impact of polymer grafting density, linker/spacer chain length, and polymer molecular weight using a range of techniques, including TGA, turbidimetry, DLS and relaxivity studies. The polymers investigated herein include UPD1-R, PNIPAm-002 and PNIPAm003 developed in Chapter 4.

Following this approach, we have successfully developed two thermo-responsive systems: one with UCST and another with LCST polymers on MSN surfaces. These systems were designed to incorporate doxorubicin and sorafenib, respectively, in addition to a positive MRI contrast agent covalently linked to internal MSN surfaces. We have confirmed the thermo-responsive behaviour of these systems using DLS and studied drug release at various temperatures. Finally, we evaluated the efficacy and safety of the developed theranostic systems through NMRD, clinical phantom MRI imaging, and *in vitro* cytotoxicity studies.

5.3 Experimental

5.3.1 Materials

Sodium bicarbonate, sodium carbonate, N-hydroxysuccinimide (NHS), sodium hydroxide (NaOH), hydrochloric acid (HCl, 37%), 2-(N-Morpholino)ethanesulfonic acid (MES), 1-ethyl-3-(3-dimethylaminopropyl)carbodiimide (EDC), Dulbecco’s Modified Eagle’s Medium, containing 4500 mg/L glucose and L-glutamine (DMEM), along with trypsin containing EDTA and dimethyl sulfoxide (DMSO), were procured from Sigma Aldrich. Penicillin-streptomycin and Dulbecco's phosphate buffered saline (DPBS) were obtained from Life Technologies, while fetal bovine serum (FBS) was from Gibco. We used 96-well flat bottom plates from Nunc. The PrestoBlue™ cell viability reagent was acquired from Invitrogen by Thermo Scientific™, and ethoxy silane functionalised polyethylene glycol (Silane-PEG2K-NH_2, 2000 g/mL) was purchased from Nanocs.

5.3.2 Methodology

5.3.2.1 Synthesis of aminated HMSNs@Gd

Mesoporous silica nanoparticles loaded with Gd-chelate on their internal surfaces (core location) were prepared according to Section 3.3.2.2, and amine groups were introduced onto their exterior surface. This is achieved by dispersing 50 mg of the nanoparticles (HMSNs@Gd) in an aqueous ethanolic solution (10 mL, 2:1 ethanol : water v/v) and subsequently adding either varying grafting densities of APTES (Mw 160.27 g/mol) at 0.2, 0.75, 1, and 2.5 mol% or silane-PEG2K-NH_2 (Mw 2000 g/mol) at 0.75 mol% relative to the number of moles of silica used in the initial nanoparticle preparation, as displayed in Figure 5. 1.

The reaction mixture was stirred overnight at room temperature, allowing the silane amine to graft onto the nanoparticles' surface. After the grafting process, the particles were washed three times with ethanol using centrifugation at 15300 rpm for 20 minutes to remove any unreacted APTES or silane-PEG2K-NH_2. Finally, the modified nanoparticles were stored in ethanol for further characterisation.

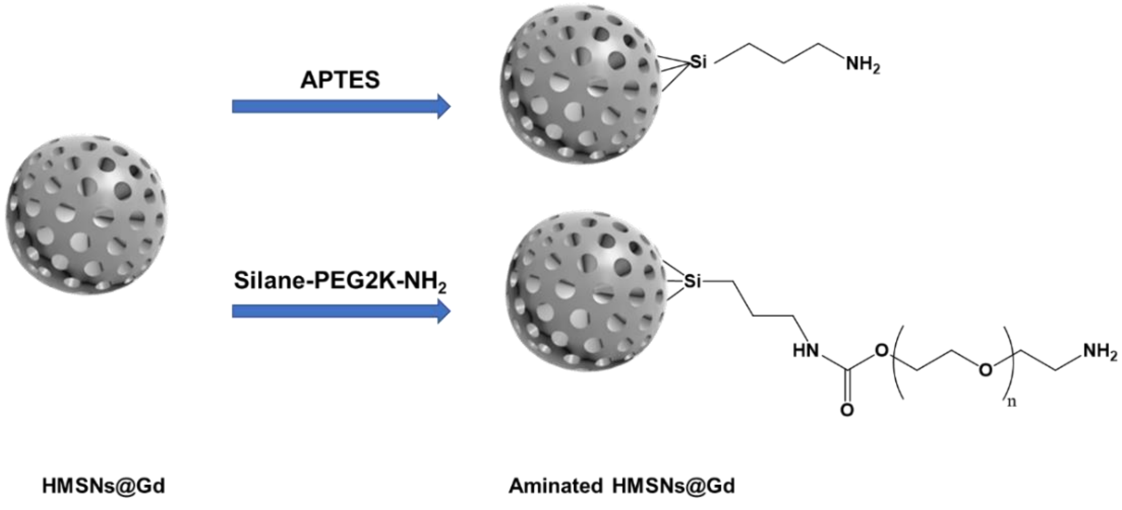

Figure 5. 1: Schematic representation of amine group grafting onto the external surface of MSNs using either APTES or silane-PEG2K-NH_2.

5.3.2.2 Grafting of LCST PNIPAm onto aminated HMSNs@Gd

To graft PNIPAM-NHS ester on the surface of aminated MSNs, the prepared aminated HMSNs@Gd (100 mg, Section 5.3.2.1) were dispersed into 30 mL of anhydrous THF and 1 mL of triethylamine. Subsequently, varying amounts of PNIPAm-NHS ester, as prepared in Chapter 4, were introduced based on the molecular weight of PNIPAm002, and 003 to achieve different grafting densities of 0.2, 0.6, 1, and 2.5 mol% when using APTES as a spacer (at concentrations of 0.2, 0.75, 1, and 2.5 mol% respectively), as shown in Figure 5. 2 and Table 5. 1. A grafting density of 0.6 mol% was applied when employing silane-PEG2K-NH_2, grafted at a concentration of 0.75 mol%, as demonstrated in Figure 5. 3 and Table 5. 1. These percentages were calculated in relation to the initial number of moles of aminated HMSNs@Gd. The mixture was stirred at room temperature overnight, enabling the polymer to adhere to the surface of the nanoparticles. Following this grafting procedure, the particles underwent three rounds of washing with water *via* centrifugation at 15300 rpm for 20 minutes to eliminate any free polymer. Ultimately, the modified nanoparticles were stored in water for subsequent analysis.

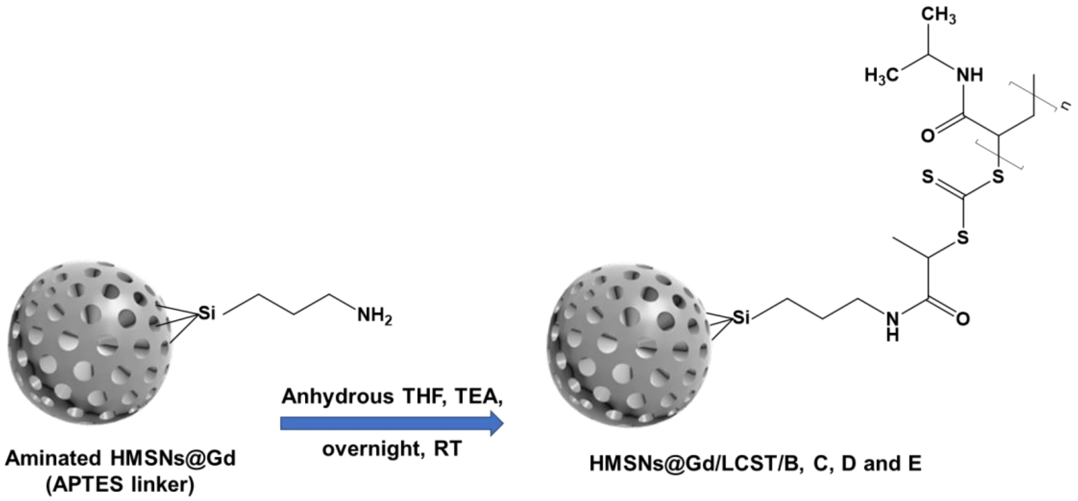

Figure 5. 2: Grafting of PNIPAm-NHS ester (PNIPAm002 and PNIPAm003 with Mw of 20,300 and 68,000 g/mol, respectively) onto aminated hydrophilic MSNs loaded with Gd (HMSNs@Gd) using APTES as a linker to produce HMSNs@Gd/LCST B, C, D and E according to the polymer and the grafting density.

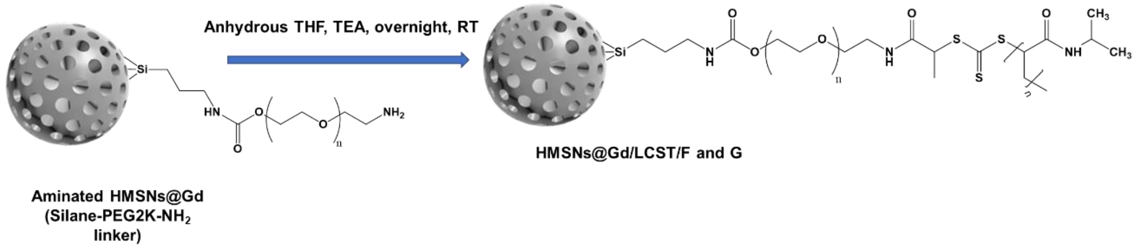

Figure 5. 3: Grafting of PNIPAm-NHS ester (PNIPAm002 and PNIPAm003 with Mw of 20,300 and 68,000 g/mol, respectively) onto aminated hydrophilic MSNs loaded with Gd (HMSNs@Gd) using silane-PEG-2K-NH$_2$ as a linker to produce HMSNs@Gd/LCST F and G according to the polymer grafted.

5.3.2.3 Grafting of UCST poly(AAm-AN) onto aminated HMSNs@Gd

To prepare UCST-grafted MSNs, the initial step involved dispersing aminated HMSNs@Gd (100 mg, Section 5.3.2.1) pre-prepared with 0.75 mol% of either APTES or silane-PEG2K-NH$_2$ (Figure 5. 4 and Figure 5. 5, respectively) in a bicarbonate buffer (20 mL, pH 8.5) at a temperature of 50 °C. Simultaneously, in a separate flask, a mixture was prepared consisting of MES buffer (5 mL, pH 5.5), poly(AAm-co-AN) (UPD1-R, 0.1 mol%), EDC (0.2 mol%), and N-hydroxysuccinimide (0.4 mol%). This solution was allowed to undergo activation at room temperature for 20 minutes. Subsequently, the MES-reagent solution was introduced into the bicarbonate solution while stirring, and the mixture was left to react for 24 hours at 50 °C. The resulting nanoparticles were washed with hot water three times via centrifugation before being dispersed in water (Table 5. 1).

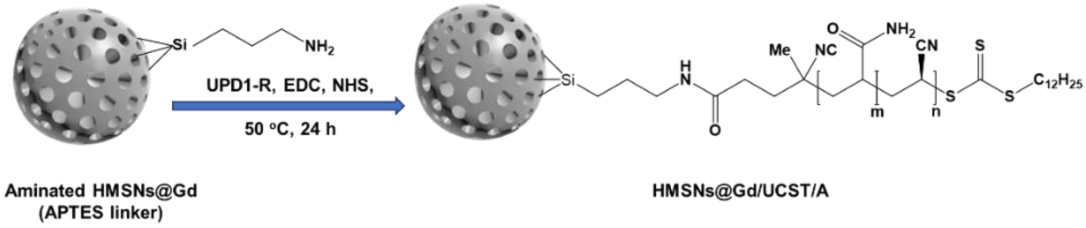

Figure 5. 4: Grafting of poly(AAm-co-AN) onto aminated hydrophilic MSNs loaded with Gd (HMSNs@Gd) using APTES as a linker to produce HMSNs@Gd/UCST/A.

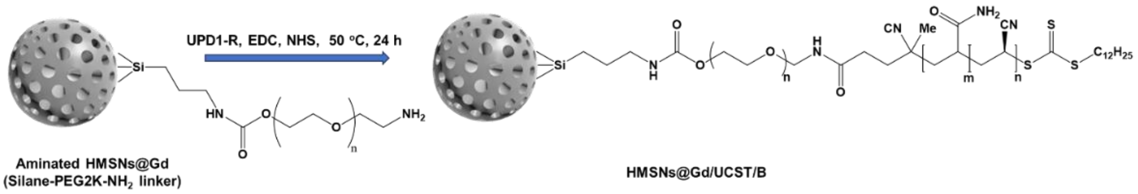

Figure 5. 5: Grafting of poly(AAm-co-AN) onto aminated hydrophilic MSNs loaded with Gd (HMSNs@Gd) using silane-PEG-2K-NH_2 as a linker to produce HMSNs@Gd/UCST/B.

5.3.2.4 Synthesis of all-in-one theranostic MSNs

5.3.2.4.1 Doxorubicin HCl loaded HMSNs@Gd/UCST (HMSNs@Gd/UCST/Dox)

In order to load the hydrophilic drug doxorubicin HCl into MSNs, the process involved two main steps. Initially, UCST grafted MSNs (HMSNs@Gd/UCST/B) were prepared as detailed in Section 5.3.2.3. Subsequently, 200 mg of the nanoparticles were dispersed in a concentrated aqueous solution of doxorubicin (5 mg/mL) at a weight ratio of 2:1 (Dox: MSNs w/w). The dispersions were then stirred overnight at 50 °C to facilitate the polymer's structural confirmation, ensuring the presence of soluble open chains that allow the encapsulation of doxorubicin within the MSNs as displayed in Figure 5. 6.

To eliminate any excess or unbound doxorubicin, the dispersions were immersed in cold water for a duration of 10 minutes. Afterward, centrifugation was carried out at 15,300 rpm for another 10 minutes at 15 °C. The resulting supernatant was meticulously removed. The loaded HMSNs@Gd/UCST/Dox nanoparticles were subjected to three further washings using centrifugation at 15,300 rpm for 10 minutes and cold water. These cold washes were crucial to modify the polymer's conformation, preventing premature drug release. Finally, the nanoparticles containing the loaded doxorubicin were dispersed in water for storage.

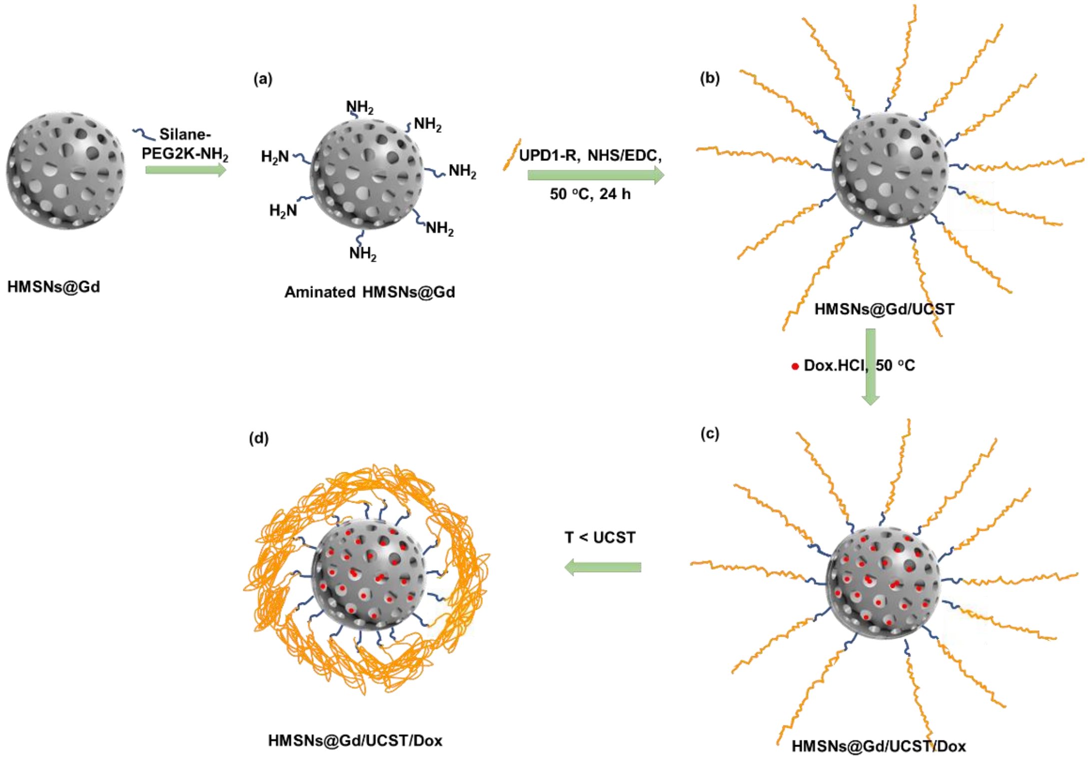

Figure 5. 6: Graphical representation of the synthesis of doxorubicin-loaded thermo-responsive MSNs.

5.3.2.4.2 Sorafenib tosylate loaded HMSNs@Gd/LCST (HMSNs@Gd/LCST/Sor)

For the loading of sorafenib, 200 mg of aminated HMSNs@Gd (modified with 0.75 mol% silane PEG-2K-NH$_2$) were combined with a concentrated sorafenib solution in tetrahydrofuran (1 mg/mL) at a 1:1 ratio (w/w) of sorafenib to MSNs. Detailed procedures are outlined in Section 3.3.2.3.2. The resulting mixture was stirred overnight at room temperature. Subsequently, the solvent was gradually removed at 60°C until about 2 mL of solvent remained.

Next, the grafting of LCST PNIPAm003 was performed. 200 mg of sorafenib-loaded nanoparticles were dispersed in 30 mL of anhydrous THF and 1 mL of triethylamine. Then, PNIPAm003 was added to achieve a grafting density of 0.6 mol%, considering silane-PEG2K-NH$_2$ linker was at 0.75 mol% (Figure 5. 7). The dispersion was left to stir overnight at room temperature. Afterward, the dispersion was subjected to centrifugation at 15,300 rpm for 10 minutes at 40 °C to separate the unloaded free drug and ungrafted polymer in the supernatant. Following centrifugation, HMSNs@Gd/LCST/Sor were washed once with THF. Then, they underwent three washes with warm water using centrifugation. Finally, the nanoparticles were dispersed in water for storage.

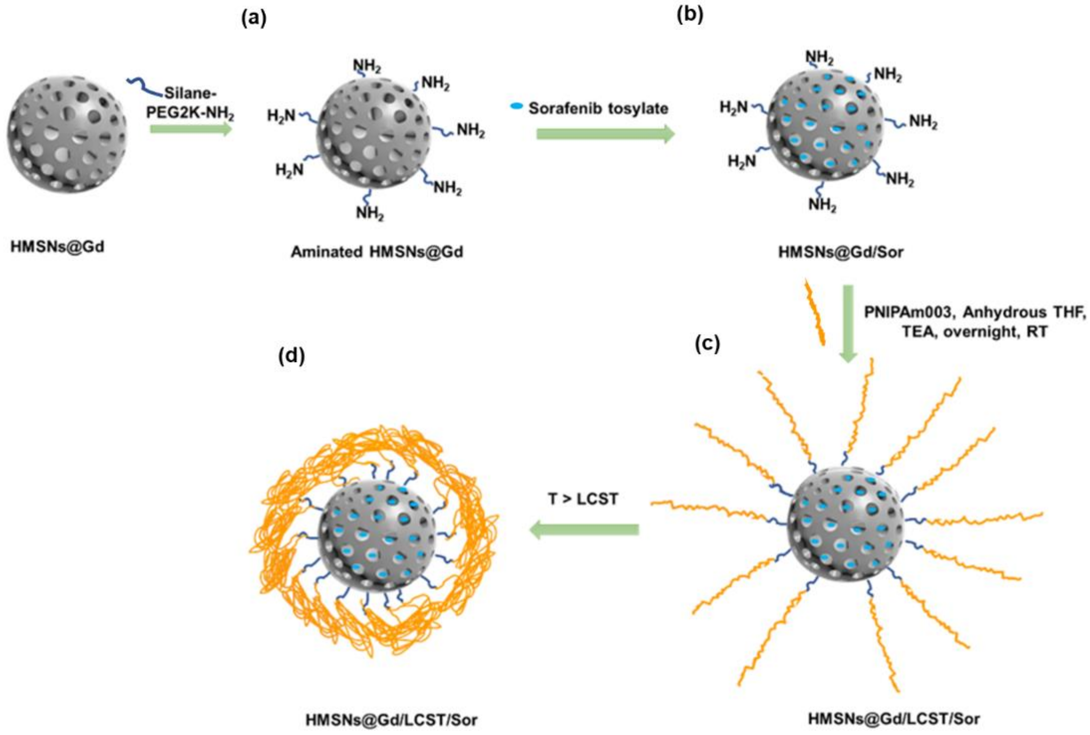

Figure 5. 7: Graphical representation of the synthesis of sorafenib-loaded thermo-responsive MSNs.

5.3.2.5 Relaxivity and MRI studies

An Oxford Instruments MQC+ benchtop NMR analyser with a resonant frequency of 23.4 MHz (single-field relaxometry) was used to determine the relaxivity (r_1) of Gd^{3+}-loaded nanoparticles dispersed in either ultrapure water or drug release media at different temperatures, as discussed in Chapter 3, Section 3.3.2.5.

Nuclear magnetic resonance dispersion (NMRD) profiles were measured on an HTS-110 3T Magnet System for magnetic fields from 10 MHz to 128 MHz (fast-field cycling relaxometry). NMRD profiles were recorded at 25 and 37 °C. Samples were dispersed in 1 mL of ultrapure water and were carefully sonicated prior to measurement.

T1-weighted magnetic resonance (MR) images were obtained of polymer grafted MSNs with and without drug. The imaging was conducted using a 3 T Philips Ingenia CX MRI scanner (Philips Healthcare) employing a 3D T1-weighted gradient−echo sequence. The imaging parameters were set as follows: repetition time (TR = 7 ms), echo time (TE = 3.5 ms), field of view (FOV) = 200 x 200 x 60 mm^3, resolution = 600 x 600 µm, and slice thickness = 0.6 mm. The dispersions of polymer grafted MSNs in ultrapure water with a Gd^{3+} concentration of 0.05 mM were measured at three different temperatures: 23 °C, 39 °C, and 48 °C. The phantom imaging were recorded by Prof Geoff JM Parker and Dr. Mina Kim from the Centre for Medical Image Computing, University College London.

Inductively coupled plasma optical emission spectroscopy (ICP-OES) was employed to measure gadolinium concentration as described previously in Chapter 3, Section 3.3.2.6.

5.3.2.6 Cytotoxicity assay

To assess the cytotoxicity of the formulations, human liver cancer cells (Huh-7) and human embryonic kidney cells (HEK 293) were used. Both cell lines were cultured at 37 °C under 5 % CO_2, in Dulbecco's modified Eagle's medium with high glucose and L-glutamine (DMEM, 445 mL). The medium was supplemented with penicillin-streptomycin (5 mL) and fetal bovine serum (50 mL). Cell cultures were passaged when they reached 70-90% confluence, using a trypsin solution (0.25% in EDTA, 2 mL). For cell viability experiments, cells with passage numbers under 20 were employed for both Huh-7 and HEK-293.

To determine the cytotoxicity of free-form doxorubicin and sorafenib, as well as MSNs loaded with these drugs, 96-well plates were seeded with Huh-7 and HEK-293 cells at a density of $1x10^4$ and $2.4x10^4$ cells per well, respectively (90 µL per well). The plates were then incubated for 24 hours at 37 °C in a 5% CO_2 environment. Subsequently, the cells were exposed to varying concentrations of both drugs and incubated for an additional 24 hours at 37 °C.

Doxorubicin and sorafenib were assessed over a concentration range spanning from 0.2 µg/mL to 50 µg/mL. After treating the cells with the drugs, they were washed once with sterile PBS before introducing PrestoBlue™ reagent (10 µL to 90 µL media). The reagent was then allowed to incubate for 2 hours, after which absorbance values were measured at both 570 nm and 600 nm. All treated cells were compared to control untreated cells, which were considered 100% viable and treated with complete media. The data were expressed as the mean ± SD of triplicate experiments.

5.3.2.7 Physicochemical characterisation

Dynamic light scattering (DLS), Fourier-transform infrared spectroscopy (FTIR) and thermogravimetric analysis (TGA) were performed as described in Chapter 3 (Section 3.3.2.6). Drug release studies were performed as described previously in Section 3.3.2.4. The cloud point of the polymers was determined using turbidimetry as well as dynamic light scattering (DLS) as previously described in Chapter 4 (Section 4.3.2.5).

5.3.2.8 Statistical analysis

The data were expressed as mean values with their respective standard deviations. Statistical analysis of cell culture data was conducted employing Prism 7.0 software (GraphPad Software). Two-way ANOVA followed by Tukey's multiple comparison test was used to compare more than two groups and their interaction. Statistical significance was defined as p-values below 0.05.

5.4 Results and discussion

5.4.1 Grafting of thermo-responsive polymers to MSNs

To create all-in-one theranostic thermo-responsive MSNs, we first introduced the thermo-responsive polymers synthesised in Chapter 4 onto the external surface of the MSNs which were internally loaded with a Gd-chelate (as described in Chapter 3). This was achieved by varying grafting densities, employing polymers of different molecular weights, and utilising spacer linkers such as APTES or silane-PEG2K-NH_2 as detailed in Table 5. 1. The aim was to investigate the impact of these variables on the overall performance of the responsive system.

Table 5. 1: Polymer grafted MSNs using either the LCST polymers (PNIPAm002 or PNIPAm003) or UCST polymer (UPD1-R) with APTES or silane-PEG2K-NH_2 as a linker.

Formulae codes	Grafted polymer	Linker Grafting density (mol%)	Polymer Grafting density (mol%)	Linker/ spacer
HMSNs@Gd/LCST/A	PNIPAm002	0	2.5	None / control
HMSNs@Gd/LCST/B	PNIPAm002	0.2	0.2	APTES
HMSNs@Gd/LCST/C	PNIPAm002	1	1	APTES
HMSNs@Gd/LCST/D	PNIPAm002	2.5	2.5	APTES
HMSNs@Gd/LCST/E	PNIPAm002	0.75	0.6	APTES
HMSNs@Gd/LCST/F	PNIPAm002	0.75	0.6	Silane-PEG2K-NH_2
HMSNs@Gd/LCST/G	PNIPAm003	0.75	0.6	Silane-PEG2K-NH_2
HMSNs@Gd/UCST/A	UPD1-R	0.75	0.1	APTES
HMSNs@Gd/UCST/B	UPD1-R	0.75	0.1	Silane-PEG2K-NH_2

- Mw of LCST (PNIPAm002) = 20,300 g/mol, cloud point = 32.9 °C.
- Mw of LCST (PNIPAm003) = 68,000 g/mol, cloud point = 34.6 °C.
- Mw of UCST (UPD1-R) = 120,500, cloud point = 36.5 °C.

To assess the influence of grafting density, the NHS-ester PNIPAm-002 was grafted at different molar densities (0.2, 1, and 2.5 mol%) onto aminated

HMSNs@Gd with equivalent amine molar modification; these samples were labelled HMSNs@Gd/LCST/B, C, D, respectively, with a control sample where the polymer was added to MSNs with no amine modification to ensure that behaviour observed was not due to physisorption alone in sample HMSNs@Gd/LCST/A. This grafting process occurred in a single step under anhydrous conditions, utilising APTES as a linker in the first case, as shown in Figure 5. 2. FTIR and TGA analyses were evaluated to assess the success of the grafting.

The absorption bands of PNIPAm at 3300, 1650, and 1540 cm^{-1}, representing N–H stretching, C=O stretching, and N-H bending, respectively, aligned with those of HMSNs@Gd/LCST/D when the maximum polymer grafting density was used. At lower densities, the polymer stretches were not strong enough to be observed. However, these peaks coincided with the silica absorption peaks, making it challenging to clearly differentiate them at lower polymer grafting densities (Figure 5. 8).[16, 17] In addition, it is clear that the control sample does not appear to have polymer bands associated with it, despite using a high amount, indicating that the grafting process was likely successful and physisorption was unlikely to be occurring.

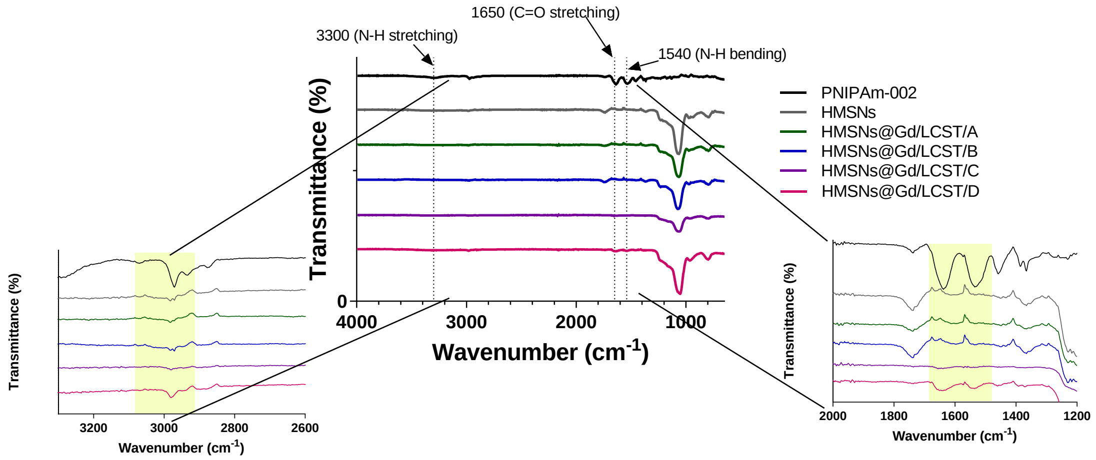

Figure 5. 8:FTIR spectra of LCST PNIPAm-NHS ester grafted onto hydrophilic MSNs with different grafting densities.

In Figure 5. 9, TGA showed the success of PNIPAm002 grafting. The higher the grafting density the higher the weight loss between 300-450 °C due to polymer degradation (4.8, 7.1 and 10.2 % in case of HMSNs@Gd/LCST/B,C and D, respectively). TGA showed that the presence of the linker is necessary for the success of grafting, since no weight loss occurs in HMSNs@Gd/LCST/A (control sample, prepared by mixing HMSNs@Gd and PNIPAm002 under the same reaction conditions, to evaluate if there is any physisorption or polymer adsorption). It should be noted that there is no mass loss associated with degradation of Gd-chelate species on the MSNs because the grafting density is so low (as previously noted in Chapter 3).

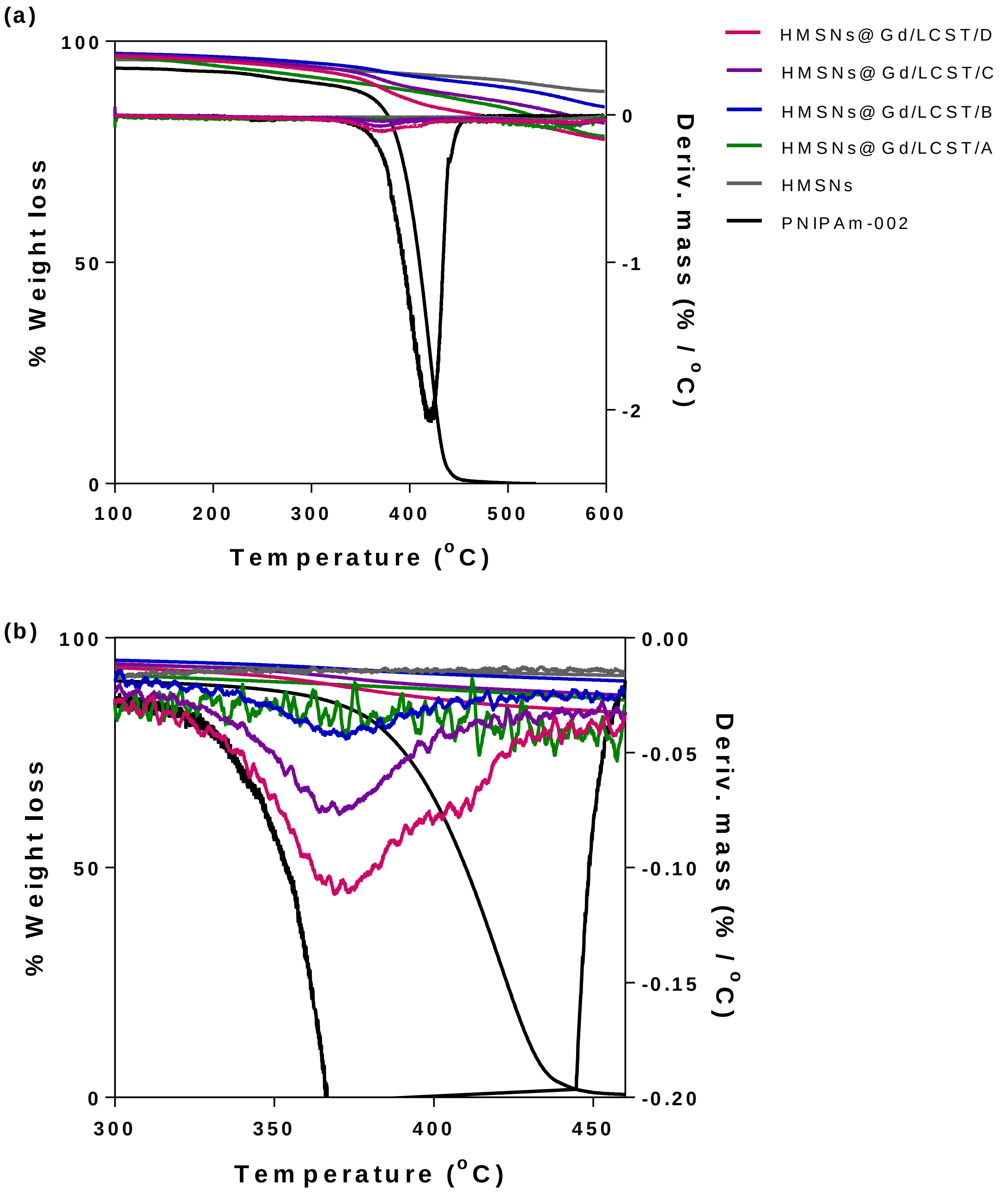

Figure 5. 9: TGA of LCST PNIPAm-NHS ester grafted onto hydrophilic MSNs with different grafting densities where (a) represents the weight loss occurred at the temperature range of 100-600 ºC while (b) represents the temperature range of 300-450 ºC.

To explore the impact of polymer grafting density on the thermo-responsive characteristics of the prepared MSNs, turbidimetry studies were conducted using 5 mg of HMSNs@Gd/LCST in aqueous suspension. To mitigate the scattering influence arising from the nanoparticles, the transmittance data were normalised. The transition temperatures recorded were 36.5 °C, 48.0 °C, and 41.7 °C during heating, and 23.8 °C, 45.8 °C, and 36.2 °C during cooling for HMSNs@Gd/LCST/B, HMSNs@Gd/LCST/C, and HMSNs@Gd/LCST/D, respectively as shown in Figure 5. 10.

It is worth noting that while the free polymer PNIPAm002 exhibited transition temperatures of 32.9 °C and 24.3 °C upon heating and cooling, respectively, as previously discussed in Chapter 4 (Section 4.4.2), the difference in the transition temperatures of the free and grafted polymer can be attributed to the polymer's rigidity and steric hindrance on the MSNs' surface. This results in greater energy being required to transition the soluble open coils into insoluble globules. However, the grafting density of 2.5 mol% demonstrated a lower energy requirement than that of 1 mol%. This can be elucidated by the closer proximity of polymer chains at higher grafting densities, facilitating the formation of both intermolecular and intramolecular hydrogen bonds.[18, 19]

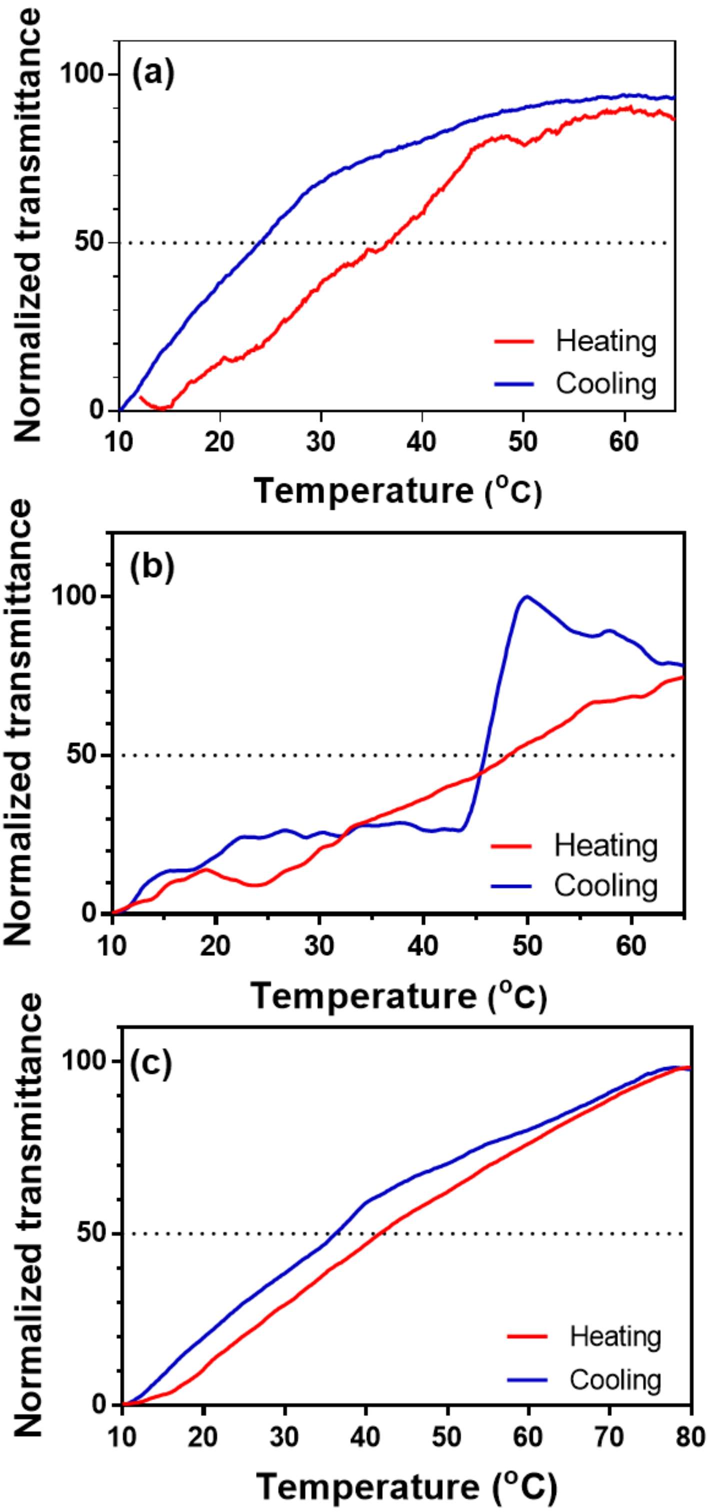

Figure 5. 10: Turbidimetry plots of (a) HMSNs@Gd/LCST/B, (b) HMSNs@Gd/LCST/C, and (c) HMSNs@Gd/LCST/D in water (5 mg/mL), measured at 500 nm using UV-Vis, data represented as mean of three cycles.

Relaxivity values were evaluated to study how varying grafting densities of PNIPAm002 can affect the water accessibility to the paramagnetic center.

The relaxivity values at 23 MHz of both the initial HMSNs@Gd and the polymer-grafted MSNs were measured and assessed at temperatures of 25 °C and 45 °C. For MSNs loaded with Gd chelate, alterations in temperature impact the relaxivity values due to changes in Brownian motion and τ_R. Therefore, we consistently represent the change in r_1 (as percentage) to facilitate a clearer comparison with the parent sample at each temperature. This normalisation accounts for shifts in the particle behaviour attributed to the polymer grafted, rather than focusing on the temperature effect.

Upon employing a grafting density of 1 mol% (HMSNs@Gd/LCST/C), at 25 °C, there was a 10.8% increase in r_1 compared to the MSNs only due to the expansion of the polymer structure, impacting τ_R and boosting r_1. However, at 45 °C, the polymer contracted into insoluble globules, limiting water access to the Gd contrast agent, and reducing τ_R, leading to an overall decrease of ~25% in r_1 value, and 14.7% decrease compared to the parent HMSNs (Figure 5. 11). A similar trend was noted in HMSNs@Gd/LCST/B (0.2 mol%). However, the extent of change was less apparent because of the low grafting density.

At a grafting density of 2.5 mol% (HMSNs@Gd/LCST/D), the pattern reversed. The relaxivity decreased by half at 25 °C (52%) but increased to nearly the same value as the parent HMSNs@Gd at 45 °C (Figure 5. 11). This phenomenon may have occurred because the high grafting density of 2.5 mol% impeded water access to Gd-chelate. In this scenario, heating becomes essential to facilitate water accessibility, effectively switching on the MRI signal.

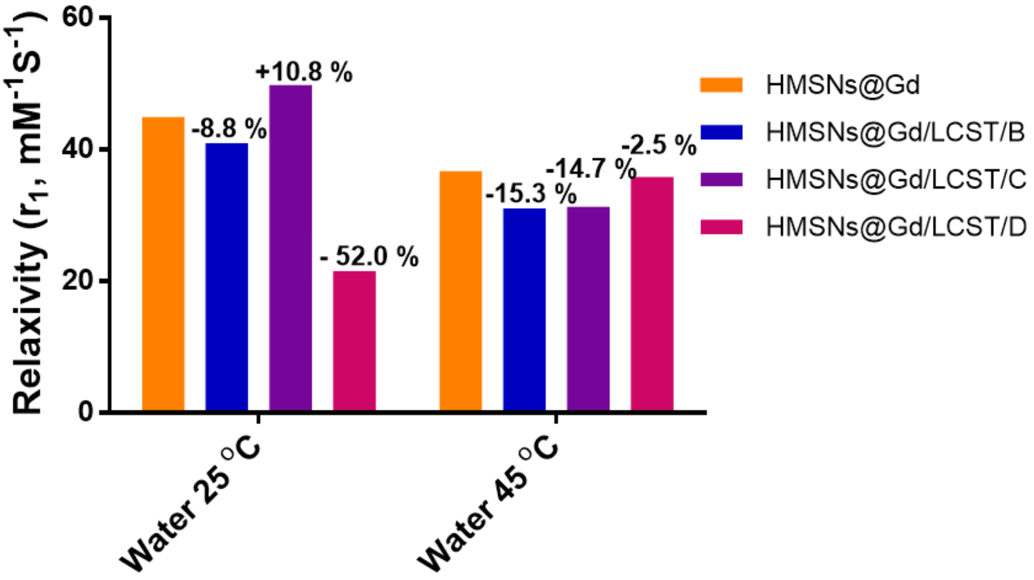

Figure 5. 11: ^{1}H r_1 relaxivity values of *LCST PNIPAm-NHS ester grafted onto hydrophilic MSNs with different grafting densities at 23.4 MHz.*

Having successfully confirmed the polymer grafting utilising APTES as a linker, and noting that the grafting density had a significant impact on both the thermo-responsive behaviour and MRI signal at different temperatures, our next objective was to investigate the influence of linker chain length between the polymer and the MSNs. We aimed to make this comparison while maintaining the same grafting density for both APTES and silane-PEG2K-NH_2 at 0.75 mol%.

The use of silane-PEG2K-NH_2 for grafting responsive polymers onto the surface of MSNs has been previously explored in the literature.[20, 21] The long chain of silane-PEG2K-NH_2 allows unrestricted polymer conformational changes. However, it is crucial to limit the grafting density of PEG to low values to prevent diffusion into the mesopores, which could affect drug release and hinder water accessibility.[21] As a result, we opted for a low chain-length PEG (PEG 2000) and a grafting density of 0.75 mol% to achieve the right balance in our study. We grafted the LCST polymer PNIPAm002 onto HMSNs@Gd, employing either APTES or silane-PEG2K-NH_2 as a linker, with a polymer grafting density of 0.6 mol%. The impact of the linker was assessed using turbidimetry as well as relaxivity values.

The transition temperature according to turbidimetry was observed to shift to higher values when utilising silane-PEG2K-NH_2 as the linker (Figure 5.

12). This shift can be attributed to the enhanced mobility of polymer associated with PEG2K-NH_2, which provides sufficient space for the soluble chains of LCST polymer that hinders both inter and intra-polymer interactions upon heating, therefore requiring higher temperatures to facilitate the composition change.

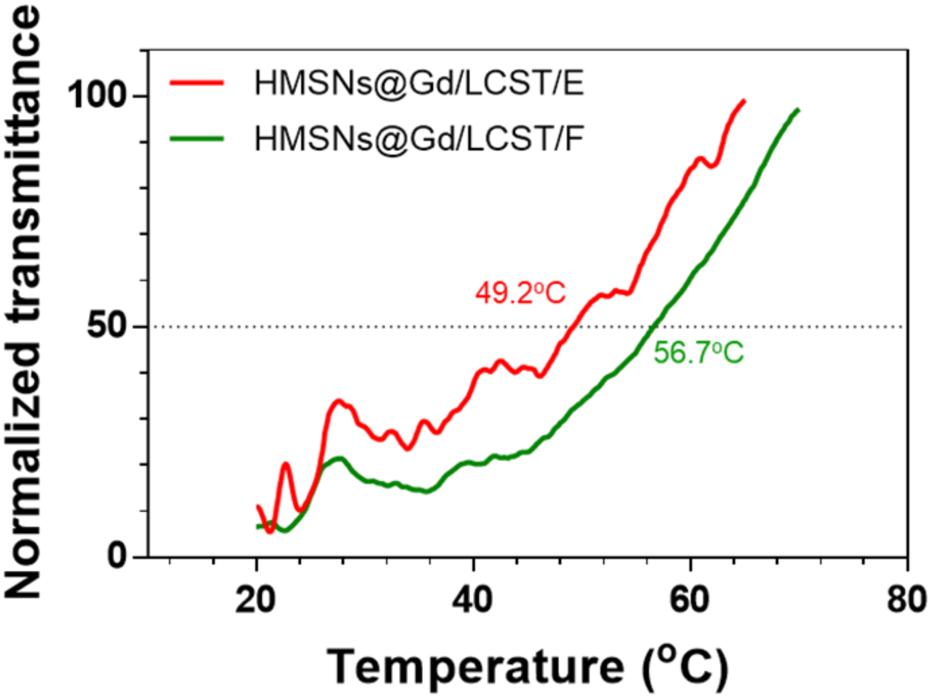

Figure 5. 12:Turbidimetry plots of heating cycles of HMSNs@Gd/LCST prepared using different linkers at 500 nm in water (5 mg/mL) measured using UV-Vis.

As can be seen in Figure 5. 13, at a temperature of 25 °C, the incorporation of APTES led to a 68.7% reduction in relaxivity (r_1) compared to HMSNs. This reduction changed slightly to 61% upon heating to 45 °C. The primary reason for this slight decline may be due to the short chain length of APTES. This hinders water access to the anchored paramagnetic centre within the pores, primarily due to the constrained nature of the grafted polymer, which may obstruct the pores irrespective of its conformational transition.

Conversely, silane-PEG2K-NH_2 (HMSNs@Gd/LCST/F) led to a decrease in r_1 compared to HMSNs, due to the presence of polymers of the surface leading to some obstruction of water accessibility to the internalised

Gd, this decrease was less compared to the amine-linked sample (HMSNs@Gd/LCST/E). The relaxivity increased with increasing temperature when compared to the parent HMSNs@Gd at 45 °C. This behaviour is attributed to the higher mobility of PNIPAM002 when grafted using the long chain silane-PEG2K-NH2, which permits the globular polymer to contract, thereby exposing the pores and facilitating water interaction with the Gd-chelate.

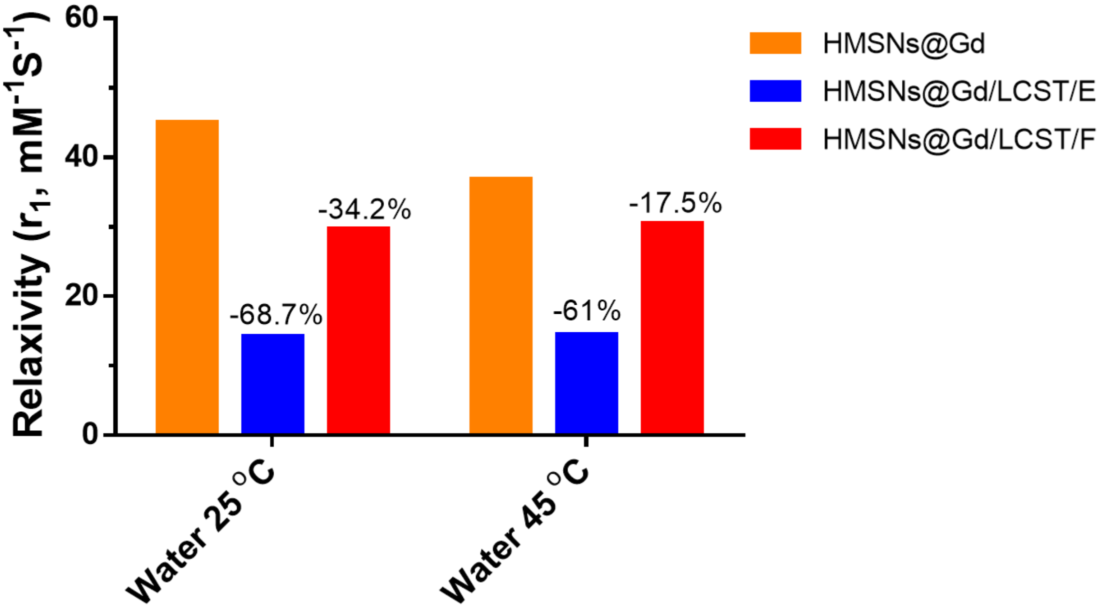

Figure 5. 13: ^{1}H r_1 relaxivity values of LCST PNIPAm-NHS ester grafted onto hydrophilic MSNs with different linker/spacer. Data obtained at 23.4 MHz.

The impact of polymer molecular weight on MRI signal modulation was next explored using the same linker, silane-PEG2K-NH2, and maintaining a grafting density of 0.75 mol%. Two different polymers, PNIPAm002 (with a molecular weight of 20,300 g/mol) and PNIPAm003 (with a molecular weight of 68,000 g/mL) prepared in Chapter 4, were grafted onto the system and relaxivity studies were conducted. This produced samples HMSNs@Gd/LCST/F and HMSNs@Gd/LCST/G respectively.

Comparing these results to the parent sample, HMSNs@Gd, we observed that HMSNs@Gd/LCST/F (PNIPAm002) exhibited a similar decrease in relaxivity at 25 °C and 30 °C by 34.2% and 34.4%, respectively. However, upon heating to 45 °C, the relaxivity r_1 only decreased by 17.5% (Figure 5. 14). In contrast, HMSNs@Gd/LCST/G (PNIPAm003) showed a notable increase in r_1 of 41.4% and 37.6% at 25 °C and 30 °C, respectively, when compared to the parent HMSNs. Nevertheless, there was an abrupt drop to 67.8% at 45 °C as displayed in Figure 5. 14. This phenomenon can be explained by considering that longer polymer chain lengths result in a more pronounced τ_R effect and improves water accessibility within the extended, soluble polymer chains below the cloud point. However, at 45 °C, the transition of the polymer into insoluble globules affects both τ_R and water accessibility, particularly when using the longer chain polymer (PNIPAm003).

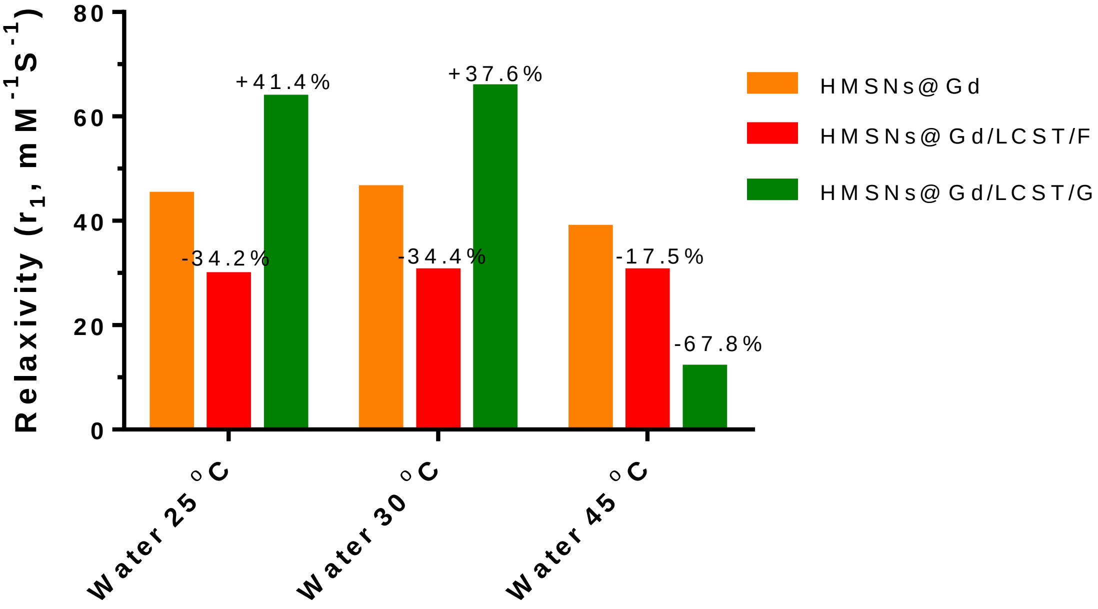

Figure 5. 14: H r_1 relaxivity values of *LCST PNIPAm-NHS ester with different molecular weight grafted onto hydrophilic MSNs. Data recorded at 23.4 MHz.*

5.4.2 All-in-one theranostic thermo-responsive MSNs

After investigating how different grafting variables affect the performance of the responsive system, we decided to utilise silane-PEG2K-NH_2 as a linker to prepare the all-in-one theranostic systems as detailed in

Sections 5.3.2.4.1 and 5.3.2.4.2 due to their MRI performance. This choice is based on to the high molecular weight of both polymers involved (68,000 g/mol and 120,500 g/mol for PNIPAm003 and UPD1-R, respectively), necessitating a longer chain linker to facilitate improved mobility. Moreover, it is worth noting that PEGylated nanoparticles have been reported to enhance colloidal stability, resulting in a more homogeneous polymer coating.[22]

The preparation of all-in-one formulations were evaluated using TGA and DLS. TGA analysis has confirmed both polymer grafting and drug loading. For HMSNS@Gd/UCST/Dox, Figure 5. 15 illustrates the weight loss occurring in the temperature range of 200-250 °C, which corresponds to the degradation of doxorubicin. The weight loss within the range of 250-500 °C is attributed to UPD1-R. In the case of HMSNs@Gd/LCST/Sor, Figure 5. 16 demonstrates the weight loss in the range of 200-300 °C, specific to sorafenib degradation, as well as within the temperature range of 350-450 °C, associated with PNIPAm003.

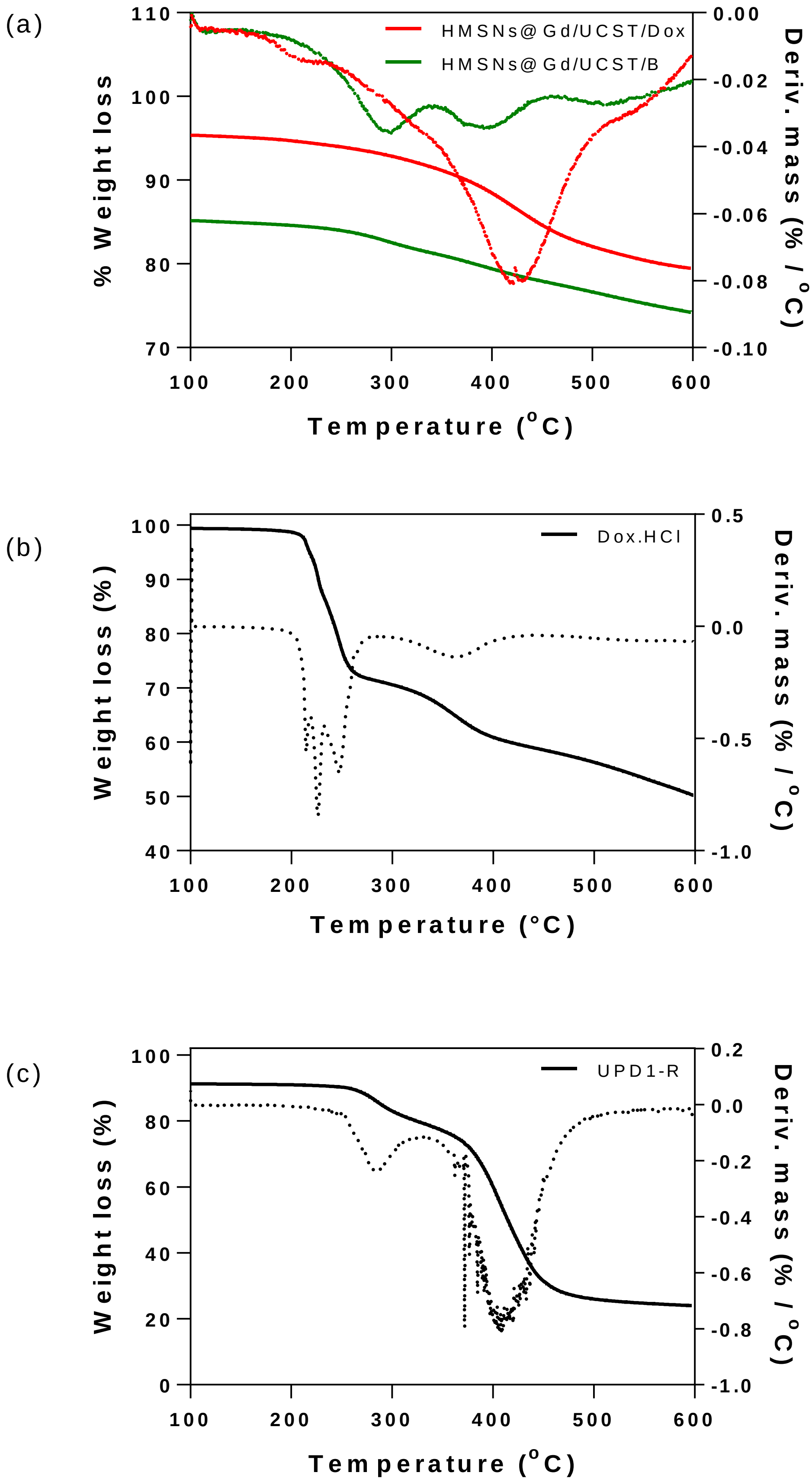

Figure 5. 15: TGA of (a) HMSNs@Gd/UCST/B and HMSNs@Gd/UCST/Dox, (b) Doxorubicin.HCl, and (c) UPC1-R. Weight loss percentages (%) are represented by solid lines, while the first derivative is depicted using dotted lines.

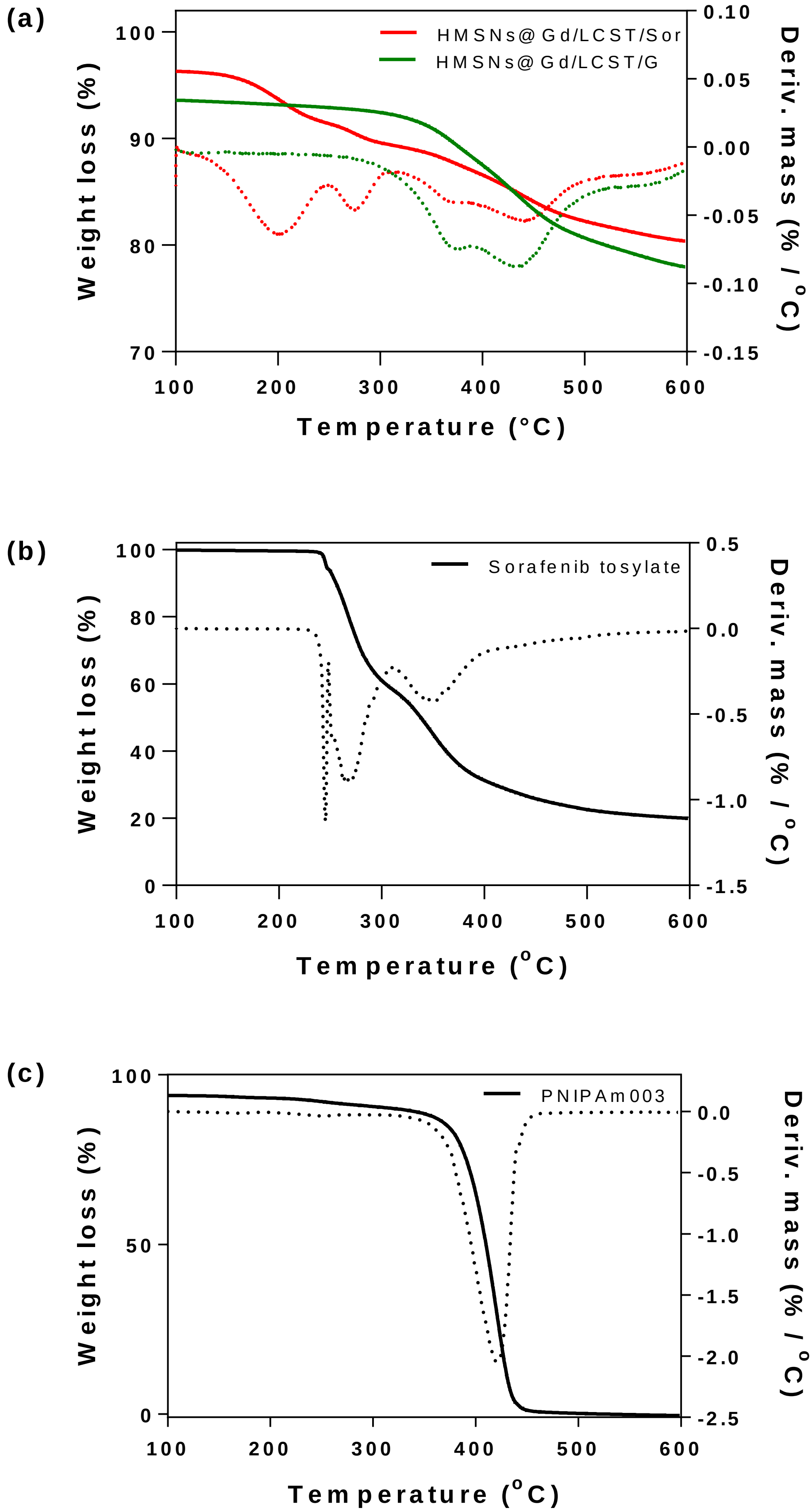

Figure 5. 16:Thermogravimetric analysis (TGA) of (a) HMSNs@Gd/LCST/G and HMSNs@Gd/LCST/Sor, (b) sorafenib tosylate and (c) PNIPAm003. Weight loss percentages (%) are represented by solid lines, while the first derivative is depicted using dotted lines.

Table 5. 2: DLS measurements in water at 25 °C, and DLC and EE evaluated using UV/Vis and HPLC for doxorubicin and sorafenib, respectively.

Formulae	**Particle size (D_{H})[a*] (nm)**	**Polydispersity index (PdI)[b*]**	**ζ-potential (mV)[*]**	**DLC (%)**	**EE (%)**
HMSNs@Gd	164.5 ± 6.0	0.2 ± 0.1	-16.3 ± 0.1	---	---
HMSNs@Gd/Dox	221.8 ± 8.4	0.2 ± 0.01	-18.7 ± 1.5	24.2 ± 5.6	11.4 ± 2.6
HMSNs@Gd/Sor	202.1 ± 8.1	0.2 ± 0.1	-23.9 ± 1.80	46.3 ± 2.0	44.7 ± 1.9
HMSNs@Gd/UCST/Dox	349.6 ± 3.0	0.3 ± 0.03	-9.4 ± 0.8	21.7 ± 10.9	10.9 ± 5.3
HMSNs@Gd/LCST/Sor	877.9 ± 62.2	0.5 ± 0.1	-4.2 ± 1.3	12.7 ±13.8	11.9 ±13.0

[a] Hydrodynamic diameter extracted by cumulant analysis of the data.
[b] Polydispersity index from cumulant fitting.
[*] All values represent mean ± standard deviation (n=3).

Table 5. 2 shows an increase in D_{H} compared to parent HMSNs@Gd at 25 °C following the grafting of both UCST and LCST polymers (349.6 ± 3.0 nm and 887.9 ± 62.2 nm, respectively), along with an increase in ζ-potential values (-9.4 ± 0.8 mv and -4.2 ± 1.3 mV, respectively), serves as confirmation of the successful development of all-in-one systems where the polymers effectively cover the negatively charged silica surface.[22] Furthermore, LCST-grafted MSNs appear notably larger because, at 25 °C, they are in an open conformation and therefore observed as larger by DLS.

The DLC% and EE% before and after polymer functionalisation remained relatively consistent in the case of doxorubicin. However, there was a nearly 75% decrease in the sorafenib-loaded system (Table 5. 2). This decrease can be attributed to the sequence of drug loading and polymer grafting, where sorafenib was loaded first before dispersing the loaded MSNs into anhydrous THF for polymer grafting. This process may have caused some solubilisation and release of sorafenib into the solvent during polymer grafting.

The DLS technique especially (derived count rate, kcps) exhibited greater sensitivity in detecting the transition temperature compared to changes in the average sample hydrodynamic diameter (D_H). This heightened sensitivity can be attributed to its strong dependence on aggregate size, which follows a sixth power (D^6) relationship, and the additional increase in count rate due to heightened scattering contrast as a denser, collapsed polymer forms.[11, 23, 24] Employing this approach for these samples, the inflection points observed on each curve signify the transition points. In the case of HMSNs@Gd/UCST/Dox, a sharp decrease in the derived count rate occurred at 38 °C (Figure 5. 17, a). For HMSNs@Gd/LCST/Sor, this transition point was observed at a lower temperature of 34 °C (Figure 5. 17, b). The shift of the transition point to a lower temperature in the case of grafted UCST and a higher temperature in the case of grafted LCST, compared to the free polymer form, has been previously discussed in the literature.[18, 19] Furthermore, the elevation in polydispersity, from 0.3 for doxorubicin-loaded MSNs and 0.5 for sorafenib-loaded MSNs, to values surpassing 1 during the heating process, serves as additional confirmation of the transition, signifying the emergence of multiple distinct populations (Figure 5. 17).

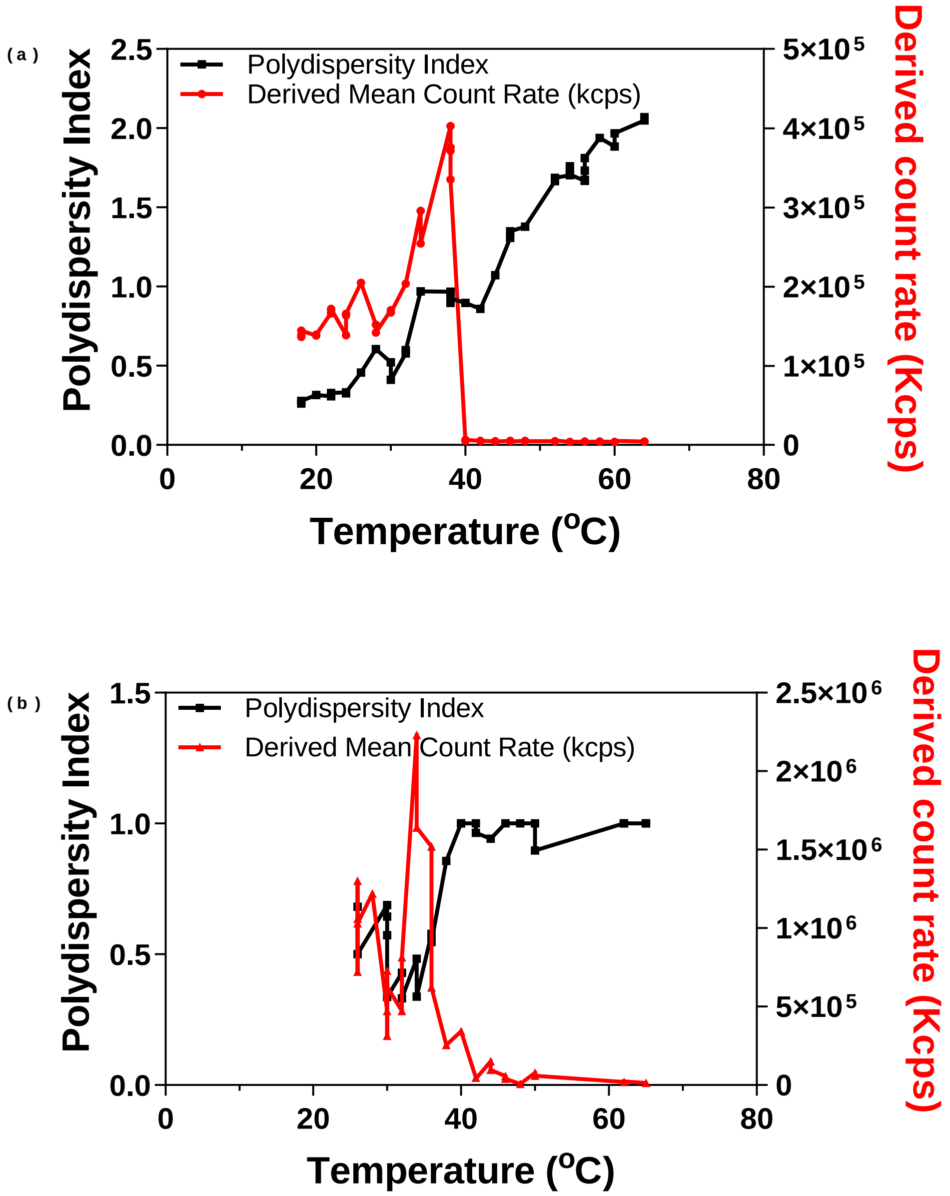

Figure 5. 17: Temperature-dependant DLS data of (a) of HMSNs@Gd/UCST/Dox and (b) of HMSNs@Gd/LCST/Sor in water (5mg/mL).

To evaluate the thermo-responsive drug release capabilities of the developed all-in-one systems, we dispersed the prepared formulations into release media: PBS at pH 7.4 for doxorubicin and PBS at pH 7.4 with 1% w/w Tween 80 for sorafenib. Samples were collected at various time intervals to measure cumulative drug release at temperatures of 25 °C, 37 °C, and 45 °C.

For HMSNs@Gd/UCST/Dox, the cumulative drug release after 24 hours at 37 °C and 45 °C reached a peak of 7.2% and 6.3%, respectively, closely mirroring the ungrafted polymer formulation (HMSNs@Gd/Dox) with a 6.6% cumulative release, indicating that polymer chains have transitioned (or are in the process of transitioning) to their ‘open’ conformation and permit drug release through diffusion. At 25 °C, the maximum drug release percentage was reduced to 2.6% after 6 hours, followed by a slight decrease at 24 h (Figure 5. 18, a). This change in the release profile rate can be attributed to the grafted polymer hindering drug diffusion at 25 °C. At this temperature, the UCST polymer chains aggregate, obstructing the pores. As the temperature increases, the polymer chains gradually open into a soluble coil form, facilitating release.

Figure 5. 18, b illustrates a small gradual rise in sorafenib release upon heating, reaching maximum values of 0.1, 0.2, and 2.7 % after 24 hours at 25, 37, and 45 °C, respectively. However, only the release profile at 45 °C for HMSNs@Gd/LCST/Sor matched that of the parent HMSs@Gd/Sor (2.3% at 37 °C). This is attributed to the open soluble chains of PNIPAm003, which impede the release of the hydrophobic drug sorafenib. This fast release occurs at 45 °C when the transition to insoluble globules is complete.

From these results, we can see that using silane-PEG2K-NH_2 as a spacer still allows the release of the drug at globular insoluble forms. In addition, the chemistry and solubility of the grafted polymers at different temperatures, as well as their chain length, can impact drug release, in addition to the typical conformational transitions.

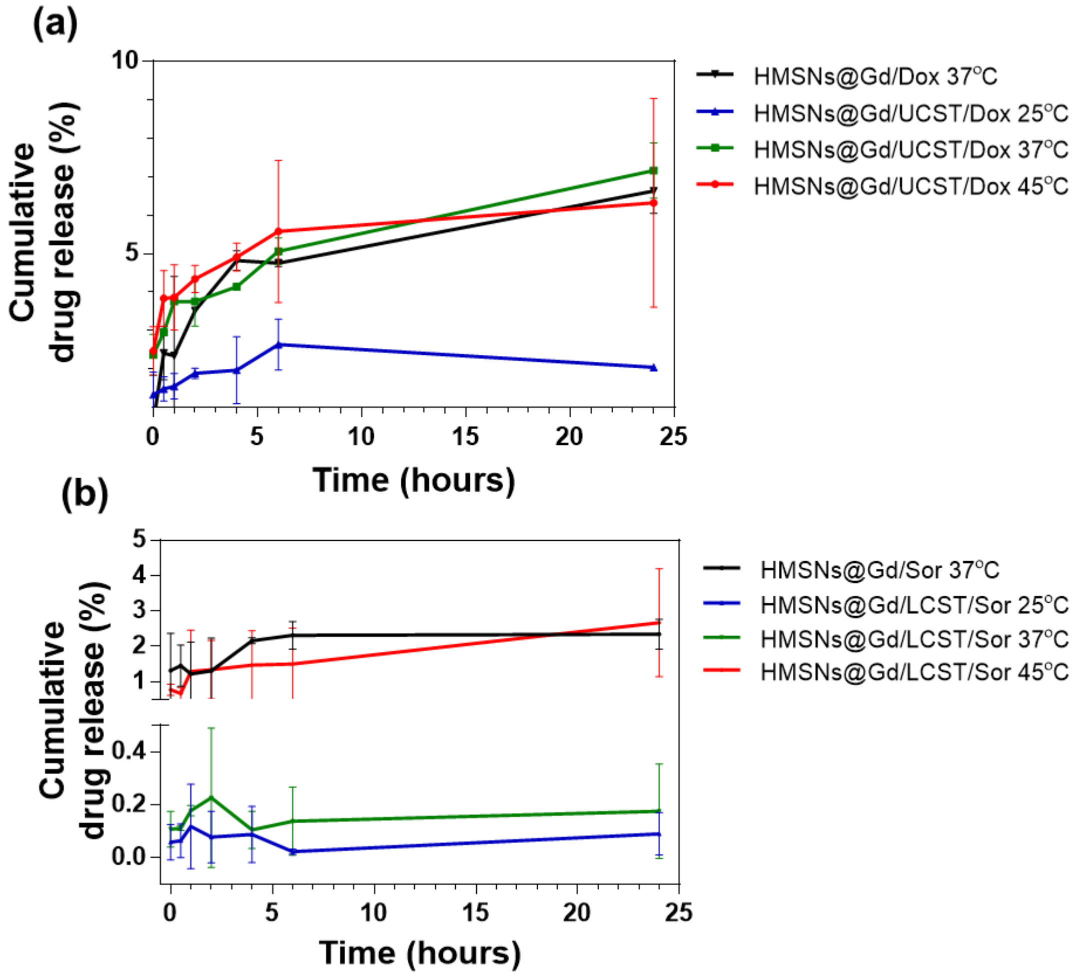

Figure 5. 18: Cumulative drug release profiles for (a) doxorubicin and (b) sorafenib from HMSNs@Gd with or without thermo-responsive polymers, examined at various temperatures. All values represent mean ± standard deviation (n=3 independent syntheses).

To assess the impact of polymer conformational changes and drug release on the MRI signal, we dispersed the prepared systems in their respective drug release media. Subsequently, we recorded the relaxation time and r_1 values at specific time intervals and different temperatures. As discussed in Chapter 3 (Section 3.4.1.2.2), it is important to note that the dispersion media can influence the relaxivity data. Therefore, we also dispersed the control formulations with or without drug (HMSNs@Gd) in either PBS at pH 7.4 for doxorubicin or PBS at pH 7.4 with 1% Tween 80 for sorafenib. In both cases, the control samples without drug exhibited a consistent plateau of relaxivity values during the 6-hour experiment at various temperatures.

In Figure 5. 19a, we observed an increase in r_1 values upon heating HMSNs@Gd/UCST/Dox. At 25 °C, where drug release was minimal due to the UCST polymer being in its globular insoluble form, the relaxivity values remained at very low levels, as expected. At both 37 and 45 °C, the relaxivity profile matched that of the ungrafted HMSNs@Gd/DOX, similar to the drug release data shown in Figure 5. 18a. This change in r_1 as a response to polymer conformational changes has been documented in the literature.[20, 25] It is influenced by water accessibility to the gadolinium chelate within the pores, which is hindered by the globular insoluble form of the polymer. Additionally, the doxorubicin can interact with the DOTA chelate, affecting the local tumbling rate (τ_{RL}) and restricting water diffusion.

When examining LCST-grafted HMSNs@Gd/Sor, the application of heat produced contrasting results (Figure 5. 19, b). As the polymer underwent conformational changes, transitioning into an insoluble globular form as the temperature increased, it impeded water accessibility and lowering relaxivity. Despite an improved drug release profile at 45 °C (Figure 5. 18b), the hydrophobic insoluble characteristics of the LCST polymer had a more pronounced impact on the MRI signal. However, at 25 °C, the r_1 values remained elevated compared to the original HMSNs@Gd/Sor, primarily owing to an increase in the diameter due to the grafted open polymer chain (measuring 349.6 ± 3.0 nm). This contributed to a longer τ_R, although it was unrelated to the drug release process.

The unexpected behaviour observed in Figure 5. 18b finds support in the study conducted by Yuan et al.,[25] where they identified the formation of a water cap region around the polymer-grafted MSNs exhibiting significantly different water mobility. This distinction in water mobility may contribute to varied drug release behaviours, as pertinent to my research. In this scenario, it is plausible that, in the open conformation (at 25 °C), the polymer grafting density or length may not be sufficient to impede drug release, resulting in behaviour similar to the non-polymer-modified particles. Conversely, at higher temperatures and in the closed conformation, the formation of a water cap inhibits the release of the hydrophobic sorafenib.

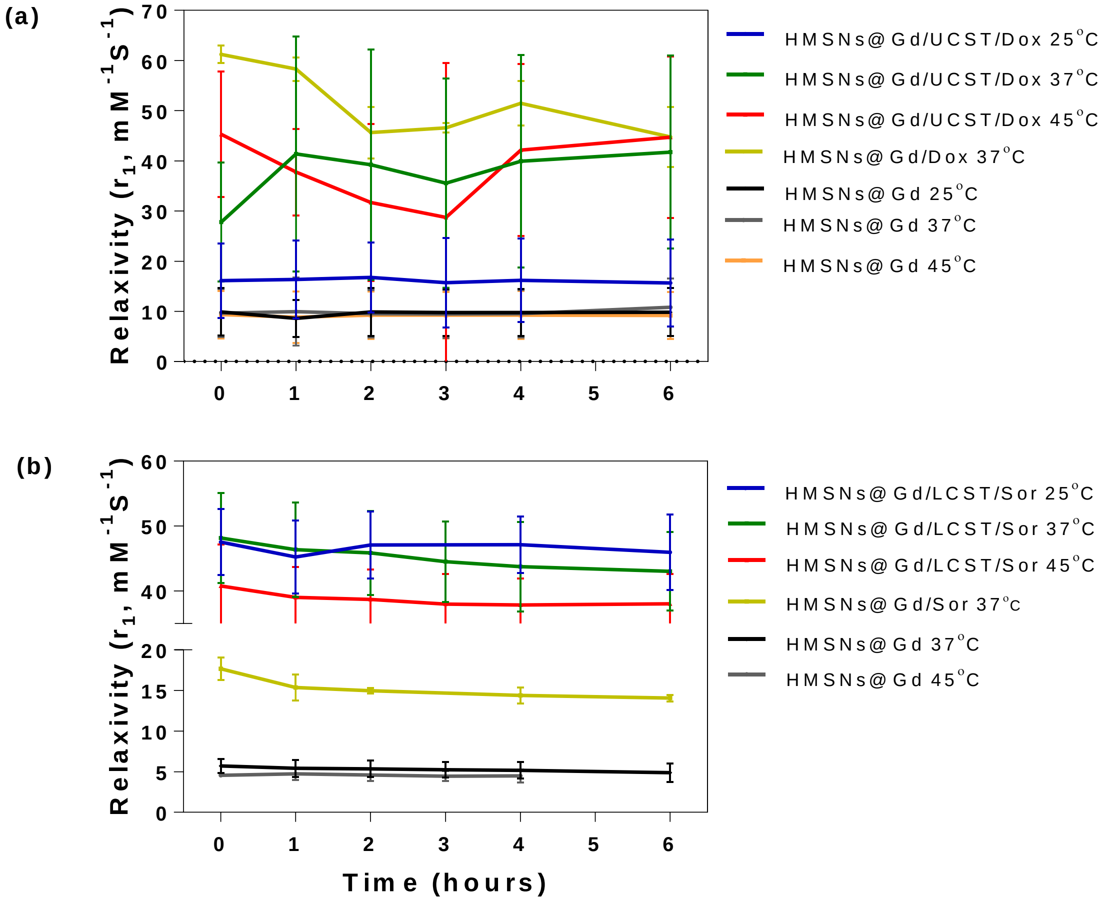

Figure 5. 19: ^{1}H r_1 relaxivities profiles of (a) doxorubicin and (b) sorafenib loaded-HMSNs@Gd with or without thermo-responsive polymers examined at various temperatures. Data collected at 23.4 MHz. All values represent mean ± standard deviation (n=3 independent syntheses).

Nuclear Magnetic Resonance Dispersion (NMRD) analyses were performed to delve into how the thermo-responsive polymer influences the MRI signal across various magnetic field strengths, ranging from 0.01 to 105 MHz at 25 and 37 °C in water. The maximum of this peak is of much interest to us as it can be interpreted by local and global tumbling rate (τ_{RL} and τ_{RG}).

At 25 °C, HMSNs@Gd/LCST exhibited a peak maximum of 11.4 mM^{-1}s^{-1} at 32 MHz, while HMSNs@Gd/UCST displayed a peak maximum of 17.6 mM^{-1}s^{-1} at 42 MHz (Figure 5. 20). The diminished peak maxima at lower frequencies and reduced longitudinal relaxivity values in LCST- grafted MSNs can be ascribed to a lower water exchange rate, influenced by the LCST hydrophilic chains being in an open soluble state at 25 °C. This state may impede diffusion and the water exchange rate with the paramagnetic center inside the pore channels.

In sorafenib-loaded samples, HMSNs@Gd/LCST/Sor displayed an increase in the r_1 value from 18.4 $mM^{-1}s^{-1}$ at 25 °C to 23.6 $mM^{-1}s^{-1}$ at 37 °C, showcasing a 28.3 % rise in relaxivity values (Figure 5.20). This contradicts the behaviour observed in ungrafted HMSNs@Gd/Sor in Chapter 3 (Section 3.4.2.2), where relaxivity values decreased with heating. This inconsistency underscores the effect of polymer conformational changes. At higher temperatures, the insoluble polymer chain contracts and collapses, enabling water access and interaction with the Gd-chelate. Similar temperature-responsive behaviour was noted in HMSNs@Gd/UCST/Dox, where r_1 increased from 20.8 $mM^{-1}s^{-1}$ to 24.4 $mM^{-1}s^{-1}$, reflecting a 17.3 % increase upon heating from 25 °C to 37 °C (Figure 5.20).

Although UCST undergoes a conformational change to a soluble, open hydrophilic coil when heated, the increase in size can contribute to a decrease in tumbling rate τ_R and, subsequently, r_1. The peak maxima also shifted to a lower frequency, from 32 MHz to 22 MHz, indicating a slower water exchange.

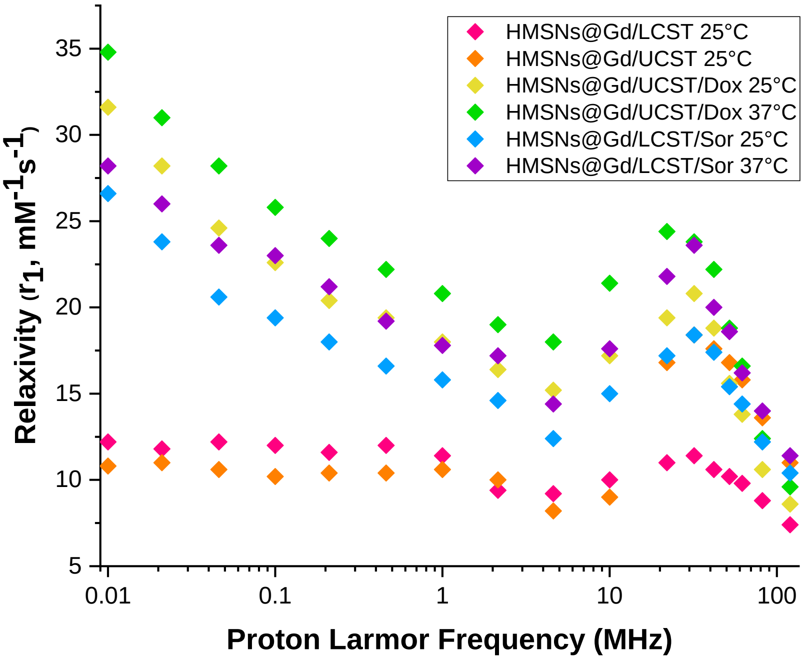

Figure 5. 20: ^{1}H NMRD profiles of HMSNs@Gd/LCST and HMSNs@Gd/UCSt with and without drug at 298 K and 318 K.

T1-weighted images were obtained using a 3T MRI scanner to assess the impact of polymer grafting and drug loading in our developed theranostic MSNs on MRI signal characteristics. It was found that the grafting of both polymers in HMSNs@Gd/UCST and HSNs@Gd/LCST appears to extend the T_1 relaxation time at all different temperatures, as shown in Figure 5. 21. This observation highlights the significance of not only polymer transition but also the length of polymer chains in influencing the MRI signal. Notably, these factors can even influence and disrupt water diffusion within the pores housing the Gd-chelates.

In a direct comparison between the relaxation times of the all-in-one theranostic system HMSNs@Gd/UCST/Dox and HMSNs@Gd/UCST, an interesting result came to light. The introduction of drug loading substantially enhanced the MRI signal by accelerating the T_1 relaxation time, particularly during the application of heat. This effect was most prominent at 48 °C, where the T_1 time decreased from 2 ms to 1 ms (Figure 5. 21). It is worth noting that our earlier drug release study (Figure 5. 18) indicated that drug release reached its peak when exposed to a temperature of 45 °C.

Comparing HMSNs@Gd/LCST/Sor to HMSNs@Gd/LCST, we observed longer T_1 values at 25 °C in the drug loaded MSNs, which diminished to half of their initial values at 45 °C. This enhanced MRI signal (with decreased T_1 values) can be attributed to the displacement of the drug by water within the pores, which promotes interaction with the paramagnetic centre and consequentially leads to a reduction in the relaxation time.[27, 28]

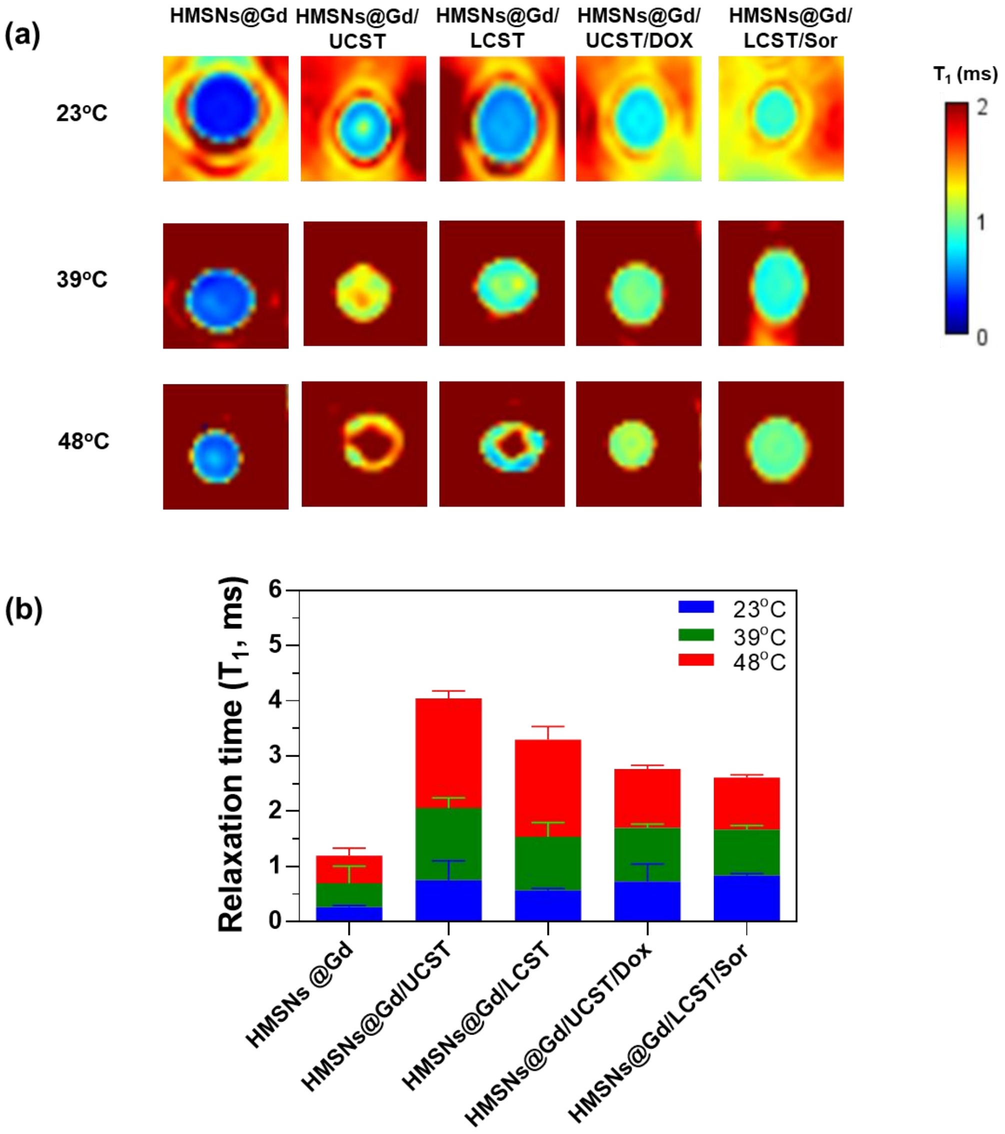

Figure 5. 21: MRI phantom imaging where (a) T1-weighed maps (0-2 ms scale), and (b) T1-weighed relaxation time are recorded at varying temperature at 3T. [Gd^{3+}] = 0.05 mM.

To assess the impact of the prepared systems on cell viability, we employed the PrestoBlue™ cell viability reagent, a resazurin-based metabolic assay designed to identify metabolically active cells. When introduced to cells, the PrestoBlue™ reagent undergoes a colour change, turning pink (resorufin), owing to the reducing environment of viable cells.[28] This alteration in colour was detected through absorbance measurements at both 570 nm and 600 nm. The resulting data can be represented as the percentage reduction of the PrestoBlue™ reagent, which correlates with cell viability using Equation 5. 1:

$$\%Reduction\ of\ PrestoBlue^{™}\ reagent = \frac{(O2 \times A1) - (O1 \times A2)}{(R1 \times N2) - (R2 \times N1)} \times 100$$

Equation 5. 1

Where:

O1=molar extinction coefficient of oxidized PrestoBlue™ reagent at 570 nm (80586).

O2=molar extinction coefficient of oxidized PrestoBlue™ reagent at 600 nm (117216).

R1= molar extinction coefficient of reduced PrestoBlue™ reagent at 570 nm (155677).

R2= molar extinction coefficient of reduced PrestoBlue™ reagent at 600 nm (14652).

A1=absorbance of test wells at 570 nm A2=absorbance of test wells at 600 nm.

N1=absorbance of media only wells at 570 nm.

N2=absorbance of media only wells at 600 nm.

Both human liver cancer cells (Huh-7) and human embryonic kidney cells (HEK 293) were treated with different doses of free and loaded drug in HMSNs@Gd with and without polymer (0.2 µg/mL to 50 µg/mL). In the case of doxorubicin, both HMSNs@Gd/Dox and HMSNs@Gd/UCST/Dox exhibited cell viability levels exceeding 80% and 90%, respectively when compared to untreated control cells in healthy HEK 293 cells. This stands in contrast to the free drug solution, which led to a significant decrease in viability when the dose was increased to 50 µg/mL, as opposed to doses of 0.2 and 0.5 µg/mL (resulting in p-values of 0.03 and 0.02, respectively) as shown in Figure 5. 22.

The cell viability of liver cancer cells (Huh-7) following treatment with both Dox-loaded MSNs, with or without polymer at various doses, did not appear to differ significantly from that of healthy HEK 293 cells. Furthermore, the impact of dose escalation on these formulations was found to be inconsequential. However, Huh-7 cells displayed a heightened sensitivity to free Dox solution, exhibiting a notable dose-dependent response. This sensitivity was evident through a substantial reduction in cell viability following treatment with 2.5, 10, and 50 µg/mL, with p-values lower than 0.05 in comparison to doses of 0.2, 0.5, and 1 µg/mL as displayed in Figure 5. 22.

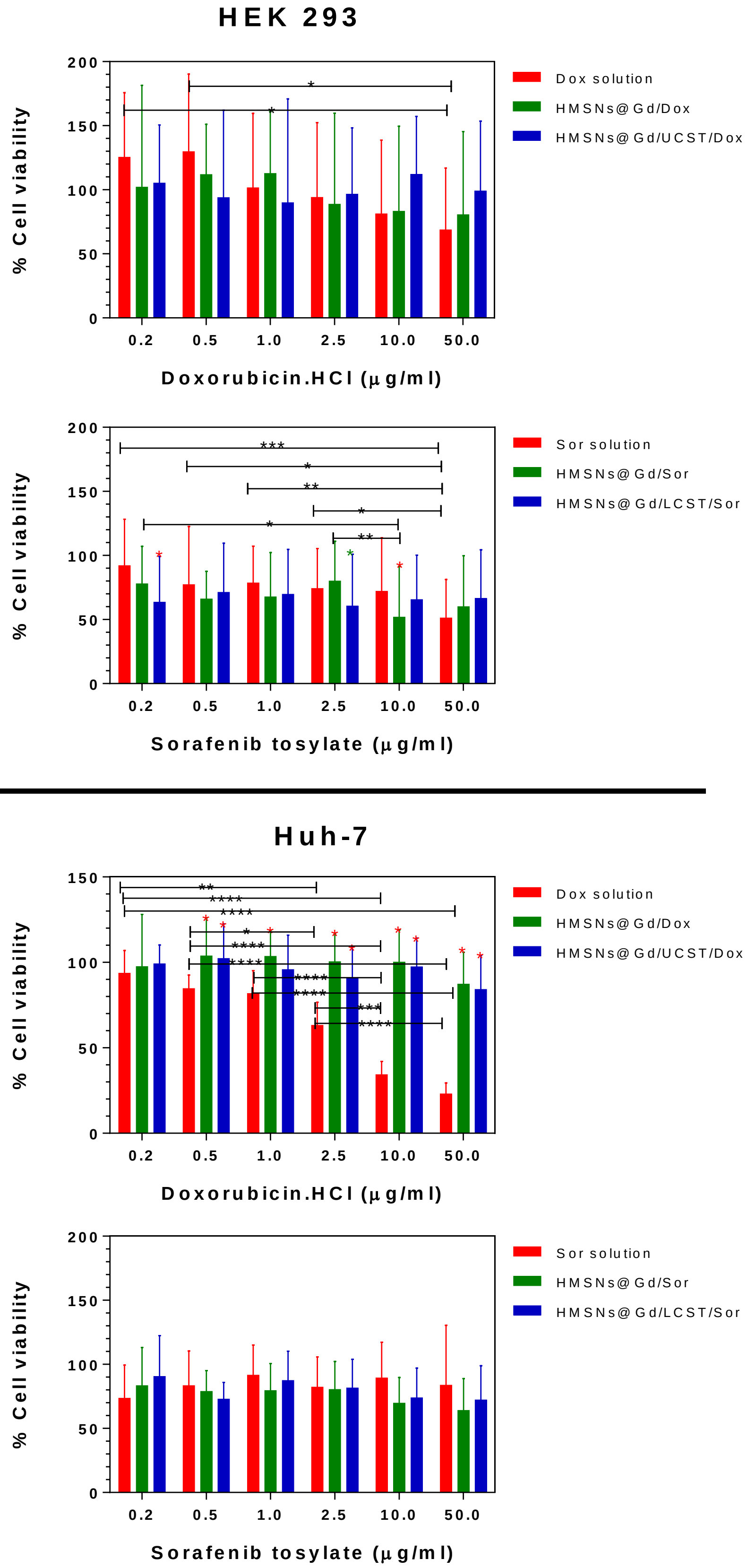

*Figure 5. 22:Cell viability of doxorubicin and sorafenib tosylate both free and loaded into HMSNs@Gd, with or without grafted polymer, in human embryonic kidney (HEK 293) and human liver cancer cells (Huh-7). All the values are expressed as mean ± standard deviation; n = 3, **** $p < 0.0001$, *** $p < 0.001$, and ** $p < 0.01$ and * $p < 0.05$.*

To facilitate a comprehensive comparison across all formulations, the half-maximal inhibitory concentration (IC50) was calculated. In this regard, the doxorubicin solution displayed IC50 values of 96.32 and 4.901 µg/mL for HEK 293 and Huh-7 cells, respectively (Figure 5. 23). These values were notably lower than those observed for both HMSNs@Gd/Dox and HMSNs@Gd/UCST/Dox, reflecting the slower and controlled release of the drug from these formulations.

For sorafenib, HEK 293 cells exhibited greater sensitivity to the drug in both the loaded and free forms. However, for the loaded MSNs, cell viability was notably higher than with free drug treatment, especially at the highest dose of 50 µg/mL. Furthermore, the free drug displayed a clear dose-dependent cytotoxicity relationship, as a substantial decrease in viability was evident with increasing doses, particularly at 10 and 50 µg/mL (Figure 5. 22).

In the case of liver cancer cells (Huh-7), there was no significant difference between the loaded and unloaded sorafenib formulations. Nevertheless, the cytotoxicity appeared qualitatively more pronounced with the sorafenib-loaded formulations HMSNs@Gd/Sor and HMSNs@Gd/LCST/Sor (Figure 5. 22).

The IC50 values for HMSNs@Gd/LCST/Sor were 41.16 and 84.25 µg/mL in HEK 293 cells and Huh-7 cells, respectively. In contrast, the free sorafenib solution exhibited a lower IC50 (32.13 µg/mL) for HEK 293 cells and a higher IC50 (201 µg/mL) for Huh-7 cells (Figure 5. 23). These findings indicate that HMSNs@Gd/LCST/Sor promotes better viability in healthy cells and exerts a more pronounced cytotoxic effect on liver cancer cells when compared to the free drug.

However, it is worth noting that the IC50 of HMSNs@Gd/LCST/Sor for Huh-7 cells remains higher than that for HEK 293 cells. This issue could potentially be solved through the developed stimuli-responsive controlled drug release system. Such a system, when coupled with localised hyperthermia, would enable targeted drug release, selectively affecting cancerous cells while sparing the healthy ones. This approach holds promise for mitigating cytotoxicity and reducing severe side effects.

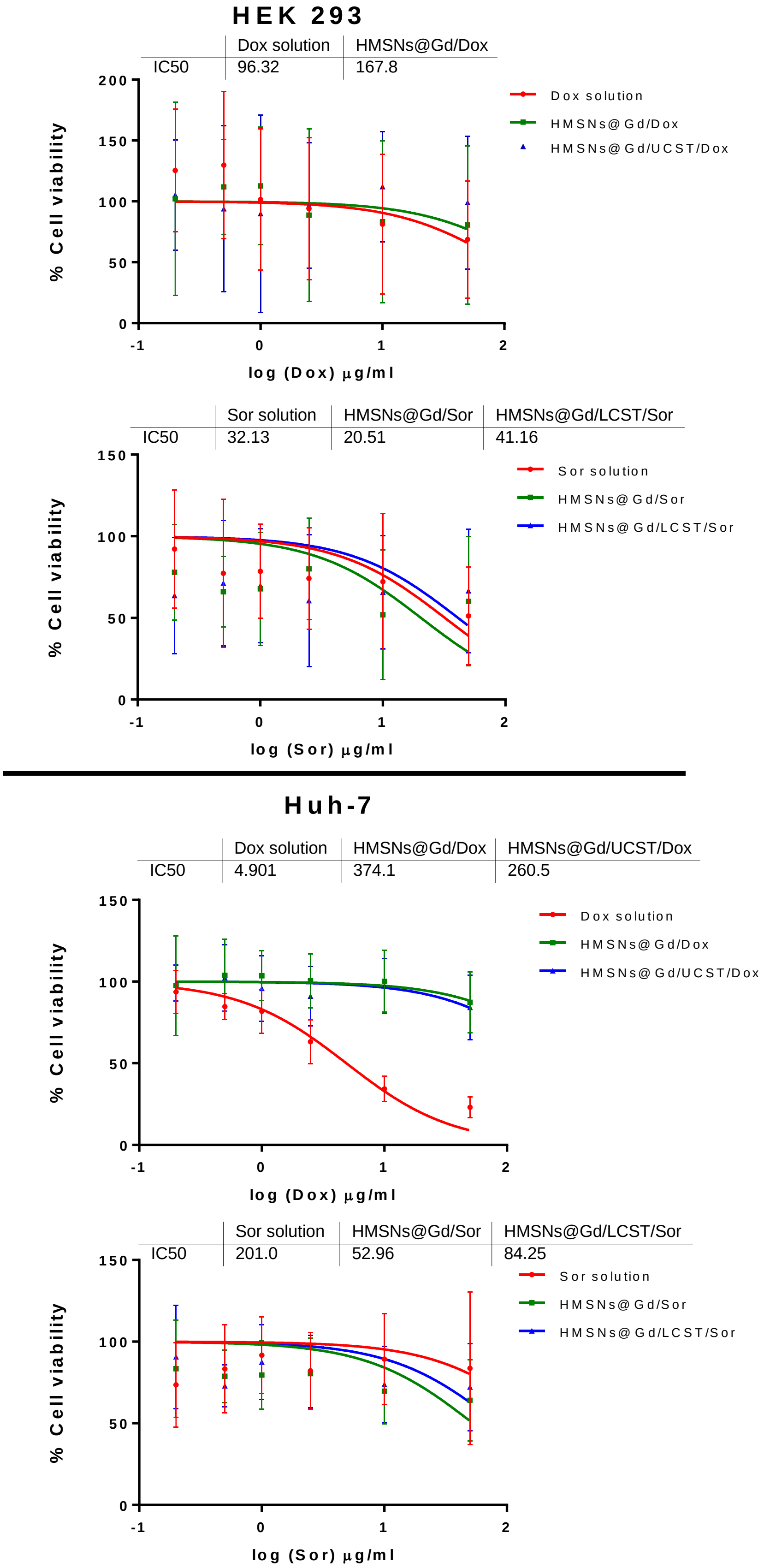

HEK 293

	Dox solution	HMSNs@Gd/Dox
IC50	96.32	167.8

	Sor solution	HMSNs@Gd/Sor	HMSNs@Gd/LCST/Sor
IC50	32.13	20.51	41.16

Huh-7

	Dox solution	HMSNs@Gd/Dox	HMSNs@Gd/UCST/Dox
IC50	4.901	374.1	260.5

	Sor solution	HMSNs@Gd/Sor	HMSNs@Gd/LCST/Sor
IC50	201.0	52.96	84.25

Figure 5. 23:Dose-response curve used to calculate half maximal inhibitory concentration (IC50) values of doxorubicin and sorafenib tosylate both free and loaded into HMSNs@Gd, with or without grafted polymer, in human embryonic kidney cells (HEK 293) and human liver cancer cells (Huh-7). All the values are expressed as mean ± standard deviation; n = 3.

5.5 Conclusions

In this chapter, we explored the successful grafting of APTES or silane-PEG2K-NH_2 linkers onto MSNs' surface, examining the effects of grafting density, polymer chain length, and linker length through turbidimetry and relaxivity studies. Grafting LCST onto MSNs led to an increased transition temperature compared to the free polymer, dependent on the polymer grafting percentage. Single-field relaxation studies showed that the grafting density of PNIPAm002 impacted relaxivity response at varying temperatures. For example, at 45 °C, 0.2 mol% and 1 mol% grafting density resulted in a 15.3% and 14.7% decrease in r_1 compared to parent HMSNs@Gd. Conversely, 2.5 mol% grafting inhibited water accessibility to Gd-chelate at 25 °C, reducing r1 by 52% compared to parent HMSNs. However, at 45 °C, the polymer underwent a collapsed contraction, allowing water accessibility and resulting in nearly similar r_1 to the parent HMSNs@Gd.

To assess the effect of the linker on MRI signal, we employed both APTES and silane-PEG2K-NH2 with PNIPAM002. MSNs grafted with silane-PEG2K-NH_2 were more responsive to temperature change, displaying a 50% increase in r1 upon heating compared to the parent HMSNs@Gd, whereas using APTES only resulted in a 10% increase. Therefore, we chose to use silane-PEG2K-NH2 to create an all-in-one theranostic thermo-responsive system.

In developing the all-in-one MSNs, we selected PNIPAm003 and UPD1-R as LCST and UCST polymers, respectively, to be grafted onto MSNs using silane-PEG2K-NH_2. Sorafenib and doxorubicin loading was applied to the MSNs to produce HMSNs@Gd/LCST/Sor and HMSNs@Gd/UCST/Dox. The synthesis was confirmed using TGA, DLS, and TEM before evaluating the effect of the thermo-responsive polymer grafting on drug release at different temperatures (25, 37, and 45 °C). HMSNs@Gd/UCST/Dox showed cumulative drug release percentages similar to the ungrafted polymer HMSNs@Gd/Dox at both 37 and 45 °C (7.2% and 6.3%, respectively). However, at 25 °C, a minor release of 2.6% was observed. In contrast, HMSNs@Gd/LCST/Sor showed negligible sorafenib release at 25 and 37 °C (0.1% and 0.2%, respectively), but at 45 °C, the drug release was 2.7%, similar to the release of sorafenib from ungrafted polymer HMSNs@Gd/Sor at 37 °C (2.3%). The change in the release profile rate at 25 °C can be attributed to the grafted polymer hindering drug diffusion, whereas at 45 °C, the transition to insoluble globules is complete, facilitating faster release.

Finally, we examined the all-in-one system's behaviour using relaxivity studies. In the case of HMSNs@Gd/UCST/Dox, r_1 remained low at 25 °C compared to the polymer ungrafted HMSNs@Gd/Dox, while r_1 matched the parent at 37 and 45 °C. This change in r_1 as a response to polymer conformational changes is influenced by water accessibility to the gadolinium chelate within the pores. When examining LCST-grafted HMSNs@Gd/Sor, the application of heat produced contrasting results. As the polymer underwent conformational changes, transitioning into an insoluble globular form as the temperature increased, it impeded water accessibility and lowered relaxivity. However, at 25 °C, the r_1 values remained elevated compared to the original HMSNs@Gd/Sor, primarily owing to an increase in diameter due to the grafted open polymer chain. This contributed to a longer τ_R.

In the cell viability assessment using PrestoBlue™ reagent, we tested various formulations on human liver cancer cells (Huh-7) and human embryonic kidney cells (HEK 293). Doxorubicin-loaded MSNs (HMSNs@Gd/Dox and HMSNs@Gd/UCST/Dox) exhibited cell viabilities over 80% and 90%, respectively, in HEK 293 cells, contrasting with a significant decrease in viability with free doxorubicin as the dose was raised to 50 µg/mL. Huh-7 cells showed heightened sensitivity to free doxorubicin, displaying a dose-dependent response.

The half-maximal inhibitory concentration (IC50) was calculated to enable comparison across formulations. For doxorubicin, the IC50 values were considerably lower for the solution (96.32 µg/mL for HEK 293 and 4.901 µg/mL for Huh-7) compared to both HMSNs@Gd/Dox and HMSNs@Gd/UCST/Dox, reflecting the controlled drug release. In the case of sorafenib, HEK 293 cells were more sensitive to both the loaded and free forms, with notably higher cell viability in the loaded MSNs at the highest dose (50 µg/mL). The IC50 values for HMSNs@Gd/LCST/Sor were 41.16 µg/mL and 84.25 µg/mL in HEK 293 and Huh-7 cells, respectively.

These findings suggest that using silane-PEG2K-NH2 as a spacer still allows drug release in globular insoluble forms. The chemistry, solubility of the grafted polymers at different temperatures, and their chain length can impact drug release, in addition to the typical conformational transitions. Moreover, HMSNs@Gd/LCST/Sor promotes better viability in healthy cells and exerts a stronger cytotoxic effect on liver cancer cells compared to the free drug, presenting potential for controlled drug release in targeted cancer treatment when combined with localised hyperthermia.

5.6 References

1. F. Bray, J. Ferlay, et al., CA: A Cancer Journal for Clinicians, 2018, 68, 394-424.
2. J. M. Llovet, R. K. Kelley, et al., Nature Reviews Disease Primers, 2021, 7, 6.
3. D. Wang, H. Lin, et al., ACS Applied Materials & Interfaces, 2018, 10, 31114-31123.
4. L. Yu, Y. Chen, et al., Biomaterials, 2018, 161, 292-305.
5. A. Baliś, K. Wolski, et al., Polymers, 2020, 12, 888.
6. C. Li, Y. Zhang, et al., Advanced Materials, 2018, 30, 1706150.
7. G. Zhang, M. Yang, et al., ACS Applied Materials & Interfaces, 2014, 6, 8042-8047.
8. D. Wang, X. Li, et al., Int J Nanomedicine, 2019, 14, 7665-7679.
9. B. Hildebrandt, P. Wust, et al., Crit Rev Oncol Hematol, 2002, 43, 33-56.
10. P. R. Stauffer, Int J Hyperthermia, 2005, 21, 731-744.
11. M. Schroffenegger, R. Zirbs, et al., Polymers, 2018, 10, 451.
12. Y. Zhu, M. Zhang, et al., Journal of Drug Delivery Science and Technology, 2022, 70, 103197.
13. Z. Tian, X. Yu, et al., Microporous and Mesoporous Materials, 2018, 256, 1-9.
14. M. Hei, J. Wang, et al., J Mater Chem B, 2017, 5, 9497-9501.
15. S. Ramezanian, J. Moghaddas, et al., 2023.
16. J.-H. Park, J.-W. Jang, et al., International Journal of Polymer Science, 2019, 2019, 3824207.
17. J. Hu, X. Liu, et al., Biomacromolecules, 2023, 24, 1345-1354.
18. E. D. H. Mansfield, S. K. Filippov, et al., Journal of Colloid and Interface Science, 2021, 590, 249-259.
19. K. I. S. Mongcopa, R. Poling-Skutvik, et al., Soft Matter, 2018, 14, 6102-6108.
20. J. Pellico, C. M. Ellis, et al., Chemical Communications, 2019, 55, 8540-8543.

21. M. Bouchoucha, R. C.-Gaudreault, et al., Advanced Functional Materials, 2014, 24, 5911-5923.
22. E. Guisasola, A. Baeza, et al., RSC Advances, 2016, 6, 42510-42516.
23. C. Lavigueur, J. G. García, et al., Polymer Chemistry, 2011, 2, 333-340.
24. L. Massi, A. Najer, et al., Journal of Materials Chemistry B, 2020, 8, 8894-8907.
25. D. Yuan, C. M. Ellis, et al., Chemical Communications, 2023, 59, 6008-6011.
26. Z. Zhang, Y. Wang, et al., Biomaterials Advances, 2022, 134, 112716.
27. Z. Zhang, C. J. R. Wells, et al., International Journal of Pharmaceutics, 2021, 609, 121155.
28. N. Lall, C. J. Henley-Smith, et al., Int J Microbiol, 2013, 2013, 420601.

Chapter 6.

Conclusions and future work

6.1 Conclusions

In this thesis, we embarked on a multifaceted exploration aimed at advancing the field of stimuli-responsive theranostics. Our journey unfolded across several chapters, each addressing crucial aspects of developing an efficient theranostic system for hepatocellular carcinoma (HCC).

In Chapter two, we delved into an exhaustive investigation of the factors affecting the loading of doxorubicin HCl (a hydrophilic drug) and sorafenib tosylate (a hydrophobic drug) into MSNs. Through meticulous exploration, we uncovered that the optimal loading capacities were achieved by employing hydrophilic mesoporous silica nanoparticles (HMSNs) and hydrophobic mesoporous silica nanoparticles (HPMSNs) with a weight ratio of 2:1 and 1:1 (drug to silica, w/w) for doxorubicin and sorafenib, respectively. In the subsequent stage of preparation and characterisation processes outlined in this chapter, we carefully selected the adsorption loading technique using an aqueous doxorubicin solution and the evaporation method utilising tetrahydrofuran (THF) as the solvent for the hydrophobic sorafenib loading. These methods were strategically chosen to ensure efficient drug loading and to facilitate a comprehensive characterisation of the drug-loaded mesoporous silica nanoparticles.

Additionally, in Chapter three, we embarked on a thorough exploration of several crucial factors essential for optimising a theranostic MRI-active MSNs. Among the factors scrutinised, the placement of the Gd-chelate within the pore channel of the silica nanoparticles, as well as the presence of the drug, surfaced as notably significant elements profoundly influencing the system's performance. Our findings unequivocally showcased the pivotal role played by the precise location of the Gd-chelate within the nanoparticle's pore channel in enabling the system to function as an effective theranostic agent. While this trend slightly deviated from previously reported works,[1, 2] it became evident that our system's uniqueness stemmed from the varying amounts of grafted Gd in the core of the pores channel, resulting in distinct behaviour. By strategically positioning the Gd-chelate, we could amplify the interaction of the contrast agent with the surrounding environment, leading to a more accurate and sensitive MRI signal. Moreover, our research underscored the intricate interplay between the drug and the contrast agent within the theranostic system. The presence of the drug emerged as a potent modulator of MRI signal intensity across different field strengths. This modulation presented an opportunity to monitor the drug's distribution and assess the treatment's effectiveness. One profound takeaway from our investigation was the significance of isolating and meticulously studying individual factors when analysing their impact on MRI signal intensity. Understanding the effect of a specific factor necessitated keeping other parameters fixed to ensure precise and reliable results. Furthermore, as we navigated through the development of the theranostic system, we gained a deeper appreciation for the complexity of this process. It demanded careful consideration of its potential effects on the MRI signal. Variations in the system, such as drug release, could introduce variability in the MRI signal, highlighting the need for a comprehensive understanding of these alterations to accurately interpret imaging data.

Furthermore, Chapter four magnifies the significance and success in fine-tuning the transition temperature of UCST poly(AAm-co-AN) to align with biomedical applications. This fine-tuning was achieved through adept manipulation of the monomer molar ratio (ranging from 1:1, 1.5:1 to 2:1 of AAM: AN) and polymerisation time (spanning 16, 20, and 24 hours). Employing the Design of Experiments (DoE), we could develop a predictive model enabling the accurate prediction of the molecular weight of the resultant polymer. Within this exploration, a spectrum of UCSTs was obtained, ranging from 27.9 °C to 39.9 °C. Among these, polymer UPD1-R possessing a UCST of 36.5 °C emerged as a polymer with a transition temperature perfectly suited for biomedical applications. This promising result propels us forward into future work with this polymer, anticipating its substantial contribution to the realm of biomedical applications. Additionally, RAFT synthesis of PNIPAm with NHS ester at varied degrees of polymerisation (10, 120, 400) yielded a molecular weight range of 2400-68000 g/mol, demonstrating low dispersity and high homogeneity. Surprisingly, despite the substantial increase in molecular weight, the LCST exhibited only a slight shift from 32.9 to 36.4 °C, consistent with prior research.

Chapter 5 ushered us into a realm of promising advancements as we delved into the successful grafting of APTES or silane-PEG2K-NH_2 linkers onto the surface of MSNs. Our exploration encompassed a considerate examination of the effects of grafting density, polymer chain length, and linker length through comprehensive turbidimetry and relaxivity studies. The grafting of LCST onto MSNs evidenced an increased transition temperature compared to the free polymer, contingent upon the polymer grafting percentage. Moreover, our research elucidated the impact of PNIPAm grafting density on relaxivity response across varying temperatures, highlighting a decrease in r_1 at 45 °C with grafting densities of 0.2 mol% and 1 mol%. Conversely, a higher grafting density of 2.5 mol% exhibited a significant reduction in r_1 at 25°C due to hindered water accessibility to the Gd-chelate, but nearly restored r_1 to parent levels at 45 °C following a polymer contraction. Moreover, the preference for silane-PEG2K-NH_2 in MSNs grafting was affirmed, exhibiting a substantial 50% increase in r_1 upon temperature elevation, indicating its suitability for constructing a versatile all-in-one theranostic thermo-responsive system compared to the relatively modest 10% increase observed with APTES. In our pursuit to develop a comprehensive all-in-one MSN system, we carefully selected PNIPAm003 and UPD1-R as the LCST and UCST polymers to be grafted onto MSNs using silane-PEG2K-NH_2. With great precision, we applied sorafenib and doxorubicin loading to the MSNs, resulting in the creation of HMSNs@Gd/LCST/Sor and HMSNs@Gd/UCST/Dox. The synthesis was methodically confirmed using thermal gravimetric analysis (TGA) and dynamic light scattering (DLS) before proceeding to evaluate the effect of thermo-responsive polymer grafting on drug release at different temperatures (25, 37, and 45 °C). HMSNs@Gd/UCST/Dox exhibited drug release comparable to ungrafted HMSNs@Gd/Dox at 37 and 45 °C (7.2% and 6.3%, respectively). However, a minor release of 2.6% was observed at 25 °C. On the other hand, HMSNs@Gd/LCST/Sor demonstrated minimal sorafenib release at both 25 and 37 °C. The behaviour of the all-in-one system was assessed through relaxivity studies, revealing that in HMSNs@Gd/UCST/Dox, r_1 remained low at 25°C compared to ungrafted HMSNs@Gd/Dox but matched the parent at higher temperatures (37 and 45 °C). Changes in r_1 were influenced by polymer conformational shifts and water accessibility to the gadolinium chelate within the pores. Conversely, for LCST-grafted HMSNs@Gd/Sor, heating caused the polymer to transition into an insoluble globular form, reducing relaxivity due to restricted water accessibility. Notably, in cell viability tests, doxorubicin-loaded MSNs (HMSNs@Gd/Dox and HMSNs@Gd/UCST/Dox) exhibited high cell viabilities in HEK 293 cells, while Huh-7 cells showed increased sensitivity to free doxorubicin. The calculated half-maximal inhibitory concentrations (IC_{50}) for doxorubicin indicated lower values for the solution compared to the loaded forms, reflecting controlled drug release. Additionally, HMSNs@Gd/LCST/Sor displayed better viability in healthy cells and stronger cytotoxic effects on liver cancer cells compared to the free drug, demonstrating potential for controlled drug release in targeted cancer treatment when combined with localised hyperthermia. The study highlights the complex interplay of grafted polymers, temperature, and drug release dynamics in enhancing therapeutic outcomes.

In summary, the optimal drug loading ratios and techniques for MSNs are affirmed, setting a strong foundation for further drug delivery research. The pivotal role of the Gd-chelate location and drug presence in the theranostic system is portrayed, paving the way for more refined MRI contrast agents. The controlled tuning of UCST polymer transition temperatures is recognised as a breakthrough, with promising potential for biomedical applications. The successful grafting of linkers and polymers onto MSNs represents a significant advancement, allowing for controlled drug release. Finally, the exciting results in terms of cell viability assessments suggest the potential of these theranostic systems in targeted cancer treatment, laying the groundwork for future research directions in precision medicine and nanomedicine.

6.2 Future work

In future research, building upon the insights from Chapter 3, it is imperative to conduct further experiments and replicates focusing on varying the hydrophobicity of MSNs and pore size to deeply investigate their influence on water accessibility to the Gd-chelate contrast agent within MRI-active MSNs. Furthermore, in Chapter 4, enhancing the effectiveness of the Design of Experiment (DoE) method in predicting the transition temperature necessitates conducting additional replicates for each polymer and incorporating multiple centre points to ascertain the predictive power of UCST.

Moving forward to Chapter 5, a crucial area of exploration involves conducting *in vitro* cytotoxicity studies on the all-in-one thermo-responsive system at different temperatures, particularly at 45 °C, to better comprehend the effect of hyperthermia on drug release attributed to polymer conformational changes. Additionally, it is important to delve into cellular uptake investigations to validate the uptake and elucidate the mechanisms of cellular uptake at varying temperatures.

For the subsequent phases of the research, incorporating HCC (hepatocellular carcinoma) targeting is vital. This includes initial selection and evaluation of established clinically-validated HCC targeting units like alpha-fetoprotein (AFP) as well as promising non-clinical targeting units such as GPC3 (Glypican-3) to be immobilised on polymer-nanoparticles, followed by *in vitro* targeting studies.

Finally, establishing the practical therapeutic dose of the drug presents considerable challenges, particularly when employing MSNs as carriers. Although the market suggests an oral tablet dosage of 400 mg twice daily, the drug's bioavailability is significantly low, fluctuating between 38% and 49%. Significantly, available literature on nanomedicine formulations incorporating sorafenib indicates variations in *in vivo* dosing methods, including intravenous, intraperitoneal, and oral administration. These variations are influenced by the loading and release characteristics inherent in their respective dosage forms.[3-6] Consequently, specifying an exact dosage proves intricate without conducting a comprehensive pharmacokinetics study of the entire system.

Therefore, essential in vivo studies must be undertaken, encompassing pharmacokinetics determination, biodistribution studies, and assessments of antitumour efficacy. This entails ethically sourcing cancerous and non-cancerous tissue sections for measuring tumour volume and employing various analytical and MR imaging techniques for a thorough evaluation of the theranostic response.

6.3 References

1. K. He, J. Li, et al., Journal of Materials Chemistry B, 2019, **7**, 6840-6854.
2. F. Carniato, M. Muñoz-Úbeda, et al., Dalton Transactions, 2015, **44**, 17927-17931.
3. S. Yang, B. Zhang, et al., International Journal of Nanomedicine, 2016, **11**, 2329-2343.
4. G. Tom, S. Philip, et al., Life Sciences, 2018, **206**, 10-21.
5. S. Feng, J. Zhou, et al., Colloids and Surfaces B: Biointerfaces, 2019, **184**, 110498.
6. Y. Su, K. Wang, et al., Nanomedicine, 2018, **13**, 1009-1023.